Characterisation of the surface reactions and gas sensing properties of zinc oxide nanosheets.

Jones, Daniel Raymond

Characterisation of the surface reactions and gas sensing properties of zinc oxide nanosheets

Daniel Raymond Jones

Submitted to Swansea University in fulfilment of the requirements for the Degree of Doctor of Philosophy

Swansea University

2015

ProQuest LLC.
789 East Eisenhower Parkway
P.O. Box 1346
Ann Arbor, MI 48106 – 1346

Abstract

In this work, zinc oxide nanosheets are synthesised through thermal decomposition of a layered basic zinc acetate precursor and implemented in sensors to investigate the reactions of carbon monoxide, hydrogen and methane. The mean size of nanoparticles within the nanosheets is shown to increase with annealing temperature, and sintering occurs after heating at temperatures of 700°C or higher. X-ray photoelectron and photoluminescence spectroscopy techniques demonstrate that the concentrations of both lattice oxygen species and oxygen-containing surface groups may be enhanced by increasing the annealing temperature.

By using an Eley-Rideal-based physical model, the responses of the nanosheets to carbon monoxide are quantitatively related to the reaction parameters of the system. The response characteristics suggest that the carbon monoxide oxidation has activation energy 54 ± 9 kJ mol^{-1} while oxygen ionosorption has an energy barrier of 72 ± 9 kJ mol^{-1}. The sensor recoveries are consistent with corresponding values of 42 ± 7 kJ mol^{-1} and 63 ± 10 kJ mol^{-1} for carbon monoxide oxidation and oxygen ionosorption, respectively. In the absence of O^- or CO_2^- surface ions, the energy difference between the Fermi level and the conduction band minimum at the surface is estimated as 590 ± 90 meV at temperatures close to 400°C.

The hydrogen responses of non-functionalised sensors are found to converge at 440°C, despite differing at lower temperatures. This observation is incompatible with the developed model, but it is shown that the phenomenon may be rationalised by considering that the hydrogen concentration close to the sensor surface is decreased due to the rapidity of hydrogen oxidation. Gold nanoparticles significantly enhance the hydrogen response, with gold-decorated nanosheets remaining sensitive to hydrogen below 150°C. Poor sensor recovery is attributed to the formation of long-lived hydroxyl groups formed during hydrogen spillover from the gold surface.

Declarations and statements

Declaration

I hereby declare that the work reported in this thesis has not previously been accepted in substance for any degree and is not being concurrently submitted in candidature for any degree.

Signed..... (candidate)

Date.....3/11/15.....

Statement 1

Unless otherwise stated, the presented research is the result of my own investigations, and other sources have been explicitly referenced within a bibliography at the end of each chapter. No correction services have been used.

Signed..... (candidate)

Date.....3/11/15.....

Statement 2

I hereby consent for my thesis, if accepted, to be available for photocopying and for inter-library loan, and for the title and abstract to be made available to outside organisations.

Signed..... (candidate)

Date.....3/11/15.....

Contents

Acknowledgements

I dedicate this thesis to my parents, for their unwavering love and support and their unlimited patience. I am also very grateful to my girlfriend, Nicola, who has stood by me throughout my PhD and given me perspective during this time. I would like to thank my supervisor, Thierry Maffeïs, and my many colleagues, particularly Nathan Smith, Jon Evans, Adam Day, Chris Barnett, Ben Palmer and Rich Brown, for making my time at Swansea University such an enjoyable experience.

This work was funded by the European Social Fund (ESF) administered through the Knowledge Economy Skills Scholarships (KESS), WEFO reference 80300, in addition to funding provided by the University Research Fellowship scheme of the Royal Society, grant number UF090141. I am also grateful for the collaboration of Haydale Ltd.

List of publications

Below is a comprehensive list of publications to which the author has contributed during his PhD.

- D.R. Jones, T.G.G. Maffeis, "*Analysis of the kinetics of surface reactions on a zinc oxide nanosheet-based carbon monoxide sensor using an Eley-Rideal model*", Sensors and Actuators B: Chemical, Sensors and Actuators B 218 (2015) 16–24.

- N.A. Smith, J.E. Evans, D.R. Jones, A.M. Lord, S.P. Wilks, "*Growth of ZnO nanowire arrays directly onto Si via substrate topographical adjustments using both wet chemical and dry etching methods*", Materials Science and Engineering B 193 (2015) 41–48.

- A.M. Lord, T.G.G. Maffeis, M.W. Allen, D. Morgan, P.R. Davies, D.R. Jones, J.E. Evans, N.A. Smith, S.P. Wilks, *"Surface state modulation through wet chemical treatment as a route to controlling the electrical properties of ZnO nanowire arrays investigated with XPS"*, Applied Surface Science. 320 (2014) 664–669.

- A. Tarat, C.J. Nettle, D.T.J. Bryant, D.R. Jones, M.W. Penny, R.A. Brown, R. Majitha, K.E. Meissner, T.G.G. Maffeis, *"Microwave-assisted synthesis of layered basic zinc acetate nanosheets and their thermal decomposition into nanocrystalline ZnO"*, Nanoscale Research Letters 9 (2014) No.11.

- M.A. Mohd Azmi, Z. Tehrani, R.P. Lewis, K.-A.D. Walker, D.R. Jones, D.R. Daniels, S.H. Doak, O.J. Guy, *"Highly sensitive covalently functionalised integrated silicon nanowire biosensor devices for detection of cancer risk biomarker"*, Biosensors and Bioelectronics 52 (2014) 216–224.

- R.A. Brown, J.E. Evans, N.A. Smith, A. Tarat, D.R. Jones, C.J. Barnett, T.G.G. Maffeis, *"The effect of metal layers on the morphology and optical properties of hydrothermally grown zinc oxide nanowires"*, Journal of Materials Science 48 (2013) 4908–4913.

- C.J. Barnett, R.A. Brown, D.R. Jones, A. Tarat, R.J. Cobley, T.G.G. Maffeis, *"Investigation into the initial growth parameters of hydrothermally grown zinc oxide nanowires"*, Nanotechnology (IEEE-NANO), 2012 12th IEEE Conference on. IEEE (2012).

- R.A. Brown, C.J. Barnett, A. Tarat, D.R. Jones, L.W. Francis, S. Conlan, T.G.G. Maffeis, "*The viability of U-2 OS cells on Zinc Oxide nanowires observed via MTS assay in vitro*", Nanotechnology (IEEE-NANO), 2012 12th IEEE Conference on. IEEE (2012).

List of figures

Below is a comprehensive list of the figures in this thesis, including their figure numbers, captions and the page on which they appear. Where a citation has been included within a caption, the number appearing between square brackets identifies a particular reference in the bibliography at the end of the relevant section or chapter.

	ppm of H_2 at 390°C, normalised with respect to the starting resistance (a) or the response (b). Each response test was conducted at a P_{O2}/P_{TOT} value of 0.2.	
6.9	Plots showing the responses of the Sensor Au to 200 ppm of H_2 at low temperatures normalised with respect to the starting resistance (a) or the response (b). Each response test was conducted at a P_{O2}/P_{TOT} value of 0.2.	208
6.10	A plot showing the responses of the three sensors to 200 ppm of CO at 440°C, normalised with respect to the starting resistance. Each response test was conducted at a P_{O2}/P_{TOT} value of 0.2.	209

Introduction

Following a period of extensive development in the latter half of the 20th century, semiconductor-based gas sensors have become an essential, if understated, component of modern society. From applications in food [1–3] and automotive [4–7] industries to the detection of carbon monoxide in residential properties [8], there exists a widespread demand for sensors which are affordable, responsive and, in many cases, selective. The gas sensor industry had an estimated value of 1.5 billion US dollars worldwide in 2010, and is expected to reach a value of 2.3 billion US dollars by 2018 [9]. With the advance of nanotechnology, the discovery and enhancement of semiconductor nanomaterials for gas detection has emerged as a highly active area of research.

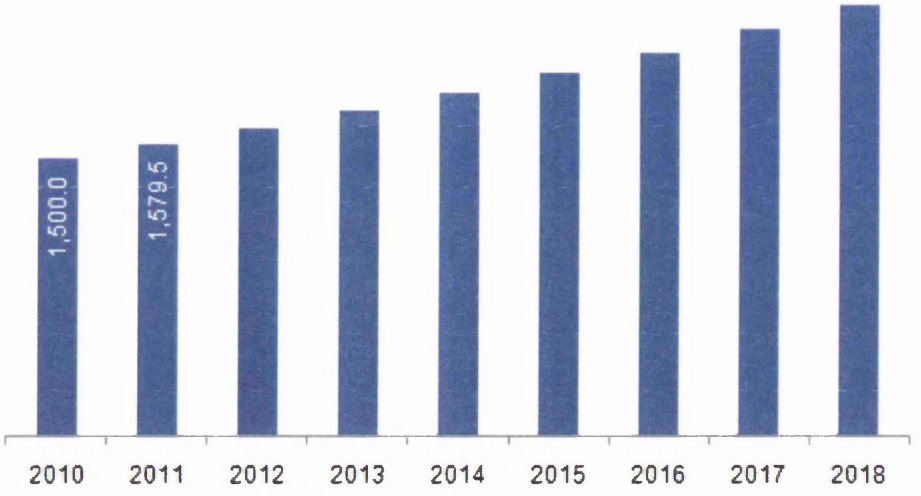

Fig. 1. A bar chart depicting the increasing market value of the gas sensor industry from 2010 to 2013 and the projected increase from 2013 to 2018 [9]**. For scale, the chart is annotated with two values which have units of millions of US dollars.**

There are many examples of different gas sensing systems, but the most common devices are electrochemical [10–17], optical [18–24] or chemiresistive [17,23–28]. Of these, the highest sensitivity and selectivity is achieved through the use of optical techniques, which use infra-red spectroscopy to measure the abundance of a particular gas species. While these instruments are indispensable in applications where such conditions are paramount, they are

often large and expensive so are not suitable in all cases. A more cost-effective option is provided by electrochemical sensing, in which gas molecules generate an electrical current by reacting to form anions within a solid electrolyte. In many instances, however, gradual degradation of the electrolyte results in poor sensor lifetime [15,16,29,30] and therefore limits its suitability in particular situations. In chemiresistive sensing, by contrast, gas detection is achieved by measuring the electrical resistance variations of a semiconductor due to electron exchange during high-temperature gas reactions at its surface. These sensors are inherently more durable than electrochemical devices, and are often the most practicable choice in scenarios where selectivity is not critical.

The first demonstration of chemiresistive gas detection was accomplished by W.H. Brattain and J. Bardeen in 1953 [29,31], who showed that the conductance of germanium may be varied at high temperature by altering the composition of gases in the surroundings. Similar experiments followed, expanding this concept to semiconducting metal oxides such as zinc oxide and culminating in the production of a practical tin oxide-based chemiresistive gas sensor by N. Taguchi in 1971 [29,32]. The use of metal oxides in gas sensing applications remains pervasive in more recent times, although the majority of research is now focussed on nanostructures rather than mesoporous films [33].

Within this work, gas sensing is achieved through use of ZnO. This material is one of the most common choices for chemiresistive sensors, with approximately 21% of relevant publications selecting ZnO ahead of other semiconducting metal oxides, as summarised in Fig. 2 [34]. Use of ZnO is not limited to gas sensing applications, however; due to its wide band gap of 3.37 eV and high exciton binding energy of 60 meV [35–40], for instance, the material has been employed for both ultraviolet lasing [41–44] and photovoltaics [45–50]. For many functions, ZnO is an attractive candidate due to its high conductivity, low cost and the ease with which it is chemically doped [51,52].

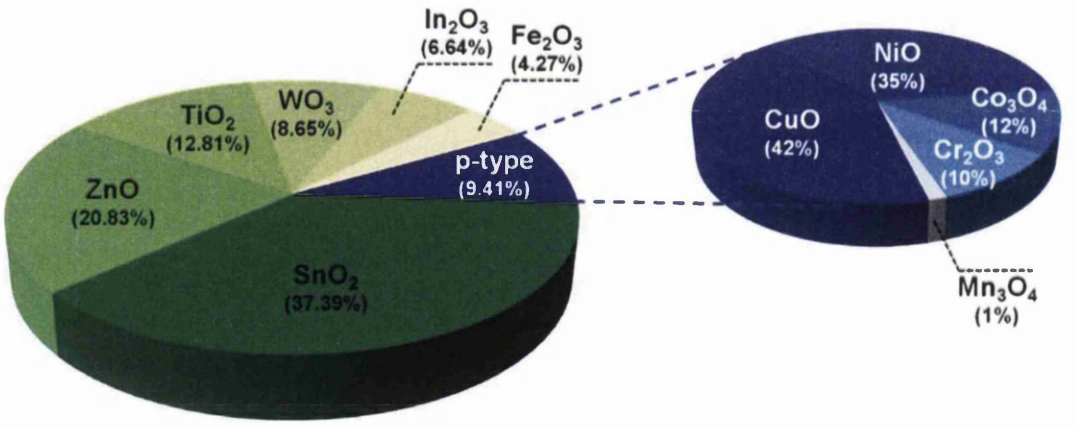

Fig. 2. Pie charts from Reference [34] **showing the proportion of gas sensing publications based on different semiconducting metal oxides, constructed using a Web of Knowledge internet search on 15/07/2013.**

To enhance the properties of chemiresistive sensors it is essential to develop an understanding of the associated physics. Seminal contributions to the theory of electrical conduction between semiconductor grains was provided in early studies by W.E. Taylor, N.H. Odell and H.Y. Fan [53] and J. Bardeen [54], while more recent research has offered greater insight into the dynamics of gas reactions on metal oxide surfaces at elevated temperatures [30,55]. Numerous theoretical models consider the catalysis of these reactions by surface additives, most notably noble metal nanoparticles [56,57], which have been used to enhance the selectivity and sensitivity of chemiresistive gas sensors and lower the required working temperature. To expand the capabilities of these devices and thereby improve their efficacy and versatility, modelling of the underlying sensing mechanisms is of irrefutable importance.

In an effort to advance the understanding of chemiresistive gas detection, the work presented herein aims to build upon existing theoretical models to offer a comprehensive analysis of the fundamental surface reactions. Quantitative evaluation of the kinetic parameters is achieved by relating a phenomenological model to the electrical response of a ZnO nanosheet-based sensor, and the investigation goes further by considering the catalytic effects of gold nanoparticles. The thesis is structured as follows:

Chapter 1 describes the fundamental theory of electrical conduction through a granular semiconductor, and relates the concentration of ionic surface species to the electrical resistance through use of Poisson's equation of electrostatics. The factors determining the position of the Fermi level are also discussed.

Chapter 2 provides a comprehensive review of relevant literature, starting with an overview of practical chemiresistive devices. The chapter continues by discussing the mathematical modelling of chemiresistive gas sensors and experimental studies which explore the reaction mechanisms of different gases at metal oxide surfaces. The properties of catalysed systems are also examined, particularly in relation to the "spillover" phenomena which are a significant component of many reaction pathways.

Chapter 3 reviews the experimental methods employed in later chapters, outlining the important operating principles and practical capabilities of each procedure. The chapter describes a variety of techniques, namely the Brunauer-Emmett-Teller (BET) method, thermogravimetric analysis (TGA), scanning electron microscopy (SEM), x-ray photoelectron spectroscopy (XPS), photoluminescence (PL) spectroscopy and gas sensing experiments. The fabrication of ZnO nanosheets and synthesis of gold nanoparticles, which are fundamental to this work, are also described in detail.

Chapter 4 explores the chemical properties of ZnO nanosheets and the LBZA precursor from which they are procured. The thermal decomposition of LBZA to ZnO is analysed through use of TGA, and the surface chemistry of both materials is investigated via spectroscopic techniques. SEM and BET are employed to examine how the morphology and surface area of the ZnO nanosheets are related to the temperature at which they are annealed.

Chapter 5 investigates the surface properties of a ZnO nanosheet-based carbon monoxide sensor by relating the electrical response to a physical model of the gas reactions. After formulating the necessary theory from first-principle considerations, a methodology is developed to facilitate the experimental estimation of reaction parameters such as rate

constants and activation energies. The resistance measurements are also used to evaluate the position of the Fermi level relative to the conduction band minimum at the surface.

Chapter 6 expands upon the ideas developed in Chapter 5 by exploring the reactions of carbon monoxide, hydrogen and methane on the surface of ZnO either with no surface additives or in the presence of gold nanoparticles. Through adaptation of the model, the measured hydrogen responses of both catalysed and non-functionalised sensors are rationalised by considering the relative magnitudes of their reaction parameters.

The presented findings are summarised in the **Concluding Remarks** section, which assesses the implications of the results and considers how the research could be expanded upon in future experiments.

References

[1] J. Hammond, B. Marquis, R. Michaels, B. Oickle, B. Segee, J. Vetelino, et al., A semiconducting metal-oxide array for monitoring fish freshness, Sensors Actuators, B Chem. 84 (2002) 113–122. doi:10.1016/S0925-4005(02)00011-4.

[2] E. Schaller, J.O. Bosset, F. Escher, "Electronic noses" and their application to food, LWT-Food Sci. Technol. 31 (1998) 305–316. doi:10.1006/fstl.1998.0376.

[3] A. Eriksson, K.P. Waller, K. Svennersten-Sjaunja, J.E. Haugen, F. Lundby, O. Lind, Detection of mastitic milk using a gas-sensor array system (electronic nose), Int. Dairy J. 15 (2005) 1193–1201. doi:10.1016/j.idairyj.2004.12.012.

[4] J. Riegel, Exhaust gas sensors for automotive emission control, Solid State Ionics. 152-153 (2002) 783–800. doi:10.1016/S0167-2738(02)00329-6.

[5] E. Ivers-Tiffée, K.H. Härdtl, W. Menesklou, J. Riegel, Principles of solid state oxygen sensors for lean combustion gas control, Electrochim. Acta. 47 (2001) 807–814. doi:10.1016/S0013-4686(01)00761-7.

[6] N. Docquier, S. Candel, Combustion control and sensors: A review, Prog. Energy Combust. Sci. 28 (2002) 107–150. doi:10.1016/S0360-1285(01)00009-0.

[7] M. Shelef, R.W. McCabe, Twenty-five years after introduction of automotive catalysts: what next?, Catal. Today. 62 (2000) 35–50. doi:10.1016/S0920-5861(00)00407-7.

[8] G.F. Fine, L.M. Cavanagh, A. Afonja, R. Binions, Metal oxide semi-conductor gas sensors in environmental monitoring, Sensors. 10 (2010) 5469–5502. doi:10.3390/s100605469.

[9] Gas Sensors Market - Global Industry Size, Share, Trends, Analysis and Forecast, 2012-2018; A report by Transparency Market Research, New York, 2013.

[10] J.W. Fergus, A review of electrolyte and electrode materials for high temperature electrochemical CO2 and SO2 gas sensors, Sensors Actuators, B Chem. 134 (2008) 1034–1041. doi:10.1016/j.snb.2008.07.005.

[11] E. Steudel, P. Birke, W. Weppner, Miniaturized solid state electrochemical CO_2 sensors, Electrochim. Acta. 42 (1997) 3147–3153. doi:10.1016/S0013-4686(97)00168-0.

[12] R. Sathiyamoorthi, R. Chandrasekaran, T. Mathanmohan, B. Muralidharan, T. Vasudevan, Study of electrochemical based gas sensors for fluorine and chlorine, Sensors Actuators, B Chem. 99 (2004) 336–339. doi:10.1016/j.snb.2003.11.031.

[13] J.F. Currie, A. Essalik, J.C. Marusic, Micromachined thin film solid state electrochemical CO2, NO2 and SO2 gas sensors, Sensors Actuators, B Chem. 59 (1999) 235–241. doi:10.1016/S0925-4005(99)00227-0.

[14] S. Akbar, P. Dutta, C. Lee, High-temperature ceramic gas sensors: A review, Int. J. Appl. Ceram. Technol. 3 (2006) 302–311. doi:10.1111/j.1744-7402.2006.02084.x.

[15] G. Korotcenkov, S. Do Han, J.R. Stetter, Review of electrochemical hydrogen sensors, Chem. Rev. 109 (2009) 1402–1433. doi:10.1021/cr800339k.

[16] J.W. Fergus, Materials for high temperature electrochemical NOx gas sensors, Sensors Actuators, B Chem. 121 (2007) 652–663. doi:10.1016/j.snb.2006.04.077.

[17] N. Yamazoe, Toward innovations of gas sensor technology, Sensors Actuators, B Chem. 108 (2005) 2–14. doi:10.1016/j.snb.2004.12.075.

[18] A. Chtanov, M. Gal, Differential optical detection of hydrogen gas in the atmosphere, Sensors Actuators, B Chem. 79 (2001) 196–199. doi:10.1016/S0925-4005(01)00875-9.

[19] P. Werle, F. Slemr, K. Maurer, R. Kormann, R. Mücke, B. Jänker, Near- and mid-infrared laser-optical sensors for gas analysis, Opt. Lasers Eng. 37 (2002) 101–114. doi:10.1016/S0143-8166(01)00092-6.

[20] H. Teichert, T. Fernholz, V. Ebert, Simultaneous in situ measurement of CO, H2O, and gas temperatures in a full-sized coal-fired power plant by near-infrared diode lasers., Appl. Opt. 42 (2003) 2043–2051. doi:10.1364/AO.42.002043.

[21] I. Galli, S. Bartalini, S. Borri, P. Cancio, D. Mazzotti, P. De Natale, et al., Molecular Gas Sensing Below Parts Per Trillion: Radiocarbon-Dioxide Optical Detection, Phys. Rev. Lett. 107 (2011) 270802. doi:10.1103/PhysRevLett.107.270802.

[22] G. Giusfredi, S. Bartalini, S. Borri, P. Cancio, I. Galli, D. Mazzotti, et al., Saturated-Absorption Cavity Ring-Down Spectroscopy, Phys. Rev. Lett. 104 (2010) 110801. doi:10.1103/PhysRevLett.104.110801.

[23] X. Chen, C.K.Y. Wong, C. a. Yuan, G. Zhang, Nanowire-based gas sensors, Sensors Actuators, B Chem. 177 (2013) 178–195. doi:10.1016/j.snb.2012.10.134.

[24] K. Arshak, E. Moore, G.M. Lyons, J. Harris, S. Clifford, A review of gas sensors employed in electronic nose applications, Sens. Rev. 24 (2004) 181–198. doi:10.1108/02602280410525977.

[25] N. Ramgir, N. Datta, M. Kaur, S. Kailasaganapathi, A.K. Debnath, D.K. Aswal, et al., Metal oxide nanowires for chemiresistive gas sensors: Issues, challenges and prospects, Colloids Surfaces A Physicochem. Eng. Asp. 439 (2013) 101–116. doi:10.1016/j.colsurfa.2013.02.029.

[26] E. Comini, C. Baratto, I. Concina, G. Faglia, M. Falasconi, M. Ferroni, et al., Metal oxide nanoscience and nanotechnology for chemical sensors, Sensors Actuators, B Chem. 179 (2013) 3–20. doi:10.1016/j.snb.2012.10.027.

[27] N. Barsan, D. Koziej, U. Weimar, Metal oxide-based gas sensor research: How to?, Sensors Actuators, B Chem. 121 (2007) 18–35. doi:10.1016/j.snb.2006.09.047.

[28] E. Comini, C. Baratto, G. Faglia, M. Ferroni, a. Vomiero, G. Sberveglieri, Quasi-one dimensional metal oxide semiconductors: Preparation, characterization and application as chemical sensors, Prog. Mater. Sci. 54 (2009) 1–67. doi:10.1016/j.pmatsci.2008.06.003.

[29] G. Neri, First Fifty Years of Chemoresistive Gas Sensors, Chemosensors. 3 (2015) 1–20. doi:10.3390/chemosensors3010001.

[30] G. Korotcenkov, Metal oxides for solid-state gas sensors: What determines our choice?, Mater. Sci. Eng. B Solid-State Mater. Adv. Technol. 139 (2007) 1–23. doi:10.1016/j.mseb.2007.01.044.

[31] W.H. Brattain, J. Bardeen, Surface properties of germanium, Bell Syst.Tech. J. 32 (1953) 1–41.

[32] N. Taguchi, Gas-detecting device, U.S. Patent 3,631,436, 1971. http://www.iaea.org/inis/collection/NCLCollectionStore/_Public/06/172/6172730.pdf.

[33] K.J. Choi, H.W. Jang, One-dimensional oxide nanostructures as gas-sensing materials: Review and issues, Sensors. 10 (2010) 4083–4099. doi:10.3390/s100404083.

[34] H.-J. Kim, J.-H. Lee, Highly sensitive and selective gas sensors using p-type oxide semiconductors: Overview, Sensors Actuators B Chem. 192 (2014) 607–627. doi:10.1016/j.snb.2013.11.005.

[35] V.A. Fonoberov, A.A. Balandin, Origin of ultraviolet photoluminescence in ZnO quantum dots: Confined excitons versus surface-bound impurity exciton complexes, Appl. Phys. Lett. 85 (2004) 5971–5973. doi:10.1063/1.1835992.

[36] V.A. Fonoberov, K.A. Alim, A.A. Balandin, F. Xiu, J. Liu, Photoluminescence investigation of the carrier recombination processes in ZnO quantum dots and nanocrystals, Phys. Rev. B - Condens. Matter Mater. Phys. 73 (2006) 165317. doi:10.1103/PhysRevB.73.165317.

[37] A. Teke, Ü. Özgür, S. Doğan, X. Gu, H. Morkoç, B. Nemeth, et al., Excitonic fine structure and recombination dynamics in single-crystalline ZnO, Phys. Rev. B - Condens. Matter Mater. Phys. 70 (2004) 195207. doi:10.1103/PhysRevB.70.195207.

[38] B.K. Meyer, H. Alves, D.M. Hofmann, W. Kriegseis, D. Forster, F. Bertram, et al., Bound exciton and donor-acceptor pair recombinations in ZnO, Phys. Status Solidi Basic Res. 241 (2004) 231–260. doi:10.1002/pssb.200301962.

[39] C. Boemare, T. Monteiro, M.J. Soares, J.G. Guilherme, E. Alves, Photoluminescence studies in ZnO samples, Phys. B. 308-310 (2001) 985–988.

[40] H. Alves, D. Pfisterer, a. Zeuner, T. Riemann, J. Christen, D.M. Hofmann, et al., Optical investigations on excitons bound to impurities and dislocations in ZnO, Opt. Mater. (Amst). 23 (2003) 33–37. doi:10.1016/S0925-3467(03)00055-7.

[41] M.H. Huang, S. Mao, H. Feick, H. Yan, Y. Wu, H. Kind, et al., Room-temperature ultraviolet nanowire nanolasers., Science. 292 (2001) 1897–1899. doi:10.1126/science.1060367.

[42] Z. Hai, C.X. Shan, B. Yao, B.H. Li, J.Y. Zhang, Z.Z. Zhang, et al., Ultralow-threshold laser realized in zinc oxide, Adv. Mater. 21 (2009) 1613–1617. doi:10.1002/adma.200802907.

[43] G.P. Zhu, C.X. Xu, J. Zhu, C.G. Lv, Y.P. Cui, Two-photon excited whispering-gallery mode ultraviolet laser from an individual ZnO microneedle, Appl. Phys. Lett. 94 (2009) 19–22. doi:10.1063/1.3077011.

[44] D.C. Reynolds, D.C. Look, B. Jogai, Optically pumped ultraviolet lasing from ZnO, Solid State Commun. 99 (1996) 873–875. doi:10.1016/0038-1098(96)00340-7.

[45] H.-M. Cheng, W.-F. Hsieh, High-efficiency metal-free organic-dye-sensitized solar cells with hierarchical ZnO photoelectrode, Energy Environ. Sci. 3 (2010) 442. doi:10.1039/b915725e.

[46] S.H. Ko, D. Lee, H.W. Kang, K.H. Nam, J.Y. Yeo, S.J. Hong, et al., Nanoforest of hydrothermally grown hierarchical ZnO nanowires for a high efficiency dye-sensitized solar cell, Nano Lett. 11 (2011) 666–671. doi:10.1021/nl1037962.

[47] K. Keis, C. Bauer, G. Boschloo, A. Hagfeldt, K. Westermark, H. Rensmo, et al., Nanostructured ZnO electrodes for dye-sensitized solar cell applications, J. Photochem. Photobiol. A Chem. 148 (2002) 57–64. doi:10.1016/S1010-6030(02)00039-4.

[48] M.H. Kumar, N. Yantara, S. Dharani, M. Graetzel, S. Mhaisalkar, P.P. Boix, et al., Flexible, low-temperature, solution processed ZnO-based perovskite solid state solar cells, Chem. Commun. 49 (2013) 11089–11091. doi:10.1039/c0xx00000x.

[49] L. Loh, S. Dunn, Recent Progress in ZnO-Based Nanostructured Ceramics in Solar Cell Applications, J. Nanosci. Nanotechnol. 12 (2012) 8215–8230. doi:10.1166/jnn.2012.6680.

[50] A. Omar, H. Abdullah, Electron transport analysis in zinc oxide-based dye-sensitized solar cells: A review, Renew. Sustain. Energy Rev. 31 (2014) 149–157. doi:10.1016/j.rser.2013.11.031.

[51] M.D. McCluskey, S.J. Jokela, Defects in ZnO, J. Appl. Phys. 106 (2009) 0–13. doi:10.1063/1.3216464.

[52] U. Özgür, Y.I. Alivov, C. Liu, a. Teke, M. a. Reshchikov, S. Doğan, et al., A comprehensive review of ZnO materials and devices, J. Appl. Phys. 98 (2005) 041301. doi:10.1063/1.1992666.

[53] W.E. Taylor, N.H. Odell, H.Y. Fan, Grain boundary barriers in germanium, Phys. Rev. 88 (1952) 867–875. doi:10.1103/PhysRev.88.867.

[54] J. Bardeen, On the theory of the a-c impedance of a contact rectifier, Bell Syst.Tech. J. 28 (1949) 428.

[55] M.E. Franke, T.J. Koplin, U. Simon, Metal and metal oxide nanoparticles in chemiresistors: Does the nanoscale matter?, Small. 2 (2006) 36–50. doi:10.1002/smll.200500261.

[56] C. Wang, L. Yin, L. Zhang, D. Xiang, R. Gao, Metal oxide gas sensors: Sensitivity and influencing factors, Sensors. 10 (2010) 2088–2106. doi:10.3390/s100302088.

[57] G. Korotcenkov, Gas response control through structural and chemical modification of metal oxide films: state of the art and approaches, Sensors Actuators B Chem. 107 (2005) 209–232. doi:10.1016/j.snb.2004.10.006.

Chapter 1 – Background theory

1.1. An overview of chemiresistive gas sensing mechanisms

In the bid to develop more sensitive and selective chemiresistive gas sensors, it is essential to first develop an understanding of the underlying physical principles. A successful model of the system ought to predict how the sensing operation is influenced by a change in the operating conditions, such as the working temperature or the composition of the surrounding gas, and provide an insight into the effects due to surface catalysts. This chapter outlines the basic theory of metal oxide-based sensors, and reviews the theory concerning electron conduction through a granular semiconductor.

As a starting-point, most theoretical treatments of resistive gas sensors utilise the concept of "ionosorption" of oxygen at the semiconductor surface [1–3]. At elevated temperatures, adsorbed molecules of O_2 interact strongly with the conduction band of the metal oxide and form anionic species by accepting electrons from the surface, as depicted in Fig. 1.1. This reaction leads to the development of an electric potential, ϕ, at the surface which causes the conduction band to bend upwards. The band bending occurs over a characteristic distance x_{dep}, which is commonly referred to as the "depletion width" and is closely-related to the Debye length of the material [4–7]. Under an applied electric potential, V_{app}, the flow of electrons between two adjacent semiconductor nanoparticles is therefore additionally impeded due to the formation of surface ions, increasing the electrical resistance of the junction. For many systems, it is sufficient to assume a uniformly distributed positive charge density, ρ_{dep}, within the depleted region of the semiconductor, as plotted in Fig. 1.2 (a). The form of the corresponding electric potential in the vicinity of the semiconductor boundary is shown in Fig. 1.2 (b), while the energy of an electron in this region, $-q\phi$, where q is the electron charge, is depicted in Fig. 1.2 (c).

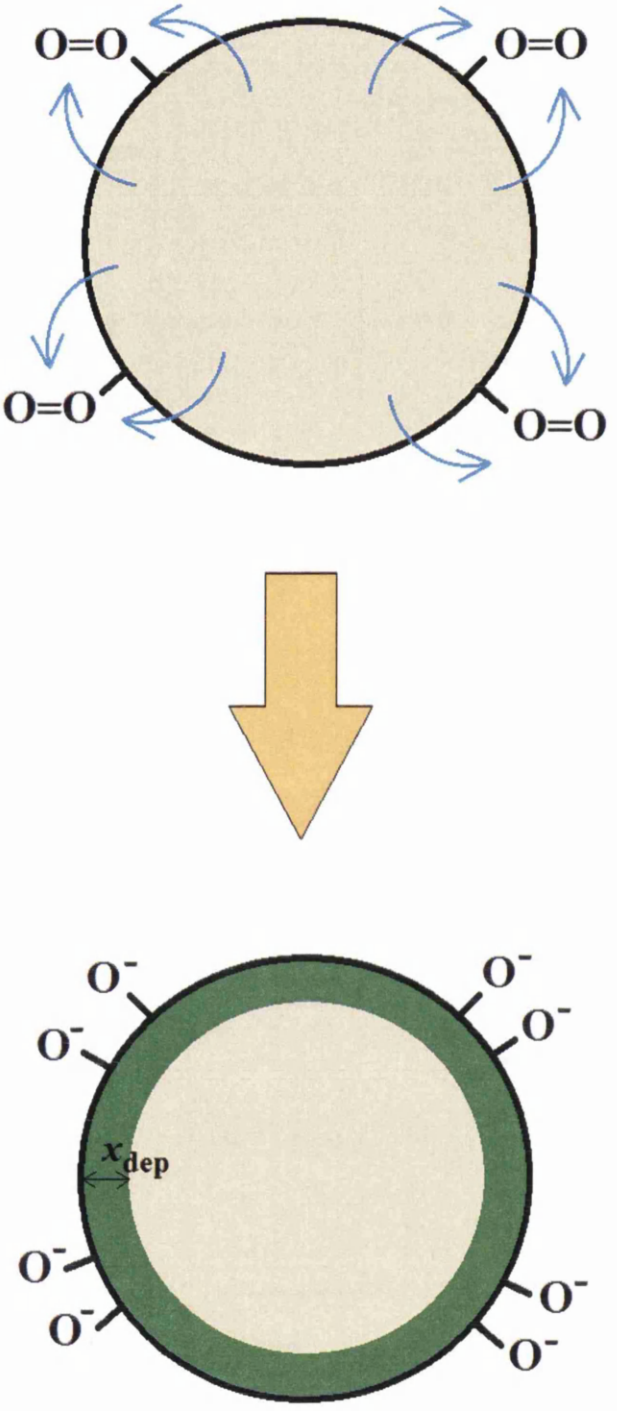

Fig. 1.1. A diagram illustrating the formation of anionic oxygen species (here shown as monovalent O^- ions) from chemisorbed diatomic oxygen molecules at the surface of a semiconductor particle. Transfer of an electron from the semiconductor is depicted by a blue arrow, while the resulting region of positive charge at the surface, which has a width x_{dep}, is represented by the green area.

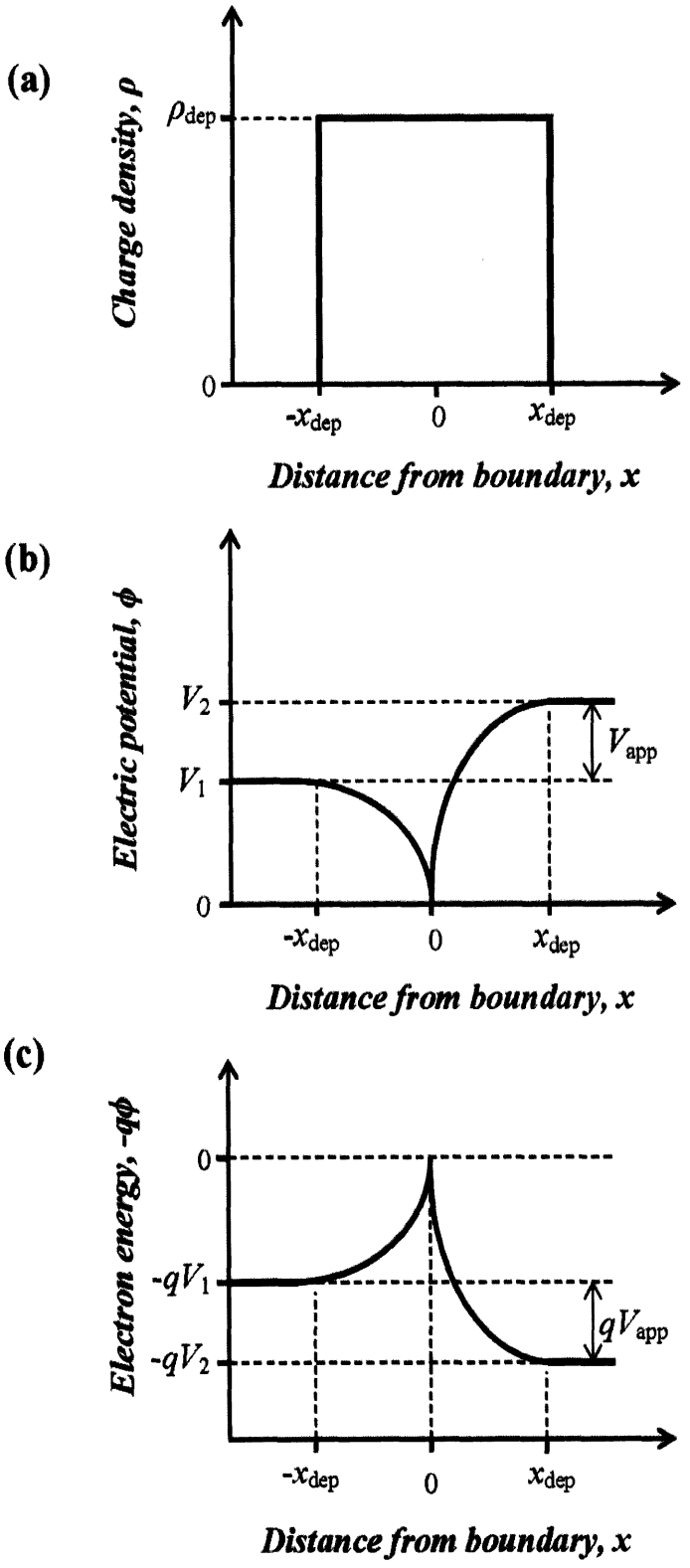

Fig. 1.2. Qualitative plots showing the charge distribution (a), electric potential (b) and the electron energy (c) as a function of the distance from the boundary between two semiconductors under an applied potential difference, V_{app}.

must consider the Poisson equation for the electrostatics of the system [4,5,8]. In general, the electric potential, ϕ, associated with a charge density ρ_{dep} in a material of relative permittivity ε is given by

$$\nabla^2\phi = -\frac{\rho_{dep}}{\varepsilon\varepsilon_0} \tag{1.1}$$

where ε_0 is the permittivity of free space. Within a depletion region containing ions of charge q_{dep} at a concentration per unit volume N_{dep}, the potential therefore satisfies the equation

$$\frac{d^2\phi}{dx^2} = -\frac{N_{dep}q_{dep}}{\varepsilon\varepsilon_0} \tag{1.2}$$

Here, the parameter x denotes the distance into the material, normal to the surface. It has been assumed that charge located at a given distance below the metal oxide surface is distributed isotropically, allowing Poisson's equation to be treated in one dimension. Taking N_{dep} to be constant and integrating Eq. (1.2) twice with respect to x, one obtains

$$\phi(x) = -\frac{N_{dep}q_{dep}}{2\varepsilon\varepsilon_0}x^2 + c_1x + c_2 \tag{1.3}$$

where c_1 and c_2 are constants. Using Fig. 1.2 (b) to impose the conditions that ϕ goes to zero when x is zero and $d\phi/dx$ is zero when x equals x_{dep}, Eq. (1.3) may be rewritten as

$$\phi(x) = -\frac{N_{dep}q_{dep}}{2\varepsilon\varepsilon_0}x\left(x - 2x_{dep}\right) \tag{1.4}$$

It is possible to make further progress by realising that any charge within the depletion region must be balanced by opposing charges elsewhere, and by assuming that the cations in the depletion region originate exclusively from the formation of singly-ionised anions at the surface. If the semiconductor is comprised of spherical grains of radius r, the number of surface ions per unit area, n_{surf}, is given by

$$n_{surf} = N_{dep}\frac{q_{dep}}{3qr^2}\left(r^3 - \left(r - x_{dep}\right)^3\right) \tag{1.5}$$

where q is the electron charge. When r is much greater than x_{dep}, Eq. (1.5) becomes

$$n_{surf} \approx \frac{q_{dep}}{q} N_{dep} x_{dep} \tag{1.6}$$

Substituting Eq. (1.6) into Eq. (1.4), the magnitude of the potential difference between the bulk semiconductor and the surface may be expressed as

$$\boldsymbol{\phi_B = \left|\phi(x_{dep}) - \phi(0)\right| = \frac{q^2 n_{surf}^2}{2\varepsilon\varepsilon_0 q_{dep} N_{dep}}} \tag{1.7}$$

which finally relates the surface potential to the area concentration of adsorbed ions. Using the relation $\theta_O = n_{surf}/n_{sites}$, where n_{sites} is the total number of sites per unit area and θ_O is the fraction of sites occupied by surface ions, one obtains the equation

$$\boldsymbol{\phi_B = \frac{q^2 n_{sites}^2}{2\varepsilon\varepsilon_0 q_{dep} N_{dep}} \theta_O^2} \tag{1.8}$$

Provided that the applied potential across the sample is sufficiently low, it will be shown later that the electrical resistance, R, is given by

$$\boldsymbol{R = R_0 \exp\left(\frac{q\phi_B}{k_B T}\right)} \tag{1.9}$$

where k_B is Boltzmann's constant, T is temperature, and R_0 is the resistance when no surface ions are present. Combining parameters into a temperature single dependent variable, α, it follows that

$$\boldsymbol{R = R_0 \exp\left(\alpha \theta_O^2\right)} \tag{1.10}$$

where

$$\boldsymbol{\alpha = \frac{q^3 n_{sites}^2}{2\varepsilon\varepsilon_0 k_B T q_{dep} N_{dep}}} \tag{1.11}$$

It is evident from Eq. (1.11) that if ε, q_{dep}, N_{dep} and n_{sites} are temperature-invariant, α is expected to exhibit an inverse proportionality to T.

According to Eq. (1.10), the relationship between R and θ_O adopts a straightforward form but depends on a variety of physical parameters of the system. In particular, the degree of band bending is clearly influenced by the nature and concentration of defects within the depletion region. To further explore the resistance behaviour, the following sections shall address the effect of inter-band defect states on the conduction band of the semiconductor. Moreover, by outlining the first-principles derivation of Eq. (1.9) in detail, it will be shown that the nature of the pre-exponential factor, R_0, is strongly affected by the magnitude of the surface potential.

1.2. The drift-diffusion model of current flow

To relate the electrical conductivity of a semiconductor to its intrinsic physical properties, it is often useful to consider the diffusion and drift of electrons across a boundary [4,9–11]. According to this model, the total flux of conventional current (which corresponds to the flow of positive charge, and is therefore equal to and opposite the electron current flux) is given by

$$\boldsymbol{J} = \boldsymbol{\sigma}.\boldsymbol{E} - \boldsymbol{D}.\nabla\boldsymbol{\rho} \tag{1.12}$$

where $\boldsymbol{\sigma}$ is the conductivity tensor, $\boldsymbol{E}$ is the electric field strength, $\boldsymbol{D}$ is the diffusivity tensor and ρ is the electric charge density. The first term on the right-hand side of Eq. (1.12) corresponds to the drift of positively charged carriers in the direction of the applied electric field, while the second results from the diffusion of these carriers according to Fick's first law. It is clear from Fig. 1.3, which shows the directions of the drift and diffusion components of conventional current either side of the potential boundary from Fig. 1.2 (b), that while the drift current is always directed towards the semiconductor interface, the diffusion current is directed away from it. The direction of each current may be understood by recognising that electrons within the bulk semiconductor tend to diffuse into the region of

lower electron density close to the interface, while electrons within this region migrate away from the interface in order to minimise their potential energy.

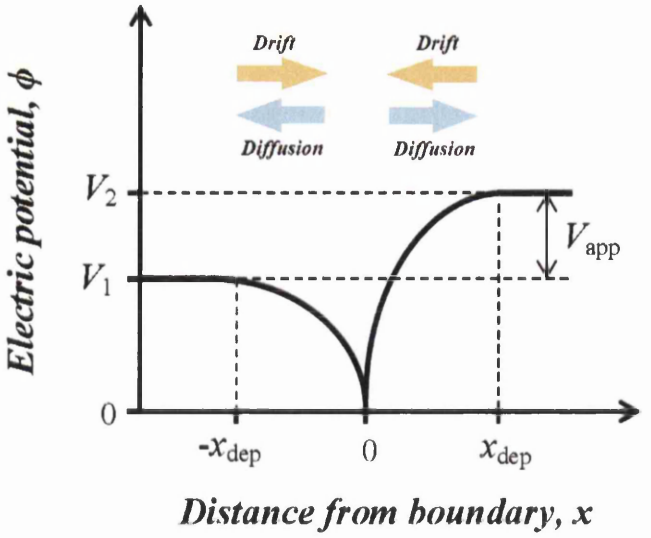

Fig. 1.3. An annotated plot showing the directions of the drift and diffusion currents on either side of the potential boundary depicted in Fig. 1.2 (b). Each current corresponds to the flow of positive charge.

As implied by Fig. 1.3, an isotropic system may be treated in one dimension and Eq. (1.12) therefore simplifies to

$$J_x = \sigma E_x - D\frac{\mathrm{d}\rho}{\mathrm{d}x} = \sigma E_x + qD\frac{\mathrm{d}n}{\mathrm{d}x} \tag{1.13}$$

where J_x and E_x are the x-components of the vectors J and E, respectively, and the x-axis is taken to lie perpendicular to the potential boundary. The charge density gradient across the barrier is equal to the derivative of the electron concentration, n, with respect to x multiplied by the electronic charge, $-q$. The conductivity of an isotropic semiconductor, σ, is linked to n via the equation

$$\sigma = q\mu n \tag{1.14}$$

where μ is the electron mobility. Moreover, at a particular temperature, T, μ is related to D and q through the Einstein-Smoluchowski relation,

$$\mu = \frac{qD}{k_B T} \tag{1.15}$$

Therefore, Eq. (1.13) can be written as

$$J_x = \mu k_B T \left(\frac{qn}{k_B T} E_x + \frac{\mathrm{d}n}{\mathrm{d}x} \right) \tag{1.16}$$

Eq. (1.16) may be multiplied by an integrating factor, f, given by

$$f = \exp\left(-\frac{q\phi}{k_B T} \right) \tag{1.17}$$

where ϕ is the electric potential which satisfies the formula

$$E_x = -\frac{\mathrm{d}\phi}{\mathrm{d}x} \tag{1.18}$$

Since

$$\frac{\mathrm{d}f}{\mathrm{d}x} = -\frac{qf}{k_B T}\frac{\mathrm{d}\phi}{\mathrm{d}x} = \frac{qE_x}{k_B T} f \tag{1.19}$$

one obtains the expression

$$f J_x = \mu k_B T \frac{\mathrm{d}}{\mathrm{d}x}(fn) \tag{1.20}$$

and so, integrating with respect to x across the boundary region of one grain,

$$J_x \int_{-x_{dep}}^{0} \exp\left(-\frac{q\phi(x)}{k_B T} \right) \mathrm{d}x = \mu k_B T \left[n(x) \exp\left(-\frac{q\phi(x)}{k_B T} \right) \right]_{-x_{dep}}^{0} \tag{1.21}$$

Here, the boundary region in one grain has width x_{dep}, and so the total barrier width is $2x_{\mathrm{dep}}$. The coordinate x is defined relative to the semiconductor interface, so that negative and positive values of x correspond to positions to the left and right of the boundary, respectively.

As shown in Fig. 1.2 (b), which illustrates how the electric potential varies across the boundary region, the potential decreases quadratically as x goes from $-x_{dep}$ to zero, and then increases in a similar manner from zero to x_{dep}. According to the physical arguments outlined previously, the potential at position x, $\phi(x)$, is given by

$$\boldsymbol{\phi(x) = A\left(|x| - x_{dep}\right)^2 + B} \qquad \boldsymbol{0 \leq |x| \leq x_{dep}} \tag{1.22}$$

where A and B are parameters set by the boundary conditions and the physics of the system. To the right of the interface, where x is greater than zero, the electric potential is raised by an applied voltage, V_{app}. Relative to the conduction band in the bulk of the left-hand grain, the boundary potential has a peak magnitude of $-V_1$. Conversely, the potential difference between the barrier peak and the conduction band in the bulk of the right-hand grain is equal to $-V_2$. The difference between V_2 and V_1 is equal to V_{app}, as illustrated by Fig. 1.2 (b). It should be noted that while the electric potential reaches a minimum value at the semiconductor interface, the electron energy has a maximum at the same point, as shown by Fig. 1.2 (c).

To proceed, one must consider the boundary conditions of $\phi(x)$. From Fig. 1.2 (b),

$$\boldsymbol{\phi\left(-x_{dep}\right) = V_1} \tag{1.23}$$

$$\boldsymbol{\phi\left(x_{dep}\right) = V_2} \tag{1.24}$$

and

$$\boldsymbol{\phi(0) = 0} \tag{1.25}$$

The gradient of ϕ must also equal zero when x is $\pm x_{dep}$. Imposing these conditions, Eq. (1.22) becomes

$$\boldsymbol{\phi(x) = V_1\left(1 - \left(\frac{x}{x_{dep}} + 1\right)^2\right)} \qquad \boldsymbol{-x_{dep} \leq x \leq 0} \tag{1.26}$$

and

$$\phi(x) = V_2\left(1 - \left(\frac{x}{x_{dep}} - 1\right)^2\right) \qquad 0 \le x \le x_{dep} \tag{1.27}$$

Introducing Eq. (1.26) into Eq. (1.21), the current flux approaching the boundary from the left-hand grain is given by

$$J_x^L = F_L\left(n_s - n_b \exp\left(-\frac{qV_1}{k_BT}\right)\right) \tag{1.28}$$

where n_b is the carrier concentration in the bulk (away from the barrier region), n_s is the concentration of carriers at $x = 0$, and

$$F_L = \mu k_B T\left(\int_{-x_{dep}}^{0} \exp\left(-\frac{q\phi(x)}{k_BT}\right) dx\right)^{-1} \tag{1.29}$$

Similarly, the flux leaving the boundary into the second grain is described by the equation

$$J_x^R = F_R\left(n_b \exp\left(-\frac{qV_2}{k_BT}\right) - n_s\right) \tag{1.30}$$

where

$$F_R = \mu k_B T\left(\int_{0}^{x_{dep}} \exp\left(-\frac{q\phi(x)}{k_BT}\right) dx\right)^{-1} \tag{1.31}$$

The current approaching the interface from the left must exit the interface on the right, so

$$F_L\left(n_s - n_b \exp\left(-\frac{qV_1}{k_BT}\right)\right) = F_R\left(n_b \exp\left(-\frac{qV_2}{k_BT}\right) - n_s\right) \tag{1.32}$$

Rearrangement of Eq. (1.32) yields

$$n_s = n_b\left(\frac{F_L \exp\left(-\frac{qV_1}{k_BT}\right) + F_R \exp\left(-\frac{qV_2}{k_BT}\right)}{F_L + F_R}\right) \tag{1.33}$$

The total potential applied across the boundary, V_{app}, is equal to the difference between V_2 and V_1, hence

$$n_s = n_b \left(\frac{F_L + F_R \exp\left(-\frac{qV_{app}}{k_B T}\right)}{F_L + F_R} \right) \exp\left(-\frac{qV_1}{k_B T}\right) \tag{1.34}$$

Substituting this expression into either Eq. (1.28) or Eq. (1.30) gives the current flux through the boundary as

$$J_x = -\frac{n_b F_L F_R}{F_L + F_R} \exp\left(-\frac{qV_1}{k_B T}\right)\left(1 - \exp\left(-\frac{qV_{app}}{k_B T}\right)\right) \tag{1.35}$$

One should note that since both F_L and F_R are greater than zero, a positive value of V_{app} leads to a negative value of J_x. This behaviour follows physically as J_x represents the flow of positive charge, and is therefore directed along the negative x-axis when the electric potential is higher on the right-hand side of the boundary than the left.

It is now necessary to evaluate the integrals in Eq. (1.29) and Eq. (1.31). Recalling the definition of E_x given by Eq. (1.18), F_L and F_R may be written as

$$F_L = -\mu k_B T \left(\int_{\phi(-x_{dep})}^{\phi(0)} \frac{1}{E_x(\phi)} \exp\left(-\frac{q\phi}{k_B T}\right) d\phi \right)^{-1} \tag{1.36}$$

and

$$F_R = -\mu k_B T \left(\int_{\phi(0)}^{\phi(x_{dep})} \frac{1}{E_x(\phi)} \exp\left(-\frac{q\phi}{k_B T}\right) d\phi \right)^{-1} \tag{1.37}$$

respectively. As ϕ is described by a quadratic function of x, it is clear than E_x is not independent of ϕ. However, as will be discussed in detail later, if the potential gradient is sufficiently steep it is reasonable to replace $E_x(\phi)$ with $E_x(0)$, the electric field strength at the peak of the potential barrier. It must be remembered that this simplification is only valid when qV_1 and qV_2 are much greater than $k_B T$. The expressions for F_L and F_R now become

$$F_L \approx \mu q E_{xL}(0)\left(1-\exp\left(-\frac{qV_1}{k_BT}\right)\right)^{-1} \tag{1.38}$$

and

$$F_R \approx -\mu q E_{xR}(0)\left(1-\exp\left(-\frac{qV_2}{k_BT}\right)\right)^{-1} \tag{1.39}$$

Substituting Eq. (1.38) and Eq. (1.39) into Eq. (1.35) yields

$$J_x = \frac{\mu q n_b E_{xL}(0)E_{xR}(0)}{E_{xL}(0)\left(1-\exp\left(-\frac{qV_2}{k_BT}\right)\right)-E_{xR}(0)\left(1-\exp\left(-\frac{qV_1}{k_BT}\right)\right)}\exp\left(-\frac{qV_1}{k_BT}\right)\left(1-\exp\left(-\frac{qV_{app}}{k_BT}\right)\right) \tag{1.40}$$

The zero-bias conductance (given by the reciprocal of the zero-bias resistance) for a boundary of cross-sectional area A is defined by the equation

$$G_0 = \frac{A}{V_{app}}\lim_{V_{app}\to 0}|J_x| \tag{1.41}$$

and is therefore given by

$$G_0 \approx \frac{A\mu q^2 n_b |E_{xL}(0)||E_{xR}(0)|}{k_BT|E_{xL}(0)-E_{xR}(0)|}\exp\left(-\frac{q\phi_B}{k_BT}\right) \tag{1.42}$$

where ϕ_B is the magnitude of the barrier height at zero applied potential, equal to both V_1 and V_2. The exponential terms in the denominator of Eq. (1.40) have been neglected as $q\phi_B$ is much greater than k_BT. Noting that $E_{xR}(0)$ is equal to $-E_{xL}(0)$ when V_{app} is zero, Eq. (1.42) simplifies to

$$G_0 \approx \frac{A\mu q^2 n_b E_{xL}(0)}{2k_BT}\exp\left(-\frac{q\phi_B}{k_BT}\right) \tag{1.43}$$

To eliminate $E_{xL}(0)$ from Eq. (1.43), it must be expressed as a function of ϕ_B. After solving Poisson's equation, it was shown that

$$\phi_B = \frac{q^2 n_{surf}^2}{2\varepsilon\varepsilon_0 q_{dep}N_{dep}} = \frac{q_{dep}N_{dep}x_{dep}^2}{2\varepsilon\varepsilon_0} \tag{1.44}$$

From the definition of E_x and the form of $\phi(x)$ given in Eq. (1.26), $E_{xL}(0)$ is described by the expression

$$E_{xL}(0) = \frac{2|\phi_B|}{x_{dep}} = \sqrt{\frac{2q_{dep}N_{dep}\phi_B}{\varepsilon\varepsilon_0}} \tag{1.45}$$

Hence, the equation for G_0 may be written as

$$G_0 = \frac{A\mu q^2 n_b}{k_B T}\sqrt{\frac{q_{dep}N_{dep}\phi_B}{2\varepsilon\varepsilon_0}}\exp\left(-\frac{q\phi_B}{k_B T}\right) \tag{1.46}$$

Eq. (1.46) is consistent with the resistance relationship given by Eq. (1.9), and offers a functional form for the pre-exponential parameter in Eq. (1.1), labelled R_0. One should note that R_0 depends on the value of ϕ_B in this regime, and is therefore influenced by factors such as the concentrations of ionised surface species. It follows that R_0 does not remain constant during the course of a reaction at the semiconductor surface.

Although Eq. (1.46) provides a straightforward and useful relationship between G_0 and ϕ_B, it should be remembered that it is only an approximate solution; when evaluating the integrals in Eq. (1.36) and Eq. (1.37), the dependence of E_x on ϕ_B was ignored. Returning to the more accurate expressions for F_L and F_R given in Eq. (1.29) and Eq. (1.31), respectively, one may show that

$$F_L = \frac{\mu}{x_{dep}}\sqrt{k_B T q V_1}\exp\left(\frac{qV_1}{k_B T}\right)\left(\int_0^{\sqrt{\frac{qV_1}{k_B T}}}\exp(x'^2)\,dx'\right)^{-1} \tag{1.47}$$

and

$$F_R = \frac{\mu}{x_{dep}}\sqrt{k_B T q V_2}\exp\left(\frac{qV_2}{k_B T}\right)\left(\int_0^{\sqrt{\frac{qV_2}{k_B T}}}\exp(x'^2)\,dx'\right)^{-1} \tag{1.48}$$

where

$$x' = \frac{1}{x_{dep}}\sqrt{\frac{qV_1}{k_BT}}\left(x + x_{dep}\right) \qquad -x_{dep} \le x \le 0 \tag{1.49}$$

and

$$x' = \frac{1}{x_{dep}}\sqrt{\frac{qV_2}{k_BT}}\left(x - x_{dep}\right) \qquad 0 \le x \le x_{dep} \tag{1.50}$$

These expressions for F_L and F_R yield the equation

$$G_0 = \frac{A\mu q^{3/2} n_b}{2}\sqrt{\frac{q_{dep}N_{dep}}{2\varepsilon\varepsilon_0 k_B T}}\left(\int_0^{\sqrt{\frac{q\phi_B}{k_BT}}} \exp(x'^2)\,dx'\right)^{-1} \tag{1.51}$$

Although the integral in Eq. (1.51) cannot be solved analytically, it is possible to make additional progress by noting that when $q\phi_B$ is much greater than k_BT, the integral is dominated by the region of x' closest to the non-zero limit. The series expansion of $\exp(x^2)$ is given by

$$\exp(x^2) = \sum_{n=0}^{\infty}\frac{x^{2n}}{n!} \tag{1.52}$$

Integrating with respect to x between zero and a positive limit, a, yields

$$\int_0^a \exp(x^2)dx = \sum_{n=0}^{\infty}\frac{a^{2n+1}}{n!(2n+1)} \tag{1.53}$$

As a tends to infinity,

$$\lim_{a\to\infty}\sum_{n=0}^{\infty}\frac{a^{2n+1}}{n!(2n+1)} \approx \frac{1}{2a}\exp(a^2) \tag{1.54}$$

In this limit, the zero-bias conductance becomes

$$\lim_{\phi_B \to \infty} G_0 = \frac{A\mu q^2 n_b}{k_B T} \sqrt{\frac{q_{dep} N_{dep} \phi_B}{2\varepsilon\varepsilon_0}} \exp\left(-\frac{q\phi_B}{k_B T}\right) \tag{1.55}$$

which is identical to Eq. (1.46). It is therefore clear that Eq. (1.46) is only valid for very large surface potentials.

1.3. The thermoelectronic emission model of current flow

Since the diffusion model is only applicable in the case where $q\phi_B$ is much greater than $k_B T$, an alternative approach is required when the surface potential does not satisfy this condition. One such option is the "thermoelectronic emission model", which considers the number of electrons with sufficient energy to pass over the potential barrier from each side [4,9]. To the left of the boundary, where the electric potential is V_1, electrons have mean thermal velocity v_{th} and are present at a concentration n_b. On the other side of the barrier, the electron concentration and mean velocity are the same, but the electric potential is V_2. The total volume of electrons approaching the barrier per unit time is proportional to v_{th} and n_b, and is therefore the same for both sides of the barrier. The probability of an electron being thermally activated over the barrier is described by a Maxwell-Boltzmann distribution, and so the total electron flux crossing the boundary to the right is given by

$$J_x = q n_b v_{th} \left(\exp\left(-\frac{qV_1}{k_B T}\right) - \exp\left(-\frac{qV_2}{k_B T}\right)\right) \tag{1.56}$$

It is important to note that the mean free path of electrons must exceed the width of the potential barrier for the thermoelectronic emission theory to be justified, as scattering within the boundary region has not been considered. In other words, electrons crossing the barrier are assumed to travel at constant velocity without changing direction.

To proceed, it is helpful to eliminate either V_1 or V_2 by recognising that the difference between the two potentials is equal to the applied potential, V_{app}. Eq. (1.56) therefore becomes

$$J_x = q n_b v_{th} \exp\left(-\frac{qV_1}{k_B T}\right)\left(1 - \exp\left(-\frac{qV_{app}}{k_B T}\right)\right) \tag{1.57}$$

From Eq. (1.57) and Eq. (1.41), the zero-bias conductance is related to ϕ_B via the expression

$$G_0 = \frac{Aq^2 n_b v_{th}}{k_B T} \exp\left(-\frac{q\phi_B}{k_B T}\right) \tag{1.58}$$

If the velocities of electrons are described by a Maxwell distribution, the mean velocity is given by

$$v_{th} = \sqrt{\frac{8k_B T}{\pi m^*}} \tag{1.59}$$

where m^* is the effective mass of the electrons. Eliminating v_{th} from Eq. (1.58) yields

$$G_0 = 2Aq^2 n_b \sqrt{\frac{2}{\pi m^* k_B T}} \exp\left(-\frac{q\phi_B}{k_B T}\right) \tag{1.60}$$

which is again compatible with the form of Eq. (1.9). In this case, the pre-exponential parameter, R_0, has no dependence on ϕ_B and is therefore not influenced by chemical reactions at the semiconductor surface.

As mentioned above, the thermoelectronic emission model is only valid when the total width of the potential barrier is less than the mean free path of the electrons, l_{sc}, which is given by

$$l_{sc} = v_{th}\tau_{sc} = \tau_{sc}\sqrt{\frac{8k_B T}{\pi m^*}} \tag{1.61}$$

where τ_{sc}, the mean time between scattering events for a given electron, is related to the electron mobility, μ, via the equation

$$\mu = \frac{q\tau_{sc}}{m^*} \tag{1.62}$$

Eliminating τ_{sc} from Eq. (1.61) gives

$$l_{sc} = \frac{\mu}{q}\sqrt{\frac{8m^* k_B T}{\pi}} \tag{1.63}$$

and hence the condition for the thermoelectronic emission model to remain valid is

$$\frac{\mu}{q}\sqrt{\frac{8m^* k_B T}{\pi}} \geq 2x_{dep} \tag{1.64}$$

Substituting for x_{dep} using Eq. (1.44) and rearranging, this condition becomes

$$\frac{q\phi_B}{k_B T} \leq \frac{\mu^2 m^* q_{dep} N_{dep}}{\pi\varepsilon\varepsilon_0 q} \tag{1.65}$$

In summary, it has been shown that the exponential relationship between R and ϕ_B, as expressed by Eq. (1.9), is recovered using both the drift-diffusion model of conduction and thermoelectronic emission theory. Through the former treatment, which applies in situations where $q\phi_B$ is much larger than the thermal energy, $k_B T$, it may be shown that

$$R_0 = \frac{k_B T}{A\mu q^2 n_b}\sqrt{\frac{2\varepsilon\varepsilon_0}{q_{dep} N_{dep}\phi_B}} \qquad q\phi_B \gg k_B T \tag{1.66}$$

In this regime, R_0 is therefore expected to increase as the magnitude of the surface potential is lowered, and further depends on the nature of ionic species within the depletion region. Conversely, the thermoelectronic emission model yields the relation

$$R_0 = \frac{1}{2Aq^2 n_b}\sqrt{\frac{\pi m^* k_B T}{2}} \qquad \frac{q\phi_B}{k_B T} \leq \frac{\mu^2 m^* q_{dep} N_{dep}}{\pi\varepsilon\varepsilon_0 q} \tag{1.67}$$

wherein R_0 exhibits no dependence on the characteristics of the surface potential or the depletion region. In a non-degenerate semiconductor, the concentration of electrons in the bulk conduction band may be expressed as [11]

$$n_b = N_C \exp\left(-\frac{E_{C,b} - E_F}{k_B T}\right) \tag{1.68}$$

where $E_{C,b}$ is the energy of the conduction band edge in the bulk of the semiconductor, E_F is the Fermi Energy, and N_C is the "effective density of states" in the conduction band given by

$$N_C = 4\sqrt{2}\left(\frac{\pi m^* k_B T}{h^2}\right)^{\frac{3}{2}} \tag{1.69}$$

Here, h denotes Planck's constant. It is therefore clear that although Eq. (1.66) and Eq. (1.67) predict slightly different proportionalities between R_0 and T, the difference is likely to be small due to the exponential temperature-dependence of n_b.

Although Eq. (1.9) relates ϕ_B to a measurable quantity, R, Eq. (1.68) reveals that the magnitude of the surface potential cannot be determined without knowledge of the energy difference $E_{C,b}$-E_F. To demonstrate this point more explicitly, it is helpful to recognise that Eq. (1.9) may be rewritten as

$$R = R_0' \exp\left(\frac{E_{C,b}+q\phi_B-E_F}{k_B T}\right) \tag{1.70}$$

where

$$R_0' = \frac{n_b}{N_C} R_0 \tag{1.71}$$

According to both the drift-diffusion and thermoelectronic emission conduction models,

$$R_0' \propto T^{\eta} \tag{1.72}$$

where the value of the constant η depends on the particular theory used. Consequently, it is possible to rearrange Eq. (1.70) to give

$$\ln(R) - \eta \ln(T) = \frac{E_{C,b}+q\phi_B-E_F}{k_B T} \tag{1.73}$$

which contains only measurable quantities on the left-hand side. It follows that the energy difference between the conduction band edge at the surface, $E_{C,b}+q\phi_B$, and the Fermi level

may be determined experimentally, specifically from the gradient of the relationship between $\ln(R)$-$\eta\ln(T)$ and $1/T$. For this reason, Eq. (1.73) will prove particularly useful in Chapter 5. The degree of band bending, however, cannot be deduced from such a relationship, as the value of $q\phi_B$ remains unknown. In the following section it will be demonstrated that calculation of $E_{C,b}$-E_F, and hence $q\phi_B$, may be achieved following an electroneutrality argument, but requires knowledge of the inter-band donor and acceptor states in the semiconductor.

1.4. The influence of deep-level donors on the position of the Fermi level

Before discussing the case of ZnO, the position of the Fermi level will first be considered for a non-degenerate n-type semiconductor containing only shallow donors. In this case, the Fermi energy in the bulk material may be determined through a straightforward application of Boltzmann statistics in an electroneutrality argument [12,13]. As the donor states are situated close to the conduction band, it is possible to assume that they are full ionised. If each donor state donates a single electron, the concentration of electrons in the conduction band, n_C, is therefore approximately equal to the density of donor states, N_D. Assuming that the energy difference between the conduction band minimum and the Fermi level is much larger than the thermal energy, k_BT, one obtains the expression

$$\boldsymbol{n_C = N_C \exp\left(-\frac{E_{C,b}-E_F}{k_BT}\right) = N_D} \tag{1.74}$$

Rearrangement of Eq. (1.74) yields

$$\boldsymbol{E_F = E_{C,b} - k_BT \ln\left(\frac{N_C}{N_D}\right)} \tag{1.75}$$

which suggests that an increase in the temperature or a decrease in the density of donor states results in the Fermi level shifting to a lower energy value. This behaviour is necessitated by the requirement that n_C remains equal to N_D.

However, for a semiconductor such as ZnO which contains deep-lying uncompensated donor states, the situation is more complicated. In particular, it is no longer possible to assume that the donor states are fully ionised, as the position of the donor state energy relative to the Fermi level is not known. For this reason, the occupancy of the donor states cannot be calculated using Boltzmann statistics as before, and the more precise Fermi-Dirac distribution must be used instead. Following the formalism outlined by G. Roberts *et al.* [13], electroneutrality requires that the total positive electric charge density provided by the ionised donor states must equal the negative charge density of the conduction band electrons. If the donor states are singly-ionised and have energy $E_{D,b}$ and spin degeneracy g, one may therefore write

$$N_D\left(1-\frac{1}{1+\frac{1}{g}\exp\left(\frac{E_{D,b}-E_F}{k_BT}\right)}\right)=N_C\exp\left(-\frac{E_{C,b}-E_F}{k_BT}\right) \tag{1.76}$$

The left-hand side of Eq. (1.76) corresponds to the concentration of ionised donor states, and is constructed by first recognising that, in the absence of spin degeneracy, the electron-occupancy of the donor level is given by the Fermi-Dirac probability distribution. The factor g arises due to multiple electron occupancy each donor state, allowing a singly-ionised donor state to possess various possible spin configurations. In cases where the donor states may be occupied by two electrons, for example, each singly-ionised donor state has two possible spin configurations so g has a value of two. As the semiconductor is assumed to be non-degenerate (i.e. the magnitude of $E_{C,b}$-E_F is much greater than the thermal energy, k_BT), the concentration of conduction band electrons may be determined using the Boltzmann approximation of the Fermi-Dirac equation, as before.

To formulate an expression for E_F from Eq. (1.76), it is helpful to define a new variable, f, as

$$f\equiv\exp\left(\frac{E_F}{k_BT}\right) \tag{1.77}$$

Subsequent rearrangement of Eq. (1.76) yields the quadratic equation

$$f^2 + \frac{f}{g}\exp\left(\frac{E_{D,b}}{k_B T}\right) - \frac{N_D}{gN_C}\exp\left(\frac{E_{D,b}+E_{C,b}}{k_B T}\right) = 0 \tag{1.78}$$

for which one obtains the physical solution

$$f = \frac{1}{2g}\exp\left(\frac{E_{D,b}}{k_B T}\right)\left(-1 + \sqrt{1 + 4g\frac{N_D}{N_C}\exp\left(\frac{E_{C,b}-E_{D,b}}{k_B T}\right)}\right) \tag{1.79}$$

Taking the natural logarithm of Eq. (1.79) and eliminating f, it is possible to show that

$$E_F = E_{D,b} + k_B T \ln\left(\frac{1}{2g}\left(-1 + \sqrt{1 + 4g\frac{N_D}{N_C}\exp\left(\frac{E_{C,b}-E_{D,b}}{k_B T}\right)}\right)\right) \tag{1.80}$$

In contrast to the case of a non-degenerate conductor containing only shallow donors, Eq. (1.80) suggests that an increase in T or N_D may either raise or lower the value of E_F, depending on the values of the system parameters. More specifically, if the magnitudes of N_D and $E_{C,b}$-$E_{D,b}$ are sufficiently high, the argument of the logarithm is greater than one and E_F therefore approaches $E_{C,b}$ as the temperature is increased. In this regime, the Fermi level is situated above the energy of the donor states. Conversely, if the argument of the logarithm has a value less than one, E_F is lower than $E_{D,b}$ and correlates negatively with temperature. Fig. 1.4 shows how E_F varies as a function of temperature for assorted values of N_D/N_C, adopting values of $E_{C,bulk}$-$E_{D,bulk}$ and m^* that are characteristic of a ZnO system. More specifically, the donor states are assumed to lie 700 meV below the conduction band minimum [14,15], while m^* is approximated 0.24 times the free electron mass [16–19].

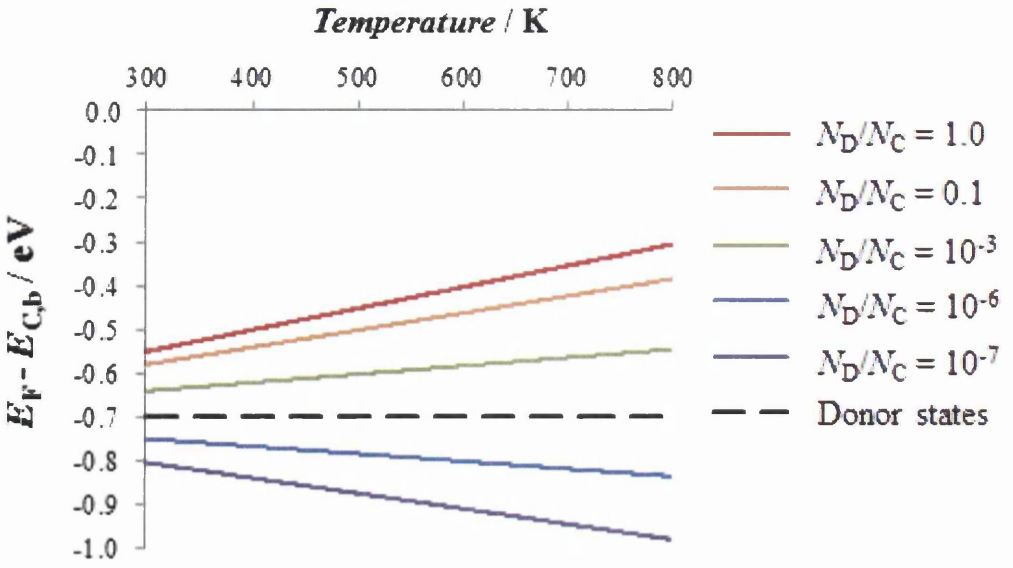

Fig. 1.4. A plot depicting the variation of the Fermi energy, relative to the conduction band minimum, as a function of temperature for assorted values of N_D/N_C. Typical values of 700 meV and 2.2×10^{-31} kg (0.24 times the mass of a free electron) have been adopted for $E_{C,b}$-$E_{D,b}$ and m^*, respectively.

It is instructive to note that Eq. (1.75) actually represents a special case of Eq. (1.80), where E_F is much lower than $E_{D,b}$. To realise this scenario, the argument of the logarithm must be much less than one, which in turn implies that

$$4g\frac{N_D}{N_C}\exp\left(\frac{E_{C,b}-E_{D,b}}{k_BT}\right) \ll 1 \tag{1.81}$$

Imposing this condition and applying a first-order binomial approximation to the argument of the logarithm, one may show that

$$\frac{1}{2g}\left(-1+\sqrt{1+4g\frac{N_D}{N_C}\exp\left(\frac{E_{C,b}-E_{D,b}}{k_BT}\right)}\right) \approx \frac{N_D}{N_C}\exp\left(\frac{E_{C,b}-E_{D,b}}{k_BT}\right) \tag{1.82}$$

where all dependence on the spin degeneracy factor, g, has been lost. By substituting this approximation into Eq. (1.80), one recovers the form of Eq. (1.75).

Having outlined the fundamental theory governing the operation of chemiresistive gas sensors, the next chapter will address the nature of the gas reactions at a metal oxide surface and provide an overview of existing phenomenological models in the literature. In addition, the effects of surface catalysts, specifically noble metal nanoparticles, will be discussed in detail, describing how these additives have been used to enhance both the sensitivity and selectivity of metal oxide-based gas sensors.

References

[1] A. Gurlo, Interplay between O2 and SnO2: Oxygen ionosorption and spectroscopic evidence for adsorbed oxygen, ChemPhysChem. 7 (2006) 2041–2052. doi:10.1002/cphc.200600292.

[2] A. Kolmakov, M. Moskovits, Chemical Sensing and Catalysis By One-Dimensional Metal-Oxide Nanostructures, Annu. Rev. Mater. Res. 34 (2004) 151–180. doi:10.1146/annurev.matsci.34.040203.112141.

[3] M.A. Carpenter, S. Mathur, A. Kolmakov, Metal Oxide Nanomaterials for Chemical Sensors, Springer, New York, 2013.

[4] N. Barsan, U. Weimar, Conduction model of metal oxide gas sensors, J. Electroceramics. 7 (2001) 143–167. doi:10.1023/A:1014405811371.

[5] C. Malagù, V. Guidi, M. Stefancich, M.C. Carotta, G. Martinelli, Model for Schottky barrier and surface states in nanostructured n-type semiconductors, J. Appl. Phys. 91 (2002) 808–814. doi:10.1063/1.1425434.

[6] E. Comini, C. Baratto, G. Faglia, M. Ferroni, a. Vomiero, G. Sberveglieri, Quasi-one dimensional metal oxide semiconductors: Preparation, characterization and application as chemical sensors, Prog. Mater. Sci. 54 (2009) 1–67. doi:10.1016/j.pmatsci.2008.06.003.

[7] M.E. Franke, T.J. Koplin, U. Simon, Metal and metal oxide nanoparticles in chemiresistors: Does the nanoscale matter?, Small. 2 (2006) 36–50. doi:10.1002/smll.200500261.

[8] F Greuter, G Blatter, Electrical properties of grain boundaries in polycrystalline compound semiconductors, Semicond. Sci. Technol. 5 (1990) 111–137.

[9] A. Broniatowski, Electronic States at Grain Boundaries in Semiconductors, in: G. Harbeke (Ed.), Polycryst. Semicond., Springer, New York, 1985: pp. 95–117.

[10] W.E. Taylor, N.H. Odell, H.Y. Fan, Grain boundary barriers in germanium, Phys. Rev. 88 (1952) 867–875. doi:10.1103/PhysRev.88.867.

[11] R. Stratton, Surface Barriers at Semiconductor Contacts, Proc. Phys. Soc. Sect. B. 69 (1956) 513–527. doi:10.1088/0370-1301/69/5/303.

[12] K.K. Chin, Approximate graphical method of solving Fermi level and majority carrier density of semiconductors with multiple donors and multiple acceptors, J. Semicond. 32 (2011) 062001. doi:10.1088/1674-4926/32/6/062001.

[13] G.G. Roberts, N. Apsley, R.W. Munn, Temperature Dependent Electronic Conduction in Semiconductors, Phys. Rep. 60 (1980) 59–150.

[14] F.A. Selim, M.H. Weber, D. Solodovnikov, K.G. Lynn, Nature of native defects in ZnO, Phys. Rev. Lett. 99 (2007) 85502. doi:10.1103/PhysRevLett.99.085502.

[15] M.W. Allen, S.M. Durbin, Influence of oxygen vacancies on Schottky contacts to ZnO, Appl. Phys. Lett. 92 (2008) 90–93. doi:10.1063/1.2894568.

[16] W.S. Baer, Faraday Rotation in ZnO: Determination of the Electron Effective Mass, Phys. Rev. 154 (1967) 785–789.

[17] L.E. Brus, Electron–electron and electron-hole interactions in small semiconductor crystallites: The size dependence of the lowest excited electronic state, J. Chem. Phys. 80 (1984) 4403. doi:10.1063/1.447218.

[18] M. Oshikiri, Y. Imanaka, F. Aryasetiawan, G. Kido, Comparison of the electron effective mass of the n-type ZnO in the wurtzite structure measured by cyclotron resonance and calculated from first principle theory, Phys. B Condens. Matter. 298 (2001) 472–476. doi:10.1016/S0921-4526(01)00365-9.

[19] B.K. Meyer, H. Alves, D.M. Hofmann, W. Kriegseis, D. Forster, F. Bertram, et al., Bound exciton and donor-acceptor pair recombinations in ZnO, Phys. Status Solidi Basic Res. 241 (2004) 231–260. doi:10.1002/pssb.200301962.

Chapter 2 – Literature review

2.1. An overview of ZnO-based gas sensors

As a result of the high demand for responsive but affordable gas sensors, much recent research into chemiresistive devices has centred on readily available metal oxide semiconductors. Of these, ZnO stands out as a particularly versatile option due to its propensity to form nanostructures, providing a high specific surface area for gas adsorption. Through application of experimental techniques such as chemical vapour deposition (CVD) and wet-chemical synthesis, it is possible to realise a variety of ZnO morphologies, ranging from nanowires [1–8] to nanosheets and nanobelts [8–13].

Since the turn of the century, a substantial body of work has been published regarding practical ZnO-based gas sensors. Several publications explore the properties of a single ZnO nanowire [14–22], sometimes making use of the field effect provided by a metallic back-gate to control the electrical conductivity of the material [20–24]. One such example is depicted in Fig. 2.1, which appears as Fig. 1 in the original study [18]. A significant advantage of single-nanowire devices is their associated reproducibility, as it is possible to tailor the dimensions of the selected nanowire as required. It should be noted, however, that despite the high controllability afforded by these sensors, their practical usefulness is limited by the difficulty of their fabrication. To achieve a more marketable product, it is essential for the manufacturing process to be both cost-effective and scalable.

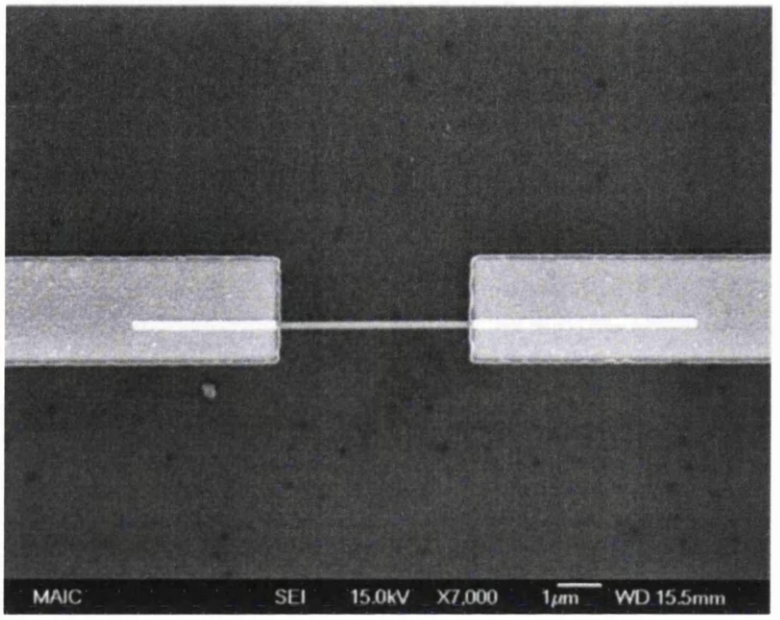

Fig. 2.1. An SEM image from Reference [18] **showing a gas sensor consisting of a single ZnO nanowire bridging the gap between two metallic contacts.**

Instead of using a single nanowire, many studies make use of a ZnO nanowire array in either a vertical [25–29] or lateral configuration [30–36] between two conductive contacts. As shown in Fig. 2.2, the former arrangement requires nanowires to be grown from a suitable substrate, typically silicon, before a conductive "top-contact" is added to create an electrical pathway between the free ends of the nanowires. Due to the vertical alignment of the nanowires, it is possible to create an extremely high surface area by incorporating a large number of nanowires into the device. Unfortunately, fabrication of the conductive top-contact is not straightforward and typically involves several lithographic steps.

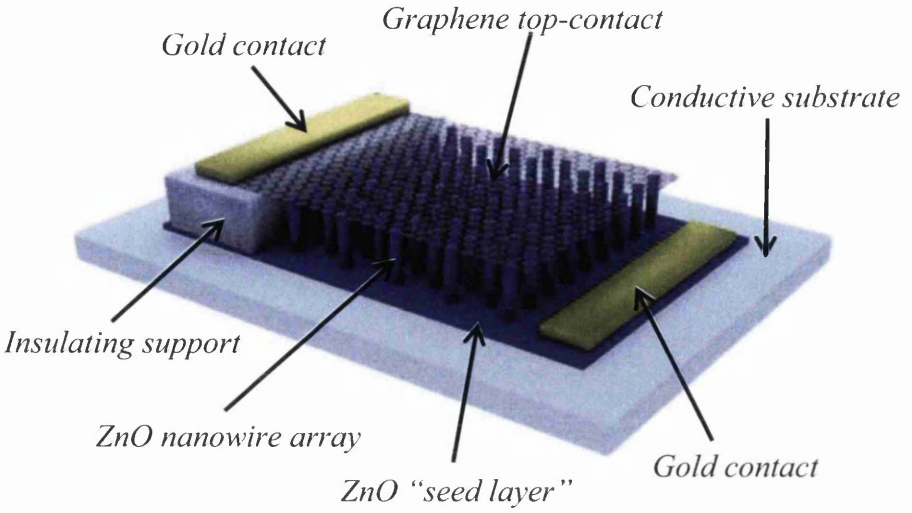

Fig. 2.2. An illustration of a chemiresistive gas sensor, adapted from Fig. 1 in Reference [27]. **The device consists of two conductive contacts separated by an array of ZnO nanowires, with gold contacts added to allow electrical contact to the external circuitry.**

The alternative nanowire configuration, where the nanowires provide conductive pathways between two lateral contacts, may be achieved through a more straightforward fabrication procedure. Some groups opt to bridge the contacts using nanowire arrays grown heterogeneously on the sensor surface [30–33], as depicted in Fig. 2.3 (adapted from Fig. 1(b) of Reference [30]). By contrast, other researchers choose to transfer nanowires grown separately by first incorporating them into a paste [34,35,37,38]. The latter methodology affords great versatility to the sensor fabrication, as the growth of the nanowires is not limited by the nature of the substrate material. Indeed, in this procedure there is no necessity to obtain the nanowires through heterogeneous growth from a surface, a typically slow process which cannot easily be scaled. Instead, the nanowires may be grown homogeneously in suspension and subsequently filtered and cleaned prior to use. For instance, B. Shouli *et al.* [34] report several techniques for producing a suspension of ZnO nanostructures, each requiring a solution of various precursors to be heated for an extended period in an autoclave. In one such procedure, a solution containing sodium dodecyl sulphate (SDS), sodium hydroxide and zinc nitrate hexahydrate was heated at 85°C for five hours in a sealed, Teflon-

lined stainless steel autoclave, yielding a suspension of nanowires with lengths of several microns; the deposited nanowires are shown in Fig. 2.4, which appears in the original publication as Fig. 5.

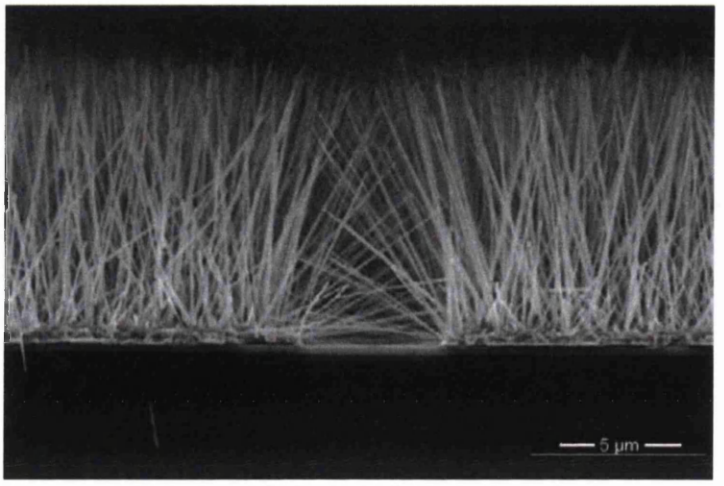

Fig. 2.3. An SEM image showing ZnO nanowires grown using CVD on two catalytic 2 nm-thick Au films separated by a region containing no growth. The image is adapted from Fig. 1 (b) of Reference [30]**. The two catalysed areas are connected electrically through contact of nanowires over the region of no-growth.**

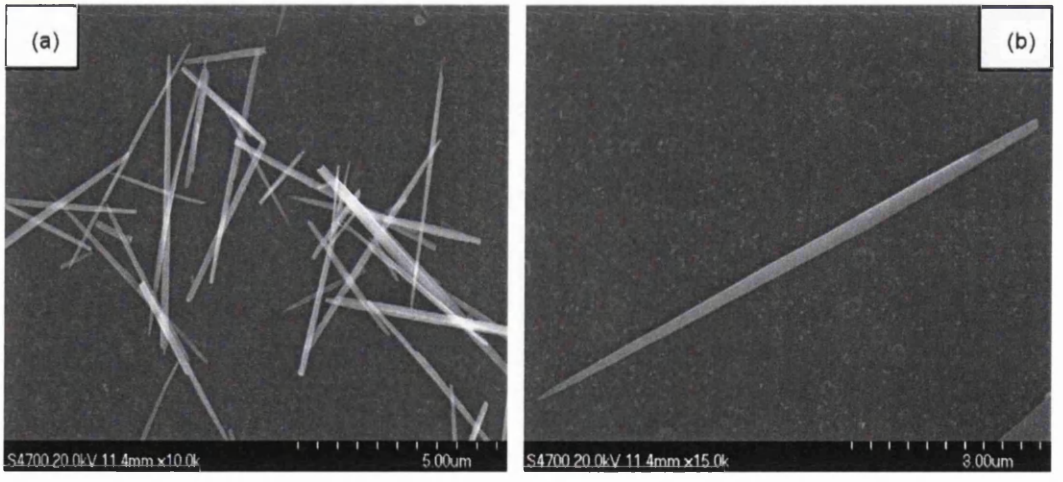

Fig. 2.4. SEM images depicting ZnO nanowires grown in suspension through reaction of sodium dodecyl sulphate (SDS), sodium hydroxide and zinc nitrate hexahydrate at 85°C for five hours in a sealed, Teflon-lined stainless steel autoclave vessel. The images are reproduced from Reference [34]**, where they appear as images (a) and (b) of Fig. 5.**

Although the synthesis of ZnO nanostructures is often accomplished by heating a solution for several hours in a water bath or an autoclave, some researchers have achieved more rapid fabrication by instead stimulating nanostructure formation through microwave heating [39–49]. One particularly common approach is to use a conventional microwave oven to obtain a suspension of a zinc compound with a layered hydrozincite structure [50–52], such as layered basic zinc acetate (LBZA, also referred to as zinc hydroxy acetate) [42,48,52–59] or basic zinc nitrate (BZN, sometimes called zinc hydroxy nitrate) [43,46,49,51], which thermally decomposes to ZnO when annealed at a sufficiently high temperature. Due to the layered structure of hydrozincite materials, they naturally adopt the form of quasi-two-dimensional nanosheets. For example, in a study by Z. Jing and J. Zhan [42], nanosheets with a hydrozincite structure were obtained by microwaving a solution containing zinc acetate and urea for thirty minutes, maintaining the temperature at 95°C and stirring throughout. After centrifuging, washing and drying the precipitate, it was annealed in air at 400°C for two hours to thermally decompose the material. As shown by the SEM images in Fig. 2.5, which appears as Fig. 1 of the publication, the transformation to ZnO retains the quasi-two-dimensional morphology of the nanostructures but increases their porosity.

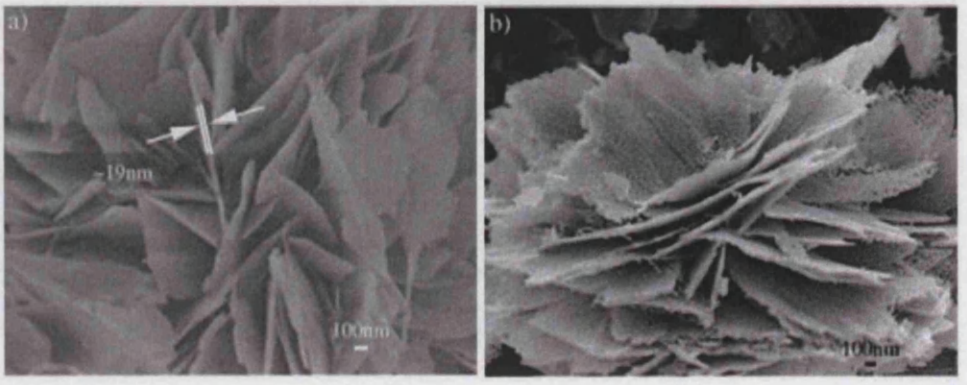

Fig. 2.5. SEM images from Reference [42] showing nanosheets obtained via a solution-based reaction between zinc acetate and urea, both before (a) and after (b) annealing in air at 400°C for two hours. The as-formed compounds, which possess a hydrozincite structure, thermally decompose to ZnO during the annealing procedure, increasing the porosity of the nanosheets but retaining their quasi-two-dimensional morphology.

2.2. Relating the gas response to the dynamics of surface reactions

In the previous chapter it was shown that the electrical resistance of a semiconductor boundary is strongly influenced by the formation of ionic surface species, which may occur at sufficiently high temperature. In particular, it was recognised that the ionisation of adsorbed O_2 molecules requires electrons to be removed from the conduction band, leading to upward band bending and inhibiting current flow through the surface. Introduction of a reducing gas such as CO or H_2 leads to the removal of the surface oxygen anions in the form of neutral molecules such as CO_2 or H_2O, thereby returning electron density to the semiconductor and lowering the resistance. Using Poisson's equation for electrostatics, a straightforward expression was derived to relate the resistance of the system, R, to the proportion of surface sites occupied by ionic species, θ_O, in terms of two temperature-dependent parameters, α and R_0. However, to make further progress it is necessary to formulate a physical model of the surface reactions in order to determine how their properties influence the time-variation of θ_O and, most importantly, how the equilibrium concentration of surface species is related to the reaction parameters of the system.

When considering the nature of the surface reactions, it is essential to make use of suitable physical assumptions in order to obtain a practically useful model. In the case of systems where no catalytic additives are present, many authors assume that the surface sites are occupied solely by ionic oxygen species, neglecting the adsorption of reducing gas molecules [60–67]. Without this simplification, there exists competition for unoccupied surface sites between different species, leading to an array of coupled differential equations that are of little use experimentally. Ignoring the adsorption of reducing gas molecules reduces the number of equations required to provide a complete description of the system, and also lowers the number of reactions to be considered. This is often a reasonable assumption as the concentration of reducing gases is typically at least one thousand times less than that of atmospheric oxygen. Of particular note is the reaction between the reducing gas and surface oxygen ions; within the simplified model, where no surface sites are occupied by reducing gas molecules, one need only account for the direct interaction between ionic oxygen and incident reducing gas from the surroundings. This reaction regime, known as the Eley-Rideal mechanism, is illustrated in Fig. 2.6, which shows a typical reaction between CO molecules

and singly-ionised oxygen at the surface of an archetypal n-type semiconductor at elevated temperature.

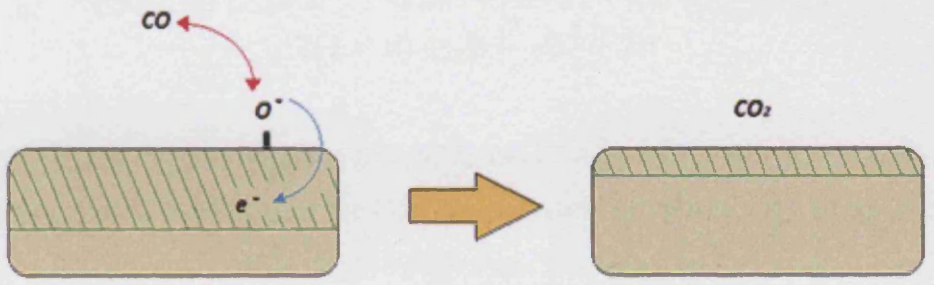

Fig. 2.6. An illustration of the oxidation of CO at an n-type semiconductor surface via an Eley-Rideal mechanism. The reaction releases electrons back to the conduction band of the semiconductor, reducing the width of the depleted surface region (represented by the green, hatched region).

Before constructing the requisite differential equations to describe the system, it is first necessary to identify the surface reactions that must be included in the model. Using a similar notation to that adopted by S. Nakata *et al.* [67], the formation and recombination of O^- ions are commonly described by the chemical equations

$$nS + \frac{1}{2}O_2 + e^- \overset{k_1}{\rightarrow} O_S^- + (n-1)S \tag{2.1}$$

and

$$O_S^- + (n-1)S \overset{k_{-1}}{\longrightarrow} nS + \frac{1}{2}O_2(b) + e^- \tag{2.2}$$

respectively, where n denotes the number of unoccupied surface sites, S, prior to O^- formation, O_S^- corresponds to an O^- ion located at a surface site, e^- is a conduction band electron, and k_1 and k_{-1} are the rate constants for O^- formation and recombination, respectively. However, the ionosorption reaction described by Eq. (2.1) involves both dissociation and ionisation of adsorbed O_2 molecules, so the equation does not necessarily

represent an elementary reaction step. For this reason, some authors [63–65] prefer to consider the dissociation and ionisation of the O_2 molecule as two distinct stages of the overall ionosorption reaction, writing

$$nS + \frac{1}{2}O_2 \xrightarrow{k_1'} O_S + (n-1)S \tag{2.3}$$

and

$$O_S + e^- \xrightarrow{k_1''} O_S^- \tag{2.4}$$

where O_S corresponds to an electrically-neutral oxygen atom that is adsorbed at a surface site, and k_1' and k_1'' are the rate constants for the dissociation and ionisation reactions, respectively. In the presence of a reducing gas, X, the O^- ions react according to

$$X + O_S^- \xrightarrow{k_{2X}} XO_S^- \tag{2.5}$$

followed by

$$XO_S^- \xrightarrow{k_{3X}} XO + S + e^- \tag{2.6}$$

where k_{2X} and k_{3X} are the rate constants for the respective reactions, and XO_S^- represents a reactive charged intermediate located at a surface site. It should be noted that this reaction is considered to be irreversible, so that any XO_S^- species must eventually decompose to produce a molecule of XO and return an electron to the conduction band of the semiconductor.

After identifying the appropriate chemical equations, it is possible to determine how the concentrations of different surface species vary as a function of time. If the dissociation and ionisation of O_2 molecules are regarded as separate elementary steps, one must formulate differential equations to describe the time-varying concentrations of both the O^- ions and neutral O atoms, in addition to the reactive intermediates, XO_S^-. By alternatively assuming a

single-step formation mechanism, it is common to express the rate of change of the O^- concentration, $[O_S^-]$, as [66,67]

$$\frac{d[O_S^-]}{dt} = k_1 \left(\frac{P_{O2}}{P_{TOT}}\right)^{1/2} ([S_0] - [O_S^-]) - k_{-1}[O_S^-] - k_{2X}\left(\frac{P_X}{P_{TOT}}\right)[O_S^-] \quad (2.7)$$

where P_{O2} and P_X are the partial pressures of O_2 and X in the surroundings, respectively, P_{TOT} is the total pressure and $[S_0]$ is the total concentration of surface sites, either vacant or occupied. As one molecule of O_2 yields two O^- ions, the rate of O^- formation is proportional to the square root of P_{O2} and scales linearly with the concentration of exposed sites. It is important to note that despite the presence of conduction electrons in Eq. (2.1), the electron concentration is accounted for in relatively few studies [63–65]. Although the omission of the electron concentration from Eq. (2.7) is typically not rationalised, it is possible that the authors regard the initial chemisorption and dissociation of the O_2 molecule as the rate-determining step of the O^- formation reaction. The second term of Eq. (2.7), containing rate constant k_{-1}, corresponds to the recombination of O^- ions described by Eq. (2.2), while the third is attributed to the formation of XO_S^- intermediates due to the reaction between O^- ions and incident molecules of X. In a similar manner, the concentration of XO_S^- intermediates, $[XO_S^-]$, is governed by the differential equation

$$\frac{d[XO_S^-]}{dt} = k_{2X}\left(\frac{P_X}{P_{TOT}}\right)[O_S^-] - k_{3X}[XO_S^-] \quad (2.8)$$

where the first term corresponds to the formation of XO_S^- intermediates due to the reaction of X molecules with O^- ions, and the second accounts for the conversion of the intermediates to the XO product. Throughout the derivation, it is assumed that the surface sites are not obstructed by molecules of O_2 or X, and that the resulting molecules of XO instantly desorb from the surface.

In all of the theoretical treatments summarised above, the formation of monovalent O^- ions is assumed without justification, and no other types of ionic oxygen are considered. Since the form of the resulting differential equations depends strongly on the nature of the surface ions, it is clearly important to experimentally determine which species are present. To this end, a

variety of studies have investigated the surface reactions at metal oxide surfaces using a multitude of spectroscopic procedures, including Fourier-transformed infra-red (FTIR) spectroscopy [68–70], electron paramagnetic resonance (EPR) spectroscopy (often referred to as electron spin resonance spectroscopy, or ESR) [71–79] and X-ray photoelectron spectroscopy (XPS) [80,81]. By combining temperature-programmed desorption (TPD) experiments, in which the rate of oxygen desorption is measured as a function of temperature [82], with EPR and conductivity measurements, an early investigation by N. Yamazoe *et al.* [75] revealed that O_2^- ions are formed at the surface of SnO_2 up to a temperature of approximately 150°C, while oxygen continues to ionosorb in the form of O^- ions up to around 560°C. The reported TPD measurements have been reproduced in more recent studies [83,84]. Similar results were obtained in a comparable TPD experiment on ZnO conducted by K. Tanaka and G. Blyholder [76], who measured maximum oxygen desorption at temperatures of 180-190°C and 285-295°C. Through use of EPR spectroscopy, the desorption peak appearing at lower temperature was attributed to O_2^- ions, while the oxygen desorbed at higher temperature was tentatively ascribed to O^- species. In a further study by M. Iwamoto *et al.* [78], the oxygen desorption from ZnO was once more found to be maximised at two separate temperatures, as shown by the TPD chromatogram displayed in Fig. 2.7. Although the authors again used EPR to relate the low-temperature desorption peak, centred at 190°C, to the presence of O_2^- ions, they were more reluctant to assign the high-temperature desorption peak, at 320°C, to O^- ions; as remarked elsewhere [85], despite widespread agreement that surface oxygen predominantly exists in the form of O^- ions at high temperature, the EPR measurements responsible for this interpretation are often contradictory.

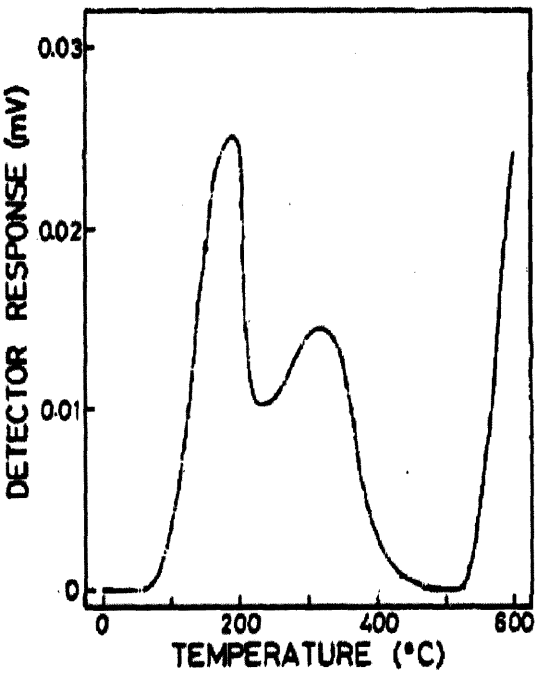

Fig. 2.7. A temperature-programmed desorption (TPD) chromatogram of oxygen from ZnO following pre-adsorption of oxygen at room temperature. The plot has been adapted from Fig. 3 of Reference [78].

To further elucidate which oxygen species take part in the reaction with a reducing gas, FTIR spectroscopy is often invaluable. In one investigation by D. Koziej *et al.* [68], this technique was used to distinguish between reactive intermediates formed during the oxidation of CO gas at an SnO_2 surface, in turn allowing the corresponding oxygen reactant to be identified. The authors reason that while O^- radicals react with molecules of CO to produce CO_2^- intermediates, this species is not generated during the reaction between CO and O_2^- ions; instead, the interaction yields either the monovalent CO_3^- ion or the more energetically stable CO_3^{2-} ion. It should be recognised that the formation of CO_3^{2-} ions is a possibility in both cases, as two O^- ions may react with a single molecule of CO. Importantly, each intermediate is associated with a different signal in the FTIR spectrum due to the different vibrational frequencies of their respective bonds. At temperatures of 300°C or below, all three intermediates were detected following reaction of CO at the SnO_2 surface. Increasing the temperature to 400°C led to the FTIR spectrum containing none of the characteristic intermediate signals, indicating that the reaction of CO proceeded through a single step with

no metastable states. One such reaction, identified by the authors, is described by the equation

$$CO + O^- \rightarrow CO_2 + e^- \tag{2.9}$$

in which the oxidation of a CO molecule by an O^- ion generates a stable molecule of CO_2 and returns an electron to the semiconductor conduction band.

The predominance of O^- ions at high temperature has also been demonstrated theoretically. According to a Monte-Carlo simulation of a SnO_2 surface by U. Pulkkinen *et al.* [86], O_2 is mostly ionosorbed as O_2^- ions at low temperatures, with no O^- ions existing below 500 K. As shown by Fig. 2.8, dissociation of the O_2^- radicals at higher temperatures leads to the formation of O^- ions, which becomes the dominant species at a temperature of approximately 700 K. However, in contrast to the results of the TPD experiments outlined previously, the model predicts the co-existence of O^- and O_2^- ions up to around 900 K, above which the dissociation of O_2^- ions may be considered complete. Neutrally-charged "bridging" oxygen atoms, denoted O, are predicted at all temperatures, and are over forty times more abundant than the ionic species.

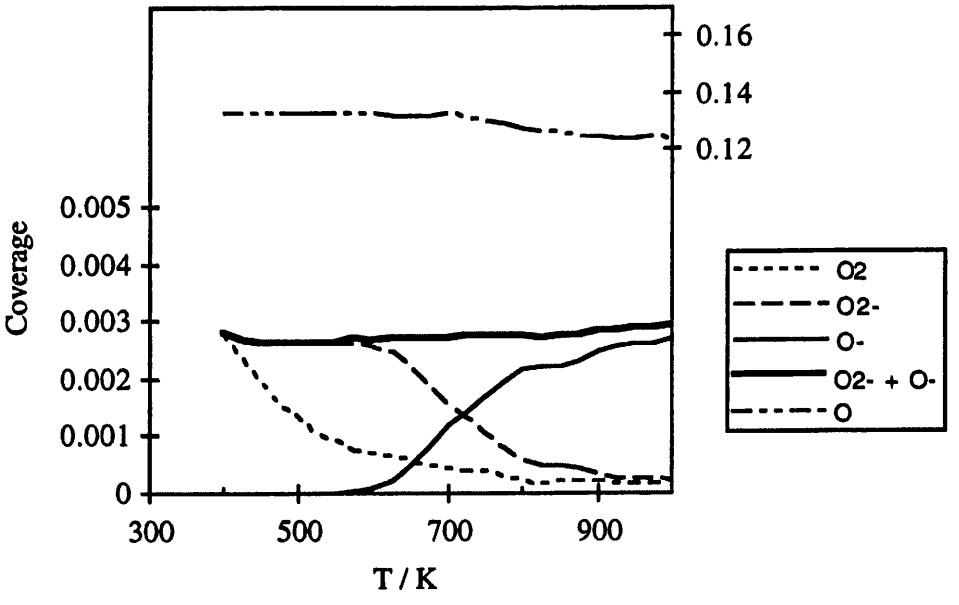

Fig. 2.8. A plot showing the coverage of different surface oxygen species at a SnO_2 surface as a function of temperature, as predicted by a Monte-Carlo simulation. The plot is reproduced from Reference [86], **where it appears as Fig. 2.**

When modelling the surface reactions of a metal oxide-based gas sensor, it is often appropriate to assume an Eley-Rideal scheme to describe the interaction between reactive species. In the presence of surface catalysts, however, such a model does not necessarily provide an accurate representation of the physical system due to enhanced adsorption of the reducing gas molecules. An alternative approach, wherein the reaction between adsorbed species is considered, shall be discussed in the following section, in addition to a review of relevant experimental works in the literature.

2.3. The catalytic properties of noble metal nanoparticles

In order to enhance the sensitivity and selectivity of chemiresistive gas sensors, researchers commonly catalyse the gas reactions using nanoparticles of noble metals such as gold [87–91], platinum [92–96] or palladium [97–100]. In general, these catalysts operate by facilitating the adsorption and dissociation of reducing gas molecules and/or formation of oxygen ions, thus providing a low-energy pathway for the reaction between the two species. Due to the favourability of this reaction, the Eley-Rideal mechanism typically does not provide an appropriate description of a catalysed system. Instead, it is often necessary to consider Langmuir-Hinshelwood reaction steps in which interaction occurs between species adsorbed at adjacent surface sites [60–62,101–104], as illustrated in Fig. 2.9 [102]. In the depicted example, the reducing gas adsorbs on the noble metal catalyst whereas ionosorption of oxygen occurs predominantly at the metal oxide surface, so the reaction may only occur following migration of one or both of the species to the interface between the two materials. This movement of species from the surface catalyst to the metal oxide support is known as "spillover" [62,102,105–119].

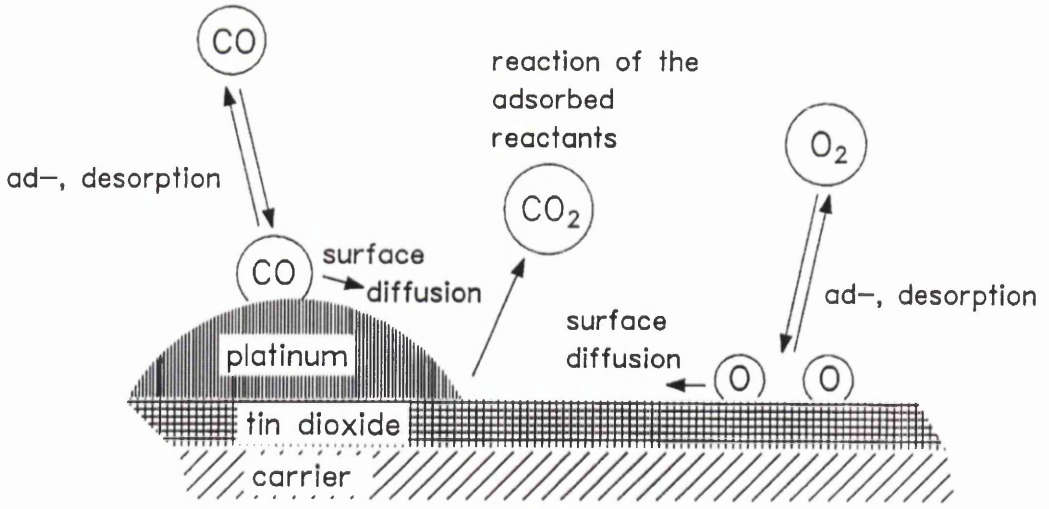

Fig. 2.9. An illustration of the oxidation of CO on Pt-catalysed SnO_2, which appears in Reference [102] **as Fig. 8. Molecules of CO first adsorb at the Pt surface before diffusing to the SnO_2 support during a process known as "spillover". Reaction between the spilt-over CO molecules and ionosorbed oxygen leads to the production of CO_2 gas.**

Chemical reactions in the presence of noble metal catalysts have been investigated using a variety of experimental procedures, including FTIR spectroscopy [71,107,108,111,113,115,120–124], temporal analysis of products (TAP) measurements [115,125–129] and X-ray techniques [116,130]. In the case of H_2, molecular dissociation at the noble metal surface generates monatomic hydrogen radicals which may spillover onto the metal oxide support. The spilt-over species subsequently interact with ionosorbed oxygen to form hydroxyl radicals, thereby enhancing the vibrational O-H signal in the FTIR spectrum of the sample. Although the hydroxyl species may themselves react to produce molecules of water, it has been demonstrated through FTIR and TPD experiments that the radicals are long-lived at temperatures below 200°C [107,131–133]. The irreversible nature of hydroxyl formation at low temperatures is of practical significance, as it is associated with a low rate of sensor recovery [109,112,134].

To study the spillover effect during the catalysed oxidation of CO, multiple groups have measured the "turn-over frequency" (TOF) at the surface of Au-catalysed TiO_2 [125,127–129,135–137], defined as the number of moles of reactant converted to product per mole of

reaction sites. By constructing an Arrhenius plot for the rate of CO oxidation, it has been demonstrated that the activation energy of the reaction increases sharply at around 320–350K, indicating that a mechanistic change occurs at this temperature [135,136,138]. To further explore this phenomenon, T. Fujitani and I. Nakamura [135] measured the rate of CO_2 formation at 300 K and 400 K and normalised the results with respect to either the total number of exposed Au atoms (referred to as TOF-S) or the quantity of TiO_2 "perimeter sites" located in the immediate vicinity of the Au nanoparticles (denoted TOF-P). As shown by the plots displayed in Fig. 2.10, the relationship between the turnover frequency and Au nanoparticle size varied considerably between the two temperatures. In particular, it was shown that while TOF-P was not influenced by the morphology of the catalyst at 300 K, increasing the temperature to 400 K led to constant TOF-S and direct proportionality between TOF-P and nanoparticle size. These observations suggest that the oxidation of CO occurs predominantly at perimeter sites at 300 K, corroborating the suggestion that the reaction proceeds following spillover of CO onto the TiO_2 support. Conversely, the constant value of TOF-S at 400 K indicates that at this temperature the interaction between chemisorbed CO and ionosorbed oxygen takes place on the surface of the Au catalyst, and is therefore not dependent on the spillover process.

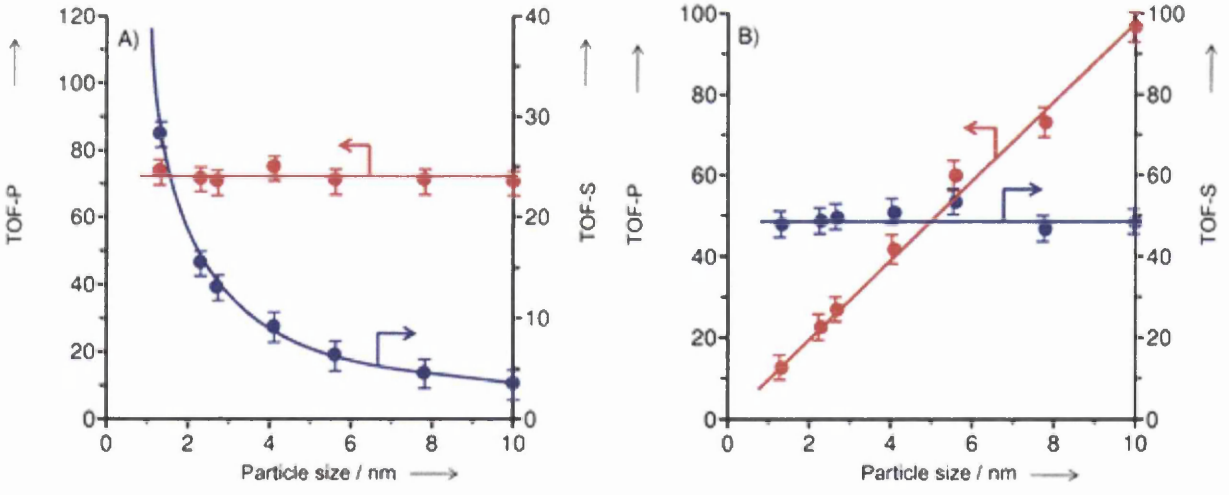

Fig. 2.10. Plots from Reference [135] **depicting the rate of CO oxidation at an Au-catalysed TiO_2 surface normalised with respect to either the number of Au nanoparticle perimeter sites (TOF-P, red curves) or the number of exposed Au atoms (TOF-S, blue curves) as a function of the nanoparticle size, at 300 K (A) and 400 K (B).**

The CO exposure of Au-catalysed TiO_2 surfaces provides a valuable insight into the nature of the oxidation mechanisms. However, the physical interpretation of these results may not be directly applicable to systems based on other metal oxides due to the different reducibility of these materials [115,121,125,129,137,139,140]. This point is illustrated by D. Widmann *et al.* [125], who used a TAP reactor to explore CO oxidation on different metal oxides in the presence of Au nanoparticles. To determine the reducibility of each material, the authors calculated the number of O_2 molecules retained by each system following many successive periods of oxygen exposure at 120°C. This measure, known as the "oxygen storage capacity" (OSC), was subsequently correlated to the reactivity of the catalysed support by measuring the TOF of CO and the number of CO molecules converted to CO_2 during CO exposure at the same temperature. As shown by Fig. 2.11, the more reducible supports, which are commonly referred to as "active" materials [115,137,140], resulted in the highest rate of CO oxidation. Moreover, it is suggested by M. Schubert *et al.* [137] that the TOF is more strongly dependent on the size of Au nanoparticles in the case of less active, or more "inert", supports due to a dearth of available oxygen ions. In turn, the authors surmise that the mechanism of CO oxidation is influenced by the reducibility of the metal oxide.

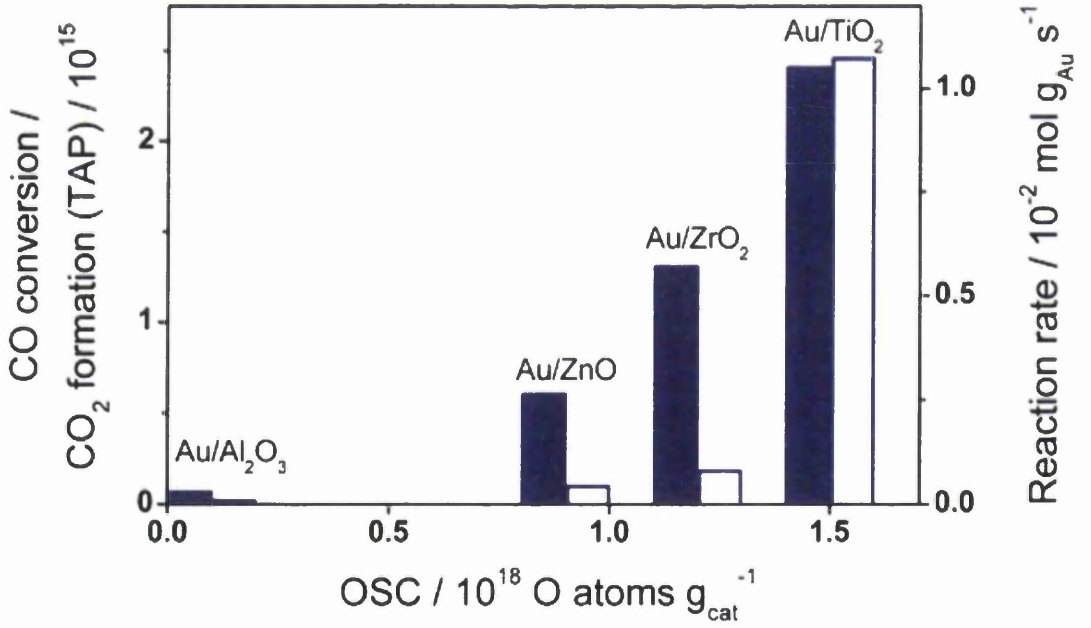

Fig. 2.11. A plot from Reference [125] **showing the number of CO molecules converted to CO_2 (filled bars) by Au-catalysed metal oxides as a function of oxygen storage capacity (OSC) at 120°C. The reaction rate (TOF) for each metal oxide is represented by an empty bar.**

The experimental studies described hitherto help to guide the mathematical modelling of catalysed metal oxide-based gas sensors. In some cases, as discussed previously, it is appropriate to assume that the reducing gas first chemisorbs to the noble metal catalyst before a spillover process leads to reaction with ionosorbed oxygen at perimeter sites. Following the approach adopted by A. Setkus [101], this assumption allows the surface concentrations of O^- ions and adsorbed reducing gas molecules, denoted $[O_S^-]$ and $[X_{ad}]$, respectively, to be described by the differential equations

$$\frac{d[O_S^-]}{dt} = k_1 \left(\frac{P_{O2}}{P_{TOT}}\right)^{1/2} ([S_0] - [O_S^-]) - k_{-1}[O_S^-] - k_{2X}[X_{ad}][O_S^-] \tag{2.10}$$

and

$$\frac{d[X_{ad}]}{dt} = k_{1X} \left(\frac{P_X}{P_{TOT}}\right) ([S_{cat}] - [X_{ad}]) - k_{-1X}[X_{ad}] - k_{2X}[X_{ad}][O_S^-] \tag{2.11}$$

where the rate constants of O^- formation and chemisorption of reducing gas molecules are represented by k_1 and k_{1X}, respectively, k_{-1} and k_{-1X} are the respective rate constants of O^- recombination and reducing gas desorption, and k_{2X} is the rate constant for the reaction of the two species. The concentration of ionosorption sites on the metal oxide surface is denoted $[S_0]$, as before, while the concentration of chemisorption sites on the noble metal surface catalyst is labelled as $[S_{cat}]$. It should be recognised that Eq. (2.10) and Eq. (2.11) are only applicable in the case of a bimolecular reaction between the two species, wherein a single molecule of reducing gas reacts with an O^- ion to form a molecule of product, XO, and release an electron to the conduction band of the semiconductor. Although the chemisorbing reducing gas molecules do not compete with ionosorbing oxygen for metal oxide surface sites, the two differential equations are coupled due to the dependence of the reaction term on the concentrations of both reactants, $[O_S^-]$ and $[X_{ad}]$. In contrast to the Eley-Rideal mechanism, therefore, the concentration of O^- ions is intimately related to the concentration of chemisorbed reducing gas molecules, and neither quantity may be determined without knowledge of the other. It is notable that alternative treatments assume that the two species compete for chemisorption sites at the catalyst surface [60–62,102,103], increasing the inter-dependence of the differential equations and further complicating analysis of the system.

Owing to these difficulties, the properties of catalysed systems, explored in Chapter 6, shall only be considered in a qualitative manner within the present work.

Within this chapter, existing phenomenological models of chemiresistive gas sensors have been reviewed and rationalised through consideration of spectroscopic and TPD studies of the surface reactions. The majority of the research presented in this thesis aims to build on the body of work presented here, applying similar theoretical treatments to model the reactions of different gases at a ZnO surface either with or without surface catalysts present. By making suitable physical approximations, it will be shown that several reaction parameters may be estimated from the electrical response of a ZnO-based sensor to carbon monoxide gas, while more rapidly oxidising gases such as hydrogen must be analysed using a more complicated model. The properties of a catalysed system are also investigated, specifically in the case of ZnO nanosheets decorated by gold nanoparticles.

References

[1] C. Geng, Y. Jiang, Y. Yao, X. Meng, J.A. Zapien, C.S. Lee, et al., Well-Aligned ZnO Nanowire Arrays Fabricated on Silicon Substrates, Adv. Funct. Mater. 14 (2004) 589–594. doi:10.1002/adfm.200305074.

[2] P.-C. Chang, Z. Fan, W.-Y. Tseng, J. Hong, W.-A. Chiou, G.J. Lu, Characterization ZnO Nanowires Synthesized by Vapor Trapping CVD Method , Microsc. Microanal. 10 (2004) 5133–5137. doi:10.1017/S1431927604886215.

[3] N.S. Ramgir, K. Subannajui, Y. Yang, R. Grimm, R. Michiels, M. Zacharias, Reactive VLS and the reversible switching between VS and VLS growth modes for ZnO nanowire growth, J. Phys. Chem. C. 114 (2010) 10323–10329. doi:10.1021/jp909377b.

[4] G.-C. Yi, C. Wang, W.I. Park, ZnO nanorods: synthesis, characterization and applications, Semicond. Sci. Technol. 20 (2005) S22–S34. doi:10.1088/0268-1242/20/4/003.

[5] L.E. Greene, B.D. Yuhas, M. Law, D. Zitoun, P. Yang, Solution-grown zinc oxide nanowires., Inorg. Chem. 45 (2006) 4977–4984. doi:10.1021/ic0601900.

[6] L.E. Greene, M. Law, J. Goldberger, F. Kim, J.C. Johnson, Y. Zhang, et al., Low-temperature wafer-scale production of ZnO nanowire arrays, Angew. Chemie - Int. Ed. 42 (2003) 3031–3034. doi:10.1002/anie.200351461.

[7] L. Vayssieres, Growth of Arrayed Nanorods and Nanowires of ZnO from Aqueous Solutions, Adv. Mater. 15 (2003) 464–466. doi:10.1002/adma.200390108.

[8] H. Hu, X. Huang, C. Deng, X. Chen, Y. Qian, Hydrothermal synthesis of ZnO nanowires and nanobelts on a large scale, Mater. Chem. Phys. 106 (2007) 58–62. doi:10.1016/j.matchemphys.2007.05.016.

[9] X. Wang, Y. Ding, C.J. Summers, Z.L. Wang, Large-scale synthesis of six-nanometer-wide ZnO nanobelts, J. Phys. Chem. B. 108 (2004) 8773–8777. doi:10.1021/jp048482e.

[10] X.Y. Kong, Z.L. Wang, Polar-surface dominated ZnO nanobelts and the electrostatic energy induced nanohelixes, nanosprings, and nanospirals, Appl. Phys. Lett. 84 (2004) 975–977. doi:10.1063/1.1646453.

[11] W. Wang, B. Zeng, J. Yang, B. Poudel, J. Huang, M.J. Naughton, et al., Aligned ultralong ZnO nanobelts and their enhanced field emission, Adv. Mater. 18 (2006) 3275–3278. doi:10.1002/adma.200601274.

[12] X.Y. Zhang, J.Y. Dai, H.C. Ong, N. Wang, H.L.W. Chan, C.L. Choy, Hydrothermal synthesis of oriented ZnO nanobelts and their temperature dependent photoluminescence, Chem. Phys. Lett. 393 (2004) 17–21. doi:10.1016/j.cplett.2004.06.012.

[13] A. Tarat, R. Majithia, R.A. Brown, M.W. Penny, K.E. Meissner, Synthesis of nanocrystalline ZnO nanobelts via pyrolytic decomposition of zinc acetate nanobelts and their gas sensing behavior, Surf. Sci. 606 (2012) 715–721. doi:10.1016/j.susc.2011.12.010.

[14] O. Lupan, G. Chai, L. Chow, Novel hydrogen gas sensor based on single ZnO nanorod, Microelectron. Eng. 85 (2008) 2220–2225. doi:10.1016/j.mee.2008.06.021.

[15] O. Lupan, V. V. Ursaki, G. Chai, L. Chow, G.A. Emelchenko, I.M. Tiginyanu, et al., Selective hydrogen gas nanosensor using individual ZnO nanowire with fast response at room temperature, Sensors Actuators, B Chem. 144 (2010) 56–66. doi:10.1016/j.snb.2009.10.038.

[16] O. Lupan, L. Chow, T. Pauporté, L.K. Ono, B. Roldan Cuenya, G. Chai, Highly sensitive and selective hydrogen single-nanowire nanosensor, Sensors Actuators, B Chem. 173 (2012) 772–780. doi:10.1016/j.snb.2012.07.111.

[17] G.Y. Chai, O. Lupan, E.V. Rusu, G.I. Stratan, V.V. Ursaki, V. Şontea, et al., Functionalized individual ZnO microwire for natural gas detection, Sensors Actuators A Phys. 176 (2012) 64–71. doi:10.1016/j.sna.2012.01.012.

[18] Y.W. Heo, L.C. Tien, D.P. Norton, B.S. Kang, F. Ren, B.P. Gila, et al., Electrical transport properties of single ZnO nanorods, Appl. Phys. Lett. 85 (2004) 2002–2004. doi:10.1063/1.1792373.

[19] S.N. Das, J.P. Kar, J.-H. Choi, T.I. Lee, K.-J. Moon, J.-M. Myoung, Fabrication and Characterization of ZnO Single Nanowire-Based Hydrogen Sensor, J. Phys. Chem. C. 114 (2010) 1689–1693. doi:10.1021/jp910515b.

[20] Z. Fan, J.G. Lu, Gate-refreshable nanowire chemical sensors, Appl. Phys. Lett. 86 (2005) 1–3. doi:10.1063/1.1883715.

[21] Z. Fan, D. Wang, P.-C. Chang, W.-Y. Tseng, J.G. Lu, ZnO nanowire field-effect transistor and oxygen sensing property, Appl. Phys. Lett. 85 (2004) 5923–5925.

[22] J. Goldberger, D.J. Sirbuly, M. Law, P. Yang, ZnO nanowire transistors, J. Phys. Chem. B. 109 (2005) 9–14. doi:10.1021/jp0452599.

[23] P. Chang, Z. Fan, C. Chien, High-performance ZnO nanowire field effect transistors, Appl. Phys. Lett. 89 (2006) 133113. doi:10.1063/1.2357013.

[24] S. Mubeen, M. Moskovits, Gate-tunable surface processes on a single-nanowire field-effect transistor., Adv. Mater. 23 (2011) 2306–12. doi:10.1002/adma.201004203.

[25] L. Liao, H.B. Lu, J.C. Li, H. He, D.F. Wang, D.J. Fu, et al., Size dependence of gas sensitivity of ZnO nanorods, J. Phys. Chem. C. 111 (2007) 1900–1903. doi:10.1021/jp065963k.

[26] P.M. Parthangal, R.E. Cavicchi, M.R. Zachariah, A universal approach to electrically connecting nanowire arrays using nanoparticles—application to a novel gas sensor architecture, Nanotechnology. 17 (2006) 3786–3790. doi:10.1088/0957-4484/17/15/029.

[27] J. Yi, J.M. Lee, W.I. Park, Vertically aligned ZnO nanorods and graphene hybrid architectures for high-sensitive flexible gas sensors, Sensors Actuators, B Chem. 155 (2011) 264–269. doi:10.1016/j.snb.2010.12.033.

[28] J.Y. Park, S.-W. Choi, S.S. Kim, Fabrication of a Highly Sensitive Chemical Sensor Based on ZnO Nanorod Arrays, 5 (2009) 353–359. doi:10.1007/s11671-009-9487-3.

[29] A. Kolmakov, M. Moskovits, Chemical Sensing and Catalysis By One-Dimensional Metal-Oxide Nanostructures, Annu. Rev. Mater. Res. 34 (2004) 151–180. doi:10.1146/annurev.matsci.34.040203.112141.

[30] M.W. Ahn, K.S. Park, J.H. Heo, D.W. Kim, K.J. Choi, J.G. Park, On-chip fabrication of ZnO-nanowire gas sensor with high gas sensitivity, Sensors Actuators, B Chem. 138 (2009) 168–173. doi:10.1016/j.snb.2009.02.008.

[31] T.J. Hsueh, C.L. Hsu, S.J. Chang, I.C. Chen, Laterally grown ZnO nanowire ethanol gas sensors, Sensors Actuators, B Chem. 126 (2007) 473–477. doi:10.1016/j.snb.2007.03.034.

[32] Q. Ahsanulhaq, J.H. Kim, J.S. Lee, Y.B. Hahn, Electrical and gas sensing properties of ZnO nanorod arrays directly grown on a four-probe electrode system, Electrochem. Commun. 12 (2010) 475–478. doi:10.1016/j.elecom.2010.01.023.

[33] C.M. Chang, M.H. Hon, I.C. Leu, Preparation of ZnO nanorod arrays with tailored defect-related characterisitcs and their effect on the ethanol gas sensing performance, Sensors Actuators, B Chem. 151 (2010) 15–20. doi:10.1016/j.snb.2010.09.072.

[34] B. Shouli, C. Liangyuan, L. Dianqing, Y. Wensheng, Y. Pengcheng, L. Zhiyong, et al., Different morphologies of ZnO nanorods and their sensing property, Sensors Actuators, B Chem. 146 (2010) 129–137. doi:10.1016/j.snb.2010.02.011.

[35] X. Jiaqiang, C. Yuping, C. Daoyong, S. Jianian, Hydrothermal synthesis and gas sensing characters of ZnO nanorods, Sensors Actuators, B Chem. 113 (2006) 526–531. doi:10.1016/j.snb.2005.03.097.

[36] W.J. Park, K.J. Choi, M.H. Kim, B.H. Koo, J.L. Lee, J.M. Baik, Self-assembled and highly selective sensors based on air-bridge-structured nanowire junction arrays, ACS Appl. Mater. Interfaces. 5 (2013) 6802–6807. doi:10.1021/am401635e.

[37] C.S. Rout, S. Hari Krishna, S.R.C. Vivekchand, A. Govindaraj, C.N.R. Rao, Hydrogen and ethanol sensors based on ZnO nanorods, nanowires and nanotubes, Chem. Phys. Lett. 418 (2006) 586–590. doi:10.1016/j.cplett.2005.11.040.

[38] C. Liangyuan, L. Zhiyong, B. Shouli, Z. Kewei, L. Dianqing, C. Aifan, et al., Synthesis of 1-dimensional ZnO and its sensing property for CO, Sensors Actuators, B Chem. 143 (2010) 620–628. doi:10.1016/j.snb.2009.10.009.

[39] X. Chu, T. Chen, W. Zhang, B. Zheng, H. Shui, Investigation on formaldehyde gas sensor with ZnO thick film prepared through microwave heating method, Sensors Actuators, B Chem. 142 (2009) 49–54. doi:10.1016/j.snb.2009.07.049.

[40] P. Rai, H.-M. Song, Y.-S. Kim, M.-K. Song, P.-R. Oh, J.-M. Yoon, et al., Microwave assisted hydrothermal synthesis of single crystalline ZnO nanorods for gas sensor application, Mater. Lett. 68 (2012) 90–93. doi:10.1016/j.matlet.2011.10.029.

[41] A. Qurashi, N. Tabet, M. Faiz, T. Yamzaki, Ultra-fast microwave synthesis of ZnO nanowires and their dynamic response toward hydrogen gas, Nanoscale Res. Lett. 4 (2009) 948–954. doi:10.1007/s11671-009-9317-7.

[42] Z. Jing, J. Zhan, Fabrication and gas-sensing properties of porous ZnO nanoplates, Adv. Mater. 20 (2008) 4547–4551. doi:10.1002/adma.200800243.

[43] T. Krishnakumar, R. Jayaprakash, N. Pinna, N. Donato, A. Bonavita, G. Micali, et al., CO gas sensing of ZnO nanostructures synthesized by an assisted microwave wet chemical route, Sensors Actuators, B Chem. 143 (2009) 198–204. doi:10.1016/j.snb.2009.09.039.

[44] J.J. Hassan, M.A. Mahdi, C.W. Chin, H. Abu-Hassan, Z. Hassan, Room temperature hydrogen gas sensor based on ZnO nanorod arrays grown on a SiO2/Si substrate via a microwave-assisted chemical solution method, J. Alloys Compd. 546 (2013) 107–111. doi:10.1016/j.jallcom.2012.08.040.

[45] N.F. Hamedani, A.R. Mahjoub, A.A. Khodadadi, Y. Mortazavi, Microwave assisted fast synthesis of various ZnO morphologies for selective detection of CO, CH4 and ethanol, Sensors Actuators, B Chem. 156 (2011) 737–742. doi:10.1016/j.snb.2011.02.028.

[46] M. Chen, Z. Wang, D. Han, F. Gu, G. Guo, Porous ZnO polygonal nanoflakes: Synthesis, use in high-sensitivity NO2 gas sensor, and proposed mechanism of gas sensing, J. Phys. Chem. C. 115 (2011) 12763–12773. doi:10.1021/jp201816d.

[47] J.J. Hassan, M.A. Mahdi, C.W. Chin, H. Abu-Hassan, Z. Hassan, A high-sensitivity room-temperature hydrogen gas sensor based on oblique and vertical ZnO nanorod arrays, Sensors Actuators B Chem. 176 (2013) 360–367. doi:10.1016/j.snb.2012.09.081.

[48] A. Tarat, C.J. Nettle, D.T.J. Bryant, D.R. Jones, M.W. Penny, R.A. Brown, et al., Microwave-assisted synthesis of layered basic zinc acetate nanosheets and their thermal decomposition into nanocrystalline ZnO., Nanoscale Res. Lett. 9 (2014) 11. doi:10.1186/1556-276X-9-11.

[49] J. Huang, Y. Wu, C. Gu, M. Zhai, Y. Sun, J. Liu, Fabrication and gas-sensing properties of hierarchically porous ZnO architectures, Sensors Actuators B Chem. 155 (2011) 126–133. doi:10.1016/j.snb.2010.11.036.

[50] L. Poul, N. Jouini, F. Fievet, Layered hydroxide metal acetates (metal = zinc, cobalt, and nickel): Elaboration via hydrolysis in polyol medium and comparative study, Chem. Mater. 12 (2000) 3123–3132. doi:10.1021/cm991179j.

[51] T. Biswick, W. Jones, A. Pacuła, E. Serwicka, J. Podobinski, The role of anhydrous zinc nitrate in the thermal decomposition of the zinc hydroxy nitrates Zn5(OH)8(NO3)2·2H2O and ZnOHNO3·H2O, J. Solid State Chem. 180 (2007) 1171–1179. doi:10.1016/j.jssc.2007.01.012.

[52] T. Biswick, W. Jones, A. Pacuła, E. Serwicka, J. Podobinski, Evidence for the formation of anhydrous zinc acetate and acetic anhydride during the thermal degradation of zinc hydroxy acetate, Zn5(OH)8(CH3CO2)2·4H2O to ZnO, Solid State Sci. 11 (2009) 330–335. doi:10.1016/j.solidstatesciences.2008.06.018.

[53] D. Luković Golić, G. Branković, M. Počuča Nešić, K. Vojisavljević, A. Rečnik, N. Daneu, et al., Structural characterization of self-assembled ZnO nanoparticles obtained by the sol-gel method from Zn(CH(3)COO)(2)·2H(2)O., Nanotechnology. 22 (2011) 395603. doi:10.1088/0957-4484/22/39/395603.

[54] E. Kandare, J.M. Hossenlopp, Thermal degradation of acetate-intercalated hydroxy double and layered hydroxy salts, Inorg. Chem. 45 (2006) 3766–3773. doi:10.1021/ic060071k.

[55] S. Baruah, J. Dutta, Hydrothermal growth of ZnO nanostructures, Sci. Technol. Adv. Mater. 10 (2009) 013001. doi:10.1088/1468-6996/10/1/013001.

[56] D. Sun, M. Wong, L. Sun, Y. Li, N. Miyatake, H.J. Sue, Purification and stabilization of colloidal ZnO nanoparticles in methanol, J. Sol-Gel Sci. Technol. 43 (2007) 237–243. doi:10.1007/s10971-007-1569-z.

[57] Z.H. Liang, Y.J. Zhu, G.F. Cheng, Y.H. Huang, Synthesis of ZnO nanosheets by room-temperature decomposition of a layered precursor synthesized by microwave heating, J. Mater. Sci. 42 (2007) 477–482. doi:10.1007/s10853-006-1069-5.

[58] Q. Cui, K. Yu, N. Zhang, Z. Zhu, Porous ZnO nanobelts evolved from layered basic zinc acetate nanobelts, Appl. Surf. Sci. 254 (2008) 3517–3521. doi:10.1016/j.apsusc.2007.11.044.

[59] E. Hosono, S. Fujihara, T. Kimura, H. Imai, Growth of layered basic zinc acetate in methanolic solutions and its pyrolytic transformation into porous zinc oxide films, J. Colloid Interface Sci. 272 (2004) 391–398. doi:10.1016/j.jcis.2003.10.005.

[60] S. Nakata, S. Akakabe, M. Nakasuji, K. Yoshikawa, Gas Sensing Based on a Nonlinear Response: Discrimination between Hydrocarbons and Quantification of Individual Components in a Gas Mixture., Anal. Chem. 68 (1996) 2067–72. doi:10.1021/ac9510954.

[61] H. Busse, M. Voss, D. Jerdev, B. Koel, M. Paffett, Adsorption and reaction of gaseous H (D) atoms with D (H) adatoms on Pt (111) and Sn/Pt (111) surface alloys, Surf. Sci. 490 (2001) 133–143. doi:10.1016/S0039-6028(01)01323-1.

[62] I. Kocemba, J. Rynkowski, The influence of catalytic activity on the response of Pt/SnO2 gas sensors to carbon monoxide and hydrogen, Sensors Actuators, B Chem. 155 (2011) 659–666. doi:10.1016/j.snb.2011.01.026.

[63] A. Varpula, S. Novikov, A. Haarahiltunen, P. Kuivalainen, Transient characterization techniques for resistive metal-oxide gas sensors, Sensors Actuators B Chem. 159 (2011) 12–26. doi:10.1016/j.snb.2011.05.059.

[64] A. Fort, M. Mugnaini, S. Rocchi, M.B. Serrano-Santos, V. Vignoli, R. Spinicci, Simplified models for SnO2 sensors during chemical and thermal transients in mixtures of inert, oxidizing and reducing gases, Sensors Actuators B Chem. 124 (2007) 245–259. doi:10.1016/j.snb.2006.12.030.

[65] K. Darcovich, F.F. Garcia, C.A. Jeffrey, J.J. Tunney, M.L. Post, Coupled microstructural and transport effects in n-type sensor response modeling for thin layers, Sensors Actuators A Phys. 147 (2008) 378–386. doi:10.1016/j.sna.2008.06.007.

[66] R. Ionescu, E. Llobet, S. Al-Khalifa, J.W. Gardner, X. Vilanova, J. Brezmes, et al., Response model for thermally modulated tin oxide-based microhotplate gas sensors, Sensors Actuators B Chem. 95 (2003) 203–211. doi:10.1016/S0925-4005(03)00420-9.

[67] S. Nakata, K. Takemura, K. Neya, Non-linear dynamic responses of a semiconductor gas sensor: Evaluation of kinetic parameters and competition effect on the sensor response, Sensors Actuators B Chem. 76 (2001) 436–441. doi:10.1016/S0925-4005(01)00652-9.

[68] D. Koziej, K. Thomas, N. Barsan, F. Thibault-Starzyk, U. Weimar, Influence of annealing temperature on the CO sensing mechanism for tin dioxide based sensors-Operando studies, Catal. Today. 126 (2007) 211–218. doi:10.1016/j.cattod.2007.03.011.

[69] S. Lenaerts, J. Roggen, G. Maes, FT-IR characterization of tin dioxide gas sensor materials under working conditions, Spectrochim. Acta Part A Mol. Biomol. Spectrosc. 51 (1995) 883–894. doi:10.1016/0584-8539(94)01216-4.

[70] A.A. Davydov, IR spectroscopic study of oxygen states and its reactivity on the surface of tin dioxide, J. Appl. Spectrosc. 56 (1992) 365–371. doi:10.1007/BF00665032.

[71] H. Liu, H. Liu, A.I. Kozlov, A.P. Kozlova, T. Shido, K. Asakura, et al., Active Oxygen Species and Mechanism for Low-Temperature CO Oxidation Reaction on a TiO2-Supported Au Catalyst Prepared from Au(PPh3)(NO3) and As-Precipitated Titanium Hydroxide, J. Catal. 185 (1999) 252–264. doi:10.1006/jcat.1999.2517.

[72] M. Okumura, J.M. Coronado, J. Soria, M. Haruta, J.C. Conesa, EPR Study of CO and O2 Interaction with Supported Au Catalysts, J. Catal. 203 (2001) 168–174. doi:http://dx.doi.org/10.1006/jcat.2001.3307.

[73] C. Naccache, P. Meriaudeau, M. Che, A.J. Tench, Identification of oxygen species adsorbed on reduced titanium dioxide, Trans. Faraday Soc. 67 (1971) 506. doi:10.1039/tf9716700506.

[74] P.C. Gravelle, F. Juillet, P. Meriaudeau, S.J. Teichner, Surface reactivity of reduced titanium dioxide, Discuss. Faraday Soc. 52 (1971) 140. doi:10.1039/df9715200140.

[75] N. Yamazoe, J. Fuchigami, M. Kishikawa, T. Seiyama, Interactions of tin oxide surface with O2, H2O AND H2, Surf. Sci. 86 (1979) 335–344. doi:10.1016/0039-6028(79)90411-4.

[76] K. Tanaka, G. Blyholder, Adsorbed oxygen species on zinc oxide in the dark and under illumination, J. Phys. Chem. 76 (1972) 3184–3187. http://pubs.acs.org/doi/abs/10.1021/j100666a014.

[77] Z. Hao, L. Fen, G.. Lu, J. Liu, L. An, H. Wang, In situ electron paramagnetic resonance (EPR) study of surface oxygen species on Au/ZnO catalyst for low-temperature carbon monoxide oxidation, Appl. Catal. A Gen. 213 (2001) 173–177. doi:10.1016/S0926-860X(00)00898-X.

[78] M. Iwamoto, Y. Yoda, N. Yamazoe, T. Seiyama, Study of metal oxide catalysts by temperature programmed desorption. 4. Oxygen adsorption on various metal oxides, J. Phys. Chem. 82 (1978) 2564–2570. doi:10.1021/j100513a006.

[79] J.P. Ahn, S.H. Kim, J.K. Park, M.Y. Huh, Effect of orthorhombic phase on hydrogen gas sensing property of thick-film sensors fabricated by nanophase tin dioxide, Sensors Actuators, B Chem. 94 (2003) 125–131. doi:10.1016/S0925-4005(03)00264-8.

[80] K. Tabata, T. Kawabe, Y. Yamaguchi, Y. Nagasawa, Chemisorbed oxygen species over the (110) face of SnO2, Catal. Surv. from Asia. 7 (2003) 251–259. doi:10.1023/B:CATS.0000008164.21582.92.

[81] M.A. Henderson, W.S. Epling, C.L. Perkins, C.H.F. Peden, U. Diebold, Interaction of Molecular Oxygen with the Vacuum-Annealed TiO 2 (110) Surface: Molecular and Dissociative Channels, J. Phys. Chem. B. 103 (1999) 5328–5337. doi:10.1021/jp990655q.

[82] J.M. Kanervo, T.J. Keskitalo, R.I. Slioor, A.O.I. Krause, Temperature-programmed desorption as a tool to extract quantitative kinetic or energetic information for porous catalysts, J. Catal. 238 (2006) 382–393. doi:10.1016/j.jcat.2005.12.026.

[83] F. Gaillard, M. Abdat, J.P. Joly, A. Perrard, An intermittent temperature-programmed desorption method for studying kinetics of desorption from heterogeneous surfaces, Appl. Surf. Sci. 238 (2004) 91–96. doi:10.1016/j.apsusc.2004.05.187.

[84] S. Saukko, U. Lassi, V. Lantto, M. Kroneld, S. Novikov, P. Kuivalainen, et al., Experimental studies of O2-SnO2 surface interaction using powder, thick films and monocrystalline thin films, Thin Solid Films. 490 (2005) 48–53. doi:10.1016/j.tsf.2005.04.012.

[85] A. Gurlo, Interplay between O2 and SnO2: Oxygen ionosorption and spectroscopic evidence for adsorbed oxygen, ChemPhysChem. 7 (2006) 2041–2052. doi:10.1002/cphc.200600292.

[86] U. Pulkkinen, T.T. Rantala, T.S. Rantala, V. Lantto, Simulation of oxygen exchange of {SnO_2} surface, Comput. Phys. Commun. 121--122 (1999) 720. doi:http://dx.doi.org/10.1016/S0010-4655(06)70123-0.

[87] M. Haruta, T. Kobayashi, H. Sano, N. Yamada, Novel gold catalysts for the oxidation of carbon monoxide at a temperature far below 0.DEG.C., Chem. Lett. (1987) 405–408. doi:10.1246/cl.1987.405.

[88] P. Rai, Y.S. Kim, H.M. Song, M.K. Song, Y.T. Yu, The role of gold catalyst on the sensing behavior of ZnO nanorods for CO and NO 2 gases, Sensors Actuators, B Chem. 165 (2012) 133–142. doi:10.1016/j.snb.2012.02.030.

[89] B. Bahrami, A. Khodadadi, M. Kazemeini, Y. Mortazavi, Enhanced CO sensitivity and selectivity of gold nanoparticles-doped SnO2 sensor in presence of propane and methane, Sensors Actuators, B Chem. 133 (2008) 352–356. doi:10.1016/j.snb.2008.02.034.

[90] S.-J. Chang, T.-J. Hsueh, I.-C. Chen, B.-R. Huang, Highly sensitive ZnO nanowire CO sensors with the adsorption of Au nanoparticles., Nanotechnology. 19 (2008) 175502. doi:10.1088/0957-4484/19/17/175502.

[91] R.K. Joshi, Q. Hu, F. Alvi, N. Joshi, A. Kumar, Au Decorated Zinc Oxide Nanowires for CO Sensing, J. Phys. Chem. C. 113 (2009) 16199–16202. doi:10.1021/jp906458b.

[92] N.S. Ramgir, Y.K. Hwang, S.H. Jhung, I.S. Mulla, J.S. Chang, Effect of Pt concentration on the physicochemical properties and CO sensing activity of mesostructured SnO 2, Sensors Actuators, B Chem. 114 (2006) 275–282. doi:10.1016/j.snb.2005.05.016.

[93] L. Mädler, T. Sahm, A. Gurlo, J.D. Grunwaldt, N. Barsan, U. Weimar, et al., Sensing low concentrations of CO using flame-spray-made Pt/SnO2 nanoparticles, J. Nanoparticle Res. 8 (2006) 783–796. doi:10.1007/s11051-005-9029-6.

[94] Y. Zhang, J. Xu, P. Xu, Y. Zhu, X. Chen, W. Yu, Decoration of ZnO nanowires with Pt nanoparticles and their improved gas sensing and photocatalytic performance., Nanotechnology. 21 (2010) 285501. doi:10.1088/0957-4484/21/28/285501.

[95] H. Huang, C.Y. Ong, J. Guo, T. White, M.S. Tse, O.K. Tan, Pt surface modification of SnO2 nanorod arrays for CO and H2 sensors, Nanoscale. 2 (2010) 1203–1207. doi:10.1039/c005273f.

[96] L.C. Tien, P.W. Sadik, D.P. Norton, L.F. Voss, S.J. Pearton, H.T. Wang, et al., Hydrogen sensing at room temperature with Pt-coated ZnO thin films and nanorods, Appl. Phys. Lett. 87 (2005) 1–3. doi:10.1063/1.2136070.

[97] C.-M. Chang, M.-H. Hon, I.-C. Leu, Improvement in CO sensing characteristics by decorating ZnO nanorod arrays with Pd nanoparticles and the related mechanisms, RSC Adv. 2 (2012) 2469. doi:10.1039/c2ra01016j.

[98] C.M. Chang, M.H. Hon, I.C. Leu, Outstanding H2 sensing performance of Pd nanoparticle-decorated ZnO nanorod arrays and the temperature-dependent sensing mechanisms, ACS Appl. Mater. Interfaces. 5 (2013) 135–143. doi:10.1021/am302294v.

[99] B.B. Rao, Zinc oxide ceramic semi-conductor gas sensor for ethanol vapour, Mater. Chem. Phys. 64 (2000) 62–65. doi:10.1016/S0254-0584(99)00267-9.

[100] V.R. Shinde, T.P. Gujar, C.D. Lokhande, Enhanced response of porous ZnO nanobeads towards LPG: Effect of Pd sensitization, Sensors Actuators, B Chem. 123 (2007) 701–706. doi:10.1016/j.snb.2006.10.003.

[101] A. Setkus, Heterogeneous reaction rate based description of the response kinetics in metal oxide gas sensors, 87 (2002) 346–357.

[102] K. Grass, The Kinetics of Carbon Monoxide Oxidation on Tin(IV) Oxide Supported Platinum Catalysts, J. Catal. 172 (1997) 446–452. doi:10.1006/jcat.1997.1886.

[103] V.P. Zhdanov, Impact of surface science on the understanding of kinetics of heterogeneous catalytic reactions, Surf. Sci. 500 (2002) 966–985.

[104] S. Bai, T. Guo, D. Li, R. Luo, A. Chen, C.C. Liu, Intrinsic sensing properties of the flower-like ZnO nanostructures, Sensors Actuators, B Chem. 182 (2013) 747–754. doi:10.1016/j.snb.2013.03.077 Flower-like ZnO nanostructures.

[105] U. Roland, T. Braunschweig, F. Roessner, On the nature of spilt-over hydrogen, J. Mol. Catal. A Chem. 127 (1997) 61–84. doi:10.1086/447782.

[106] G.M. Pajonk, Contribution of spillover effects to heterogeneous catalysis, Appl. Catal. A Gen. 202 (2000) 157–169. doi:10.1016/S0926-860X(00)00522-6.

[107] D.A. Panayotov, J.T. Yates, Spectroscopic detection of hydrogen atom spillover from Au nanoparticles supported on TiO2: Use of conduction band electrons, J. Phys. Chem. C. 111 (2007) 2959–2964. doi:10.1021/jp066686k.

[108] D.A. Panayotov, S.P. Burrows, J.T. Yates, J.R. Morris, Mechanistic studies of hydrogen dissociation and spillover on Au/TiO 2: IR spectroscopy of coadsorbed CO and H-donated electrons, J. Phys. Chem. C. 115 (2011) 22400–22408. doi:10.1021/jp2065024.

[109] S. Shukla, S. Seal, L. Ludwig, C. Parish, Nanocrystalline indium oxide-doped tin oxide thin film as low temperature hydrogen sensor, Sensors Actuators, B Chem. 97 (2004) 256–265. doi:10.1016/j.snb.2003.08.025.

[110] N.A. Joy, C.M. Settens, R.J. Matyi, M.A. Carpenter, Plasmonic based kinetic analysis of hydrogen reactions within Au-YSZ nanocomposites, J. Phys. Chem. C. 115 (2011) 6283–6289. doi:10.1021/jp112228h.

[111] E. V. Benvenutti, L. Franken, C.C. Moro, FTIR Study of Hydrogen and Carbon Monoxide Adsorption on Pt/TiO2, Pt/ZrO2, and Pt/Al2O3, Langmuir. 15 (1999) 8140–8146. doi:10.1021/la990195s.

[112] J.M. Lee, J.E. Park, S. Kim, S. Kim, E. Lee, S.J. Kim, et al., Ultra-sensitive hydrogen gas sensors based on Pd-decorated tin dioxide nanostructures: Room temperature operating sensors, Int. J. Hydrogen Energy. 35 (2010) 12568–12573. doi:10.1016/j.ijhydene.2010.08.026.

[113] P. Wang, S.W. Yang, J.N. Kondo, K. Domen, T. Yamada, H. Hattori, Spectroscopic study of H-2 and CO adsorption on platinum-promoted sulfated zirconia catalysts, J. Phys. Chem. B. 107 (2003) 11951–11959. doi:Doi 10.1021/Jp030607c.

[114] R. Prins, Hydrogen spillover. Facts and fiction, Chem. Rev. 112 (2012) 2714–2738. doi:10.1021/cr200346z.

[115] S.T. Daniells, A.R. Overweg, M. Makkee, J.A. Moulijn, The mechanism of low-temperature CO oxidation with Au/Fe2O3 catalysts: A combined Mossbauer, FT-IR, and TAP reactor study, J. Catal. 230 (2005) 52–65. doi:10.1016/j.jcat.2004.11.020.

[116] E. Bus, J.T. Miller, J.A. van Bokhoven, Hydrogen Chemisorption on Al2O3-Supported Gold Catalysts, J. Phys. Chem. B. 109 (2005) 14581–14587. doi:10.1021/jp011140d.

[117] S.D. Lin, M.A. Vannice, Hydrogenation of Aromatic Hydrocarbons over supported Pt Catalysts. III. Reaction Models for Metal Surfaces and Acidic Sites on oxide Supports, J. Catal. 143 (1993) 563–572. doi:10.1006/jcat.1993.1299.

[118] S.C. Tsang, C.D.A. Bulpitt, P.C.H. Mitchell, A.J. Ramirez-Cuesta, Some new insights into the sensing mechanism of palladium promoted tin (IV) oxide sensor, J. Phys. Chem. B. 105 (2001) 5737–5742. doi:10.1021/jp010175a.

[119] W.C. Conner, J.L. Falconer, Spillover in Heterogeneous Catalysis, Chem. Rev. 95 (1995) 759–788. doi:10.1021/cr00035a014.

[120] A. Chiorino, M. Manzoli, F. Menegazzo, M. Signoretto, F. Vindigni, F. Pinna, et al., New insight on the nature of catalytically active gold sites: Quantitative CO chemisorption data and analysis of FTIR spectra of adsorbed CO and of isotopic mixtures, J. Catal. 262 (2009) 169–176. doi:10.1016/j.jcat.2008.12.017.

[121] F. Boccuzzi, A. Chiorino, FTIR study of carbon monoxide oxidation and scrambling at room temperature over copper supported on ZnO and TiO2. 1, J. Phys. Chem. 100 (1996) 3617–3624. http://www.scopus.com/scopus/inward/record.url?eid=2-s2.0-33748481347&partnerID=40.

[122] F. Boccuzzi, A. Chiorino, M. Manzoli, P. Lu, T. Akita, S. Ichikawa, et al., Au/TiO2 nanosized samples: A catalytic, TEM, and FTIR study of the effect of calcination temperature on the CO oxidation, J. Catal. 202 (2001) 256–267. doi:10.1006/jcat.2001.3290.

[123] F. Boccuzzi, A. Chiorino, S. Tsubota, M. Haruta, An IR study of CO-sensing mechanism on Au/ZnO, Sensors Actuators B Chem. 25 (1995) 540–543. doi:10.1016/0925-4005(95)85117-8.

[124] N.M. Gupta, A.K. Tripathi, The role of nanosized gold particles in adsorption and oxidation of carbon monoxide over Au/Fe2O3 Catalyst, Gold Bull. 34 (2001) 120–128. doi:10.1007/BF03214824.

[125] D. Widmann, R.J. Behm, Activation of molecular oxygen and the nature of the active oxygen species for co oxidation on oxide supported au catalysts, Acc. Chem. Res. 47 (2014) 740–749. doi:10.1021/ar400203e.

[126] M. Olea, M. Kunitake, T. Shido, Y. Iwasawa, TAP study on CO oxidation on a highly active Au/Ti(OH)4* catalyst, Phys. Chem. Chem. Phys. 3 (2001) 627–631.

[127] L.C. Wang, H.J. Jin, D. Widmann, J. Weissmüller, R.J. Behm, Dynamic studies of CO oxidation on nanoporous Au using a TAP reactor, J. Catal. 278 (2011) 219–227. doi:10.1016/j.jcat.2010.12.007.

[128] M. Kotobuki, R. Leppelt, D.A. Hansgen, D. Widmann, R.J. Behm, Reactive oxygen on a Au/TiO2 supported catalyst, J. Catal. 264 (2009) 67–76. doi:10.1016/j.jcat.2009.03.013.

[129] D. Widmann, Y. Liu, F. Schüth, R.J. Behm, Support effects in the Au-catalyzed CO oxidation - Correlation between activity, oxygen storage capacity, and support reducibility, J. Catal. 276 (2010) 292–305. doi:10.1016/j.jcat.2010.09.023.

[130] S.N. Reifsnyder, M.M. Otten, D.E. Sayers, H.H. Lamb, Hydrogen Chemisorption on Silica-Supported Pt Clusters: In Situ X-ray Absorption Spectroscopy, J. Phys. Chem. B. 101 (1997) 4972–4977. doi:10.1021/jp970244e.

[131] H. Pan, J. Luo, H. Sun, Y. Feng, C. Poh, J. Lin, Hydrogen storage of ZnO and Mg doped ZnO nanowires, Nanotechnology. 17 (2006) 2963–2967. doi:10.1088/0957-4484/17/12/023.

[132] S.H. Lim, J. Luo, Z. Zhong, W. Ji, J. Lin, Room-Temperature Hydrogen Uptake by TiO 2 Nanotubes, 44 (2005) 4124–4126.

[133] W.H. Doh, P.C. Roy, C.M. Kim, Interaction of hydrogen with ZnO: Surface adsorption versus bulk diffusion, Langmuir. 26 (2010) 16278–16281. doi:10.1021/la101369r.

[134] D. Buso, M. Post, C. Cantalini, P. Mulvaney, A. Martucci, Gold nanoparticle-doped TiO2 semiconductor thin films: Gas sensing properties, Adv. Funct. Mater. 18 (2008) 3843–3849. doi:10.1002/adfm.200800864.

[135] T. Fujitani, I. Nakamura, Mechanism and active sites of the oxidation of CO over Au/TiO2, Angew. Chemie - Int. Ed. 50 (2011) 10144–10147. doi:10.1002/anie.201104694.

[136] M. Haruta, When gold is not noble: Catalysis by nanoparticles, Chem. Rec. 3 (2003) 75–87. doi:10.1002/tcr.10053.

[137] M. Schubert, CO Oxidation over Supported Gold Catalysts—"Inert" and "Active" Support Materials and Their Role for the Oxygen Supply during Reaction, J. Catal. 197 (2001) 113–122. doi:10.1006/jcat.2000.3069.

[138] Y. Maeda, Y. Iizuka, M. Kohyama, Generation of oxygen vacancies at a Au/TiO2 perimeter interface during co oxidation detected by in situ electrical conductance measurement, J. Am. Chem. Soc. 135 (2013) 906–909. doi:10.1021/ja310999c.

[139] M. Comotti, W.-C. Li, B. Spliethoff, F. Schüth, Support effect in high activity gold catalysts for CO oxidation., J. Am. Chem. Soc. 128 (2006) 917–924. doi:10.1021/ja0561441.

[140] L. Li, A. Wang, B. Qiao, J. Lin, Y. Huang, X. Wang, et al., Origin of the high activity of Au/FeOx for low-temperature CO oxidation: Direct evidence for a redox mechanism, J. Catal. 299 (2013) 90–100. doi:10.1016/j.jcat.2012.11.019.

Chapter 3 – Experimental methods

3.1. Introduction

As demonstrated in the previous chapter, there exist a variety of valuable experimental procedures which may be used to explore the surface properties of ZnO nanostructures. In particular, Brunauer-Emmett-Teller (BET) analysis may be combined with scanning electron microscopy (SEM) to study the nanostructure morphology, allowing measurements of the nanostructure dimensions to be correlated with the specific surface area of the material. To investigate the chemistry of the surface and the nature of inter-band defects, the following chapters also devote considerable attention to spectroscopic measurements. More specifically, X-ray photoelectron spectroscopy (XPS) is used to examine the chemical composition of the ZnO surface, while the properties of optical defects are qualitatively assessed through the application of photoluminescence (PL) spectroscopy.

To better characterise and adapt the ZnO nanomaterials, it is essential to understand the processes involved in their fabrication. In the upcoming investigations, ZnO nanostructures are obtained by thermally decomposing layered basic zinc acetate (LBZA) nanosheets, which are in turn synthesised via a rapid wet-chemical technique. By using a procedure called thermogravimetric analysis (TGA), it is possible to monitor the progress of the LBZA decomposition as a function of temperature, thereby providing the means to identify the associated chemical intermediates and the temperatures at which they are encountered.

Having acquired ZnO nanosheets with the desired inter-granular structure and defect chemistry, the reactivity of the surface shall be studied by exposing the material to different gases and measuring their effects on the electrical conductivity. The experiments described herein employ a continuous gas flow through a custom-built chamber, passing over locally heated ZnO nanosheets deposited on alumina-mounted inter-digitated platinum contacts. In

addition to outlining the methodology of ZnO nanosheet fabrication, this chapter also details the synthesis of gold nanoparticles for use as surface catalysts in Chapter 6.

3.2. Fabrication procedures

In order to manufacture ZnO-based gas sensors in a time-effective manner, it is typically inconvenient to use conventional hydrothermal techniques. The present study adopts a similar methodology to that developed by A. Tarat *et al.* [1], in which aqueously-suspended LBZA nanosheets were synthesised via a rapid chemical reaction stimulated by microwave radiation. Using a standard 800 W kitchen microwave, a 500 mL solution containing zinc acetate dihydrate (0.1 mol L^{-1}) and hexamethylenetetramine, or HMTA, (0.04 mol L^{-1}) was heated for six minutes at full power to yield a concentrated white suspension of LBZA nanosheets. Prior to deposition and annealing, the nanosheets were centrifuged into de-ionised water to remove residual precursor molecules and hence minimise contamination of the final ZnO material. Fig. 3.1 shows an SEM image of a typical ZnO nanosheet deposited on a conductive silicon substrate, which was obtained by annealing the LBZA starting-material in a tube furnace at 400°C for thirty minutes. Although the nanosheets generally have lateral dimensions of several microns, atomic force microscopy (AFM) measurements from similar structures have shown that they possess thicknesses of less than 100 nm [1,2].

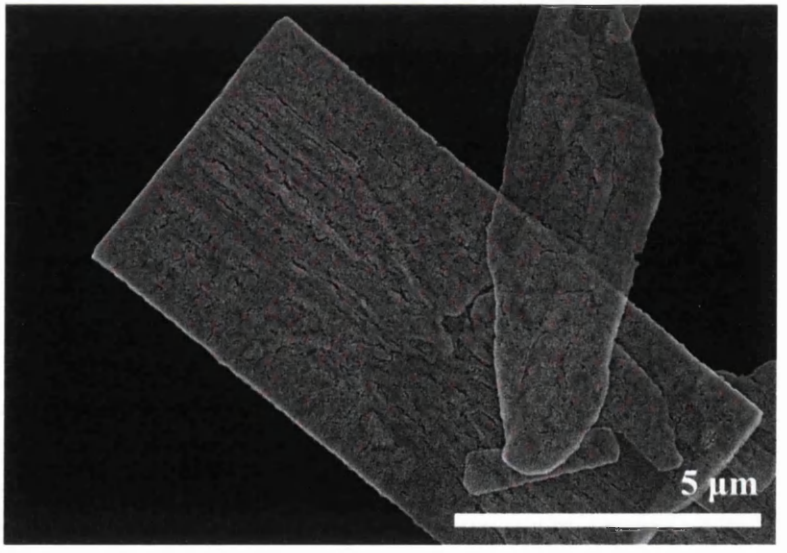

Fig. 3.1. An SEM image depicting ZnO nanosheets obtained through thermal decomposition of LBZA nanosheets at 400°C.

To prepare the gas sensors described in Chapters 5 and 6, a 100–200 μL volume of aqueously-suspended LBZA nanosheets was deposited onto each sensor substrate using a micro-pipette. Thermal decomposition of the LBZA material was carried out by annealing the devices in a tube furnace under continuous flow of dry air (80% N_2 and 20% O_2) at a rate of 900 mL min^{-1}. Guided by the TGA measurements discussed in Chapter 4, the sensors were annealed at 500°C for thirty minutes to ensure complete conversion to ZnO. For the characterisation experiments described in Chapter 4, LBZA nanosheets were instead deposited onto conductive n-type silicon and annealed at temperatures in the range 400–800°C. The ZnO nanosheet powder used in the BET and TGA experiments was acquired by first drying the centrifuged LBZA nanosheets in a glass petri dish at 60°C, before packing the resulting precipitate into a custom-built alumina crucible and annealing at the requisite temperature.

In Chapter 6, ZnO nanosheets are decorated with gold nanoparticles to investigate their effect on the sensor response to different gases. Synthesis of these nanoparticles was achieved using the Turkevich method described by S. Sivaraman *et al.* [3], in which concentrated chloroauric acid (an aqueous solution of gold (III) chloride trihydrate) is quickly added to a boiling aqueous solution of sodium citrate tribasic dihydrate with rapid stirring, as illustrated in Fig. 3.2. Over the course of several minutes, the chloroauric acid is steadily reduced by the citrate ions to produce a crimson suspension of gold nanoparticles. By ensuring that an excess of sodium citrate is present in the reacting solution, the citrate ions additionally act to stabilise the gold nanoparticles, preventing the formation of large gold aggregates. Accordingly, increasing the concentration of citrate ions is reported to decrease the mean nanoparticle diameter. In an optimised reaction used in the Sivaraman study, the molar ratio of citrate ions to gold atoms was set to a value of around twenty by adding 0.25 mL of chloroauric acid (25 mmol L^{-1}) to 24.75 mL of aqueous sodium citrate tribasic dihydrate (5 mmol L^{-1}), yielding gold nanoparticles with a mean diameter of around 7 nm.

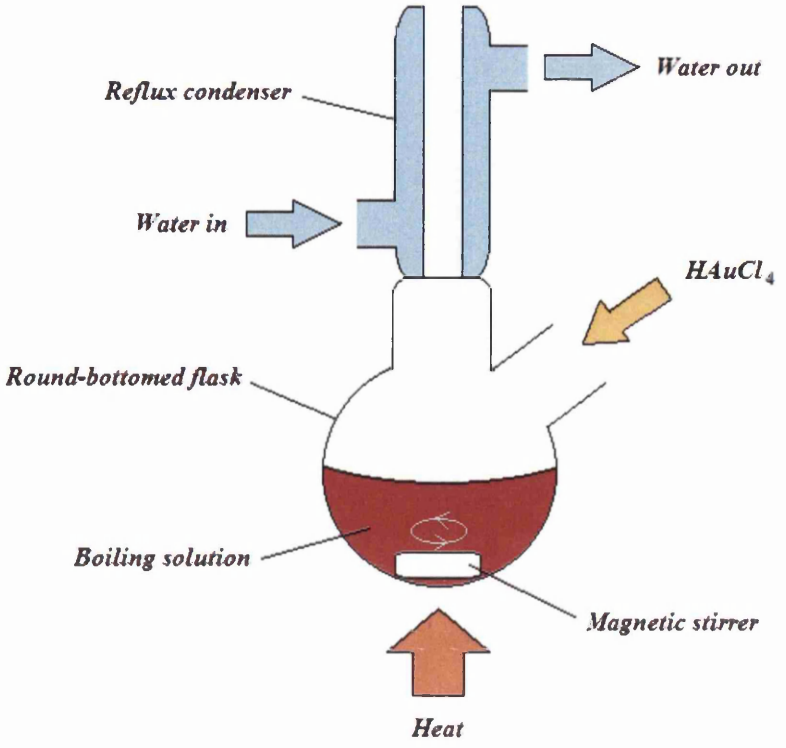

Fig. 3.2. An illustration of the apparatus used to synthesise gold nanoparticles from an aqueous solution of sodium citrate tribasic dihydrate and chloroauric acid ($HAuCl_4$).

After carrying out the Turkevich reaction, LBZA nanosheets were centrifuged into de-ionised water several times before being dispersed in the gold nanoparticle suspension. Subsequent centrifugation of this mixture resulted in the precipitation of LBZA nanosheets decorated with gold nanoparticles, and residual sodium citrate was diluted by replacing the supernatant with de-ionised water. As shown by Fig. 3.3, which depicts gold-decorated nanosheets on an alumina substrate following thermal decomposition of the LBZA at 500°C (thirty minute anneal under flow of dry air in a tube furnace), this procedure allowed the ZnO surface to be coated in a high concentration of mono-dispersed gold nanoparticles with little apparent aggregation. In this example, 0.25 mL of chloroauric acid (25 mmol L^{-1}) was added to 24.75 mL of aqueous sodium citrate tribasic dihydrate (2.5 mmol L^{-1}), resulting in the final solution containing approximately ten citrate ions for every ion of gold.

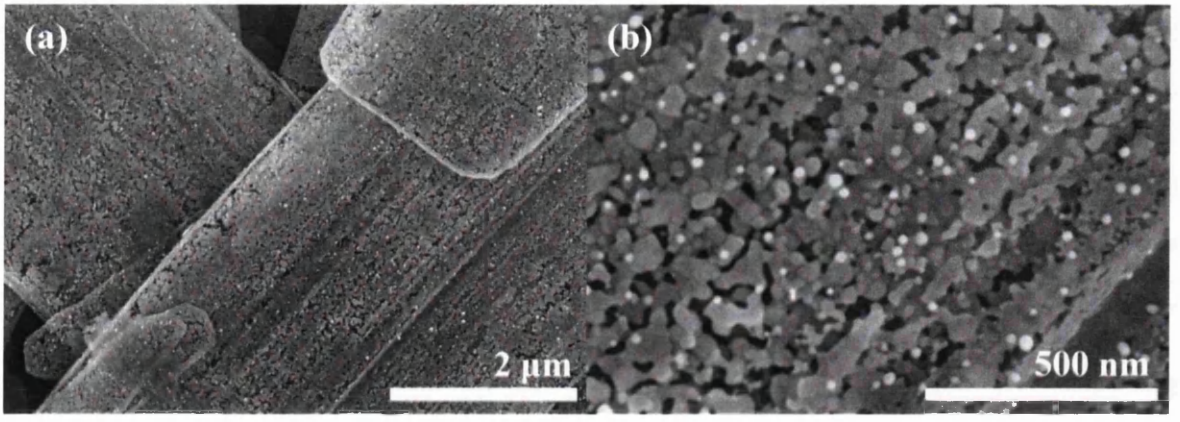

Fig. 3.3. SEM images showing ZnO nanosheets, obtained through thermal decomposition of LBZA nanosheets at 500°C, decorated by Au nanoparticles synthesised using the Turkevich technique.

3.3. Thermogravimetric analysis (TGA)

During the thermal decomposition of LBZA, the reaction progresses through several reactive intermediates [4–7]. The evolution of gaseous products such as carbon dioxide and water decreases the mass of the material, which allows the chemical composition to be deduced at each stage of the reaction through comparison to the mass prior to decomposition. In Chapter 4, a Perkin Elmer STA (Simultaneous Thermal Analyser) 6000 instrument, pictured in Fig. 3.4, is used to investigate the thermal decomposition through the TGA technique, wherein a small volume of powdered sample is packed into an alumina crucible situated on a mass balance and is gradually heated in an atmosphere of nitrogen. A typical TGA experiment involves increasing the temperature of the sample to several hundred degrees Celsius at a rate of 5°C min^{-1} while the mass is measured continuously as a function of temperature. In the case of LBZA, several studies have shown that thermal decomposition occurs in three stages, with full conversion to ZnO achieved at a temperature of approximately 390–400°C. As shown by the plot in Fig. 3.5, which is adapted from Fig. 3 of Reference [7], the mass reduces gradually as the temperature is increased to 100°C due to the evaporation of intercalated water molecules. Further heating to around 140°C leads to dehydroxylation of the material, in which hydroxyl groups are removed as molecules of water. The final stage of the reaction, corresponding to the large mass decrease between 140°C and 290°C, is associated with decomposition of the acetate ions.

Fig. 3.4. A photograph of the Perkin-Elmer STA 6000 instrument used to investigate the thermal decomposition of LBZA nanosheets in the present work.

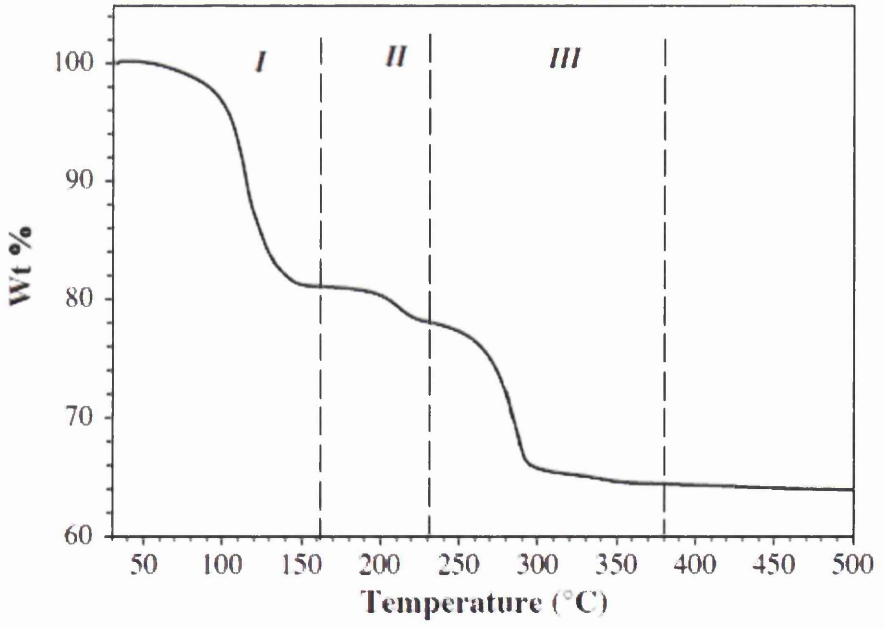

Fig. 3.5. A thermogravimetric plot, adapted from Fig. 3 of Reference [7], showing how the mass of LBZA (as a percentage of the starting mass) varies as the temperature is increased at a rate of $5^{o}C\ min^{-1}$.

3.4. Brunauer, Emmett and Teller (BET) analysis

As well as studying the decomposition of LBZA to ZnO, it is important to consider how the ZnO morphology is related to the annealing temperature. By exposing a sample powder to nitrogen gas at a temperature of around 77 K and measuring the volume of adsorbed nitrogen as a function of the gas pressure, BET analysis may be employed to calculate the specific surface area of the material. The photograph in Fig. 3.6 depicts the Nova 2000e surface area and pore size analyser used in the present investigation, which possesses a degassing chamber to remove adsorbed water from the sample powder (on the left-hand side of the photograph) and an analysis chamber in which the BET analysis is performed (on the right-hand side). Within the analysis chamber, two different cylindrical glass tubes are present in the photograph, one with a spherical glass bulb at the free end and one without. Each of these tubes is an example of an analysis "cell" in which the BET analysis of a sample powder is performed (sample cells with spherical bulbs were used in the following chapter).

Prior to the BET experiment, around 100 mg of sample powder is placed in a cell and weighed using a mass balance. After degassing and re-weighing the powder, the sample cell is inserted into the analysis chamber and cooled in a dewar of liquid nitrogen. The tube is subsequently evacuated in preparation for an adsorption test, wherein nitrogen gas is gradually admitted and the volume of adsorbed nitrogen is measured as a function of increasing system pressure. Upon reaching the atmospheric pressure, P_0, the nitrogen is slowly evacuated from the cell to investigate the desorption behaviour of the gas, continuously measuring the volume of adsorbed nitrogen as the pressure is decreased. Typical adsorption and desorption curves of mesoporous ZnO are depicted in Fig. 3.7 [8], which shows the commonly observed hysteresis between the two sets of measurements. This hysteresis results from capillary condensation and is closely related to the form and size of the pores [9–12].

Fig. 3.6. A photograph of the Nova 2000e surface area and pore size analyser used to measure the specific surface areas of the LBZA and ZnO nanosheets.

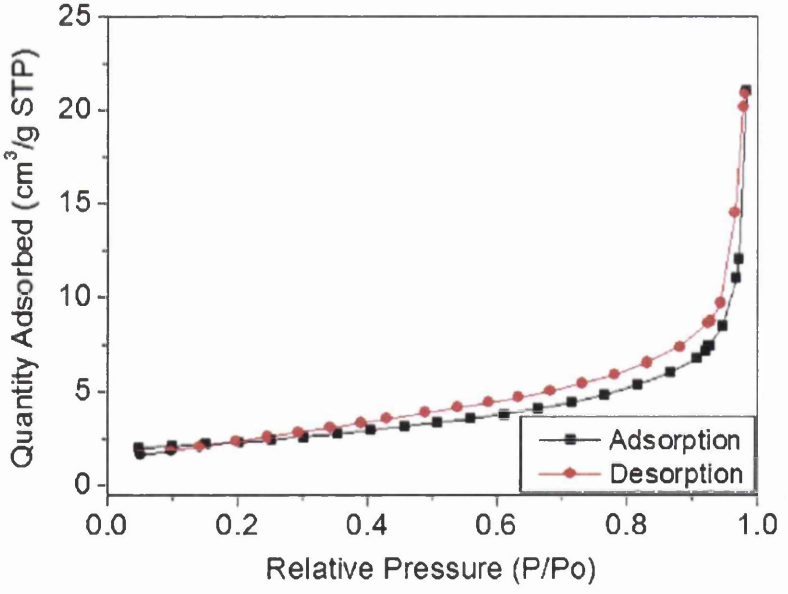

Fig. 3.7. Nitrogen adsorption and desorption isotherms of a mesoporous ZnO powder at a temperature of 77 K, adapted from Fig. 6 of Reference [8].

In the BET model of gas adsorption [9,10,13], it is assumed that gas molecules behave ideally and adsorb in multiple liquid-like layers over equivalent surface sites. Each surface site is characterised by the number of physisorbed gas molecules it holds, and the fraction of sites associated with n physisorbed molecules is denoted θ_n. For a system containing a fraction θ_0 of surface sites which possess no gas molecules, the rate of change of θ_0 is described by the equation

$$\frac{d\theta_0}{dt} = k_{-1}\theta_1 - k_1\left(\frac{P}{P_0}\right)\theta_0 \tag{3.1}$$

where k_1 and k_{-1} are the rate constants for adsorption and desorption within the first layer of gas molecules, respectively, and P is pressure exerted by the surrounding gas molecules and P_0 is the atmospheric pressure outside the analysis cell. In equilibrium, the rate of adsorption must equal the rate of desorption, hence

$$\theta_1 = \frac{k_1}{k_{-1}}\left(\frac{P}{P_0}\right)\theta_0 \tag{3.2}$$

Similarly, the fraction of sites containing just one physisorbed molecule, θ_1, changes at a rate given by

$$\frac{d\theta_1}{dt} = k_1\left(\frac{P}{P_0}\right)\theta_0 + k_{-2}\theta_2 - k_{-1}\theta_1 - k_2\left(\frac{P}{P_0}\right)\theta_1 \tag{3.3}$$

where, following the previous convention, the rate constants for adsorption and desorption within the nth layer of adsorbed molecules are represented by k_n and k_{-n}, respectively. Eq (3.3) follows physically as θ_1 is increased when an exposed site acquires a gas molecule or a molecule desorbs from a site containing two physisorbed species. Likewise, the value of θ_1 is decreased when an adsorbate within the first gas layer either desorbs or collects a second molecule from the surroundings. Again, θ_1 must remain constant in equilibrium so one may write

$$k_1\left(\frac{P}{P_0}\right)\theta_0 + k_{-2}\theta_2 - k_{-1}\theta_1 - k_2\left(\frac{P}{P_0}\right)\theta_1 = 0 \tag{3.4}$$

Combining Eq. (3.4) with Eq. (3.2), one obtains

$$k_{-2}\theta_2 = k_2\left(\frac{P}{P_0}\right)\theta_1 \tag{3.5}$$

Hence,

$$\theta_2 = \frac{k_2}{k_{-2}}\left(\frac{P}{P_0}\right)\theta_1 = \frac{k_2}{k_{-2}}\frac{k_1}{k_{-1}}\left(\frac{P}{P_0}\right)^2\theta_0 \tag{3.6}$$

where Eq. (3.2) has been used to eliminate θ_1 from the equation. By applying the same methodology to each successive layer in an iterative manner, it may be shown that

$$\theta_n = \frac{k_n}{k_{-n}}\left(\frac{P}{P_0}\right)\theta_{n-1} = \left(\prod_{i=1}^{n}\frac{k_i}{k_{-i}}\right)\left(\frac{P}{P_0}\right)^n\theta_0 \tag{3.7}$$

in equilibrium.

In the next stage of the formulation, it is further assumed that all gas layers from the second layer onwards are physically identical. Consequently,

$$k_n = k_{n-1} \qquad (n > 2) \tag{3.8}$$

and

$$k_{-n} = k_{-(n-1)} \qquad (n > 2) \tag{3.9}$$

Eq. (3.7) therefore simplifies to

$$\theta_n = \left(\frac{k_n}{k_{-n}}\left(\frac{P}{P_0}\right)\right)^{n-1}\frac{k_1}{k_{-1}}\left(\frac{P}{P_0}\right)\theta_0 \equiv x^n c\theta_0 \qquad (n \geq 1) \tag{3.10}$$

where

$$x \equiv \frac{k_n}{k_{-n}}\left(\frac{P}{P_0}\right) \tag{3.11}$$

and

$$c \equiv \frac{k_1}{k_{-1}} \frac{1}{x} \left(\frac{P}{P_0} \right) \tag{3.12}$$

For a surface containing a total of S sites, the total number of adsorbed molecules, N_a, is given by

$$N_a = \sum_{n=0}^{\infty} n\theta_n S \tag{3.13}$$

The fractional surface coverage, θ, is defined as

$$\theta \equiv \frac{N_a}{S} \tag{3.14}$$

and the total number of sites, S, may be written as

$$S = \sum_{n=0}^{\infty} \theta_n S \tag{3.15}$$

It follows that

$$\theta = \frac{\sum_{n=0}^{\infty} n\theta_n S}{\sum_{n=0}^{\infty} \theta_n S} = \frac{\sum_{n=1}^{\infty} n\theta_n}{\theta_0 + \sum_{n=1}^{\infty} \theta_n} \tag{3.16}$$

which, after making use of Eq. (3.10), becomes

$$\theta = \frac{c\theta_0 \sum_{n=1}^{\infty} n x^n}{\theta_0 + c\theta_0 \sum_{n=1}^{\infty} x^n} = \frac{c \sum_{n=1}^{\infty} n x^n}{1 + c \sum_{n=1}^{\infty} x^n} \tag{3.17}$$

To proceed, it is helpful to note that

$$\sum_{n=1}^{\infty} x^n = \frac{x}{1-x} \tag{3.18}$$

and

$$\sum_{n=1}^{\infty} nx^n = x\sum_{n=1}^{\infty} nx^{n-1} = x\frac{\mathrm{d}}{\mathrm{d}x}\sum_{n=1}^{\infty} x^n = x\frac{\mathrm{d}}{\mathrm{d}x}\left(\frac{x}{1-x}\right) = \frac{x}{(1-x)^2} \qquad (3.19)$$

Substituting Eq. (3.18) and Eq. (3.19) yields

$$\theta = \frac{cx}{(1-x)(1+(c-1)x)} \qquad (3.20)$$

which is an oft-quoted form of the BET isotherm.

It was previously stated that BET theory necessitates the assumption that the adsorbed nitrogen layers behave as a liquid, which is only appropriate at very low temperatures. Equilibrium between the surface of the adsorbed multilayers and the vapour phase requires that the rates of adsorption and desorption are equal, which for liquid nitrogen occurs when the cell pressure is the same as the atmospheric pressure, P_0. This equilibrium condition therefore requires that

$$k_n = k_{-n} \qquad (3.21)$$

from which one obtains the relation

$$x = \frac{P}{P_0} \qquad (3.22)$$

By applying Eq. (3.22) and using Eq. (3.14) to eliminate θ, Eq. (3.20) rearranges to give

$$\frac{1}{N_a\left(\frac{P_0}{P}-1\right)} = \left(\frac{c-1}{Sc}\right)\frac{P}{P_0} + \frac{1}{Sc} \qquad (3.23)$$

Dividing each term of Eq. (3.23) by the mass of a nitrogen molecule yields the most practically useful form of the BET isotherm,

$$\frac{1}{W\left(\frac{P_0}{P}-1\right)} = \left(\frac{c-1}{W_m c}\right)\frac{P}{P_0} + \frac{1}{W_m c} \qquad (3.24)$$

where W_m is the mass of a single layer of adsorbed nitrogen molecules and W is the measured mass of adsorbates. As the left-hand side of Eq. (3.24) contains only measurable quantities, it may be plotted as a function of P/P_0 to obtain estimates of the other parameters in the equation. It is important to recognise that since the right-hand side of the equation is linearly dependent on P/P_0, such a plot should have constant gradient equal to $(c\text{-}1)/W_m c$ and intercept the y-axis at the value $1/W_m c$. Moreover, it may be shown that

$$W_m = \frac{1}{y_{int}+g} \tag{3.25}$$

where y_{int} and g are the y-intercept and gradient of the plot, respectively. Since W_m is equal to the mass of a single complete layer of nitrogen molecules, knowledge of the mass and cross-sectional area of each molecule allows estimation of the total surface area.

Although the BET theory predicts direct proportionality to exist between the left-hand side of Eq. (3.24) and the ratio P/P_0, this relationship is typically only observed between P/P_0 values of approximately 0.05 and 0.3, where the gas coverage is close to one monolayer [12,13]. When the pressure of the system is too low, there are so few adsorbate molecules at the sample surface that any inhomogeneities have a significant influence on the form of the isotherm. More specifically, as the adsorption dynamics may vary significantly between the most and least active adsorption sites, Eq. (3.24) is only valid when the adsorbate concentration is sufficiently high for the adsorption properties to be averaged over the whole surface [13]. The isotherm also deviates from the linear relationship at very high values of P/P_0, in this case due to the non-uniformity of the surface; the presence of cracks and pores in the surface imposes a physical limit on the maximum number of adsorbate layers, which in turn alters the form of the BET isotherm [13].

3.5. Scanning Electron Microscopy (SEM)

Due to their sub-micrometre dimensions, the ZnO nanosheets used in the present investigation cannot be effectively examined using conventional optical microscopy. Instead, techniques such as SEM which use electrons have sufficiently high resolution to probe the topography of the material. By sweeping an electron beam in a raster scan across the surface, an SEM system is able to create a detailed topographical image of the inspected area by detecting the electrons scattered from each point. As detailed elsewhere [14–16], an electron propagating through the surface may either scatter elastically, retaining its kinetic energy, or impart momentum to electrons within the material through inelastic collisions. In the former scenario, the incident electrons are able to travel a significant distance into the material and, after colliding elastically, may exit the sample as "back-scattered electrons" (BSE). Electrons that are liberated through inelastic collisions of the incident electrons are referred to as "secondary electrons" (SE), and can only originate from close to the surface (up to a depth of 2–8 nm for typical accelerating voltages in the case of ZnO [17–19]) due to their low kinetic energies (typically less than 50 eV). This point is to be considered in greater detail later in this chapter, where the inelastic mean free paths of electrons will be discussed in relation to the more surface-sensitive XPS technique.

The internal structure of an SEM instrument is illustrated in Fig. 3.8, which is reproduced from Fig. 1.7 of Reference [14]. After electrons are generated in an electron gun by field emission, they are accelerated by an electric anode towards a series of lenses. Here, the electrons are collimated into a parallel beam by a system of magnetic condenser lenses (CL) and subsequently focussed to a spot on the specimen surface by the objective lenses (OL). The beam is swept across the sample by deflection coils, which use a magnetic field to deflect the electrons as required. The sample chamber is evacuated to a pressure of less than 5×10^{-5} Torr, allowing secondary electrons excited from the surface to travel towards the secondary electron detector. The Hitachi S4800 FE-SEM instrument used in the present investigation is pictured in Fig. 3.9.

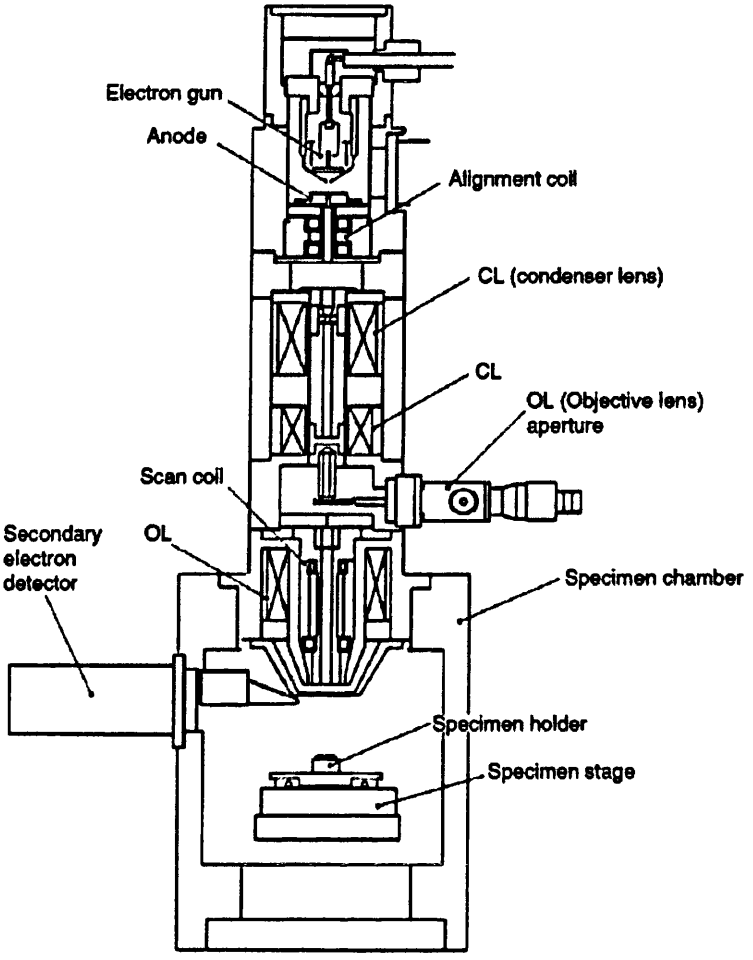

Fig. 3.8. An illustration of a typical scanning electron microscope, reproduced from Reference [14].

Fig. 3.9. The Hitachi S4800 FE-SEM employed in the present investigation.

To relate the resolution limit, d, of a scanning electron microscope, or indeed a conventional optical microscope, to the wavelength of the incident beam, λ, one may employ the formula [14]

$$\boldsymbol{d} = \frac{\mathbf{0.61}\boldsymbol{\lambda}}{\boldsymbol{n}\mathbf{sin}\boldsymbol{\alpha}} \tag{3.26}$$

where n is the refractive index of the medium (in the case of an SEM, where the electrons travel through a vacuum, n has a value of one) and α is half the opening angle of the objective lens (measured in radians). This relation is commonly known as Abbe's Equation, and may

be applied to the case of an electron beam by using the de Broglie Equation to calculate the particle wavelength from the kinetic energy. In this way, Eq. (3.26) becomes

$$d = \frac{0.61h}{n\sin\alpha\sqrt{2meV_{acc}}} \tag{3.27}$$

where h is Planck's constant, m is the electron mass, e is the electronic charge and V_{acc} is the accelerating voltage. Substituting typical values of 10^{-3}–10^{-2} radians [20] and 10 kV for α and V_{acc}, respectively, one obtains a theoretical resolution limit of several nanometres. It is clear from Eq. (3.26) that a lower value of d may be achieved by decreasing the distance between aperture and specimen (which is known as the "working distance"), thereby increasing the angle α. Alternatively, the resolution may be enhanced by employing a higher acceleration voltage, V_{acc}. However, Eq. (3.26) typically underestimates the true resolution limit as the equation does not account for detrimental experimental phenomena such as spherical aberration [16].

3.6. X-ray photoelectron spectroscopy (XPS)

For analysing the physical and chemical properties of surfaces, one particularly useful technique is XPS. This procedure involves illuminating a material, placed in an ultra-high vacuum (UHV) pressure of approximately 10^{-9} Torr [21,22], with X-rays of well-defined energy and measuring the kinetic energies of the resulting photoelectrons. Due to the quantised nature of the core energy levels, each emitted electron has a precise energy which is characteristic of the orbital from which it originated. As the energy of the incident X-rays is known, the binding energy of each orbital may be calculated from the kinetic energies of the electrons. The measured spectrum of binding energies may therefore be used to identify the elemental composition of the material. Moreover, the energy of a particular orbital is dependent on the surrounding electronic environment, resulting in a "chemical shift" of binding energy to a higher or lower value than anticipated [21,22]. In the XPS spectrum, therefore, two peaks of similar energy may correspond to the same atomic orbital of a particular element, but from atoms with different electronic environments (different bonding arrangements, for example). In practice, thermal peak broadening may result in two closely-spaced signals manifesting as components of a single, asymmetric peak.

In the following chapter, XPS is used to investigate variations in the surface chemistry between differently annealed ZnO nanosheets. The specific instrument used to conduct these measurements is a Kratos AXIS Supra system, pictured in Fig. 3.10, which utilises X-rays emitted from an aluminium source. By passing these X-rays through a 500 mm Rowland circle monochromator, the sample is exposed only to radiation from the K_α line of the aluminium X-ray spectrum, which has a characteristic energy of 1486.6 eV. As photoelectrons are generated from the sample surface they are directed into a hemispherical electron analyser by a magnetic immersion lens (also called a "snorkel lens") [23], where they are grouped according to their kinetic energy as shown in Fig. 3.11 [24]. The electrons propagate through an electric field applied between two metallic plates, traversing a curved trajectory that is dependent on the electron velocity. For a particular strength of electric field, only those electrons travelling along paths with the correct radius of curvature, r_0, are able to reach the detector at the end of the analyser; electrons which are travelling too slowly are deviated too strongly by the electric field, while electrons with too high a kinetic energy possess a trajectory which is too shallow. If the electrons were admitted directly into the analyser, however, the finite size of the hemisphere would limit the minimum achievable energy resolution of the device, particularly in the case of the most energetic electrons. In order to acquire the same energy resolution regardless of the kinetic energy, the electrons are retarded by a system of lenses to a pre-defined "pass energy" (typically of order 10 eV) prior to entering the analyser. This mode of operation, wherein the system selects which electrons are to be detected prior to their admission to the hemispherical analyser, is referred to as "fixed analyser transmission" [22,25], as the electric field between the plates of the analyser is held constant throughout an XPS scan.

Fig. 3.10. A photograph depicting the Kratos AXIS Supra XPS analyser employed in the present investigation.

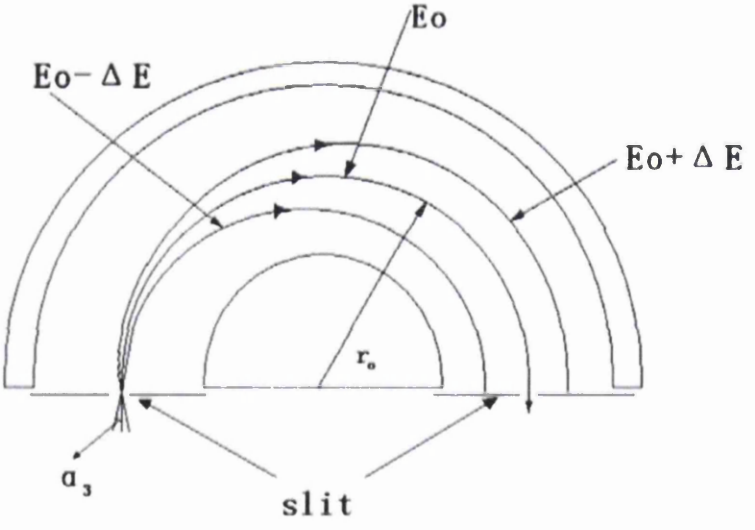

Fig. 3.11. A diagram of a typical electron analyser in an XPS system, reproduced from Reference [24]. Electrons with kinetic energy equal to the pass energy, E_0, pass through the exit-slit at the end of the analyser and are detected, while all other electrons are discarded.

In the case of electrically insulating materials, the liberation of photoelectrons results in the development of a positive electric charge and an associated potential barrier at the surface. This potential both increases the binding energy of the core electrons, thereby linearly shifting the XPS spectrum, and broadens each photoelectron peak due to the charge variations across the surface [26–29]. As the relative peak areas are used to estimate the chemical composition of the material, it is essential that this charging effect is counteracted. To replace the removed electrons, many modern XPS instruments expose the sample to a diffuse stream of low-energy electrons, often from a secondary electron source called a "flood gun" [23]. Systems such as the Kratos AXIS Supra spectrometer, however, instead use "repeller electrodes" to redirect any electrons from the specimen which are not collected by the magnetic snorkel lens, returning these electrons to the analysed area of the surface. As shown by the diagram in Fig. 3.12 [23], filaments located behind the repeller electrodes produce additional electrons that migrate through the snorkel lens and follow the magnetic field lines to the sample surface, further compensating for the liberated photoelectrons.

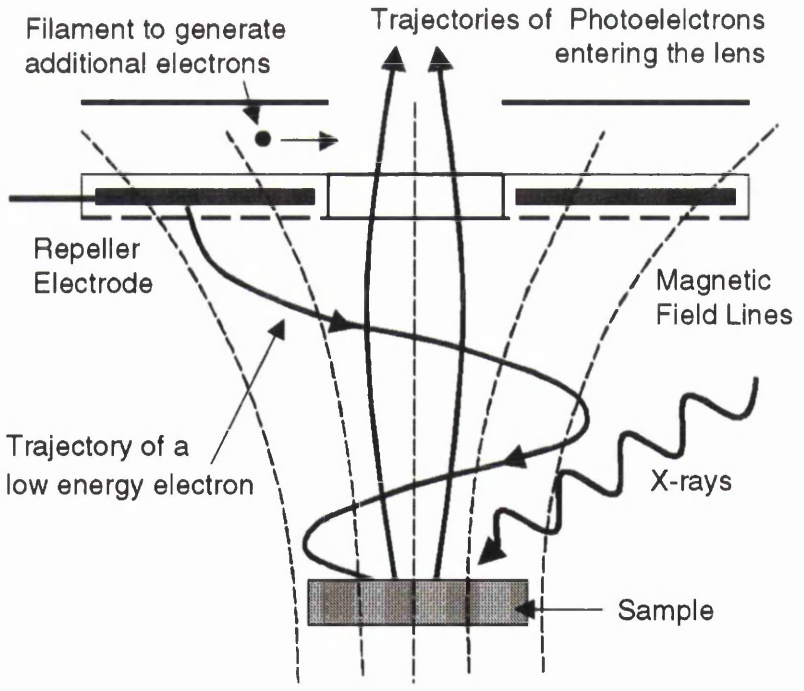

Fig. 3.12. A diagram of a typical charge compensation system in an XPS instrument which employs a magnetic snorkel lens, reproduced from Fig. 4 of Reference [23]**. Any electrons which are not gathered by the magnetic field between lens and sample are reflected back to the surface by a "repeller electrode", while additional electrons are generated by filaments located behind these electrodes.**

Although the system illustrated in Fig. 3.12 is able to effectively compensate for any positive surface charge, the different ground potentials of the spectrometer and the sample surfaces may lead to a disparity between the measured electron binding energies and their "true" values [23]. To account for this error, the measured binding energies are conventionally shifted linearly so that the C 1s peak attributed to adventitious hydrocarbons, which is present at the surface of most samples, appears at its characteristic binding energy value of 285.0 eV [23].

As photoelectrons are ejected from the core energy levels of a material, electrons from higher levels may relax to replace them. In doing so, the residual energy may be transferred to other core electrons which are subsequently emitted from the sample. This phenomenon is known as the Auger process, and results in additional peaks in the XPS spectrum [25]. It is instructive to note that the energy imparted to Auger electrons is equal to the energy difference between two core energy levels, and consequently does not depend on the energy of the incident X-rays. It follows that the binding energy of an Auger electron varies according to the X-ray energy, a property which may therefore be used to distinguish these electrons from the core photoelectrons. Each Auger peak of the XPS spectrum is labelled by three letters, each corresponding to the core orbital involved during a particular stage of the Auger process. For example, in a "KLM" process the incident X-ray excites a photoelectron from the 1s orbital (contained in the K shell), the resulting hole recombines with an electron from a 2p orbital (in the L shell), and an Auger electron is subsequently ejected from a 3p orbital (in the M shell) [30]. Possible Auger processes are summarised by the diagram in Fig. 3.13 [30], which also depicts alternative processes in which the energy from de-exciting electrons is emitted in the form of an X-ray.

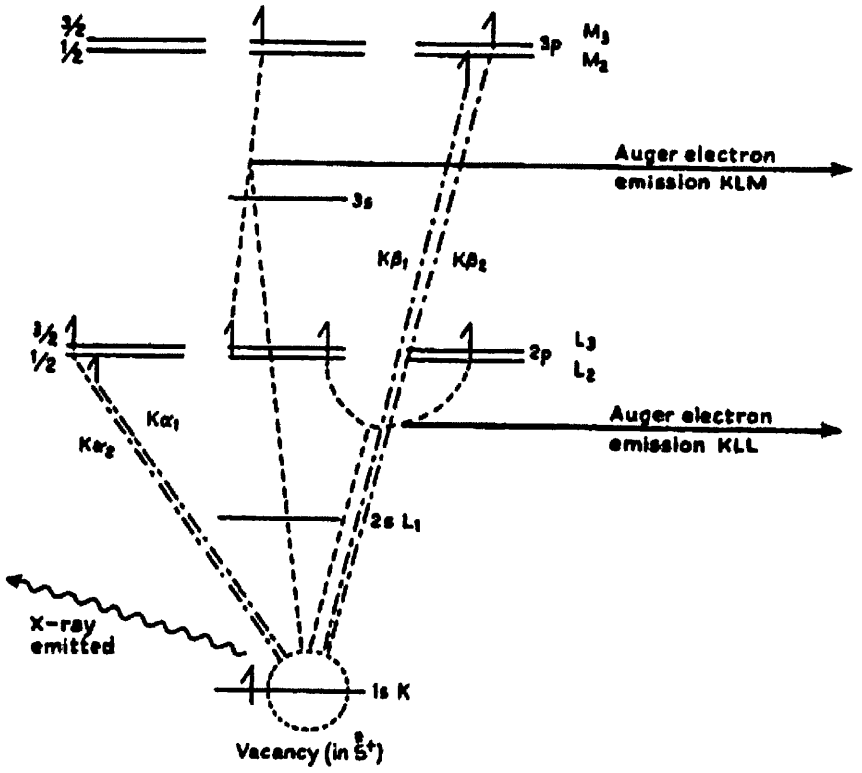

Fig. 3.13. A diagram depicting the Auger processes that may occur following the emission of a photoelectron from a material. The diagram is reproduced from Fig. 1 of [30].

As was discussed earlier in relation to the SEM technique, the escape depth of electrons from a sample is dependent on their kinetic energy. At kinetic energies above ~100 eV, the escape depth increases due to the higher inelastic mean free path (IMFP) of the electrons [31–37]. At lower energies, however, the opposite is true; inelastic electron scattering induces a higher proportion of plasmons as the kinetic energy of electrons is increased [25], thereby lowering the escape depth. Across a wide range of materials the escape depth is minimised at a kinetic energy value of 50–100 eV, where the IMFP typically diminishes to less than 1 nm [33–35]. The characteristic relationship between the IMFP and kinetic energy, depicted in Fig. 3.14 [25], is often referred to as the "universal curve" due to its general applicability to a plethora of materials.

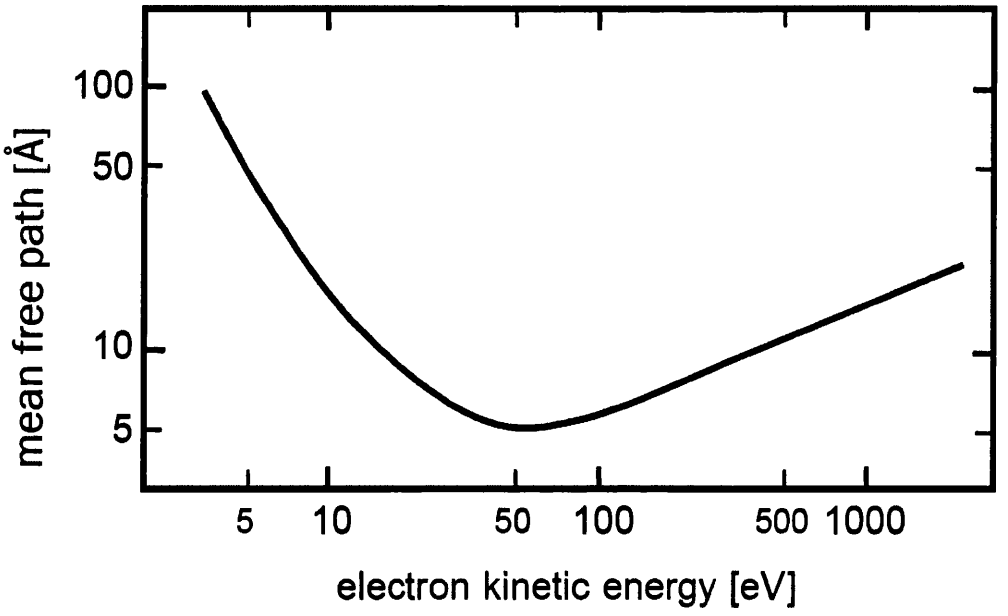

Fig. 3.14. A plot showing a typical relationship between the inelastic mean free path of electrons and their kinetic energy, reproduced from Fig. 2 of Reference [25].

In addition to using XPS to identify the core orbitals that are present in a sample, the technique may be employed to measure the maximum energy of the valence band (the "valence band maximum", or VBM) relative to the Fermi level of the material. In general, XPS systems are calibrated so that the Fermi energy coincides with zero binding energy, allowing the energy difference between the Fermi level and the VBM to be identified as the binding energy at which the measured electron count goes to zero [38–42]. Some instruments incorporate an analogous procedure called ultraviolet photoelectron spectroscopy (UPS), in which electrons are excited from the specimen using ultraviolet radiation rather than X-rays. Due to the low energy of the incident radiation, this procedure affects only electrons contained within the valence band and cannot, therefore, be used to explore the core energy levels of the material. However, as demonstrated by the UPS valence-band scan depicted in Fig. 3.15 [43], the maximum binding energy at which electrons are ejected allows the work function of the sample to be estimated, a parameter which cannot be determined using XPS. More specifically, the work function is equal to the difference between energy of the incident radiation and the maximum binding energy of emitted electrons [43–47], which may be deduced by first recognising that photoelectrons at the high-binding energy cut-off

point must have zero kinetic energy (otherwise it would be possible for more strongly-bound electrons to be ejected).

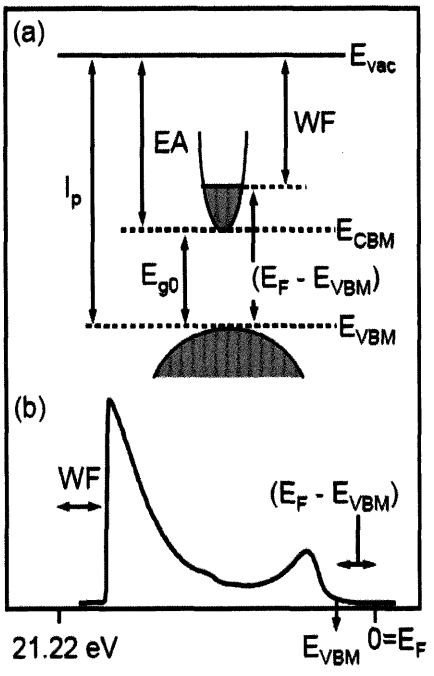

Fig. 3.15. Diagrams showing important energy levels and differences in a semiconductor (a) and a typical UPS spectrum obtained after illuminating a semiconducting material using ultraviolet radiation of energy 21.22 eV (b), reproduced from Fig. 1 of Reference [43]. **The work function (*WF*) of the sample, defined as the energy difference between the Fermi energy (E_F) and the vacuum level (E_{vac}), and the difference between the Fermi level and the valence band maximum (E_{VBM}) may be estimated from the cut-off energies of the UPS spectrum, as indicated.**

3.7. Photoluminescence (PL) spectroscopy

Another particularly useful spectroscopic technique is PL spectroscopy, in which the emission wavelengths of electrons within a material are measured following their excitation by an ultraviolet laser [48,49]. In the present study, a 7.8 mW Melles-Griot He-Cd laser, pictured in Fig. 3.16 (a), was used to produce an intense ultraviolet beam of wavelength 325 nm. The beam was directed into a band-pass filter via an optical fibre to remove any higher-order resonant peaks, before being passed through another optical fibre and a stainless steel ferrule to illuminate the sample. As shown by Fig. 3.16 (b), the ferrule was tilted at a 45°

angle to the sample surface whereas the emitted light was collected by a second stainless steel ferrule at an angle of 90°, parallel to the surface normal. This configuration was employed in order to minimise the collection of reflected laser-light, whilst maximising the number of sampled photons emitted from the illuminated material. The ferrule–sample distances were adjusted to maximise the intensity of the collected light. Due to losses in the optical fibre, the incident radiation had a measured power of 1.8 ± 0.1 mW, as measured using a handheld Thorlabs power meter. As the laser beam was focussed over an area of approximately 1 mm, the incident power density was estimated as ~2.3×10^6 mW m^{-2}. Following collection, the emitted radiation was focussed into a low-pass filter via an optical fibre to discard any ultra-violet light of wavelength 350 nm or lower, thereby removing any reflected laser-light which may be present. The filtered emission spectrum was measured using an Ocean Optics USB 2000+ spectrometer, with the measurement time set to ensure maximum signal intensity without saturation. Each PL spectrum was averaged over three scans to suppress background noise.

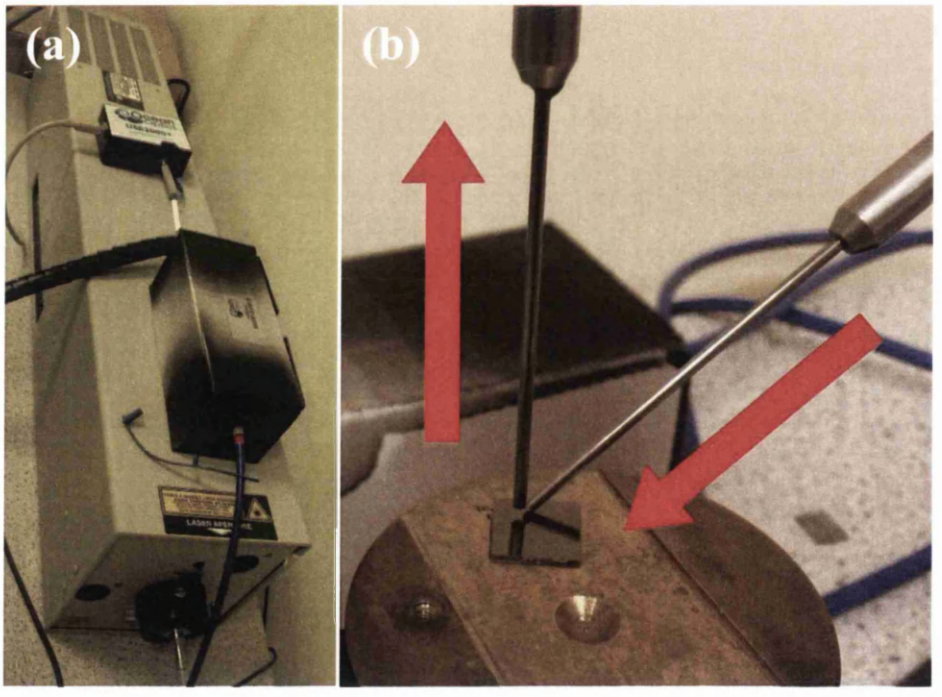

Fig. 3.16. Photographs showing the 7.8 mW Melles-Griot He-Cd laser (emitting at light of wavelength 325nm) (a) and the configuration of emitter and collector ferrules (b) employed in the present investigation (the red arrows indicate the direction of the incident laser and the emitted light from the square sample).

The excitation of electrons from the valence band of a semiconductor to the conduction band typically results in the formation of an entity known as an "exciton", which consists of an electron that is electrostatically bound to a hole in the valence band [50]. The binding energy of free excitons in ZnO is usually quoted as 60 meV [50–55], which is significantly higher than the kinetic energy of the electrons at room temperature. The excitons in this material are therefore long-lived during a room temperature PL experiment, allowing the electron and hole to recombine radiatively by releasing energy in the form of a photon. In a direct band gap semiconductor such as ZnO, the energy of this radiation is equal to the band gap of the semiconductor minus the exciton binding energy, and is consequently only marginally lower than the energy of the band gap. For this reason, the PL signal attributed to electron-hole recombination is commonly referred to as the "near-band-edge", or NBE, peak, and provides an estimate of the semiconductor band gap.

At sufficiently low temperatures (10K, for instance), it is possible to resolve the NBE signal of the PL spectrum into several distinct peaks. Many materials, including ZnO, contain inter-band donor and/or acceptor states which may interact with an exciton, altering the binding energy of the electron-hole pair [48,50–60]. It has been shown by various authors that the binding energy of bound excitons scales in direct proportion to the binding energy of the associated donor or acceptor species, a relationship known as Hayne's rule [52,53,55,58,59]. An example of a low-temperature ZnO NBE signal is depicted in Fig. 3.17, which is reproduced from Fig. 3 of Reference [52], where the different component peaks have been attributed to excitons bound to either neutrally-charged donors (conventionally labelled D^0) or neutrally-charged acceptors (denoted A^0). The excitons themselves are, by convention, represented by the letter X and suffixed by the letter A, B or C, which identify the valence band in which the hole is created [52–54,59,61] (the valence band of ZnO is split into three separate bands by crystal field and spin-orbit interactions [53]). Other components of the NBE peak are attributed to "rotator states", which are commonly identified as excited states of the donor-bound excitons [52,54,56,59,61].

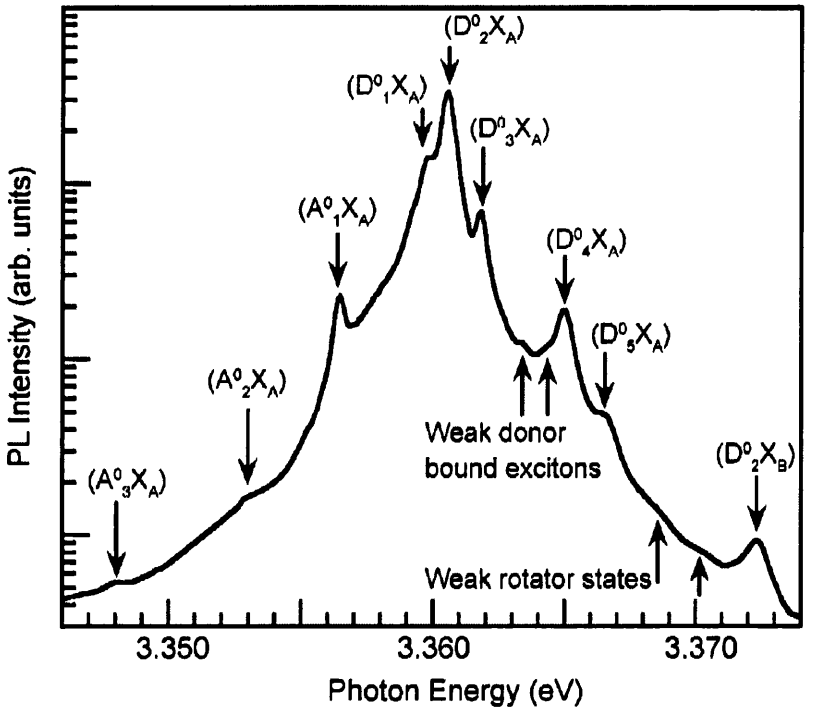

Fig. 3.17. An NBE PL spectrum of ZnO obtained at a temperature of 10 K, reproduced from Fig. 3 of Reference [52]**. The NBE signal contains components from both donor-bound excitons (D^0X) and acceptor-bound excitons (A^0X).**

Inter-band defect states also provide more direct contributions to the PL spectrum; following the promotion of valence electrons to the conduction band, photonic emission may result from recapture of the electrons by acceptors or the de-excitation of donor electrons to the valence band [49]. It is important to note, however, that conduction band electrons may alternatively return to the conduction band through non-radiative processes, producing phonons as opposed to photons. As these phenomena do not generate photons, the corresponding optically-inactive defect states cannot be identified from the PL spectrum.

In the case of ZnO, a plethora of optically-active donor and acceptor inter-band states have been detected. In particular, authors have attributed PL emission in the visible range of wavelengths to species such as oxygen vacancies [62–74] (denoted V_O), zinc vacancies [62,65,70–72,74] (V_{Zn}), interstitial oxygen [62–67,70,71] or zinc ions [62,65,71,72,74] (O_i and Zn_i, respectively), and antisite oxygen [62,67–69,71] or zinc ions [62,67] (generally

labelled X_Y, where an ion of X is located where an ion of Y ought to exist). A diagram showing the energies of various inter-band states in ZnO is displayed in Fig. 3.18 [67], which also depicts the expected transitions between these states and either the conduction or valence band; it should be recognised, however, that the precise energies of these inter-band states remains a subject of heated debate [74].

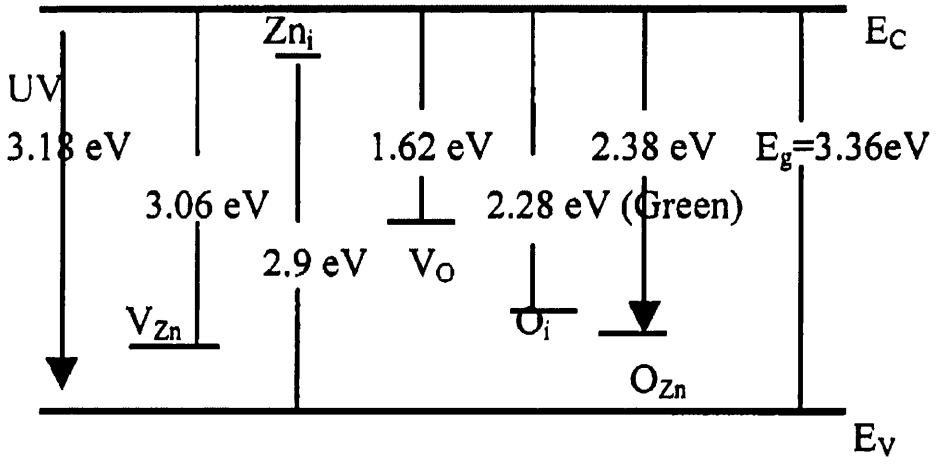

Fig. 3.18. A diagram showing the calculated energies of various inter-band defect states in ZnO, reproduced from Fig. 4 of Reference [67].

3.8. Gas sensing experiments

Following characterisation of the LBZA and ZnO nanosheets using the techniques detailed in the previous sections, the remainder of the investigation employs gas sensing experiments to explore the chemical and physical properties of the ZnO surface. Here, the experimental setup used during these studies shall be described in detail; the theoretical aspects of the tests have been extensively reviewed in Chapters 1 and 2, so shall not be considered further.

Despite the multitude of different gas sensing investigations undertaken in the following chapters, there are several experimental variables which remain constant throughout. For instance, all of the tests were conducted under continuous gas flow at a rate of 400 mL min^{-1}, which was held constant by Aalborg mass flow controllers (MFCs) regardless of the gas composition. In all cases, the flow was predominantly comprised of nitrogen and oxygen,

mostly in a 4:1 ratio, respectively, and manual valves were used to replace a fraction of the nitrogen with a reducing gas, as required. Each reducing gas was introduced at a concentration of 1000 ppm in nitrogen, and was subsequently further diluted by the simultaneous flow of oxygen and nitrogen through the system. By using an MFC to adjust the flow rate of the 1000 ppm reducing gas into the sample chamber, it was possible to precisely control the final concentration of the reducing gas. Accounting for the flow rate limitations of the MFCs, reducing gas concentrations in the range 50–200 ppm could be reliably achieved.

The gas sensing chamber used throughout the experiments, which, in addition to the sample holder and the surrounding tubing and instrumentation, was assembled by the author, is photographed in Fig. 3.19, and the overall system is illustrated in Fig. 3.20. During an experiment, oxygen, nitrogen and a particular reducing gas entered the stainless steel sample chamber via polyurethane or stainless steel tubing, as controlled by the Aalborg MFCs shown. While two of the MFCs were dedicated to nitrogen or oxygen throughout a given test, the third was used to control the flow rate of either pure nitrogen or the 1000 ppm reducing gas, depending on the phase of the experiment; the valves were used to pass pure nitrogen through the MFC during the "off" phase of the test, and then switched to replace the nitrogen with the reducing gas during the "on" phase. By utilising the same three MFCs throughout a gas test, it was possible to ensure a constant total rate of gas flow through the system. When switching between pure nitrogen and the 1000 ppm reducing gas, accumulation of gas at the inlet of the previously closed valve could result in a transient pressure spike and briefly destabilise gas flow through the corresponding MFC. To minimise the effect of this pressure spike on the sample, gases were allowed to exit the system prior to the sample chamber through an "exhaust valve" installed at the outlet of the MFC, which was kept open until the MFC was perceived to be maintaining a stable flow of gas.

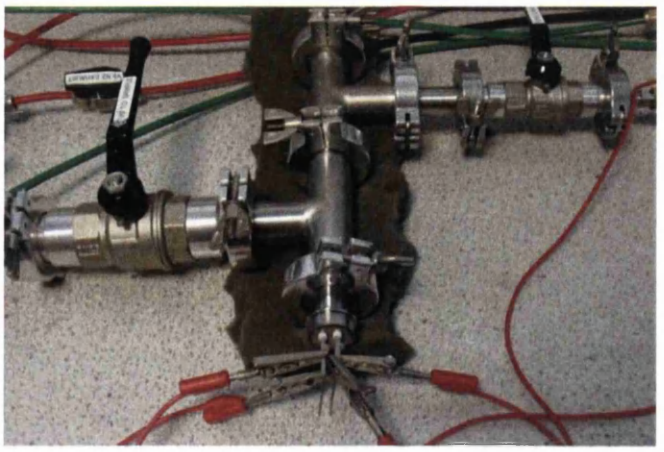

Fig. 3.19. A photograph of the custom-built "S"-shaped gas sensing chamber used in the present investigation. Gases entered through the black-handled valve at the left of the photograph (shown closed) and exited via a similar valve in the top-right of the picture. The sample, which was situated close to the second bend of the chamber at the top of the image, was connected to the external circuitry via the four contacts of the electrical feedthrough which appears at the bottom of the picture.

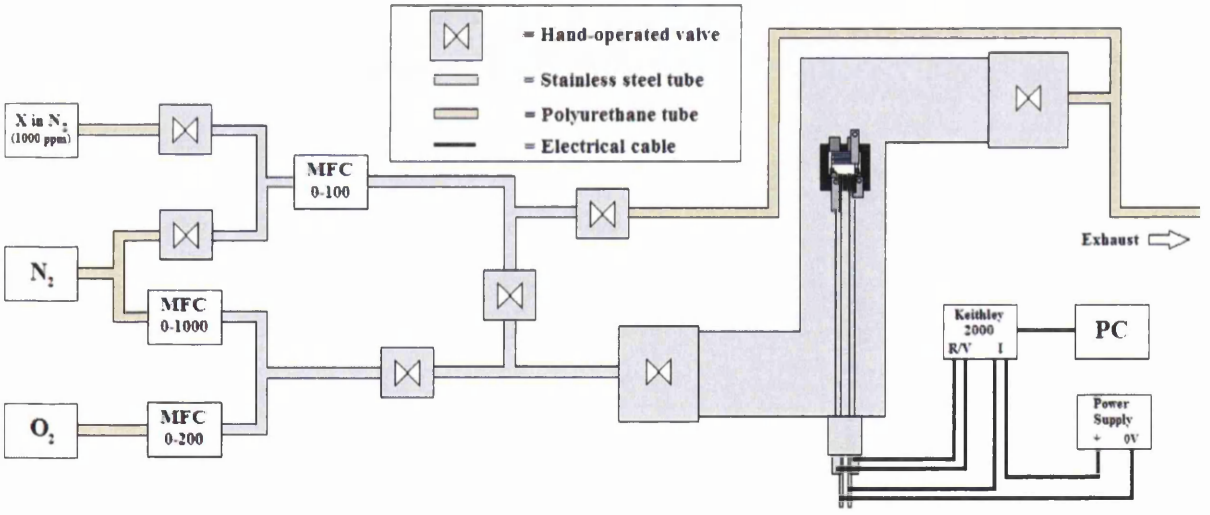

Fig. 3.20. A schematic of the overall gas sensing system, showing the positions of the gas bottles (N_2, O_2 and 1000 ppm of reducing gas X in N_2) and the tubing and valves connecting to the gas sensing chamber. The "I" ports of the Keithley 2000 multimeter were used to measure the current through the heating track of the sample, while the "R/V" ports were employed to measure either the resistance of the sensor (as shown) or the potential difference across the heating track (by connecting the wires across the two lower prongs of the electrical feedthrough). The values associated with each mass flow controller (MFC) denote the attainable range of flow rates in units of mL min^{-1}.

Within the sample chamber, a four-pronged stainless steel electrical feedthrough (manufactured by Lewvac) provided electrical connections to a custom-built slate sample holder, as pictured in Fig. 3.21 (a). A typical sample consisted of ZnO nanosheets deposited, as outlined previously, onto alumina-mounted inter-digitated contacts (purchased from the Electronics Design Centre at Case Western Reserve University in Cleveland, Ohio) with a spacing of 300 μm, as shown in Fig. 3.21 (b). The underside of the alumina-based support, henceforth to be referred to as a "gas sensing substrate", was patterned with a continuous platinum track which was used to electrically heat the sample, illustrated in Fig. 3.21 (c). Silver pads were present on both sides of the substrate to provide electrical contact between the platinum tracks and the substrate holder. To link the sample to the external circuitry via the electrical feedthrough, the sample holder connected each of the four prongs to a separate contact pad via stainless steel bolts and clips, all electrically insulated from one another by the slate mounting. The sample resistance was measured using a Keithley 2000 multimeter, and the heating current was provided by a standard adjustable 0–32 V, 0–3 A PID-controlled laboratory power supply.

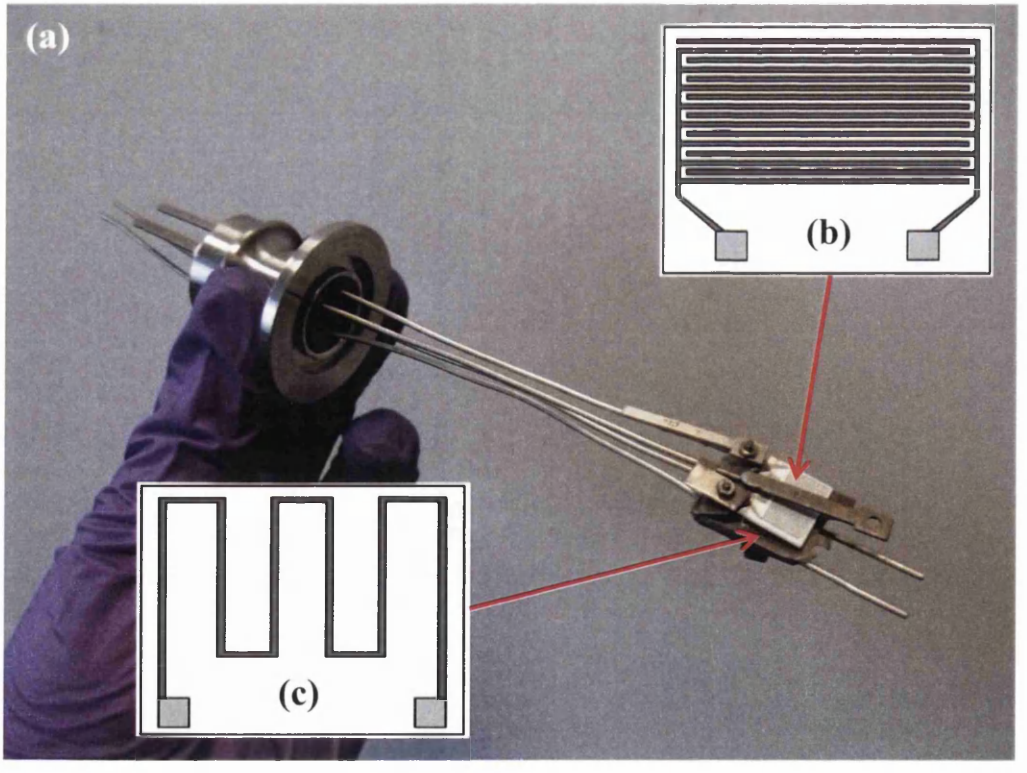

Fig. 3.21. A photograph showing a gas sensing substrate connected to the electrical feedthrough of the gas sensing chamber via a custom-built substrate holder (a), and diagrams depicting the topside (b) and underside (c) of the substrate.

As no thermocouple was connected to the sample during a gas test, it was not possible to directly measure its temperature. Instead, it was necessary to estimate the sample temperature from the measured resistance of the heating track, which required knowledge of the relationship between these two quantities. To this end, the temperature-dependence of the heating track resistance of each gas sensing substrate was measured outside the sample chamber prior to deposition of the ZnO nanosheets, using a thermocouple to measure the substrate temperature for a given applied potential difference. By measuring the current through the heating track using the Keithley 2000 multimeter, Ohm's Law could be used to plot the resistance as a function of temperature as demonstrated in Fig. 3.22. To minimise uncertainty in the measured quantities, both the applied potential difference and the current were measured continuously for approximately three minutes, and the temperature was recorded at regular intervals (typically every twenty seconds) during this period.

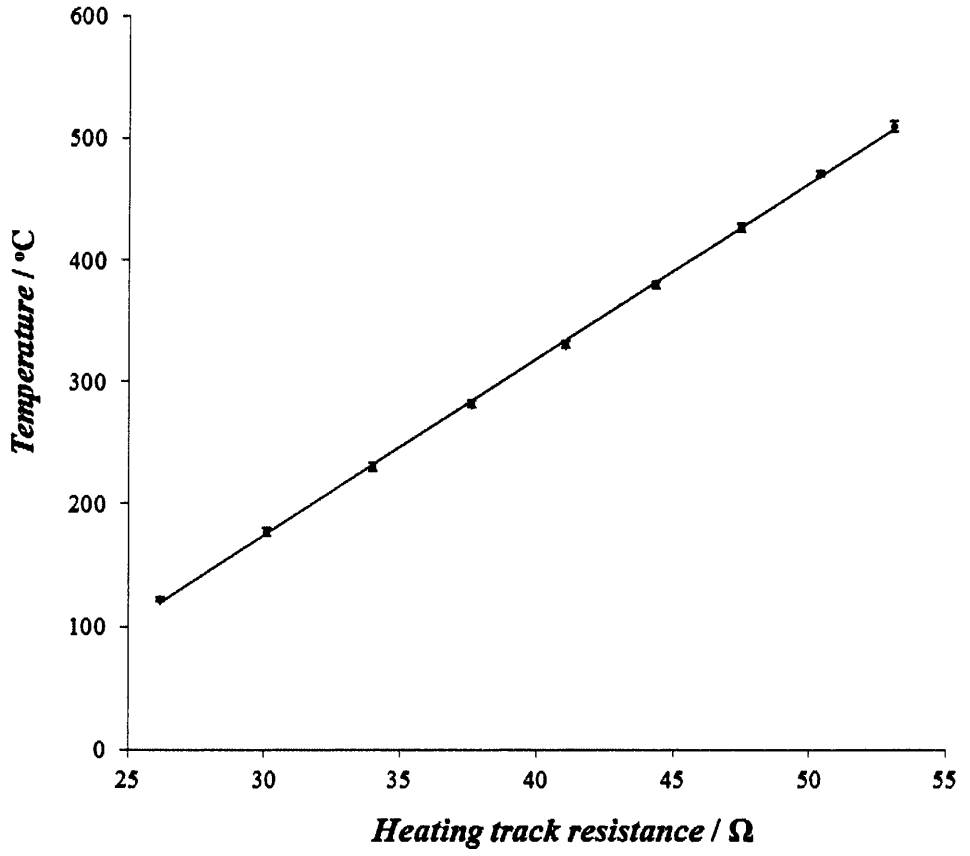

Fig. 3.22. A plot showing the resistance of a heating track as a function of temperature, which may be used as a calibration plot to calculate the temperature of the sensor from the heating track resistance during a gas sensing experiment.

In a typical gas sensing test, the sensor resistance was measured every two seconds over a period of thirty minutes, with the reducing gas introduced after one minute and turned off following a further fifteen minutes. Each data point was recorded over five cycles of the mains signal, thereby reducing the effect of any electrical current spikes which might arise during measurement. Fig. 3.23 shows a typical scan obtained by exposing ZnO nanosheets to carbon monoxide at a concentration of 200 ppm in dry air, at a temperature of approximately 400°C. The slight delay in the electrical response following the introduction of carbon monoxide may be attributed to the time required for the gas to flow from the valve to the sensor. The recovery of the sensor is similarly delayed due to the carbon monoxide taking a finite time to exit the sample chamber after this gas is turned-off.

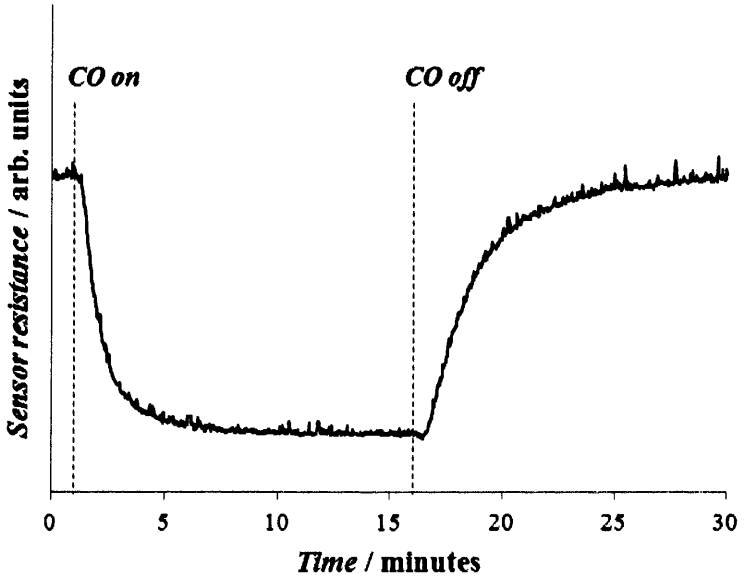

Fig. 3.23. A typical resistance scan obtained by exposing ZnO nanosheets to carbon monoxide at a concentration of 200 ppm in dry air, at a temperature of approximately 400°C. The times at which the carbon monoxide was turned on and off are indicated on the plot by dashed lines.

References

[1] A. Tarat, C.J. Nettle, D.T.J. Bryant, D.R. Jones, M.W. Penny, R.A. Brown, et al., Microwave-assisted synthesis of layered basic zinc acetate nanosheets and their thermal decomposition into nanocrystalline ZnO., Nanoscale Res. Lett. 9 (2014) 11. doi:10.1186/1556-276X-9-11.

[2] A. Tarat, R. Majithia, R.A. Brown, M.W. Penny, K.E. Meissner, Synthesis of nanocrystalline ZnO nanobelts via pyrolytic decomposition of zinc acetate nanobelts and their gas sensing behavior, Surf. Sci. 606 (2012) 715–721. doi:10.1016/j.susc.2011.12.010.

[3] S.K. Sivaraman, S. Kumar, V. Santhanam, Monodisperse sub-10 nm gold nanoparticles by reversing the order of addition in Turkevich method--the role of chloroauric acid., J. Colloid Interface Sci. 361 (2011) 543–7. doi:10.1016/j.jcis.2011.06.015.

[4] D. Luković Golić, G. Branković, M. Počuča Nešić, K. Vojisavljević, A. Rečnik, N. Daneu, et al., Structural characterization of self-assembled ZnO nanoparticles obtained by the sol-gel method from Zn(CH(3)COO)(2)·2H(2)O., Nanotechnology. 22 (2011) 395603. doi:10.1088/0957-4484/22/39/395603.

[5] E. Kandare, J.M. Hossenlopp, Thermal degradation of acetate-intercalated hydroxy double and layered hydroxy salts, Inorg. Chem. 45 (2006) 3766–3773. doi:10.1021/ic060071k.

[6] L. Poul, N. Jouini, F. Fievet, Layered hydroxide metal acetates (metal = zinc, cobalt, and nickel): Elaboration via hydrolysis in polyol medium and comparative study, Chem. Mater. 12 (2000) 3123–3132. doi:10.1021/cm991179j.

[7] T. Biswick, W. Jones, A. Pacuła, E. Serwicka, J. Podobinski, Evidence for the formation of anhydrous zinc acetate and acetic anhydride during the thermal degradation of zinc hydroxy acetate, Zn5(OH)8(CH3CO2)2·4H2O to ZnO, Solid State Sci. 11 (2009) 330–335. doi:10.1016/j.solidstatesciences.2008.06.018.

[8] C. Gu, J. Huang, Y. Wu, M. Zhai, Y. Sun, J. Liu, Preparation of porous flower-like ZnO nanostructures and their gas-sensing property, J. Alloys Compd. 509 (2011) 4499–4504. doi:10.1016/j.jallcom.2010.11.078.

[9] F. Rouquerol, J. Rouquerol, K.S.W. Sing, P. Llewellyn, G. Maurin, Adsorption by powders and porous solids: principles, methodology and applications, Academic Press, Oxford, 2013.

[10] R.I. Masel, Principles of Adsorption and Reaction on Solid Surfaces, Wiley, Hoboken, 1996.

[11] M. Thommes, Physical adsorption characterization of nanoporous materials, Chemie-Ingenieur-Technik. 82 (2010) 1059–1073. doi:10.1002/cite.201000064.

[12] S. Lowell, J.E. Shields, M.A. Thomas, M. Thommes, Characterization of Porous Solids and Powders: Surface Area, Pore Size and Density, Kluwer Academic Publishers, Dordrecht, 2004.

[13] S. Brunauer, P.H. Emmett, E. Teller, Adsorption of Gases in Multimolecular Layers, J. Am. Chem. Soc. 60 (1938) 309–319. doi:citeulike-article-id:4074706.

[14] W. Zhou, R.P. Apkarian, Z.L. Wang, Fundamentals of Scanning Electron Microscopy, in: W. Zhou, Z.L. Wang (Eds.), Scanning Microsc. Nanotechnol. Tech. Appl., Springer, New York, 2006: pp. 1–40.

[15] M.A. Furman, M.T.F. Pivi, Probabilistic model for the simulation of secondary electron emission, Phys. Rev. Spec. Top. - Accel. Beams. 5 (2002) 82–99. doi:10.1103/PhysRevSTAB.5.124404.

[16] J. Goldstein, D.E. Newbury, P. Echlin, D.C. Joy, A.D. Romig, C.E. Lyman, et al., Scanning Electron Microscopy and X-Ray Mictoanalysis: A Text for Biologists, Materials Scientists, and Geologists, Plenum Press, New York, 1992.

[17] Z. Insepov, V. Ivanov, H. Frisch, Comparison of candidate secondary electron emission materials, Nucl. Instruments Methods Phys. Res. B. 268 (2010) 3315–3320. doi:10.1016/j.nimb.2010.08.002.

[18] Z. Insepov, V. Ivanov, S.J. Jokela, I. Veryovkin, A. Zinovev, H. Frisch, Comparison of secondary electron emission simulation to experiment, Nucl. Instruments Methods Phys. Res. A. 639 (2011) 155–157. doi:10.1016/j.nima.2010.10.048.

[19] K. Kanaya, S. Ono, F. Ishigaki, Secondary electron emission from insulators, J. Phys. D. Appl. Phys. 11 (2001) 2425–2437. doi:10.1088/0022-3727/11/17/015.

[20] D. Brandon, W.D. Kaplan, Microstructural Characterization of Materials, Wiley, Hoboken, 2008.

[21] D. Briggs, Surface Analysis of Polymers by XPS and Static SIMS, Cambridge University Press, Cambridge, 1998.

[22] S. Hofmann, Auger- and X-Ray Photoelectron Spectroscopy in Materials Science: A User-Oriented Guide, Springer, New York, 2013.

[23] J.B. Metson, Charge compensation and binding energy referencing in XPS analysis, Surf. Interface Anal. 27 (1999) 1069–1072. doi:10.1002/(SICI)1096-9918(199912)27:12<1069::AID-SIA677>3.0.CO;2-A.

[24] B. Hu, L. Yu, G. Wang, S. Hutton, H. Huang, Z. Du, Exploration of transmission efficiency and quantitative measurement of the Axis Ultra electron spectrometer, Meas. J. Int. Meas. Confed. 43 (2010) 1299–1304. doi:10.1016/j.measurement.2010.07.007.

[25] A. Klein, T. Mayer, A. Thissen, W. Jaegermann, Photoelectron Spectroscopy in Materials Science and Physical Chemistry : Analysis of Composition, Chemical

Bonding and Electronic Structure of Surfaces and Interfaces, Bunsen- Mag. (2008) 124–139.

[26] J. Cazaux, About the charge compensation of insulating samples in XPS, J. Electron Spectros. Relat. Phenomena. 113 (2000) 15–33. doi:10.1016/S0368-2048(00)00190-0.

[27] J. Cazaux, Secondary electron emission and fundamentals of charging mechanisms in XPS, J. Electron Spectros. Relat. Phenomena. 178-179 (2010) 357–372. doi:10.1016/j.elspec.2009.03.007.

[28] D.R. Baer, M.H. Engelhard, D.J. Gaspar, a. S. Lea, C.F. Windisch, Use and limitations of electron flood gun control of surface potential during XPS: Two non-homogeneous sample types, Surf. Interface Anal. 33 (2002) 781–790. doi:10.1002/sia.1454.

[29] B.J. Tielsch, J.E. Fulghum, Differential charging in XPS. Part I: demonstration of lateral charging in a bulk insulator using imaging XPS, Surf. Interface Anal. 24 (1996) 422–427. doi:10.1002/(SICI)1096-9918(199606)24:6<422::AID-SIA142>3.0.CO;2-G.

[30] P.M.A. Sherwood, Auger and X-ray Photoelectron Spectroscopy, in: D. Briggs, M.C. Seah (Eds.), Pract. Surf. Anal., Wiley, Hoboken, 1990: pp. 555–586.

[31] S. Tanuma, C.J. Powell, D.R. Penn, Calculations of electron inelasticmean freepaths. IX. Data for 41 elemental solids over the 50 eV to 30 keV range, Surf. Interface Anal. 43 (2011) 689–713. doi:10.1016/j.nimb.2011.09.016.

[32] S. Tanuma, C.J. Powell, D.R. Penn, Calculations of electron inelastic mean free paths. VIII. Data for 15 elemental solids over the 50-2000 eV range, Surf. Interface Anal. 37 (2005) 1–14. doi:10.1002/sia.1997.

[33] C.J. Powell, A. Jablonski, Evaluation of Calculated and Measure Electron Inelastic Mean Free Paths Near Solid Surfaces, J. Phys. Chem. Ref. Data. 28 (1999) 19–62. doi:10.1063/1.556035.

[34] C.J. Powell, A. Jablonski, Evaluation of electron inelastic mean free paths for selected elements and compounds, Surf. Interface Anal. 29 (2000) 108–114. doi:10.1002/(SICI)1096-9918(200002)29:2<108::AID-SIA700>3.0.CO;2-4.

[35] S. Tanuma, C.J. Powell, D.R. Penn, Calculations of electron inelastic mean free paths. VIII. Data for 15 elemental solids over the 50-2000 eV range, Surf. Interface Anal. 17 (1991) 927–939. doi:10.1002/sia.1997.

[36] S. Tanuma, C.J. Powell, D.R. Penn, Calculation of electron inelastic mean free paths (IMFPs) VII. Reliability of the TPP-2M IMFP predictive equation, Surf. Interface Anal. 35 (2003) 268–275. doi:10.1002/sia.1526.

[37] S. Tanuma, C. Powell, D. Penn, Calculations of electron inelastic mean free paths (IMFPS). IV. Evaluation of calculated IMFPs and of the predictive IMFP formula TPP-• 2 for electron energies between, Surf. Interface Anal. 20 (1993) 77–89. doi:10.1002/sia.740200112.

[38] C.-H. Min, S. Cho, S.-H. Lee, D.-Y. Cho, W.G. Park, J.G. Chung, et al., Effect of oxygen partial pressure on the Fermi level of ZnO(1-x) films fabricated by pulsed laser deposition, Appl. Phys. Lett. 96 (2010) 201907. doi:10.1063/1.3432398.

[39] M.W. Allen, C.H. Swartz, T.H. Myers, T.D. Veal, C.F. McConville, S.M. Durbin, Bulk transport measurements in ZnO: The effect of surface electron layers, Phys. Rev. B - Condens. Matter Mater. Phys. 81 (2010) 1–6. doi:10.1103/PhysRevB.81.075211.

[40] E.T. Yu, E.T. Croke, D.H. Chow, D.A. Collins, M.C. Phillips, T.C. McGill, et al., Measurement of the valence band offset in novel heterojunction systems: Si/Ge (100) and AlSb/ZnTe (100), J. Vac. Sci. Technol. B Microelectron. Nanom. Struct. 8 (1990) 908–915. doi:10.1116/1.584941.

[41] H.Y. Yu, X.D. Feng, D. Grozea, Z.H. Lu, R.N.S. Sodhi, a. M. Hor, et al., Surface electronic structure of plasma-treated indium tin oxides, Appl. Phys. Lett. 78 (2001) 2595–2597. doi:10.1063/1.1367897.

[42] B.J. Coppa, C.C. Fulton, P.J. Hartlieb, R.F. Davis, B.J. Rodriguez, B.J. Shields, et al., In situ cleaning and characterization of oxygen- and zinc-terminated, n-type, ZnO{0001} surfaces, J. Appl. Phys. 95 (2004) 5856–5864. doi:10.1063/1.1695596.

[43] A. Klein, C. Körber, A. Wachau, F. Säuberlich, Y. Gassenbauer, S.P. Harvey, et al., Transparent Conducting Oxides for Photovoltaics: Manipulation of Fermi Level, Work Function and Energy Band Alignment, Materials (Basel). 3 (2010) 4892–4914. doi:10.3390/ma3114892.

[44] C.Y. Chen, J.R.D. Retamal, I.W. Wu, D.H. Lien, M.W. Chen, Y. Ding, et al., Probing surface band bending of surface-engineered metal oxide nanowires, ACS Nano. 6 (2012) 9366–9372. doi:10.1021/nn205097e.

[45] D. Cahen, A. Kahn, Electron energetics at surfaces and interfaces: Concepts and experiments, Adv. Mater. 15 (2003) 271–277. doi:10.1002/adma.200390065.

[46] P. Blumentrit, M. Yoshitake, S. Nemšák, T. Kim, T. Nagata, XPS and UPS study on band alignment at Pt-Zn-terminated ZnO(0 0 0 1) interface, Appl. Surf. Sci. 258 (2011) 780–785. doi:10.1016/j.apsusc.2011.08.095.

[47] T. Kim, M. Yoshitake, S. Yagyu, S. Nemsak, T. Nagata, T. Chikyow, XPS study on band alignment at Pt-O-terminated ZnO(000$\bar{1}$) interface, Surf. Interface Anal. 42 (2010) 1528–1531. doi:10.1002/sia.3601.

[48] S. Perkowitz, Optical Characterization of Semiconductors: Infrared, Raman and Photoluminescence Spectroscopy, Academic Press, San Diego, 1993.

[49] T.H. Gfroerer, Photoluminescence in Analysis of Surfaces and Interfaces, in: R.A. Meyers (Ed.), Encycl. Anal. Chem., Wiley, Chichester, 2000: pp. 9209–9231. doi:10.1002/9780470027318.a2510.

[50] V.A. Fonoberov, K.A. Alim, A.A. Balandin, F. Xiu, J. Liu, Photoluminescence investigation of the carrier recombination processes in ZnO quantum dots and

nanocrystals, Phys. Rev. B - Condens. Matter Mater. Phys. 73 (2006) 165317. doi:10.1103/PhysRevB.73.165317.

[51] V.A. Fonoberov, A.A. Balandin, Origin of ultraviolet photoluminescence in ZnO quantum dots: Confined excitons versus surface-bound impurity exciton complexes, Appl. Phys. Lett. 85 (2004) 5971–5973. doi:10.1063/1.1835992.

[52] A. Teke, Ü. Özgür, S. Doğan, X. Gu, H. Morkoç, B. Nemeth, et al., Excitonic fine structure and recombination dynamics in single-crystalline ZnO, Phys. Rev. B - Condens. Matter Mater. Phys. 70 (2004) 195207. doi:10.1103/PhysRevB.70.195207.

[53] B.K. Meyer, H. Alves, D.M. Hofmann, W. Kriegseis, D. Forster, F. Bertram, et al., Bound exciton and donor-acceptor pair recombinations in ZnO, Phys. Status Solidi Basic Res. 241 (2004) 231–260. doi:10.1002/pssb.200301962.

[54] C. Boemare, T. Monteiro, M.J. Soares, J.G. Guilherme, E. Alves, Photoluminescence studies in ZnO samples, Phys. B. 308-310 (2001) 985–988.

[55] H. Alves, D. Pfisterer, a. Zeuner, T. Riemann, J. Christen, D.M. Hofmann, et al., Optical investigations on excitons bound to impurities and dislocations in ZnO, Opt. Mater. (Amst). 23 (2003) 33–37. doi:10.1016/S0925-3467(03)00055-7.

[56] D. Reynolds, D. Look, B. Jogai, C. Litton, T. Collins, W. Harsch, et al., Neutral-donor–bound-exciton complexes in ZnO crystals, Phys. Rev. B. 57 (1998) 12151–12155. doi:10.1103/PhysRevB.57.12151.

[57] K. Thonke, T. Gruber, N. Teofilov, R. Schönfelder, a. Waag, R. Sauer, Donor-acceptor pair transitions in ZnO substrate material, Phys. B Condens. Matter. 308-310 (2001) 945–948. doi:10.1016/S0921-4526(01)00877-8.

[58] B.K. Meyer, J. Sann, D.M. Hofmann, C. Neumann, a Zeuner, Shallow donors and acceptors in ZnO, Semicond. Sci. Technol. 20 (2005) S62–S66. doi:10.1088/0268-1242/20/4/008.

[59] B.K. Meyer, J. Sann, S. Lautenschläger, M.R. Wagner, a. Hoffmann, Ionized and neutral donor-bound excitons in ZnO, Phys. Rev. B - Condens. Matter Mater. Phys. 76 (2007) 8–11. doi:10.1103/PhysRevB.76.184120.

[60] A.B. Djurišić, Y.H. Leung, Optical Properties of ZnO Nanostructures, Small. 2 (2006) 944–961. doi:10.1002/smll.200600134.

[61] D.C. Reynolds, D.C. Look, B. Jogai, C. Litton, G. Cantwell, W. Harsch, Valence-band ordering in ZnO, Phys. Rev. B. 60 (1999) 2340–2344. doi:10.1103/PhysRevB.60.2340.

[62] A. Janotti, C.G. Van De Walle, New insights into the role of native point defects in ZnO, J. Cryst. Growth. 287 (2006) 58–65. doi:10.1016/j.jcrysgro.2005.10.043.

[63] F. Hai-Bo, Y. Shao-Yan, Z. Pan-Feng, W. Hong-Yuan, L. Xiang-Lin, J. Chun-Mei, et al., Investigation of Oxygen Vacancy and Interstitial Oxygen Defects in ZnO Films by

Photoluminescence and X-Ray Photoelectron Spectroscopy, Chinese Phys. Lett. 24 (2007) 2108–2111. doi:10.1088/0256-307X/24/7/089.

[64] L.E. Greene, M. Law, J. Goldberger, F. Kim, J.C. Johnson, Y. Zhang, et al., Low-temperature wafer-scale production of ZnO nanowire arrays, Angew. Chemie - Int. Ed. 42 (2003) 3031–3034. doi:10.1002/anie.200351461.

[65] M. Liu, A.H. Kitai, P. Mascher, Point defects and luminescence centres in zinc oxide and zinc oxide doped with manganese, J. Lumin. 54 (1992) 35–42. doi:10.1016/0022-2313(92)90047-D.

[66] X.L. Wu, G.G. Siu, C.L. Fu, H.C. Ong, Photouminescence and cathodoluminescence studies of stoichiometric and oxygen-deficient ZnO films, Appl. Phys. Lett. 78 (2001) 2285–2287. doi:10.1063/1.1361288.

[67] B. Lin, Z. Fu, Y. Jia, Green luminescent center in undoped zinc oxide films deposited on silicon substrates, Appl. Phys. Lett. 79 (2001) 943–945. doi:10.1063/1.1394173.

[68] Z.G. Wang, X.T. Zu, S. Zhu, L.M. Wang, Green luminescence originates from surface defects in ZnO nanoparticles, Phys. E Low-Dimensional Syst. Nanostructures. 35 (2006) 199–202. doi:10.1016/j.physe.2006.07.022.

[69] D.F. Wang, T.J. Zhang, Study on the defects of ZnO nanowire, Solid State Commun. 149 (2009) 1947–1949. doi:10.1016/j.ssc.2009.07.038.

[70] B. Ha, H. Ham, C.J. Lee, Photoluminescence of ZnO nanowires dependent on O2 and Ar annealing, J. Phys. Chem. Solids. 69 (2008) 2453–2456. doi:10.1016/j.jpcs.2008.04.041.

[71] P.S. Xu, Y.M. Sun, C.S. Shi, F.Q. Xu, H.B. Pan, The electronic structure and spectral properties of ZnO and its defects, Nucl. Instruments Methods Phys. Res. Sect. B. 199 (2003) 286–290. doi:10.1016/S0168-583X(02)01425-8.

[72] S. a M. Lima, F. a. Sigoli, M. Jafelicci, M.R. Davolos, Luminescent properties and lattice defects correlation on zinc oxide, Int. J. Inorg. Mater. 3 (2001) 749–754. doi:10.1016/S1466-6049(01)00055-1.

[73] A. Janotti, C.G. Van De Walle, Oxygen vacancies in ZnO, Appl. Phys. Lett. 87 (2005) 1–3. doi:10.1063/1.2053360.

[74] M.D. McCluskey, S.J. Jokela, Defects in ZnO, J. Appl. Phys. 106 (2009) 0–13. doi:10.1063/1.3216464.

Chapter 4 – Characterising the surface properties of LBZA and ZnO nanosheets

4.1. Introduction

In Chapter 2 it was remarked that the commercial suitability of ZnO nanostructures is often limited by their low growth rate, which necessitates a growth time of several hours in many wet-chemical synthesis procedures. By contrast, microwave-based techniques are inherently rapid and are typically able to produce a high yield of nanostructures in just a few minutes, thereby enhancing the viability of the materials. It is for this reason that the present investigation employs a microwave-based procedure to procure an aqueous suspension of layered basic zinc acetate (LBZA) nanosheets which, following deposition, may be thermally decomposed to ZnO. In this chapter, the chemical properties of the decomposition process are explored via thermogravimetric analysis (TGA), and physical characterisation of the resulting ZnO nanosheets is achieved using Brunauer, Emmett and Teller analysis (BET), scanning electron microscopy (SEM) and X-ray photoelectron spectroscopy (XPS). To investigate the optical defects in the material, the photoluminescence (PL) properties of the nanosheets are examined at different stages of decomposition.

4.2. Experimental methods

4.2.1. Sample preparation

A suspension of LBZA nanosheets was obtained using the microwaving procedure detailed in the previous chapter, and was subsequently centrifuged into deionised water. Following the final centrifugation stage, the residue of LBZA nanosheets was dried on a hot-plate at 60°C and ground into a powder. Samples of the powder were then packed into an alumina crucible and annealed in a tube furnace at different temperatures, passing a 900 mL min^{-1}

flow of dry air through the furnace and annealing at the requisite temperature for thirty minutes. For the SEM analysis and spectroscopic studies, the cleaned LBZA nanosheet suspension was drop-cast onto silicon either annealed alongside the powder samples or heated on a hot-plate as required.

4.2.2. Thermogravimetric analysis (TGA)

To investigate the thermal decomposition of the LBZA nanosheets, a 38.8 mg sample of the LBZA nanosheet powder was analysed using a Perkin Elmer STA (Simultaneous Thermal Analyser) 6000 instrument. In a nitrogen atmosphere, the powder was heated at a rate of 5°C min^{-1} up to 450°C, allowing the mass of the sample to be measured as a function of temperature.

4.2.3. Scanning electron microscopy (SEM)

During the thermal decomposition process, the conversion of LBZA to ZnO results in the formation of distinct nanoparticles within each nanosheet. To measure the distribution of nanoparticle sizes, the ZnO nanosheet samples were examined using a Hitachi S4800 field emission scanning electron microscope at an accelerating voltage of 5 kV. Three locations were inspected on each sample, ensuring that a total of at least fifty independent nanoparticle measurements were obtained for every annealing temperature.

4.2.4. Brunauer, Emmett and Teller (BET) analysis

The specific surface area of each powder sample was measured using a Quantachrome Nova 2000e gas sorption system, via BET analysis. The nitrogen adsorption and desorption characteristics were measured for powders annealed at 400°C, 600°C and 800°C, as well as the untreated LBZA powder. After measuring the volume of nitrogen adsorbed as a function of the relative pressure, P/P_0 (as defined in Chapter 3), the BET model was applied to data obtained between relative pressures of 0.15 and 0.3.

4.2.5. X-ray photoelectron spectroscopy (XPS)

The surface composition of the nanosheets was investigated using a Kratos AXIS Supra X-ray photoelectron spectroscopic analyser. By exposing the samples to monochromated X-rays of energy 1486.6 eV from an aluminium source, the O(1s), C(2p) and Zn(2p) core-level peaks were measured using a step-size of 50 meV and a pass energy of 20 eV. The resulting XPS spectra were analysed using the CasaXPS program.

4.2.6. Photoluminescence (PL) spectroscopy

To further explore the variation of the LBZA nanosheet structure during thermal decomposition, a sample of LBZA nanosheets on silicon was heated stepwise on a hot-plate at temperatures up to approximately 270°C, maintaining each temperature for a period of ten minutes. The temperature was measured accurately using a K-type thermocouple. After each temperature step, three points on the sample were illuminated in turn by a 325 nm Melles-Griot He-Cd laser at an incident power density of ~2.3×10^6 mW m^{-2}. The electromagnetic spectrum from each point was recorded using an Ocean Optics USB 2000+ spectrometer, measuring over a wavelength range of 350–850 nm. To ensure that any spectral variations between successive heating steps were the result of the increased temperature rather than the additional heating time, four similar samples were each heated for ten minutes at a single temperature in the range 130-290°C. The PL spectra of the furnace-annealed samples, which were heated to temperatures between 400°C and 800°C, were measured in an identical manner, again measuring the spectrum at three different locations on each sample.

4.3. Results and discussions

4.3.1. The variation of nanosheet mass as a function of temperature

As LBZA nanosheets are annealed, the material thermally decomposes to ZnO. To identify the intermediate transitions during this process, one may employ thermogravimetric analysis, wherein the mass of a powdered sample is measured continuously as its temperature is gradually increased. Fig. 4.1 shows the mass variation of an LBZA powder as a function of temperature, which was increased at a rate of 5°C min^{-1}. If one assumes that the starting material is LBZA containing two intercalated water molecules for every five Zn^{2+} ions [1–7], the initial decrease in mass at temperatures below 110°C may be attributed to the liberation of this water.

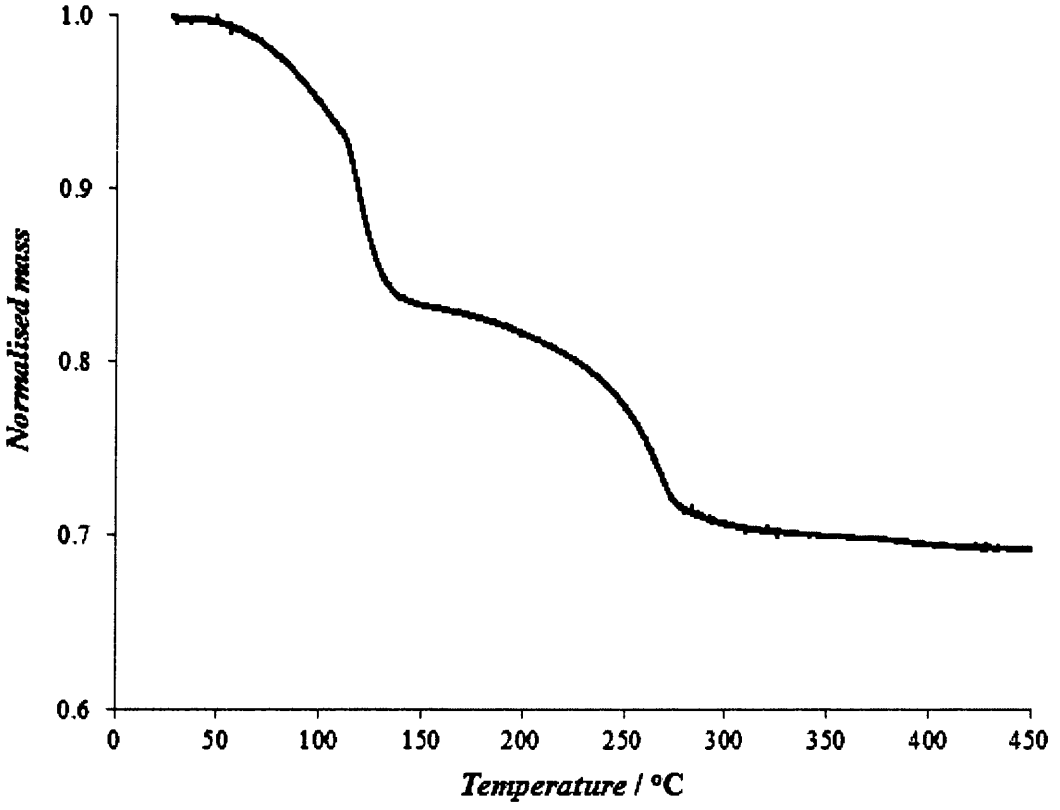

Fig. 4.1. A plot showing how the mass of an LBZA nanosheet powder varies as a function of temperature. To assist analysis, the mass is normalised with respect to the starting value.

Following the removal of the intercalated water, the mass of the powder diminished more rapidly as the temperature was ramped to 140°C, decreasing to approximately 84% of the starting value. This stage of the decomposition process corresponds to the reaction of hydroxide ions within the structure, which proceeds according to the equation [7–11]

$$Zn_5(CH_3CO_2)_2(OH)_8 \rightarrow Zn_5(CH_3CO_2)_2(OH)_{8-2x}O_x + xH_2O \qquad (4.1)$$

where x is any positive number, integer or otherwise, between zero and four. If the hydroxide ions were to react to completion, the overall reaction could be written as

$$Zn_5(CH_3CO_2)_2(OH)_8 \rightarrow Zn_5(CH_3CO_2)_2O_4 + 4H_2O \qquad (4.2)$$

However, complete removal of the hydroxide ions would result in the mass dropping to approximately 82.5% of its original value, which is marginally lower than the measured mass at this temperature. It is therefore likely that while the majority of the hydroxide ions are removed as the temperature is raised to 140°C, a small proportion remain in the structure.

Following the removal of the hydroxide ions, the chemical formula more closely resembles ZnO, the expected final product. Increasing the temperature to 270°C resulted in the mass decreasing to 72% of the starting value, which may be ascribed to the decomposition of the acetate groups to form molecules of water and carbon dioxide. It is important to note, however, that complete conversion to ZnO would lead to the mass decreasing to approximately 66% of the starting value, indicating that a significant proportion of the acetate ions are yet to decompose at this temperature. Indeed, if the hydroxide ions are completely reacted as in Eq. (4.2), the stoichiometry of the resulting compound suggests that further decomposition to ZnO is only possible if products other than water and carbon dioxide are produced. The complex nature of this decomposition stage is implied by the plot; as the temperature is raised above 270°C, the variation of mass as a function of temperature is much more gradual than at lower temperatures. Moreover, the mass of the final product was measured as approximately 69% of the starting value, which is around 3% higher than anticipated; this measurement suggests that the material differs significantly from pure ZnO, possibly containing residual carbon within its structure.

4.3.2. The relationship between surface area and annealing temperature

In addition to studying the thermal decomposition of the LBZA nanosheets, it is important to also consider how the resulting ZnO is affected when the annealing temperature is varied. To this end, SEM was employed to measure the distribution of nanoparticle sizes within the ZnO nanosheets following annealing at different temperatures. As indicated by the images in Fig. 4.2, the mean nanoparticle diameter increased significantly as the annealing temperature was increased, with the most marked change observed following an 800°C anneal. It is also evident that significant sintering occurred at temperatures of 700°C and above. A more quantitative analysis of the particle size is depicted in Fig. 4.3, which shows that the mean nanoparticle diameter increased from 18 nm at 400°C to 101 nm at 800°C. The uncertainty in the mean nanoparticle size at each temperature was determined from the standard deviation of at least fifty independent measurements taken from three different locations on the sample. An uncertainty of ±30°C has been assumed for each temperature, based on previous measurements of the temperature fluctuation within the tube furnace using a K-type thermocouple.

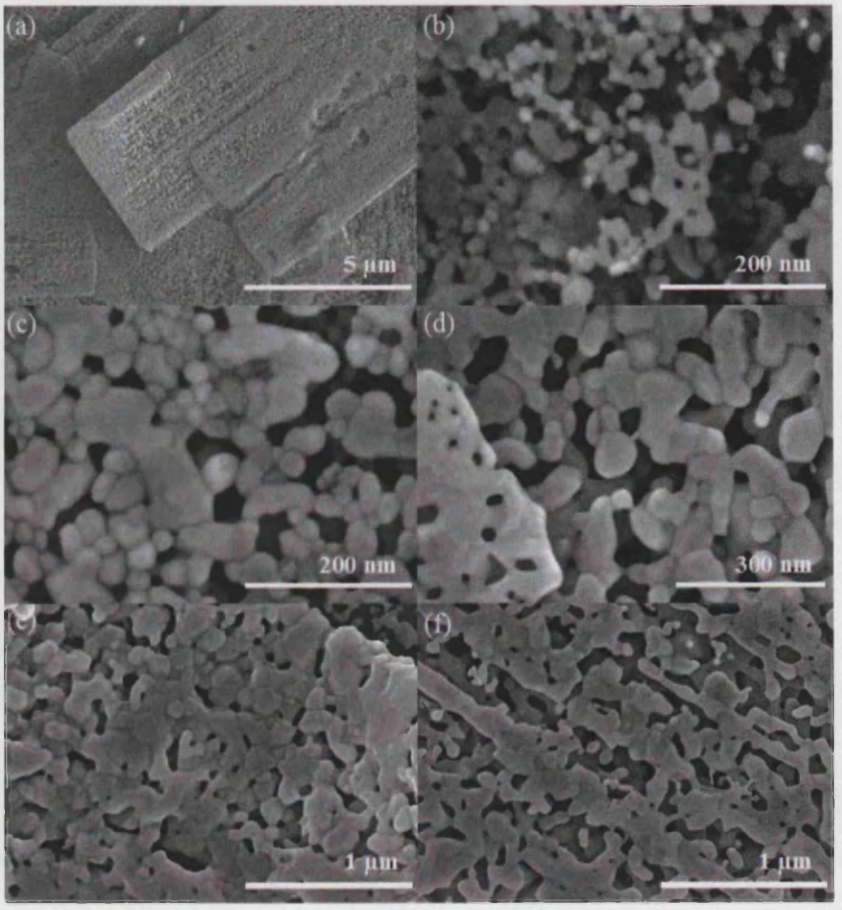

Fig. 4.2. SEM images displaying a typical ZnO nanosheet (a) and the observed topography of the nanosheet surface following annealing treatments at 400°C (b), 500°C (c), 600°C (d), 700°C (e) and 800°C (f).

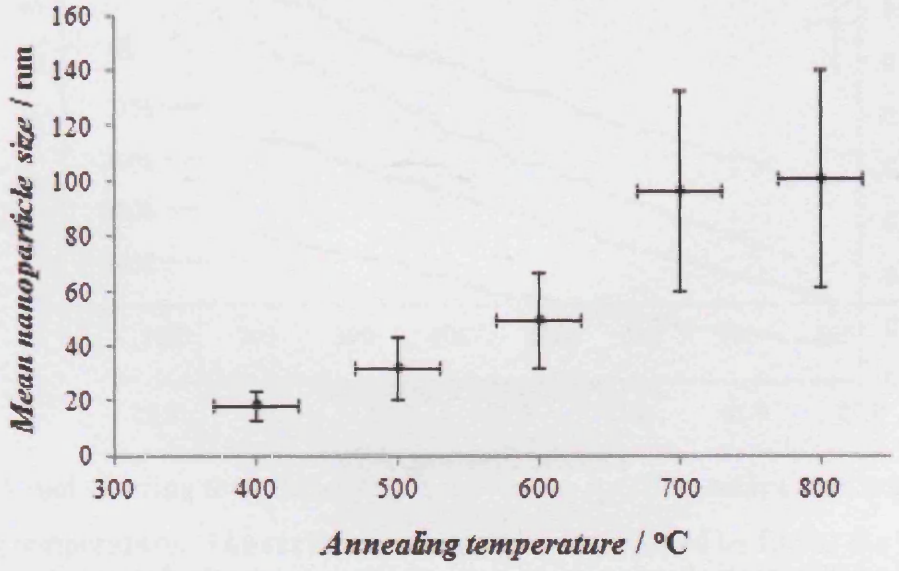

Fig. 4.3. A plot of the mean nanoparticle size as a function of the annealing temperature.

To supplement the SEM measurements, one may utilise BET analysis to determine the specific surface area of ZnO nanosheets following different annealing treatments. Fig. 4.4 depicts the measured volume of adsorbed nitrogen, per gram of powder, as a function of the normalised pressure, P/P_0 (where P and P_0 are the nitrogen pressure and atmospheric pressure, respectively), for differently annealed powders. Each curve was obtained by gradually increasing the pressure, and is therefore referred to as an "adsorption curve". The adsorption curves have been subsequently used to construct the BET plots displayed in Fig. 4.5, from which the specific surface area of each powder may be estimated as discussed in Chapter 3. For this calculation it is imperative that only the linear portion of each BET plot is used, and from Fig. 4.5 it is apparent that the required linearity exists for P/P_0 values between 0.15 and 0.3. The relationship between the specific surface area and annealing temperature is shown in Fig. 4.6. Upon annealing the LBZA powder there is a clear increase in the surface area per unit mass of material, which is likely due to the mass of each nanosheet decreasing by a factor of approximately one third during thermal decomposition to ZnO. The specific surface area of the material diminishes as the annealing temperature is elevated from 600°C to 800°C, plausibly due to the enlargement and sintering of nanoparticles observed previously. It is instructive to note that the calculated surface area values are similar to those of similar ZnO nanostructures reported elsewhere [6,12–16], which typically lie in the range 13–46 $m^2 g^{-1}$.

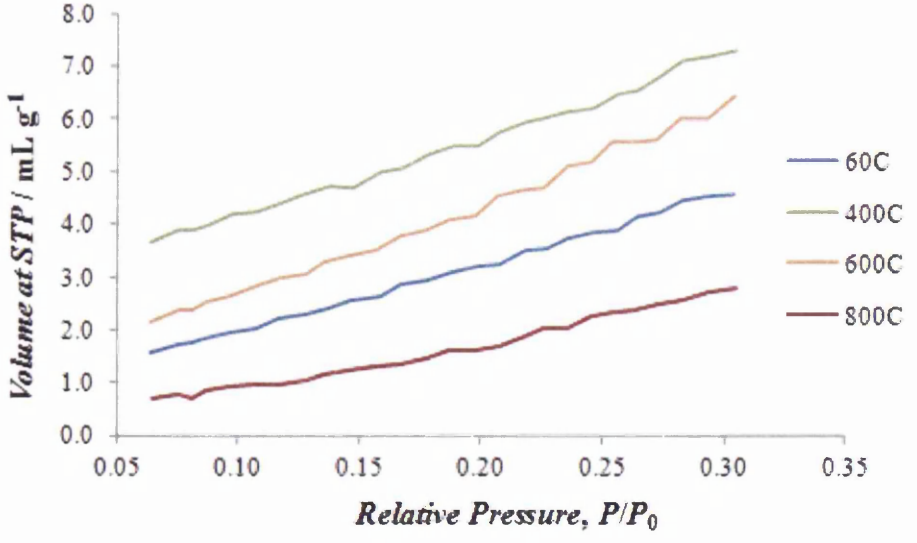

Fig. 4.4. Adsorption plots showing the volume of nitrogen adsorbed per unit mass of nanosheets as a function of increasing pressure, following annealing treatments at different temperatures. The system was maintained at a temperature of 77 K.

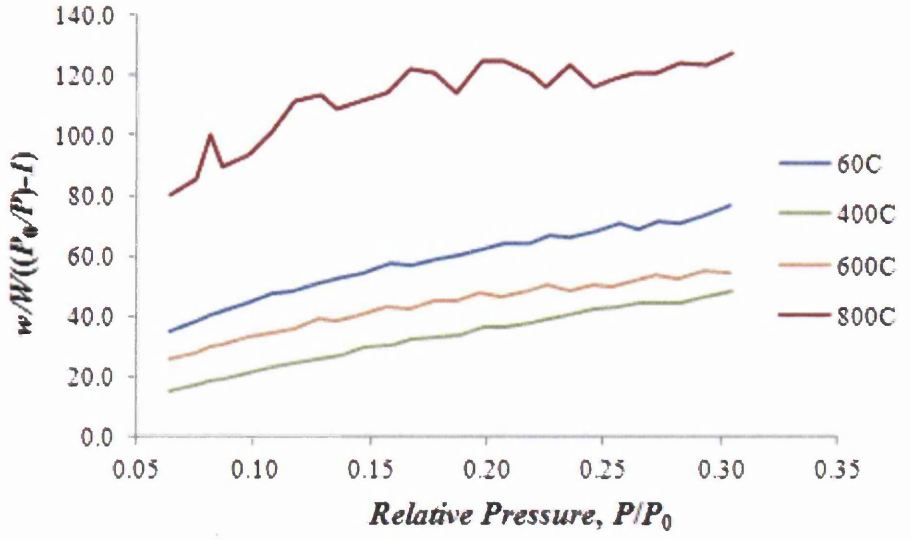

Fig. 4.5. BET plots obtained following annealing treatments at different temperatures, corresponding to the measurements shown in Fig. 4.4. The y-axis plots a unitless quantity that is related to the mass of adsorbed nitrogen, *W*, and the mass of sample powder, *w*.

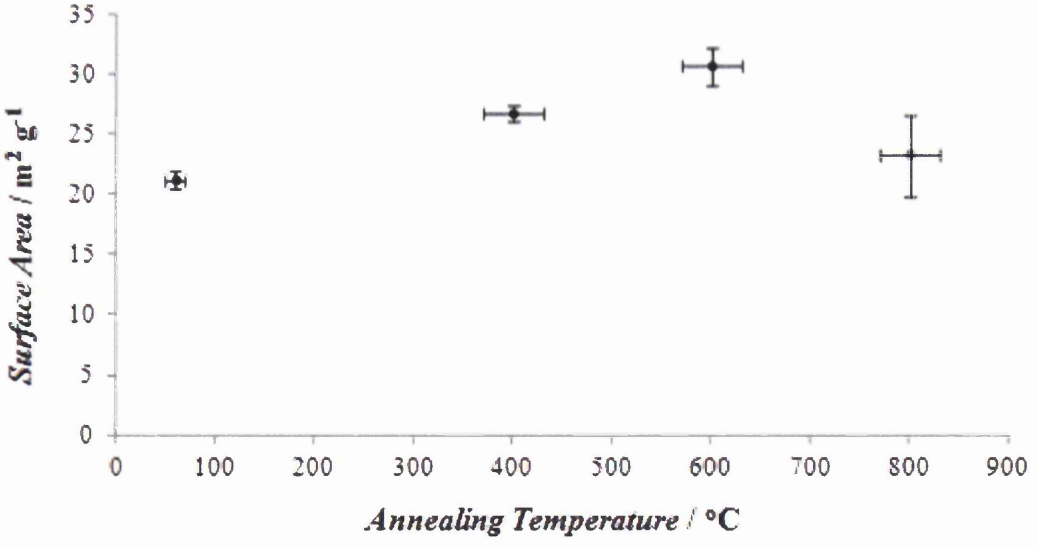

Fig. 4.6. A plot showing the relationship between the specific surface area and the annealing temperature. The surface area values are calculated by fitting the BET equation to the plots in Fig. 4.5, as detailed in Chapter 3.

4.3.3. Influence of annealing temperature on the surface chemistry

It has been demonstrated that the physical form of the nanosheets changes significantly as the annealing temperature is varied, but the effects on the internal structure of the ZnO has yet to be considered. By examining the samples using XPS, it is possible to determine how the atomic ratios of different elements are affected by the annealing temperature, in addition to deducing the presence of surface groups. In Fig. 4.7, the C 1s peaks of differently annealed samples are overlaid, in addition to spectra corresponding to untreated LBZA nanosheets. In each case, the measured count rate of electrons has been normalised with respect to the amplitude of the signal. It should be noted that the LBZA spectrum was acquired using the charge compensation facility of the XPS instrument to avoid electronic depletion of the sample; due to the electrically insulating nature of the material, the generation of photoelectrons leads to the sample acquiring a positive charge, which acts to increase the measured binding energy values and broaden the spectral peaks. By compensating for the charging effects, the XPS spectrum is shifted to lower values of binding energy and the peak broadening is suppressed.

To successfully correct the binding energies of the LBZA XPS spectrum, it is helpful to recognise that when a carbon atom is bonded to hydrogen or another atom of carbon, the corresponding C 1s signal typically appears at a binding energy in the vicinity of 285 eV [17–19]. When the carbon atom forms a σ-bond to an atom of oxygen, the binding energy of the C 1s peak is generally increased to around 287 eV [19–21], while a C-O double bond yields a C 1s signal at a binding energy of approximately 289 eV [17,19–22]. These characteristic C 1s binding energy values are witnessed across a wide range of dissimilar compounds, providing a general guide which may be used to adjust the measured binding energies of a charged sample accordingly. In the present example, the annealed ZnO nanosheet samples may indeed be deconstructed into the three anticipated components; as shown by Fig. 4.8, the primary contribution to each peak is centred at a binding energy of 285.1–285.2 eV, with smaller components appearing at energies of 286.7–286.8 eV and 289.0–289.3 eV. Each component has been fitted using a Gaussian-Lorentzian function, in accordance with common practice. As shown by the dashed black line in Fig. 4.7, the C 1s signal of the untreated LBZA nanosheets is centred at a much lower binding energy of 279.0 eV. To realise physical

binding energy values for the three components, it is necessary to translate the whole spectrum in a positive direction along the x-axis of Fig. 4.7, increasing the binding energy by approximately 6.1 eV. In this way, the C 1s signal may be deconstructed in a similar manner to before; following the adjustment, the peak contains three components centred at binding energies of 285.1 eV, 286.4 eV and 289.5 eV.

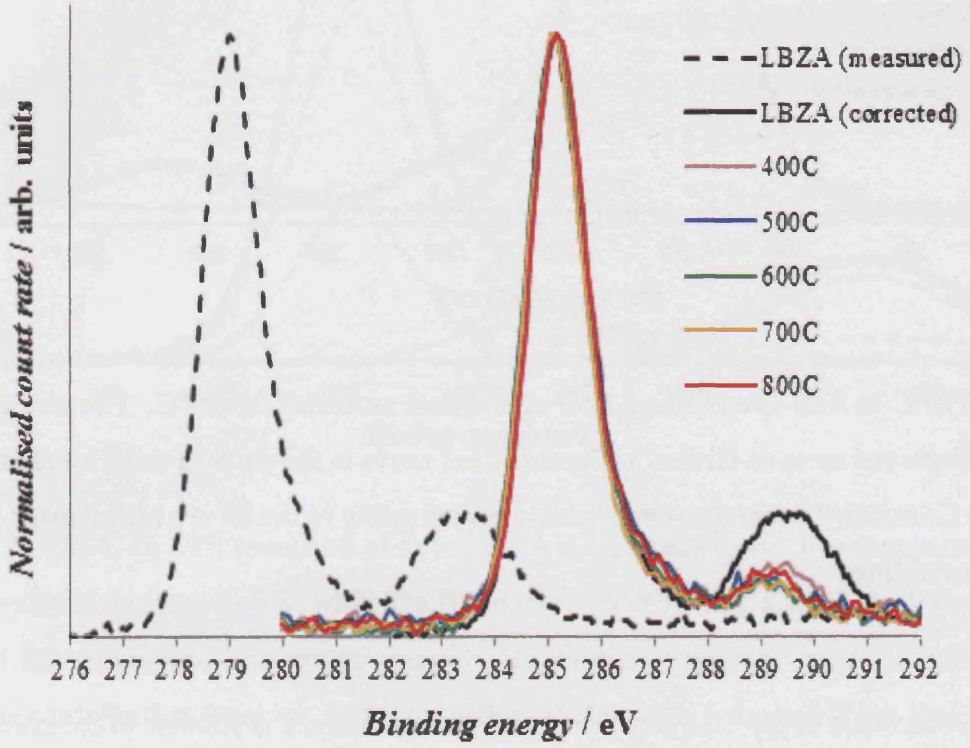

Fig. 4.7. XPS spectra showing the C 1s peaks of LBZA nanosheets annealed at different temperatures. Each spectrum is normalised with respect to the signal amplitude. The measured spectrum of the untreated sample, depicted by the dashed black line, was obtained using the charge compensation facility of the XPS instrument. The spectrum is corrected so that the primary maximum appears at the same binding energy as the main peaks of the other spectra, as shown by the solid black line.

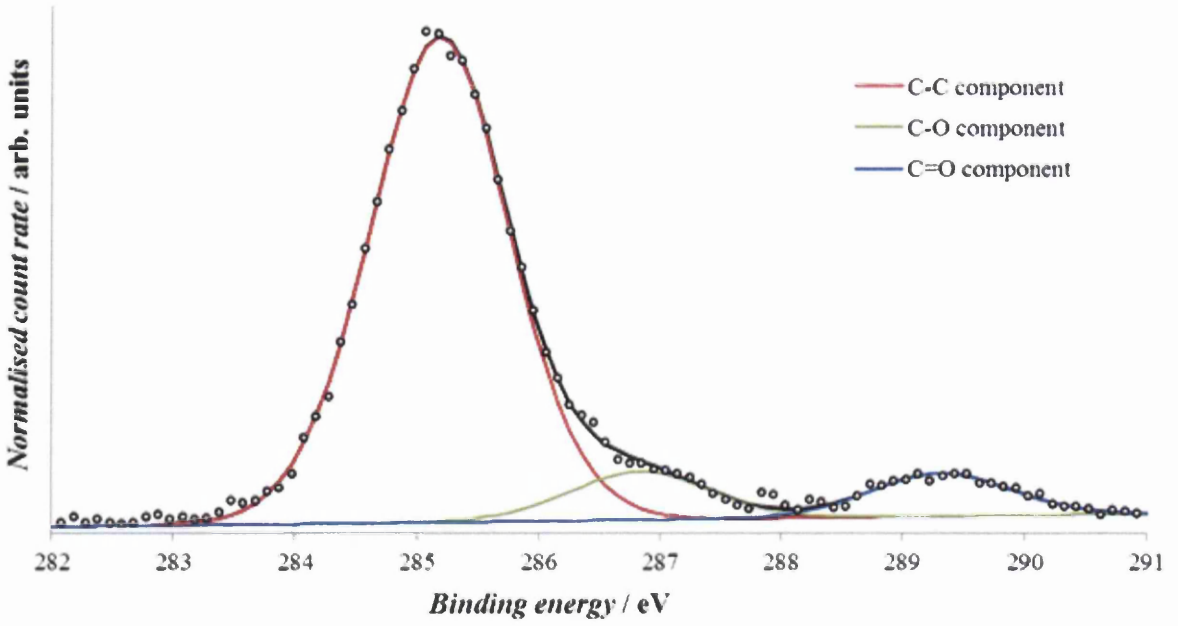

Fig. 4.8. The C 1s XPS spectrum of ZnO nanosheets annealed at 400°C. The measured data are displayed as open circles, while the fitted curve is shown by a solid black line. The three Gaussian-Lorentzian components contributing to the fit are represented by solid coloured lines.

As each component of the C 1s may be considered separately, it is possible to compare the relative abundances of the carbon-containing surface groups. Unfortunately, materials are commonly contaminated by a layer of adventitious carbon from the surroundings, impeding the analysis. For the comparison to be meaningful, it is therefore essential to subtract any contributions attributed to the adventitious carbon from the measured signal. In this instance, it is to be assumed that the bulk of each annealed sample contains only zinc and oxygen, so that any carbon encountered at the surface may be regarded as contamination. Although it is possible that some of the carbon in the annealed samples originates from the LBZA starting material, it should be noted that the areas enclosed by the C 1s signals of the annealed samples vary by just 4%. The similarity of the C 1s areas implies that the abundance of each carbon species is not dependent on the annealing temperature, supporting the suggestion that the carbon is adventitious in nature. After averaging over the five annealed samples, each component of the C 1s signal may be subtracted from the corresponding component of the untreated LBZA sample, as illustrated in Fig. 4.9. Fitting the resulting C 1s spectrum as before, the area of the component at lowest binding energy is approximately 4.4 times larger

than that of the central component. In turn, this component has an area which is 3.7 times smaller than the area of the component appearing at highest binding energy.

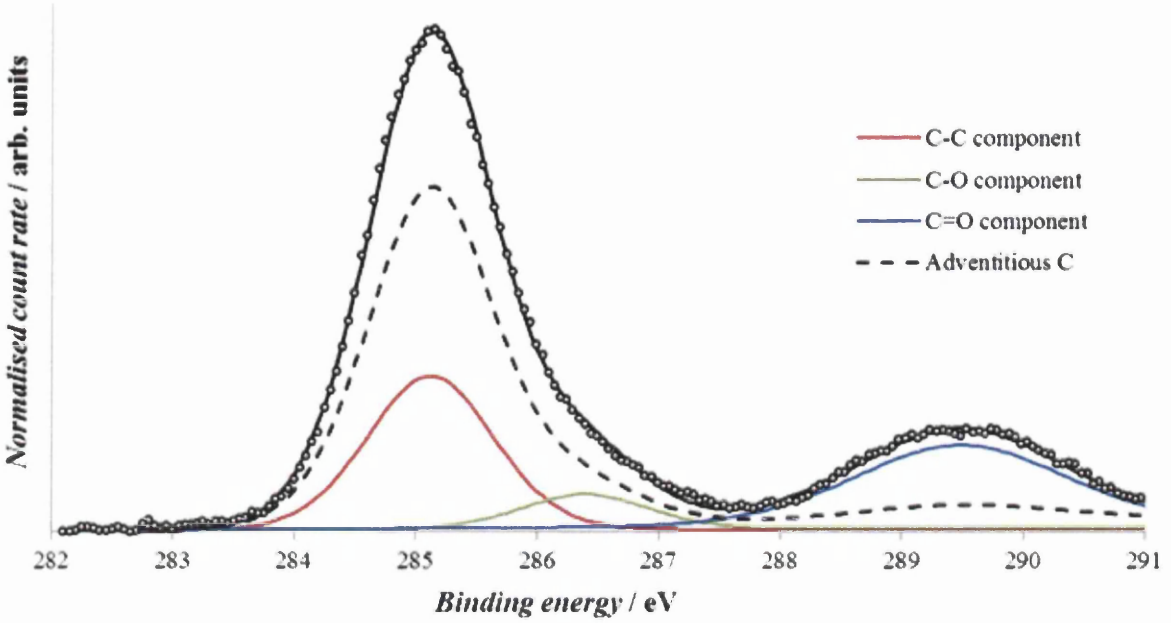

Fig. 4.9. The C 1s XPS spectrum of untreated LBZA nanosheets. The measured data are displayed as open circles, while the fitted curve is shown by a solid black line. The three LBZA Gaussian-Lorentzian components are represented by solid coloured lines, and the contribution from adventitious carbon is shown by a dashed black line.

The presence of the three components in the C 1s spectrum of the LBZA nanosheets does not follow trivially from theory; as discussed in Chapter 1, LBZA is typically described by the chemical formula $Zn_5(OH)_8C_2H_3O_2.2H_2O$ [1–5,7], where the carbon atoms are distributed equally between the two distinct chemical environments of an acetate group. However, it is possible that a third environment is created due to reaction of the acetate group with other species [23]. To account for all of the carbon atoms bonded to directly to oxygen atoms within the acetate ions, one must therefore sum the two highest energy components of the C 1s signal. The combined area of these two components corresponds to approximately half of the total area of the peak, as expected from the chemical formula.

Having considered the C 1s spectra, one may compare the O 1s peaks of the six samples. In Fig. 4.10, the O 1s peaks of differently annealed samples are overlaid following normalisation of the electron count rate with respect to the signal amplitude, as before. It was established from Fig. 4.7 that the measured spectrum of the untreated LBZA nanosheets should be energy shifted due to electrical charging of the sample; more specifically, it was shown that the binding energy values must be increased by approximately 6.1 eV. The LBZA spectrum in Fig. 4.10 is plotted following this adjustment to the measured binding energy values. For each annealed sample, the signal consists of a strong primary peak at a binding energy of 530.4–530.5 eV and a "shoulder" peak at higher binding energy, centred at around 532 eV. It is apparent that the shoulder peak, which is commonly attributed to oxygen-containing surface species [24–28], varies little between 400°C and 700°C, but increases substantially at an annealing temperature of 800°C. By contrast, the O 1s signal of the untreated LBZA nanosheets appears as a broad, symmetric peak centred at a binding energy of 532.0 eV.

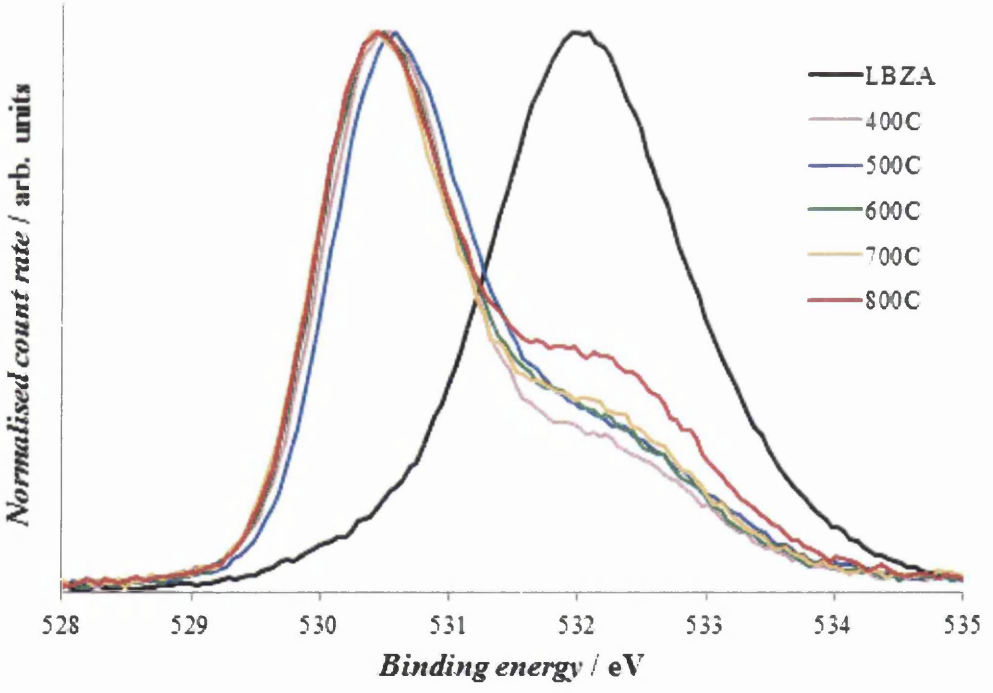

Fig. 4.10. XPS spectra showing the O 1s peaks of LBZA nanosheets annealed at different temperatures. Each spectrum is normalised with respect to the signal amplitude. The measured spectrum of the untreated sample, depicted by the solid black line, was obtained using the charge compensation facility of the XPS instrument, and the binding energies of this spectrum have been adjusted as in Fig. 4.7.

A more detailed physical interpretation of the O 1s spectra may be achieved by deconstructing the signals into their constituent Gaussian-Lorentzian components. As demonstrated in Fig. 4.11, the O 1s spectra of the annealed samples are well-represented by four independent components. The first of these, located at a binding energy of 530.4–530.5 eV, is typically identified as the component corresponding to O^{2-} ions in the bulk of the ZnO lattice [25–28]. A second component appears at a slightly higher binding energy of 531.2–531.3 eV; while this contribution is also commonly attributed to oxygen ions in the ZnO lattice (either O^{-} or O^{2-}), these species are situated in oxygen-deficient regions such as an interstitial site or the vicinity of an oxygen vacancy [25–28]. As aforementioned, the shoulder of the O 1s peak is produced by species present at the ZnO surface, and may be fitted by two components. It has previously been reasoned that one of these components, at a binding energy of 532.1–532.2 eV, belongs to the oxygen atoms of surface hydroxide groups [29–31], whereas the second, at 532.9–533.1 eV, arises from oxygen atoms bonded to carbon [19,22] or contained within loosely-bound compounds such as water [25–31].

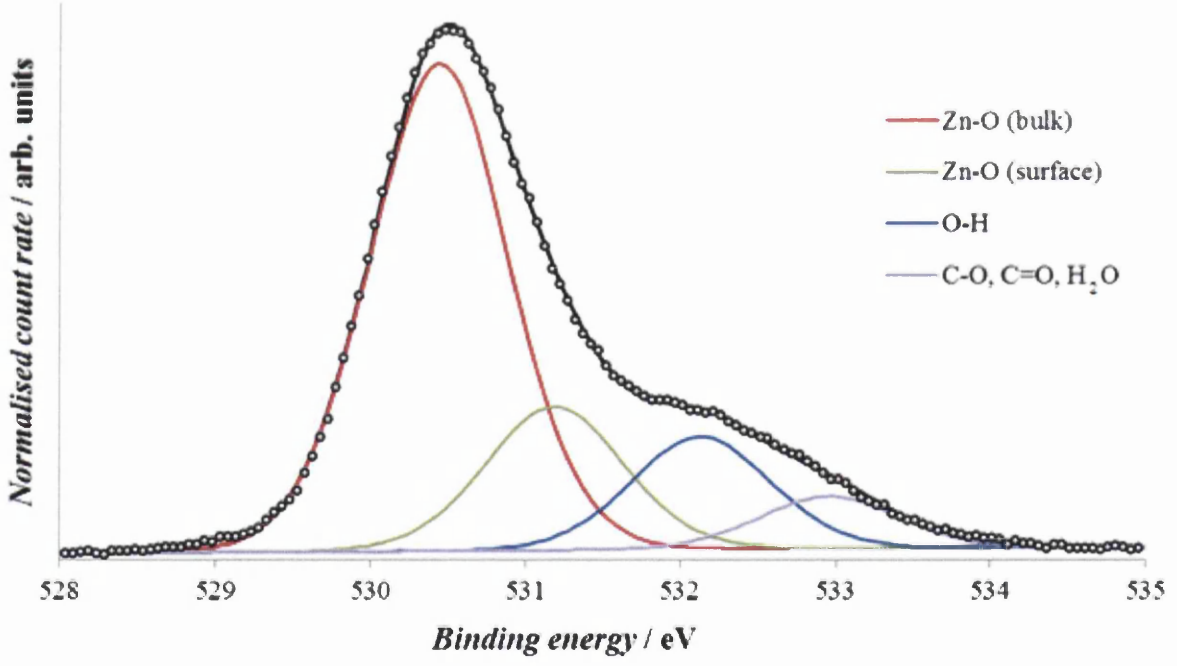

Fig. 4.11. The O 1s XPS spectrum of ZnO nanosheets annealed at 400°C. The measured data are displayed as open circles, while the fitted curve is shown by a solid black line. The four Gaussian-Lorentzian components contributing to the fit are represented by solid coloured lines.

The Zn $2p_{3/2}$ peak was also measured; in this instance, the Zn $2p_{3/2}$ signals of the five annealed samples, depicted in Fig. 4.12, are located at binding energies of 1021.8–1021.9 eV. After shifting the binding energy values as before, the peak corresponding to the untreated LBZA nanosheets is centred at a higher binding energy of approximately 1022.1 eV, but has a similar width. As the Zn $2p_{3/2}$ signal is typically not significantly affected by the electronic environment of the Zn atom [32], one would anticipate only small differences to exist between the Zn $2p_{3/2}$ peak of the LBZA sample and those of the annealed ZnO nanosheets.

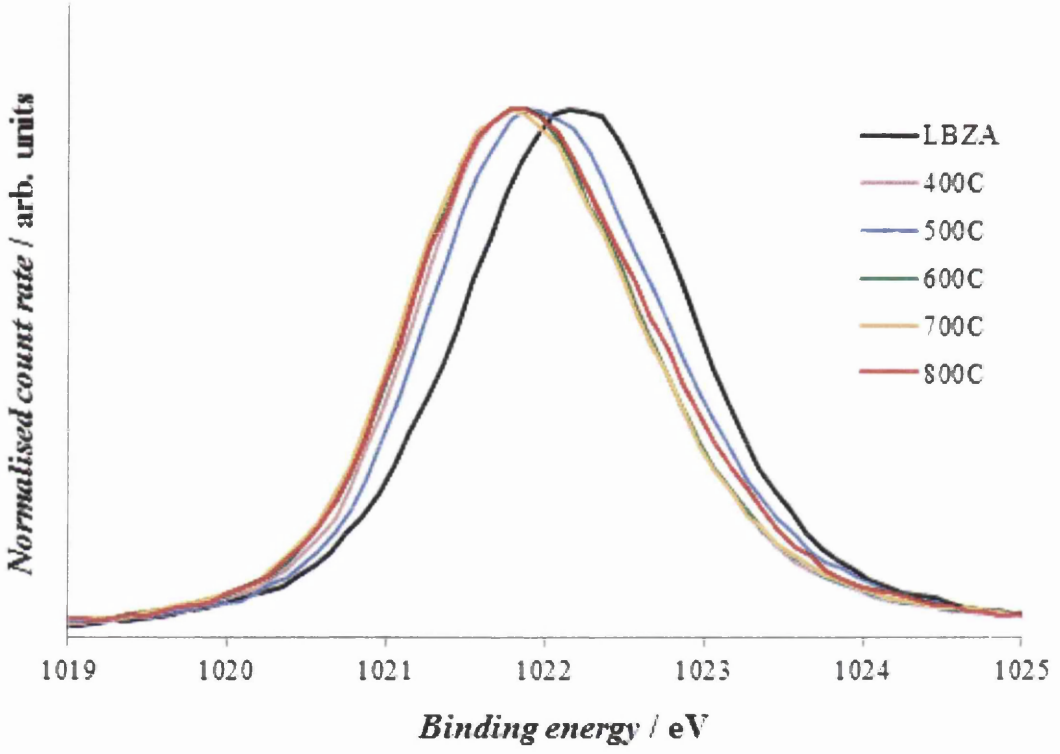

Fig. 4.12. XPS spectra showing the Zn $2p_{3/2}$ peaks of LBZA nanosheets annealed at different temperatures. Each spectrum is normalised with respect to the signal amplitude. The measured spectrum of the untreated sample, depicted by the solid black line, was obtained using the charge compensation facility of the XPS instrument, and the binding energies of this spectrum have been adjusted as in Fig. 4.7.

For the annealed samples, it was previously surmised that the two lowest energy components of the O 1s spectrum correspond to O^{2-} ions in the ZnO lattice. This suggestion may be verified by first considering the number of oxygen atoms contributing to the two components, subsequently comparing to the measured quantity of Zn^{2+} ions in the system.

To correctly compare components that belong to different elemental signals, it is necessary to divide the measured area of each component by the appropriate "atomic sensitivity factor", or ASF. For O 1s and Zn $2p_{3/2}$ signals, ASF values of 0.66 and 4.8 are typically quoted, respectively [33]. After scaling the enclosed component areas in this way, the atomic ratio of lattic oxygen (from the two low-binding energy components of the O 1s peak) to zinc (from the total enclosed area of the Zn $2p_{3/2}$ peak) is calculated from the five ZnO samples as 1.04 ± 0.06, which is very close to the expected value of one. However, the ratio exhibits a clear dependence on the annealing temperature; as shown by Fig. 4.13, the relative concentration of lattice oxygen increases in proportion to the annealing temperature, possibly indicating that the concentration of oxygen vacancies is reduced by annealing at higher temperatures.

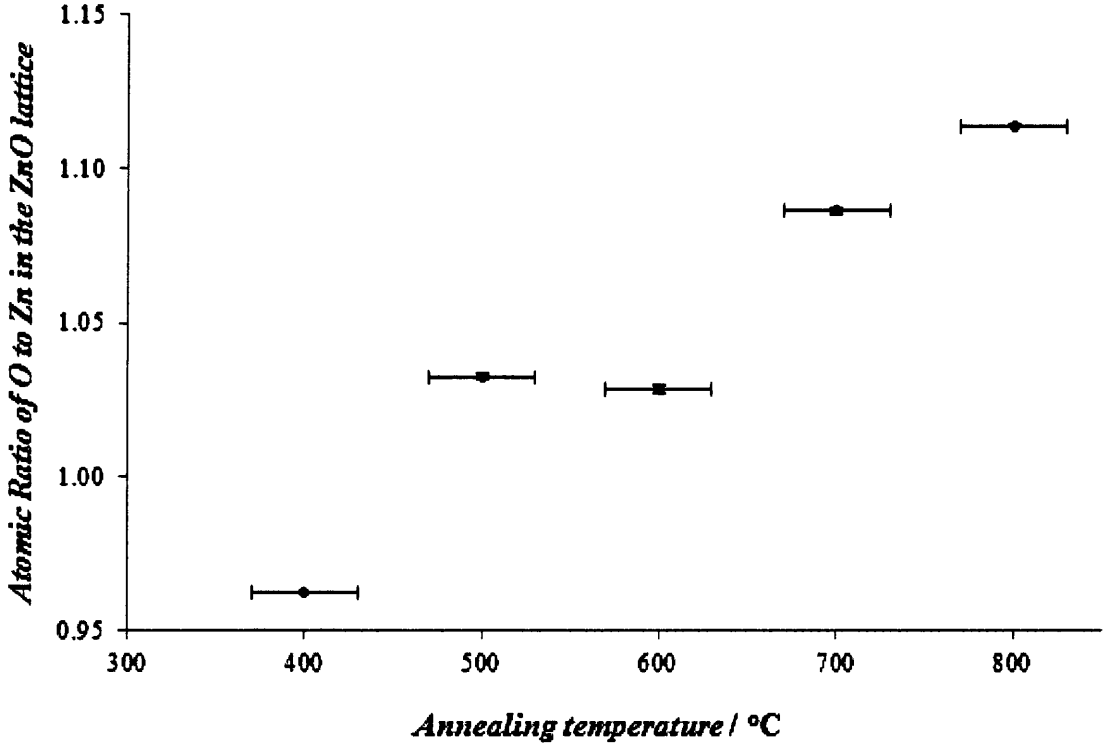

Fig. 4.13. A plot showing the ratio of O^{2-} ions to Zn^{2+} ions in the ZnO lattice as a function of the annealing temperature.

The other two components of the O1s spectra of the annealed samples, located at a binding energies of 532.1–532.2 eV and 532.9–533.1 eV, were previously attributed to surface species such as hydroxyl groups and adsorbed water molecules. Unlike the O^{2-} ions of the ZnO lattice, Fig. 4.14 shows that the concentration of oxygen atoms contained within these

surface species depends strongly on the annealing temperature; as the temperature is raised from 400°C to 800°C, the ratio of these oxygen atoms to the total number of zinc atoms is enhanced by a factor of 1.7. It is therefore apparent that increasing the annealing temperature promotes the formation of the surface species.

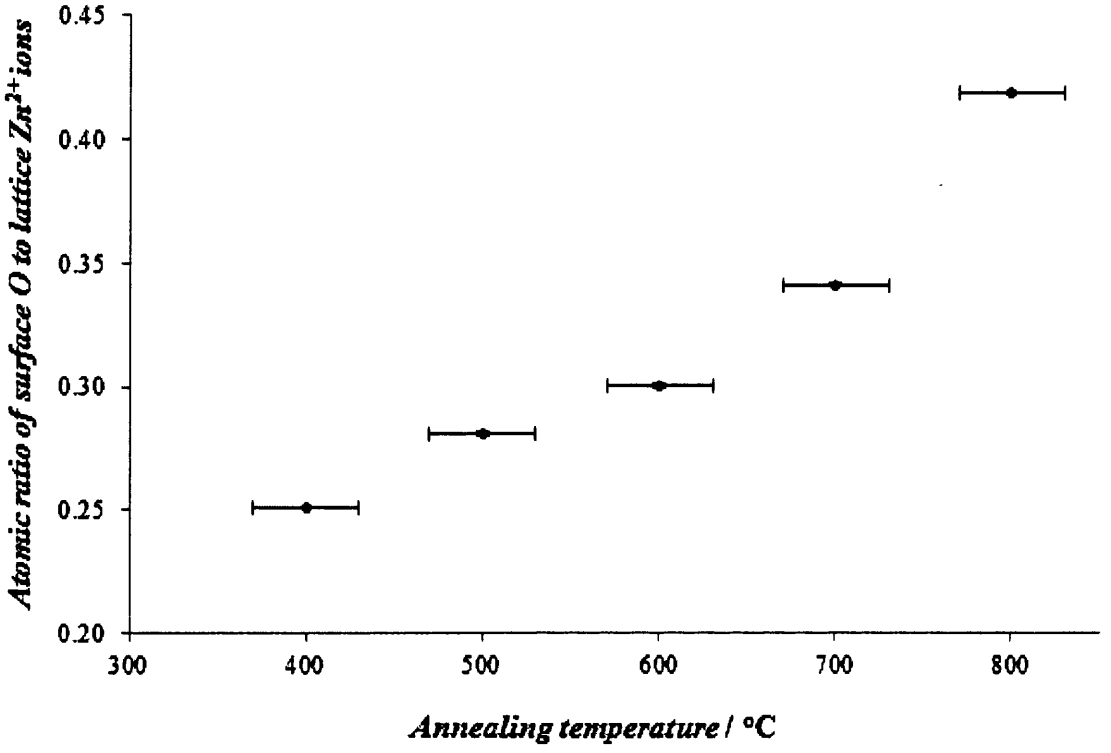

Fig. 4.14. A plot showing the ratio surface oxygen to Zn^{2+} ions in the ZnO lattice as a function of the annealing temperature.

The atomic ratios of the untreated LBZA sample should also be considered. In this case, one must compare the total enclosed area of the O 1s and the Zn $2p_{3/2}$ signals, dividing each by the appropriate ASF as before. Performing the calculation, a value of approximately 3.44 is obtained for the atomic ratio of oxygen to zinc, which is considerably higher than the theoretical figure of 2.8 calculated from the predicted stoichiometry of the material (according to the chemical formula of LBZA given previously, one expects fourteen atoms of oxygen for every five atoms of zinc). While the cause of this disparity is unclear, it is possible that the unexpectedly high proportion of oxygen may be attributed to oxygen-containing surface species such as adsorbed water molecules.

It is similarly straightforward to estimate the atomic ratio of oxygen to carbon in the untreated LBZA sample. After removing the contributions of adventitious carbon from the C 1s signal, the enclosed area may be divided by the ASF of the peak, which is typically given as 0.25 [33]. Scaling the total area of the O 1s peak by its characteristic ASF value of 0.66, the atomic ratio of oxygen to carbon is calculated as 2.96, which is significanty lower than the stoichiometric estimate of 3.5. However, if one neglects the contributions of intercalated water, which may be have been partially removed due to the ultra-high vacuum in the XPS analysis chamber, the ratio instead has a predicted value of 3.0, which is in good agreement with the experimentally acquired value.

4.3.4. The effect of annealing temperature on surface optical defects

As well as requiring a high surface area for gas adsorption, chemiresistive gas sensors also require favourable electrical characteristics. In the case of n-type semiconductors such as ZnO, the electrical conductivity is closely related to the concentration of inter-band electron donor states corresponding to species such as oxygen vacancies or interstitial oxygen ions. One way to investigate these defect states is through PL spectroscopy, wherein the material is excited by a high-frequency laser to measure its characteristic emission spectrum. As detailed in Chapter 3, each component of the visible spectrum may be attributed to the relaxation of electrons either from the conduction band to a deep acceptor state or from a deep donor state to the valence band [34,35]. Due to the multitude of different defects present in ZnO, the spectrum typically contains contributions across a wide range of visible wavelengths. The recombination of electrons in the conduction band with holes in the valence band leads to a sharp signal in the ultra-violet region of the scan, called the NBE peak [35–40], which facilitates estimation of the band gap.

To explore the formation of ZnO from the LBZA starting material, a sample of LBZA nanosheets on silicon was heated on a hot-plate in small temperature increments up to 270°C, measuring the PL spectrum of the material at room temperature following each successive heating step. Other identical LBZA nanosheet samples were each heated for ten minutes at a single temperature, for comparison. Fig. 4.15 depicts the NBE peak of PL spectra over the measured range of temperatures, and shows that the peak position shifts to higher wavelength

values with increasing annealing temperature. For reference, the plot also shows the NBE peak of LBZA nanosheets annealed in a tube furnace at 400°C under flow of dry air. The presence of an NBE peak indicates that ZnO exists within the sample, and should not therefore be observed for LBZA nanosheets prior to decomposition. One may recall, however, that the TGA measurements in Fig. 4.1 suggest that the $Zn(OH)_2$ layers of the LBZA begin to decompose at around 110°C, thereby introducing ZnO to the structure. Moreover, it is possible that the 325 nm laser is sufficiently powerful to partially decompose the $Zn(OH)_2$ units, again forming ZnO and a corresponding NBE signal in the PL spectrum.

By using each peak position to calculate the corresponding band gap of the material, one may use Fig. 4.15 to show that the band gap decreases from a value of 3.45 eV at 100°C to 3.36 eV at 400°C, which is comparable to the accepted ZnO band gap of 3.37 eV [41,42]. These estimates, which are obtained by assuming an exciton binding energy of 60 meV, are plotted as a function of temperature in Fig. 4.16. The temperature uncertainty for each data-point has been determined from the measured standard deviation in the temperature during heating, with the exception of the furnace-annealed sample for which an uncertainty of ±30°C is assumed as before. The uncertainty in the calculated band gap typically decreases as a function of increasing annealing temperature due to the decreasing width of the NBE peak. It is clear that the calculated band gaps corresponding to the stepwise-heated sample are consistent with those of the samples heated at a single temperature, suggesting that the measured trend in Fig. 4.16 does not depend on the duration of each heating step.

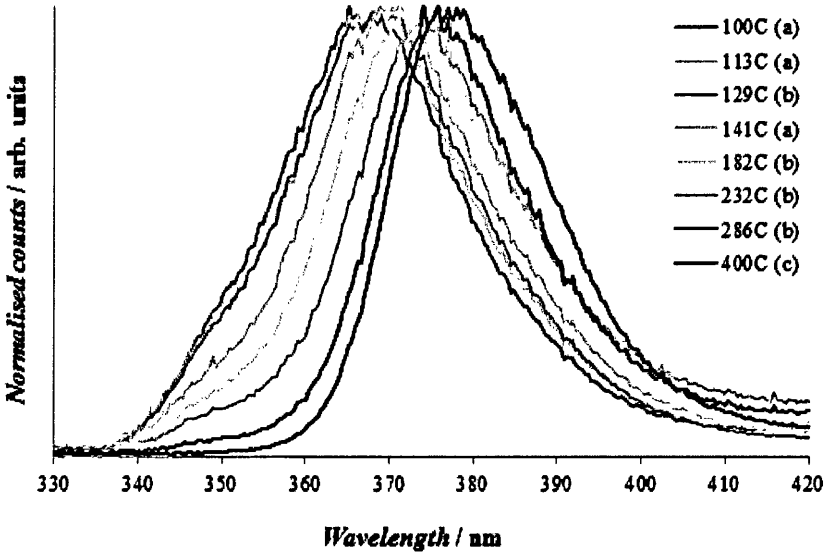

Fig. 4.15. Photoluminescence spectra showing the near-band-edge (NBE) peak of LBZA nanosheets following stepwise heating on a hot-plate at different temperatures (a), a single heat-treatment on a hot-plate at one temperature (b), or annealing under flow of dry air in a tube furnace (c).

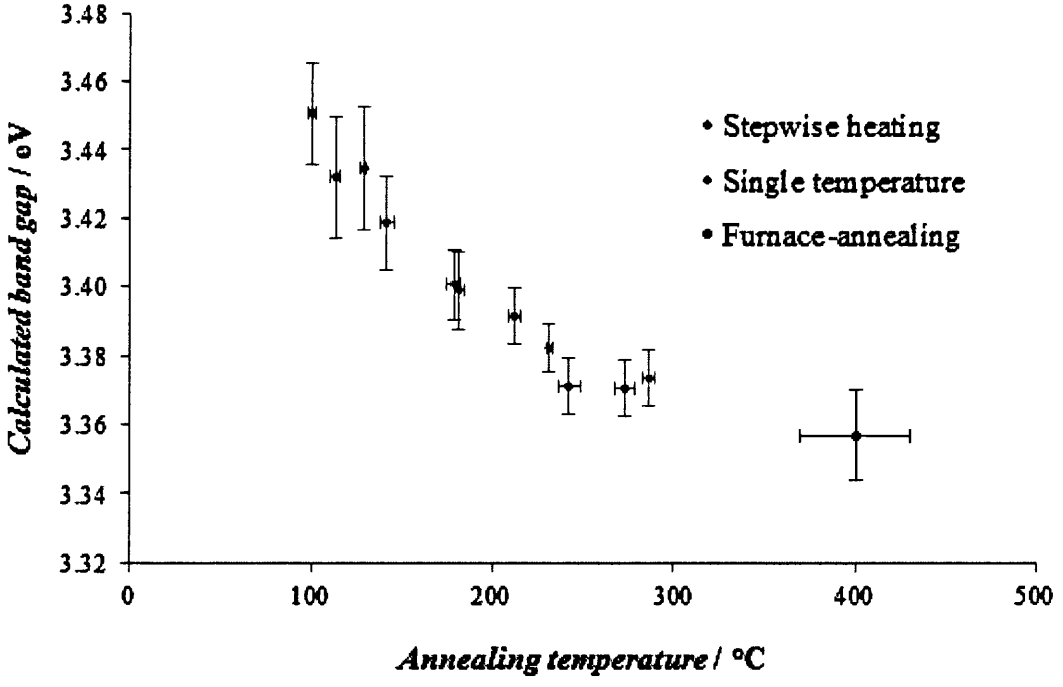

Fig. 4.16. A plot showing the variation of the band gap, calculated from the NBE peak position in Fig. 4.15, as a function of the annealing temperature.

Although the defect peak of the PL spectrum is thought to depend on the nature of defects in the material, the physical interpretation of this visible emission is subject to heated debate in the literature [43]. It is common for authors to divide the peak into two or more distinct regions based on the colour of the emitted light, with each region then considered in isolation. For instance, many studies attribute the "green luminescence" at wavelengths of 490–530 nm to surface oxygen vacancies [34,36,44–48] or oxygen ions located on zinc lattice sites (which is referred to as "antisite" oxygen) [36,45,49], while the "yellow luminescence" appearing between 560 nm and 600 nm has been attributed to surface hydroxyl groups [40,50] or interstitial oxygen species [44,46–49,51]. However, although the photoluminescence of ZnO has been studied extensively, variation of the photoluminescence properties during thermal decomposition of LBZA has yet to be investigated. Combined with the contradictory nature of existing research, it is therefore difficult to apply the conclusions of previous studies to the present work.

In an attempt to analyse each defect spectrum from a physical viewpoint, it is instructive to first recall the TGA measurements depicted in Fig. 4.1. According to these data, the thermal decomposition of LBZA proceeds in three distinct stages which occur in different temperature regimes. Based on the interpretation of Fig. 4.1 described earlier, increasing the temperature to 110°C results in the removal of all intercalated water from the LBZA structure. As the temperature is elevated further, the $Zn(OH)_2$ units begin to convert to ZnO, releasing a molecule of water for every two reacting hydroxide ions. The final decomposition stage occurs between 140°C and 270°C, and involves the thermal decomposition of the acetate ions. In the description of the LBZA structure given in Chapter 2, these ions are located in the gaps between the planar zinc hydroxide layers [9,52–55].

The PL spectra in Fig. 4.17, Fig. 4.18 and Fig. 4.19 show how the defect peak changed during thermal decomposition of the LBZA nanosheets, averaged over three different areas of each sample. For the purposes of comparison, each spectrum has been normalised with respect to the peak maximum. Guided by the TGA plot of Fig. 4.1, the spectra are separated into two separate groups corresponding to different stages of the thermal decomposition to ZnO. The traces shown in Fig. 4.17, measured after heating the LBZA nanosheets at temperatures of 140°C or lower, may be attributed to the removal of intercalated water and

the conversion of hydroxide ions to the divalent oxide anions of ZnO. Increasing the temperature from 66°C to 113°C is associated with a large red-shift of the defect peak; that is, the components at lower wavelengths are diminished while those at higher wavelengths are enhanced. It is notable that the defect peaks measured after heating at temperatures of 113°C and 129°C are remarkably similar, as are the positions of their NBE peaks. This range of temperatures covers a large proportion of the first sharp transition in the TGA plot, suggesting that the reaction of the hydroxide ions has little effect on the PL spectrum. Since the two spectra were measured following different heating procedures, their similarity also suggests that the form of the visible emission is not dependent on the heating time (i.e. the same spectrum is obtained by either heating the sample at a single temperature or heating sequentially at multiple temperatures). The high intensity of the low-wavelength components at 66°C may possibly be attributed to the presence of water molecules in the gaps between $Zn(OH)_2$ layers, as the TGA plot reveals that the removal of intercalated water persists up to approximately 110°C. Following the 141°C heat-treatment, the high-wavelength components account for a higher proportion of the overall visible spectrum. At this stage of the decomposition, the hydroxide ions are almost completely reacted and the removal of the acetate ions has begun.

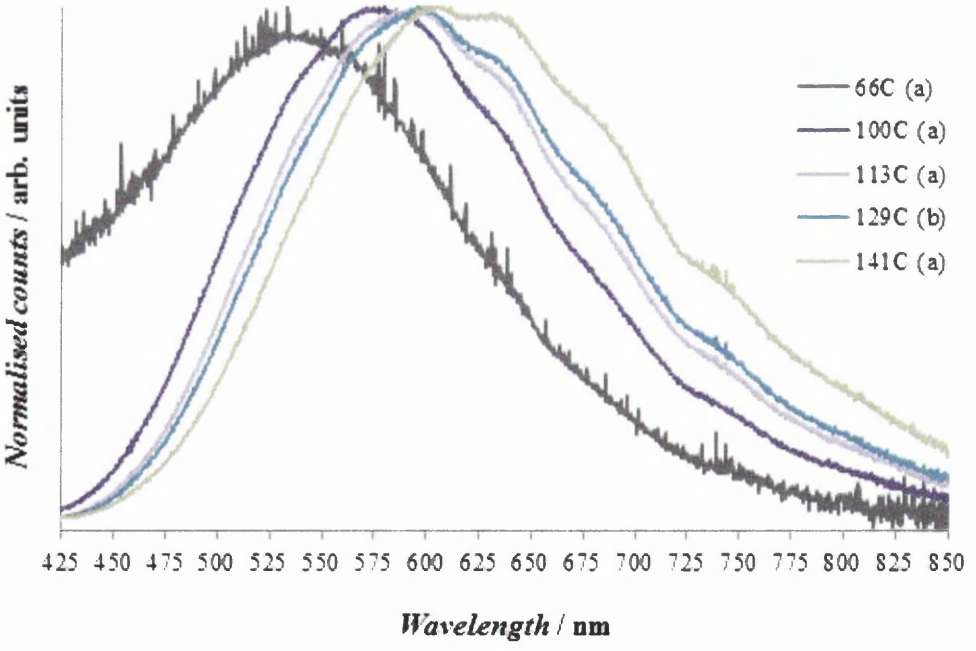

Fig. 4.17. Photoluminescence spectra showing the visible emission peak of LBZA nanosheets following stepwise heating (a) or a single heat-treatment (b) on a hot-plate at temperatures of ~140°C or lower.

Upon increasing the annealing temperature further, Fig. 4.18 shows that the form of the peak changed only slightly between 141°C and 182°C and similar spectra were obtained following either stepwise heating or heating at a single temperature, labelled (a) and (b), respectively. In the case of samples subjected to a single heat-treatment, annealing at temperatures above 182°C led to a significant enhancement of the low-wavelength components; comparing the spectra of samples heated at 232°C and 286°C, the latter exhibits a much higher relative intensity at wavelengths below 600 nm. It is worth noting, however, that the visible spectrum measured following the 232°C heat-treatment is almost identical to the corresponding emission of LBZA nanosheets annealed in a tube furnace at 400°C. From this evidence alone, it is tempting to propose that the enhancement of the low-wavelength emission is related to the presence of reactive intermediates formed between 232°C and 286°C which subsequently decompose at higher temperatures; following this reasoning, one might expect similar spectra following the 232°C and 400°C annealing treatments provided that any additional surface groups generated between these temperatures do not persist up to 400°C.

To verify the trends observed in Fig. 4.18, it is important to additionally consider the spectra of the stepwise-heated sample at temperatures above 180°C. Despite stepwise heating yielding similar spectra to singularly-heated samples at temperatures of 180°C or lower, Fig. 4.19 shows that this consistency does not exist at higher temperatures. In particular, the spectra in Fig. 4.19 vary little between annealing temperatures of 179°C and 273°C using the stepwise method of heating, despite the large changes between comparable temperatures depicted in Fig. 4.18. Furthermore, the spectrum obtained after sequential heating to 273°C does not coincide with the spectrum acquired after annealing at 400°C in a tube furnace, with the former possessing much lower normalised signal intensity at wavelengths below 600 nm than the latter. The cause of the discrepancy between stepwise and singular heat-treatments is unclear, but may possible be attributed to environmental factors such as humidity, which was not controlled during the experiments.

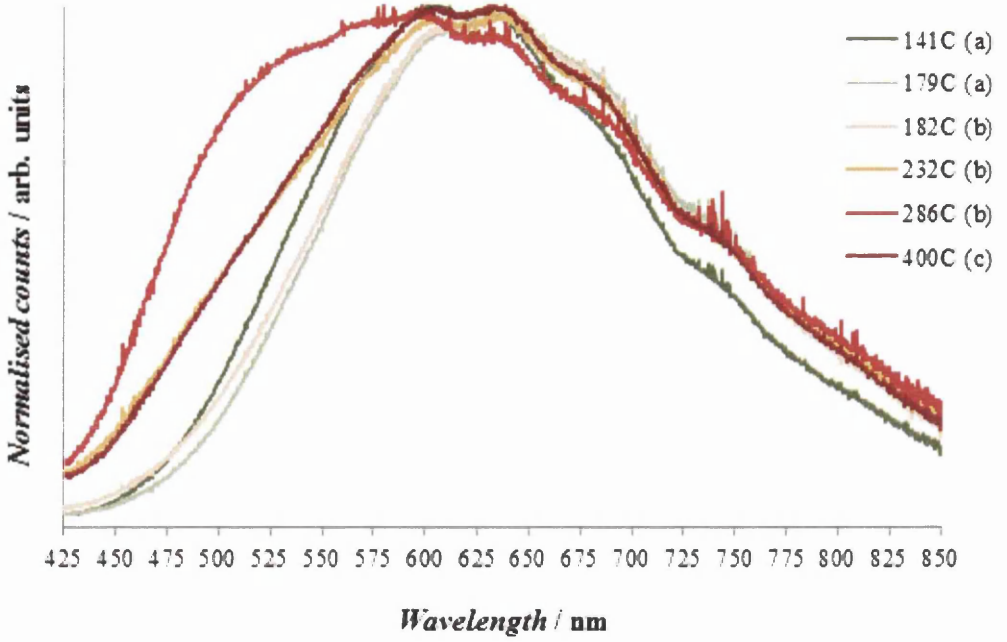

Fig. 4.18. Photoluminescence spectra showing the visible emission peak of LBZA nanosheets following stepwise heating on a hot-plate (a), a single hot-plate heat-treatment (b) or annealing under flow of dry air in a tube furnace (c) at temperatures of ~140°C or higher.

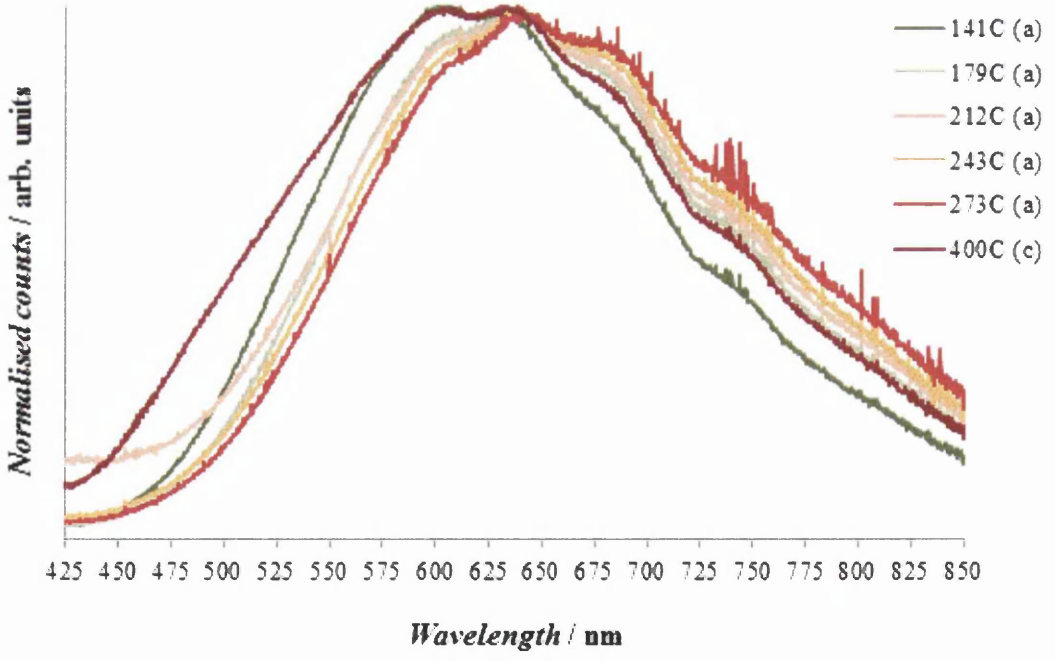

Fig. 4.19. Photoluminescence spectra showing the visible emission peak of LBZA nanosheets following stepwise heating on a hot-plate (a) or annealing under flow of dry air in a tube furnace (c) at temperatures of ~140°C or higher.

After converting the LBZA to ZnO, heating the nanosheets to higher temperatures may alter the defect spectrum through the formation of defects such as oxygen vacancies. During analysis of the XPS measurements, above, it was demonstrated that the composition of the ZnO surface is gradually modified by an increase in the annealing temperature. In particular, the ratio of oxygen to zinc in the ZnO lattice was found to increase as the temperature was raised from 400°C to 800°C, and the concentration of oxygen-containing surface species was also enhanced. Fig. 4.20 shows the defect spectra of separate ZnO nanosheet samples annealed in a tube furnace at different temperatures, in addition to a sample of LBZA nanosheets which were not annealed. Each spectrum has been normalised with respect to the respective peak maximum to aid comparison. Between 400°C and 600°C, there was a gradual red-shift in the peak wavelengths, while increasing the temperature to 700°C led to the emergence of a dominant component centred at a wavelength of approximately 520 nm. The spectrum obtained after the 800°C annealing treatment is strikingly similar to the defect peak of the LBZA material, with the two spectra exhibiting the same peak wavelength. It is therefore likely that the dominant emission component following the 800°C anneal corresponds to hydroxyl groups at the ZnO surface, producing similar contributions to the intercalated water molecules of the LBZA sample. This deduction is contradictory to previous research, wherein hydroxyl groups are identified as a source of yellow luminescence [40,50]. Due to the observation that the concentration of lattice oxygen increases in proportion to the annealing temperature, the enhancement of high-wavelength components achieved by increasing the annealing temperature from 400°C to 600°C may be attributed to the introduction of interstitial oxygen species, while the reduced contributions at lower wavelengths suggests that this emission is related to surface oxygen vacancies.

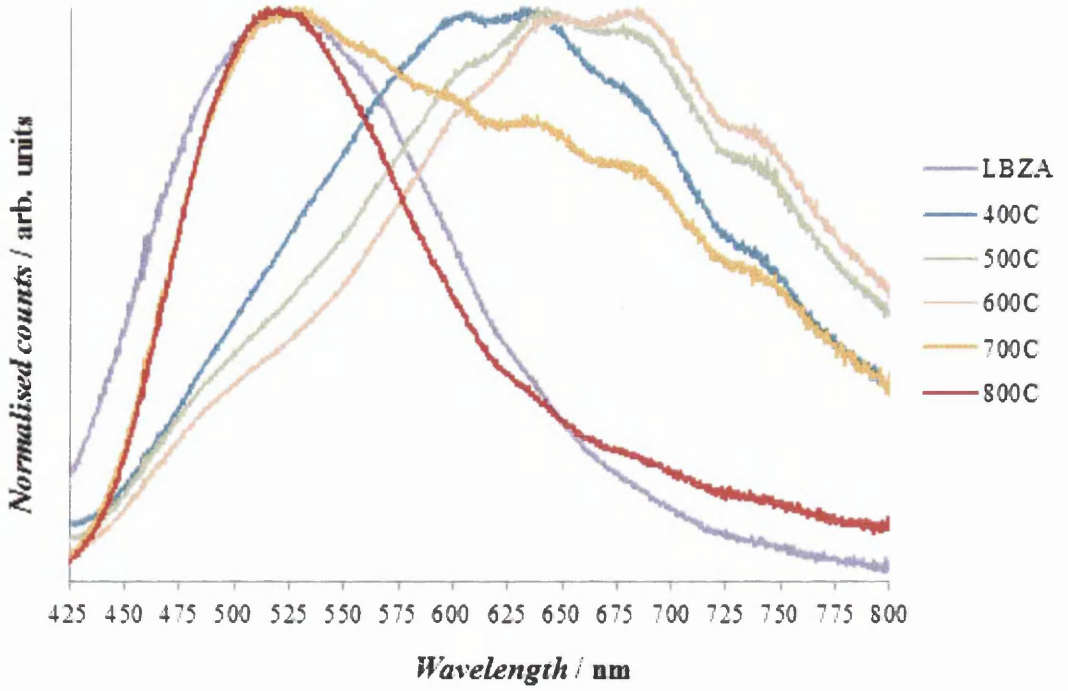

Fig. 4.20. Photoluminescence spectra showing the visible emission peak of LBZA nanosheets after annealing under flow of dry air in a tube furnace at different temperatures.

4.4. Conclusions

Through a combination of multiple complementary experimental techniques, the surface chemistries of both LBZA and ZnO nanosheets have been investigated. Moreover, the procedures have been utilised to explore the conversion of LBZA to ZnO, identifying various intermediate phases during the transition. In particular, a TGA experiment has shown that the decomposition of LBZA occurs in three distinct stages, namely the removal of intercalated water below 110°C, the reaction of hydroxide ions to form doubly-charged oxide ions between 110°C and 140°C, and the decomposition of acetate ions up to approximately 270°C. Investigations into the photoluminescence of the nanosheet material at different points during the decomposition showed that the band gap was reduced from approximately 3.45 eV at 100°C to 3.36 eV at 400°C.

Following the formation of ZnO, annealing to higher temperatures had a profound effect on the surface chemistry. In particular, XPS analysis revealed that the proportion of oxygen in the ZnO lattice increases in proportion to the annealing temperature, possibly due to the removal of oxygen vacancies and the generation of interstitial oxygen species. These changes are accompanied by an enhanced concentration of oxygen-containing surface species such as hydroxyl radicals. By relating the XPS spectra to photoluminescence measurements, it was further surmised that the oxygen-containing surface groups contribute a large component to the low-wavelength portion of the visible emission spectrum. Increasing the annealing temperature from 400°C to 600°C led to a significant red-shifting of the visible emission, implying that the removal of oxygen vacancies is associated with a decrease in the intensity of low-wavelength emission components.

The physical and chemical characterisation of ZnO nanosheets yields several significant practical insights. For instance, in gas sensing applications it is clearly important for the nanosheets to possess high surface area in order to maximise the surface to volume ratio. SEM and BET analysis showed that increasing the annealing temperature leads to growth of the ZnO nanoparticles, with sintering observed at temperatures of 700°C or higher. Furthermore, it is possible that adsorption sites at the ZnO surface are obstructed by the presence of native surface species such as hydroxyl groups, which increase in abundance as the annealing temperature is raised. It is therefore essential to limit the annealing temperature during decomposition of the LBZA nanosheets.

References

[1] A. Tarat, R. Majithia, R.A. Brown, M.W. Penny, K.E. Meissner, Synthesis of nanocrystalline ZnO nanobelts via pyrolytic decomposition of zinc acetate nanobelts and their gas sensing behavior, Surf. Sci. 606 (2012) 715–721. doi:10.1016/j.susc.2011.12.010.

[2] Q. Cui, K. Yu, N. Zhang, Z. Zhu, Porous ZnO nanobelts evolved from layered basic zinc acetate nanobelts, Appl. Surf. Sci. 254 (2008) 3517–3521. doi:10.1016/j.apsusc.2007.11.044.

[3] Z.H. Liang, Y.J. Zhu, G.F. Cheng, Y.H. Huang, Synthesis of ZnO nanosheets by room-temperature decomposition of a layered precursor synthesized by microwave heating, J. Mater. Sci. 42 (2007) 477–482. doi:10.1007/s10853-006-1069-5.

[4] D. Sun, M. Wong, L. Sun, Y. Li, N. Miyatake, H.J. Sue, Purification and stabilization of colloidal ZnO nanoparticles in methanol, J. Sol-Gel Sci. Technol. 43 (2007) 237–243. doi:10.1007/s10971-007-1569-z.

[5] S. Baruah, J. Dutta, Hydrothermal growth of ZnO nanostructures, Sci. Technol. Adv. Mater. 10 (2009) 013001. doi:10.1088/1468-6996/10/1/013001.

[6] E. Hosono, S. Fujihara, T. Kimura, H. Imai, Growth of layered basic zinc acetate in methanolic solutions and its pyrolytic transformation into porous zinc oxide films, J. Colloid Interface Sci. 272 (2004) 391–398. doi:10.1016/j.jcis.2003.10.005.

[7] D. Luković Golić, G. Branković, M. Počuča Nešić, K. Vojisavljević, A. Rečnik, N. Daneu, et al., Structural characterization of self-assembled ZnO nanoparticles obtained by the sol-gel method from Zn(CH(3)COO)(2)·2H(2)O., Nanotechnology. 22 (2011) 395603. doi:10.1088/0957-4484/22/39/395603.

[8] E. Kandare, J.M. Hossenlopp, Thermal degradation of acetate-intercalated hydroxy double and layered hydroxy salts, Inorg. Chem. 45 (2006) 3766–3773. doi:10.1021/ic060071k.

[9] L. Poul, N. Jouini, F. Fievet, Layered hydroxide metal acetates (metal = zinc, cobalt, and nickel): Elaboration via hydrolysis in polyol medium and comparative study, Chem. Mater. 12 (2000) 3123–3132. doi:10.1021/cm991179j.

[10] T. Biswick, W. Jones, A. Pacuła, E. Serwicka, J. Podobinski, Evidence for the formation of anhydrous zinc acetate and acetic anhydride during the thermal degradation of zinc hydroxy acetate, Zn5(OH)8(CH3CO2)2·4H2O to ZnO, Solid State Sci. 11 (2009) 330–335. doi:10.1016/j.solidstatesciences.2008.06.018.

[11] R. Rojas, C. Barriga, M. Angeles Ulibarri, P. Malet, V. Rives, Layered Ni(II)-Zn(II) hydroxyacetates. Anion exchange and thermal decomposition of the hydroxysalts obtained, J. Mater. Chem. 12 (2002) 1071–1078. doi:10.1039/b110145e.

[12] Z. Jing, J. Zhan, Fabrication and gas-sensing properties of porous ZnO nanoplates, Adv. Mater. 20 (2008) 4547–4551. doi:10.1002/adma.200800243.

[13] C. Chen, P. Liu, C. Lu, Synthesis and characterization of nano-sized ZnO powders by direct precipitation method, Chem. Eng. J. 144 (2008) 509–513. doi:10.1016/j.cej.2008.07.047.

[14] S. Bhattacharyya, A. Gedanken, A template-free, sonochemical route to porous ZnO nano-disks, Microporous Mesoporous Mater. 110 (2008) 553–559. doi:10.1016/j.micromeso.2007.06.053.

[15] Y.L. Wei, P.C. Chang, Characteristics of nano zinc oxide synthesized under ultrasonic condition, J. Phys. Chem. Solids. 69 (2008) 688–692. doi:10.1016/j.jpcs.2007.07.094.

[16] J. Huang, Y. Wu, C. Gu, M. Zhai, Y. Sun, J. Liu, Fabrication and gas-sensing properties of hierarchically porous ZnO architectures, Sensors Actuators, B Chem. 155 (2011) 126–133. doi:10.1016/j.snb.2010.11.036.

[17] M. Descostes, F. Mercier, N. Thromat, C. Beaucaire, M. Gautier-Soyer, Use of XPS in the determination of chemical environment and oxidation state of iron and sulfur samples: Constitution of a data basis in binding energies for Fe and S reference compounds and applications to the evidence of surface species of an oxidized py, Appl. Surf. Sci. 165 (2000) 288–302. doi:10.1016/S0169-4332(00)00443-8.

[18] T.L. Barr, S. Seal, Nature of the use of adventitious carbon as a binding energy standard, J. Vac. Sci. Technol. A Vacuum, Surfaces, Film. 13 (1995) 1239. doi:10.1116/1.579868.

[19] Y. Park, W. Kim, H. Park, T. Tachikawa, T. Majima, W. Choi, Carbon-doped TiO2 photocatalyst synthesized without using an external carbon precursor and the visible light activity, Appl. Catal. B Environ. 91 (2009) 355–361. doi:10.1016/j.apcatb.2009.06.001.

[20] M. Wohlers, H. Werner, D. Herein, T. Schedel-Niedrig, A. Bauer, R. Schlögl, Reaction of C60 and C70 with molecular oxygen, Synth. Met. 77 (1996) 299–302. doi:10.1016/0379-6779(96)80106-8.

[21] S. Sakthivel, H. Kisch, Daylight Photocatalysis by Carbon-Modified Titanium Dioxide, Angew. Chemie - Int. Ed. 42 (2003) 4908–4911. doi:10.1002/anie.200351577.

[22] G.L. Mar, P.Y. Timbrell, R.N. Lamb, Factors influencing the chemical vapor deposition of oriented ZnO films using zinc acetate, Chem. Mater. 7 (1995) 1890–1896. doi:10.1021/cm00058a020.

[23] M. Barteau, Organic reactions at well-defined oxide surfaces, Chem. Rev. (1996) 4–6. doi:10.1021/cr950222t.

[24] M. Kunat, S. Gil Girol, T. Becker, U. Burghaus, C. Wöll, Stability of the polar surfaces of ZnO: A reinvestigation using He-atom scattering, Phys. Rev. B. 66 (2002) 081402. doi:10.1103/PhysRevB.66.081402.

[25] P.-T. Hsieh, Y.-C. Chen, K.-S. Kao, C.-M. Wang, Luminescence mechanism of ZnO thin film investigated by XPS measurement, Appl. Phys. A. 90 (2007) 317–321. doi:10.1007/s00339-007-4275-3.

[26] M. Chen, Z.L. Pei, C. Sun, L.S. Wen, X. Wang, Surface characterization of transparent conductive oxide Al-doped ZnO films, 220 (2000) 254–262.

[27] X. Li, Y. Wang, W. Liu, G. Jiang, C. Zhu, Study of oxygen vacancies' influence on the lattice parameter in ZnO thin film, Mater. Lett. 85 (2012) 25–28. doi:10.1016/j.matlet.2012.06.107.

[28] J. Wang, S. Hou, H. Chen, L. Xiang, Defects-Induced Room Temperature Ferromagnetism in ZnO Nanorods Grown from ε-Zn(OH) 2, J. Phys. Chem. C. 118 (2014) 19469–19476. doi:10.1021/jp5058226.

[29] W. Eisele, A. Ennaoui, P. Schubert-bischoff, XPS , TEM and NRA investigations of Zn (Se , OH)/ Zn (OH) 2 films on Cu (In , Ga)(S , Se) 2 substrates for highly efficient solar cells, Sol. Energy Mater. 75 (2003) 17–26. doi:10.1016/S0927-0248(02)00104-6.

[30] A.M. Chaparro, C. Maffiotte, M.T. Gutiérrez, J. Herrero, Morphological and compositional study of CBD-ZnSe thin films by microscopy techniques and angle resolved XPS, Thin Solid Films. 358 (2000) 22–29. doi:10.1016/S0040-6090(99)00704-X.

[31] T.G.G. Maffeis, M.W. Penny, A. Castaing, O.J. Guy, S.P. Wilks, XPS investigation of vacuum annealed vertically aligned ultralong ZnO nanowires, Surf. Sci. 606 (2012) 99–103. doi:10.1016/j.susc.2011.09.007.

[32] C. Wöll, The chemistry and physics of zinc oxide surfaces, Prog. Surf. Sci. 82 (2007) 55–120. doi:10.1016/j.progsurf.2006.12.002.

[33] C.D. Wagner, L.E. Davis, M.V. Zeller, J.A. Taylor, R.H. Raymond, L.H. Gale, Empirical Atomic Sensitivity Factors for Quantitative Analysis by Electron Spectroscopy for Chemical Analysis, Surf. Interface Anal. 3 (1981) 211–225.

[34] H.S. Kang, J.S. Kang, J.W. Kim, S.Y. Lee, Annealing effect on the property of ultraviolet and green emissions of ZnO thin films, J. Appl. Phys. 95 (2004) 1246–1250. doi:10.1063/1.1633343.

[35] J. Liu, S. Lee, Y.H. Ahn, J.-Y. Park, K.H. Koh, Tailoring the visible photoluminescence of mass-produced ZnO nanowires, J. Phys. D. Appl. Phys. 42 (2009) 095401. doi:10.1088/0022-3727/42/9/095401.

[36] D.F. Wang, T.J. Zhang, Study on the defects of ZnO nanowire, Solid State Commun. 149 (2009) 1947–1949. doi:10.1016/j.ssc.2009.07.038.

[37] Y.G. Wang, S.P. Lau, X.H. Zhang, H.H. Hng, H.W. Lee, S.F. Yu, et al., Enhancement of near-band-edge photoluminescence from ZnO films by face-to-face annealing, J. Cryst. Growth. 259 (2003) 335–342. doi:10.1016/j.jcrysgro.2003.07.015.

[38] D. Reynolds, D. Look, B. Jogai, C. Litton, T. Collins, W. Harsch, et al., Neutral-donor–bound-exciton complexes in ZnO crystals, Phys. Rev. B. 57 (1998) 12151–12155. doi:10.1103/PhysRevB.57.12151.

[39] B.K. Meyer, H. Alves, D.M. Hofmann, W. Kriegseis, D. Forster, F. Bertram, et al., Bound exciton and donor–acceptor pair recombinations in ZnO, Phys. Status Solidi. 241 (2004) 231–260. doi:10.1002/pssb.200301962.

[40] A.B. Djurisic, Y.H. Leung, K.H. Tam, Y.F. Hsu, L. Ding, W.K. Ge, et al., Defect emissions in ZnO nanostructures, 095702 (2007). doi:10.1088/0957-4484/18/9/095702.

[41] A. Teke, Ü. Özgür, S. Doğan, X. Gu, H. Morkoç, B. Nemeth, et al., Excitonic fine structure and recombination dynamics in single-crystalline ZnO, Phys. Rev. B - Condens. Matter Mater. Phys. 70 (2004) 195207. doi:10.1103/PhysRevB.70.195207.

[42] C. Boemare, T. Monteiro, M.J. Soares, J.G. Guilherme, E. Alves, Photoluminescence studies in ZnO samples, Phys. B. 308-310 (2001) 985–988.

[43] M.D. McCluskey, S.J. Jokela, Defects in ZnO, J. Appl. Phys. 106 (2009) 0–13. doi:10.1063/1.3216464.

[44] F. Hai-Bo, Y. Shao-Yan, Z. Pan-Feng, W. Hong-Yuan, L. Xiang-Lin, J. Chun-Me:, et al., Investigation of Oxygen Vacancy and Interstitial Oxygen Defects in ZnO Films by Photoluminescence and X-Ray Photoelectron Spectroscopy, Chinese Phys. Lett. 24 (2007) 2108–2111. doi:10.1088/0256-307X/24/7/089.

[45] Z.G. Wang, X.T. Zu, S. Zhu, L.M. Wang, Green luminescence originates from surface defects in ZnO nanoparticles, Phys. E Low-Dimensional Syst. Nanostructures. 35 (2006) 199–202. doi:10.1016/j.physe.2006.07.022.

[46] B. Ha, H. Ham, C.J. Lee, Photoluminescence of ZnO nanowires dependent on O2 and Ar annealing, J. Phys. Chem. Solids. 69 (2008) 2453–2456. doi:10.1016/j.jpcs.2008.04.041.

[47] L.E. Greene, M. Law, J. Goldberger, F. Kim, J.C. Johnson, Y. Zhang, et al., Low-temperature wafer-scale production of ZnO nanowire arrays, Angew. Chemie - Int Ed. 42 (2003) 3031–3034. doi:10.1002/anie.200351461.

[48] X.L. Wu, G.G. Siu, C.L. Fu, H.C. Ong, Photouminescence and cathodoluminescence studies of stoichiometric and oxygen-deficient ZnO films, Appl. Phys. Lett. 78 (2001) 2285–2287. doi:10.1063/1.1361288.

[49] B. Lin, Z. Fu, Y. Jia, Green luminescent center in undoped zinc oxide films deposited on silicon substrates, Appl. Phys. Lett. 79 (2001) 943–945. doi:10.1063/1.1394173.

[50] H. Zhou, H. Alves, D.M. Hofmann, W. Kriegseis, B.K. Meyer, G. Kaczmarczyk, et al., Behind the weak excitonic emission of ZnO quantum dots: ZnO/Zn(OH) 2 core-shell structure, Appl. Phys. Lett. 80 (2002) 210–212. doi:10.1063/1.1432763.

[51] M. Liu, A.H. Kitai, P. Mascher, Point defects and luminescence centres in zinc oxide and zinc oxide doped with manganese, J. Lumin. 54 (1992) 35–42. doi:10.1016/0022-2313(92)90047-D.

[52] H. Morioka, H. Tagaya, M. Karasu, J. Kadokawa, K. Chiba, Effects of Zinc on the New Preparation Method of Hydroxy Double Salts, Inorg. Chem. 38 (1999) 4211–4216. doi:10.1021/ic9812149.

[53] S.H. Hwang, Y.S. Han, J.H. Choy, Intercalation of functional organic molecules with pharmaceutical, cosmeceutical and nutraceutical functions into layered double hydroxides and zinc basic salts, Bull. Korean Chem. Soc. 22 (2001) 1019–1022.

[54] M. Meyn, K. Beneke, G. Lagaly, Anion-Exchange Reactions of Hydroxy Double Salts, Inorg. Chem. 32 (1993) 1209–1215. doi:10.1021/ic00059a030.

[55] J. Choy, S. Choi, J. Oh, T. Park, Clay minerals and layered double hydroxides for novel biological applications, Appl. Clay Sci. 36 (2007) 122–132. doi:10.1016/j.clay.2006.07.007.

Chapter 5 – Investigating the kinetics of CO oxidation at the ZnO surface

5.1. Introduction

In order to develop responsive gas sensors, it is helpful to first develop an understanding of the chemical reactions occurring at the metal oxide surface. As outlined in Chapter 2, several groups have formulated theoretical models of metal oxide gas sensor response based on the underlying kinetics of these reactions at elevated temperatures. For systems containing surface catalysts such as noble metals, authors commonly employ a Langmuir-Hinshelwood reaction scheme between ionised surface oxygen and a reducing gas [1–7], which assumes that both species are adsorbed prior to their interaction. By considering the changing surface concentration of each species at the surface of the metal oxide, it is possible to relate the rate of physical reactions to measured changes in the electrical resistance of the system. However, the differential equations corresponding to different surface species are typically coupled, making it difficult to fit the model to experimental data.

In the absence of surface catalysts, the complexity of the Langmuir-Hinshelwood model may be avoided by instead assuming an Eley-Rideal reaction scheme [5–12]; in this regime, the reducing species reacts with oxygen ions directly, without first adsorbing to the surface. By neglecting adsorption of the reducing gas, there are fewer surface reactions to consider when constructing a physical description of the system. The simplicity of the Eley-Rideal process therefore facilitates modelling of the sensor response, enabling greater insight into the properties of the surface reactions.

In the present study, zinc oxide nanosheets are used to investigate the surface reactions of carbon monoxide. To study the formation of oxygen ions at the zinc oxide surface, the relationship between the sensor response and oxygen partial pressure is investigated prior to

measuring the effects of the reducing gas. By considering only Eley-Rideal interactions between carbon monoxide and surface oxygen ions, rate constants are estimated for the ionosorption of oxygen and the chemisorption of carbon monoxide molecules. Moreover, comparison of rate constant values obtained at different working temperatures makes it possible to estimate the activation energies of the surface reactions. The model is also used to estimate the position of the Fermi level relative to the conduction band minimum at the surface of the nanosheets. The majority of the work which appears this chapter has been recently published [13].

5.2. Model formulation

A simple model based on the kinetics of adsorption and desorption processes is derived as follows. As a starting point, it is assumed that each adsorbed oxygen molecule dissociates and removes electrons from the metal oxide surface, ionising to form two singly charged oxygen ions. In doing so, a positively charged depletion region is formed below the surface, increasing the electrical resistance of the metal oxide. In the absence of a reducing gas, the oxygen ions remain until they recombine to form diatomic oxygen, which lowers the electrical resistance as electrons are returned to the metal oxide.

When carbon monoxide is added to the system it may react with the surface oxygen ions, forming carbon dioxide and releasing electrons back to the metal oxide. It is proposed that the carbon monoxide chemisorbs to the surface oxygen prior to release of carbon dioxide, following an Eley-Rideal reaction mechanism. The overall system is described by the reactions

$$\frac{1}{2}O_2 + site + e_S^- \xrightarrow{k_1} O^- \tag{5.1}$$

$$O^- \xrightarrow{k_{-1}} \frac{1}{2}O_2 + site + e_s^- \tag{5.2}$$

$$O^- + CO \xrightarrow{k_{r1}} CO_2{}^- \xrightarrow{kr2} CO_2 + site + e_s^- \tag{5.3}$$

where the constants k_1 and k_{-1} are the rate constants for formation and desorption of surface O^- ions, respectively, while k_{r1} and k_{r2} correspond to the rate constants for the two steps of the irreversible reaction between the O^- ions and incident carbon monoxide via a reactive intermediate, CO_2^-. As shown in Eq. (5.1), O^- ions are created when an oxygen molecule at two unoccupied surface sites, referred to above as *site*, and becomes ionised by accepting two surface electrons, which are labelled as e_S^-. The electrons are returned to the metal oxide during the processes described by Eq. (5.2) and Eq. (5.3). For conciseness, O^- and CO_2^- species at the ZnO surface shall henceforth be referred to as "surface ions"; it should be recognised that additional ions may also be present even in the absence of O_2 or CO in the surrounding atmosphere, but the concentrations of such species shall be considered constant throughout this investigation.

It is important to note that the overall O^- formation process described by Eq. (5.1) does not necessarily occur in a single elementary step. In order to determine the form of the rate equation for the reaction, it is therefore necessary to consider the rate of each of its constituent mechanistic steps in turn. In the first stage of the reaction, a molecule of O_2 approaches an unoccupied surface site and becomes adsorbed. If the incident molecule is correctly orientated and has an appropriate kinetic energy, it may interact with the conduction band of the ZnO. This reaction may be written as

$$\frac{1}{2}\boldsymbol{O_2} + \boldsymbol{site} \xrightarrow{k_{1,1}} \frac{1}{2}\boldsymbol{O_{2,int}} \tag{5.4}$$

where $O_{2,int}$ refers to an interacting molecule of O_2. The probability of interaction is dependent on the temperature of the system, which is accounted for by the rate constant of the reaction, $k_{1,1}$. However, unless the system contains pure O_2 gas, not all of the molecules colliding at the surface are O_2; the proportion of surface collisions involving O_2 molecules is equal to P_{O2}/P_{TOT}, where P_{O2} is the O_2 partial pressure and P_{TOT} is the total gas pressure of the system. Assuming that the dissociative adsorption of an O_2 molecule at a particular site is not affected by the adsorption at adjacent sites, the rate of surface site interaction per unit area is linearly proportional to the concentration of unoccupied sites, n_{vacant}. Conversely, as one molecule of O_2 simultaneously interacts with two surface sites, the rate varies in direct

proportion to the square root of P_{O2}/P_{TOT}. Combining these considerations, the surface sites react at a rate given by

$$r_{1,1} = k_{1,1}\left(\frac{P_{O2}}{P_{TOT}}\right)^{\frac{1}{2}} n_{vacant} \tag{5.5}$$

If O^- and CO_2^- ions are present on the surface at concentrations of $[O^-]$ and $[CO_2^-]$ respectively, n_{vacant} is linked to the total concentration of surface sites, n_{sites}, via the relation

$$n_{vacant} = n_{sites} - [O^-] - [CO_2^-] \tag{5.6}$$

Following the formation of $O_{2,int}$, the double bond between the oxygen atoms begins to break as each forms a covalent bond to the ZnO surface. During this step of the reaction, each oxygen atom acquires a formal negative charge by accepting an electron from the surface site. The dissociation and ionisation of $O_{2,int}$ is described by the formula

$$\frac{1}{2}O_{2,int} + e_S^- \xrightarrow{k_{1,2}} O^- \tag{5.7}$$

and is characterised by the rate constant $k_{1,2}$. The rate of the reaction is given by

$$r_{1,2} = k_{1,2}[O_{2,int}]^{\frac{1}{2}} n_S \tag{5.8}$$

where $[O_{2,int}]$ and n_S are the concentrations of interacting O_2 molecules and surface electrons, respectively.

To deduce the rate equation for the overall reaction expressed by Eq. (5.1), one must first recognise that the mean time required for a reaction to occur is equal to the reciprocal of the reaction rate. As the duration of the overall reaction is given by the sum of the component reaction times, the rate of the reaction, r_1, obeys the expression

$$\frac{1}{r_1} = \frac{1}{r_{1,1}} + \frac{1}{r_{1,2}} = \frac{1}{k_{1,1}\left(\frac{P_{O2}}{P_{TOT}}\right)^{\frac{1}{2}} n_{vacant}} + \frac{1}{k_{1,2}[O_{2,int}]^{\frac{1}{2}} n_s} \tag{5.9}$$

In general, the rate of the overall reaction therefore depends on the concentrations of several reactants. However, if the rate of the second step is much higher than the first, it is possible to use the approximation

$$r_1 \approx k_{1,1}\left(\frac{P_{O2}}{P_{TOT}}\right)^{\frac{1}{2}} n_{vacant} \tag{5.10}$$

and k_1 becomes equivalent to $k_{1,1}$. In this case, the formation of O^- ions is not influenced by a variation in the concentration of surface electrons. Moreover, if the product $k_{1,2}n_S$ is sufficiently large, the concentration of $O_{2,int}$ species may be reasonably ignored. If these criteria are satisfied, the concentration of O^- ions varies according to

$$\frac{d[O^-]}{dt} = k_1\left(\frac{P_{O2}}{P_{TOT}}\right)^{\frac{1}{2}}(n_{sites} - [O^-] - [CO_2^-]) - k_{-1}[O^-] - k_{r1}\left(\frac{P_{CO}}{P_{TOT}}\right)[O^-] \tag{5.11}$$

which accounts for the recombination of O^- ions and their reaction with molecules of CO, as described by Eq. (5.2) and Eq. (5.3), respectively. The former reaction is expected to occur at a rate that is directly proportional to the concentration of O^- ions. This assumption is reasonable when the concentration is sufficiently high, so that the average distance between O^- ions may be assumed constant. Removal of O^- ions by CO corresponds to the third term in Eq. (5.11), which varies linearly with the partial pressure of CO due to the 1:1 stoichiometry of the reaction. Again, the rate of this mechanism is expected to exhibit a direct proportionality to the concentration of O^- ions, provided that the approach of a CO molecule is not additionally hindered by an increase in O^- concentration. It is instructive to note that Eq. (5.11) is identical to Eq. (4) in the 2001 publication by Nakata *et al.* [12]

A similar equation may be constructed to describe the time variation of the CO_2^- concentration. Considering the two-step reaction shown in Eq. (5.3), $[CO_2^-]$ is anticipated to follow the expression [12]

$$\frac{d[CO_2^-]}{dt} = k_{r1}\left(\frac{P_{CO}}{P_{TOT}}\right)[O^-] - k_{r2}[CO_2^-] \tag{5.12}$$

where the first term accounts for the formation of CO_2^- ions, as in the third term in Eq. (5.11), and the second corresponds to the oxidation of the CO_2^- ions and their subsequent desorption as CO_2 gas. Summing Eq. (5.11) and Eq. (5.12) yields

$$\frac{d}{dt}([O^-] + [CO_2^-]) = k_1 \left(\frac{P_{O2}}{P_{TOT}}\right)^{\frac{1}{2}} (n_{sites} - [O^-] - [CO_2^-]) - k_{-1}[O^-] - k_{r2}[CO_2^-] \quad (5.13)$$

which describes the how the overall concentration of surface ions varies with time. Dividing this concentration by n_{sites}, Eq. (5.13) becomes

$$\frac{d\theta_O}{dt} = k_1 \left(\frac{P_{O2}}{P_{TOT}}\right)^{\frac{1}{2}} (1 - \theta_O) - k_{-1}\theta_O - (k_{r2} - k_{-1})\frac{[CO_2^-]}{n_{sites}} \quad (5.14)$$

where θ_O denotes the fraction of the total surface sites occupied by O^- or $[CO_2]^-$ ions, and is therefore given by

$$\theta_O = \frac{[O^-]+[CO_2^-]}{n_{sites}} \quad (5.15)$$

The total ensemble of surface ions contains a fraction of CO_2^- ions, θ_{CO}, defined by

$$\theta_{CO} \equiv \frac{[CO_2^-]}{[O^-]+[CO_2^-]} \quad (5.16)$$

Substituting Eq. (5.16) into Eq. (5.14) yields

$$\frac{d\theta_O}{dt} = k_1(1 - \theta_O)\left(\frac{P_{O2}}{P_{TOT}}\right)^{1/2} - k_{-1}\theta_O - (k_{r2} - k_{-1})\theta_O\theta_{CO} \quad (5.17)$$

Similarly, division of Eq. (5.12) by the sum of $[O^-]$ and $[CO_2^-]$ produces the equation

$$\left(\frac{1}{[O^-]+[CO_2^-]}\right)\frac{d[CO_2^-]}{dt} = k_{r1}\left(\frac{P_{CO}}{P_{TOT}}\right)(1 - \theta_{CO}) - k_{r2}\theta_{CO} \quad (5.18)$$

Unfortunately, this expression is of limited use as it stands due to the presence of multiple time-dependent functions. The first time derivative of θ_{CO} is given by

$$\frac{d\theta_{CO}}{dt} = \left(\frac{1}{[O^-]+[CO_2^-]}\right)\frac{d[CO_2^-]}{dt} - \frac{[CO_2^-]}{([O^-]+[CO_2^-])^2}\frac{d}{dt}([O^-] + [CO_2^-]) \tag{5.19}$$

From the definitions of θ_O and θ_{CO}, it is helpful to identify that

$$\left(\frac{1}{[O^-]+[CO_2^-]}\right)\frac{d[CO_2^-]}{dt} = \frac{\theta_{CO}}{[CO_2^-]}\frac{d[CO_2^-]}{dt} = \theta_{CO}\frac{d}{dt}\ln([CO_2^-]) \tag{5.20}$$

and

$$\frac{[CO_2^-]}{([O^-]+[CO_2^-])^2}\frac{d}{dt}([O^-] + [CO_2^-]) = \frac{\theta_{CO}}{\theta_O}\frac{d\theta_O}{dt} = \theta_{CO}\frac{d}{dt}(\ln(\theta_O)) \tag{5.21}$$

Through use of Eq. (5.18) and Eq. (5.21), Eq. (5.19) becomes

$$\frac{d\theta_{CO}}{dt} = k_{r1}\left(\frac{P_{CO}}{P_{TOT}}\right) - \theta_{CO}\left(k_{r1}\left(\frac{P_{CO}}{P_{TOT}}\right) + k_{r2} + \frac{d}{dt}(\ln(\theta_O))\right) \tag{5.22}$$

wherein all dependence on θ_O is confined to the final term. If θ_O varies sufficiently slowly, Eq. (5.22) may be approximated by

$$\frac{d\theta_{CO}}{dt} \approx k_{r1}\left(\frac{P_{CO}}{P_{TOT}}\right) - \theta_{CO}\left(k_{r1}\left(\frac{P_{CO}}{P_{TOT}}\right) + k_{r2}\right) \tag{5.23}$$

Comparison of Eq. (5.20) and Eq. (5.21) indicates that Eq. (5.23) is valid when $\ln(\theta_O)$ changes at a much lower rate than $\ln([CO_2^-])$, which in turn requires that the magnitude of $d(\ln(\theta_O))/dt$ is much smaller than the sum of $k_{r1}(P_{CO}/P_{TOT})$ and k_{r2}. This condition is satisfied at both the start and the end of the response curve, as $d\theta_O/dt$ is zero in each of these cases. A similar justification is possible at the beginning of the sensor recovery, where θ_{CO} is equal to the value at the end of the response curve, and the end, where $d\theta_O/dt$ is zero due to the requirement of equilibrium. At intermediate times, however, the situation is less clear, and solution of Eq. (5.22) may be required.

If it is appropriate to make use of Eq. (5.23) in place of Eq. (5.22), one may obtain an analytic solution for θ_{CO}. By imposing the condition that θ_{CO} is zero before CO is introduced into the system, substitution of this solution into Eq. (5.17) gives

$$\frac{d\theta_O}{dt} + \theta_O\left(k_1\left(\frac{P_{O2}}{P_{TOT}}\right)^{\frac{1}{2}} + k_{-1} + (k_{r2} - k_{-1})\frac{\varepsilon_{CO}}{\gamma_{CO}}(1 - \exp(-\gamma_{CO}t))\right) = k_1\left(\frac{P_{O2}}{P_{TOT}}\right)^{\frac{1}{2}} \quad (5.24)$$

where

$$\gamma_{CO} = k_{r1}\left(\frac{P_{CO}}{P_{TOT}}\right) + k_{r2} \quad (5.25)$$

and

$$\varepsilon_{CO} = k_{r1}\left(\frac{P_{CO}}{P_{TOT}}\right) \quad (5.26)$$

It should be noted that time, t, is taken to be zero at the moment the CO is introduced to the system. Unfortunately Eq. (5.24) cannot be solved generally, but it is possible to obtain the steady-state solution, where $d\theta_O/dt$ is zero when t tends to infinity, which is given by

$$\theta_O(CO\ on) = \frac{K_O\left(\frac{P_{O2}}{P_{TOT}}\right)^{1/2}}{K_O\left(\frac{P_{O2}}{P_{TOT}}\right)^{1/2} + 1 + \left(\frac{k_{r2}}{k_{-1}} - 1\right)\frac{\varepsilon_{CO}}{\gamma_{CO}}} \quad (5.27)$$

where the ratio k_1/k_{-1} has been relabelled as a new parameter, K_O, the equilibrium constant for O^- formation.

The variation of θ_O and θ_{CO} during sensor recovery may be studied in a similar manner. Setting P_{CO} to zero in Eq. (5.23) and substituting the solution into Eq. (5.17) as before, θ_O is described by the equation

$$\frac{d\theta_O}{dt} + \theta_O\left(k_1\left(\frac{P_{O2}}{P_{TOT}}\right)^{1/2} + k_{-1} + (k_{r2} - k_{-1})\frac{\varepsilon_{CO}}{\gamma_{CO}}\exp(-k_{r2}t)\right) = k_1\left(\frac{P_{O2}}{P_{TOT}}\right)^{1/2} \quad (5.28)$$

Here, t is taken as zero at the moment that the CO is turned off. The steady-state solution of Eq. (5.28) is

$$\boldsymbol{\theta_O(CO\ off)} = \frac{K_O\left(\frac{P_{O2}}{P_{TOT}}\right)^{1/2}}{K_O\left(\frac{P_{O2}}{P_{TOT}}\right)^{1/2}+1} \tag{5.29}$$

It is now necessary to relate θ_O to the electrical resistance, R, of the sensor. As detailed in Chapter 1, this relationship has been derived previously by solving the Poisson Equation for electrostatics in one dimension at the interface between two metal oxide surfaces [14,15], yielding the formula

$$\boldsymbol{R = R_0 \exp\left(\alpha \theta_O^2\right)} \tag{5.30}$$

where α and R_0 are temperature-dependent constants. Eq. (5.30) is strictly only valid for sufficiently large particles, where the bulk material is unaffected by the electrical potential at the surface [15,16]. Moreover, R_0 may only be considered to be independent of θ_O within the confines of the thermoelectronic emission model, as was discussed in Chapter 1 and will be reviewed later in this chapter. The response of the sensor is defined by

$$\boldsymbol{Response} = \frac{R(CO\ off) - R(CO\ on)}{R(CO\ off)} \tag{5.31}$$

where *R(CO on)* and *R(CO off)* correspond to the equilibrium resistance of the sensor when the CO is on and off, respectively. Used together, Eq. (5.30) and Eq. (5.31) provide a useful relationship between the fractional coverage of surface ions and the response.

The formulae derived thus far may now be used to predict how the response varies with changing P_{CO}/P_{TOT}. It will be demonstrated later that it is particularly informative to consider the reciprocal of Eq. (5.27), which, after substituting θ_O*(CO off)* into the expression using Eq. (5.29), can be written as

$$\frac{1}{\theta_O(CO\ on)} = \frac{1}{\theta_O(CO\ off)} + \frac{\left(\frac{k_{r2}}{k_{-1}} - 1\right)}{K_O\left(\frac{P_{O2}}{P_{TOT}}\right)^{1/2}} \frac{\varepsilon_{CO}}{\gamma_{CO}} \tag{5.32}$$

The advantage of Eq. (5.32) is that the P_{CO}/P_{TOT} dependence is confined to just one term. Moreover, if k_{r2} is much larger than the product of k_{r1} and P_{CO}/P_{TOT}, the final term becomes directly proportional to P_{CO}/P_{TOT} as γ_{CO} is approximately equal to k_{r2}. In this case, a plot of $1/\theta_O(CO\ on)$ as a function of P_{CO}/P_{TOT} is expected to be linear.

5.3. Experimental methods

Utilising the procedure described in Chapter 3, LBZA nanosheets were prepared in aqueous suspension and centrifuged into de-ionised water over five five-minute cycles. A 200 μL volume of the suspension was drop-cast onto an alumina gas-sensing substrate and dried at 60°C, before annealing in a tube furnace at 500°C for 30 minutes under a 1 L min^{-1} flow of dry air. The sensor was tested under a continuous 400 mL min^{-1} flow of dry air (80% N_2, 20% O_2) over a temperature range of 390–490°C, using custom-built gas sensing apparatus as described in Chapter 3. To measure the response of the sensor to different concentrations of CO, a "test gas" consisting of 1000 ppm CO in N_2 was introduced to the system at a flow rate between 20 mL min^{-1} and 80 mL min^{-1}, adjusting the flow of dry air to maintain a total flow rate of 400 mL min^{-1}. In this way, the electrical response was measured over a CO concentration range of 50–200 ppm in steps of 25 ppm.

In addition to measuring the response to CO, the effect of varying the O_2 partial pressure was investigated. Ensuring a total flow rate of 400 mL min^{-1} as before, the flow rates of N_2 and O_2 were adjusted to obtain different concentration ratios of the two gases. By adopting O_2 flow rates between 20 mL min^{-1} and 80 mL min^{-1}, the sensor resistance was measured at P_{O2}/P_{TOT} values of 0.05–0.2, with a difference of 0.025 between successive points.

The ZnO nanosheets were inspected prior to the gas sensing experiments using a Hitachi S4800 field emission scanning electron microscope at an accelerating voltage of 5 kV. This

instrument was used to measure nanoparticles within several nanosheets at different locations across the sensor. To further investigate the properties of the surface potential, both X-ray photoelectron spectroscopy (XPS) and photoluminescence (PL) spectroscopy were employed. The XPS measurements were obtained using a Kratos AXIS Supra monochromated XPS system, using X-rays of energy 1486.6 eV and a pass energy of 20 eV. The PL spectra of the ZnO nanosheets were measured by illuminating the sample using a Melles-Griot He-Cd laser at a wavelength of 325 nm and an incident power density of 2.3×10^6 mW m^{-2}.

5.4. Results and discussions

5.4.1. Sensor characterisation

SEM images of the ZnO nanosheets on the surface of the gas sensing substrate are shown in Fig. 5.1. Fig. 5.1(a) shows that the nanosheets were typically several microns across, while in a previous investigation the thickness of similar nanosheets was measured as 20–100 nm [17]. The high resolution image in Fig. 5.1(b) shows that the nanosheets consisted of multiple nanoparticles of varying shapes and sizes, with some apparent sintering observed. The average nanoparticle diameter was determined to be 38nm, from more than 100 individual measurements, with a standard deviation of 18 nm. This value is consistent with the SEM measurements plotted in Fig. 4.3 of Chapter 4. In order for Eq. (5.30) to be justified, the radius of each nanoparticle must be much greater than the width of the depletion region at its surface [15,16]. However, without additional information regarding the concentration of donor states in the material, it is difficult to determine whether this condition is satisfied in the present system. It is therefore necessary to assess the applicability of Eq. (5.30) from the measured variation of the electrical resistance as a function of the oxygen partial pressure, as will be discussed later.

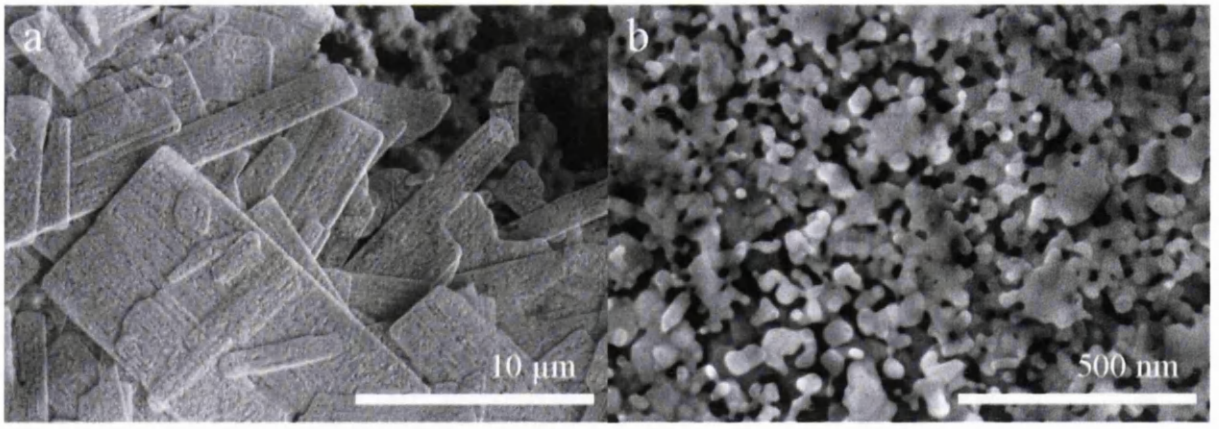

Fig. 5.1. SEM images of the zinc oxide nanosheets on the surface of the gas sensor. The platinum electrode of the sensor is visible in the top right corner of (a) and the arrangement of nanoparticles within one nanosheet is depicted in (b).

5.4.2. Variation of resistance as a function of O_2 or CO concentration

To fully explore the characteristics of the sensor, the electrical resistance was measured in the presence of different gas compositions at a variety of temperatures. As shown in Fig. 5.2, which depicts the response of the sensor to 200 ppm of CO in dry air at 484°C, the resistance was strongly affected by very low concentrations of CO at elevated temperatures. Indeed, by plotting the response as a function of CO concentration, depicted in Fig. 5.3, it is apparent that the sensor remained responsive to this gas at concentrations as low as 50 ppm over the measured temperature range.

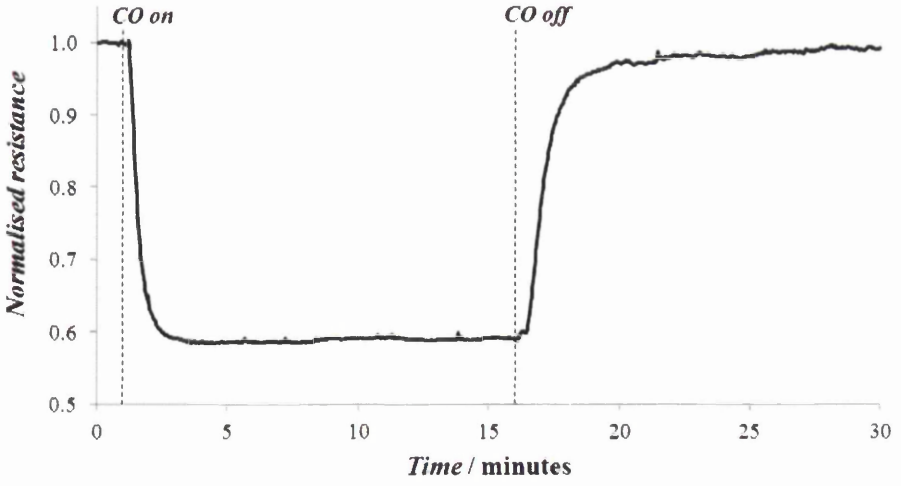

Fig. 5.2. A plot depicting the sensor response to 200 ppm of CO in dry air at 484°C.

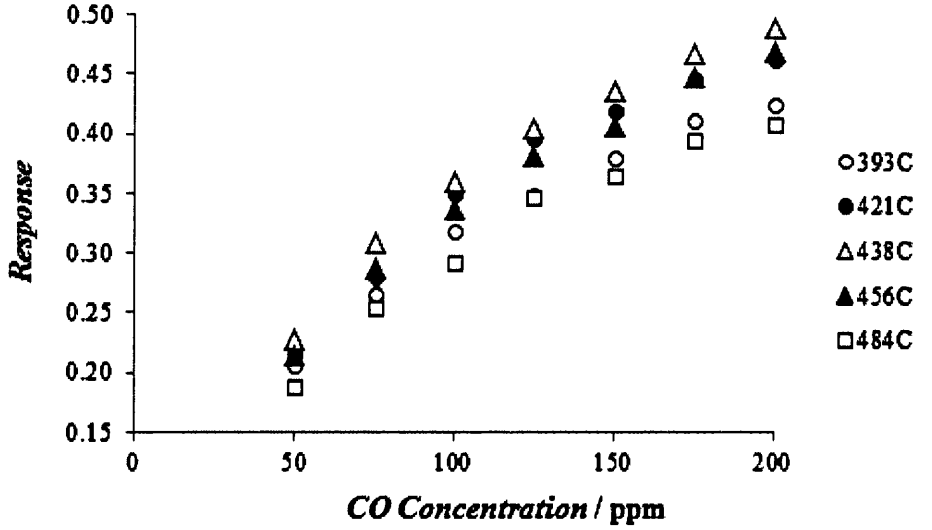

Fig. 5.3. A plot showing the variation of the sensor response as a function of CO concentration (in dry air) at different temperatures.

In the absence of CO, the resistance of the sensor was also measured at different partial pressures of O_2. Retaining the same total flow rate but varying the molar fraction of O_2 between 0.05 and 0.20, Fig. 5.4 shows that the resistance increased with increasing O_2 concentration at each temperature, as expected. From this plot it is also clear that the resistance varied significantly with temperature, decreasing by a factor of approximately four as the temperature was raised from 393°C to 484°C at a P_{O2}/P_{TOT} value of 0.2.

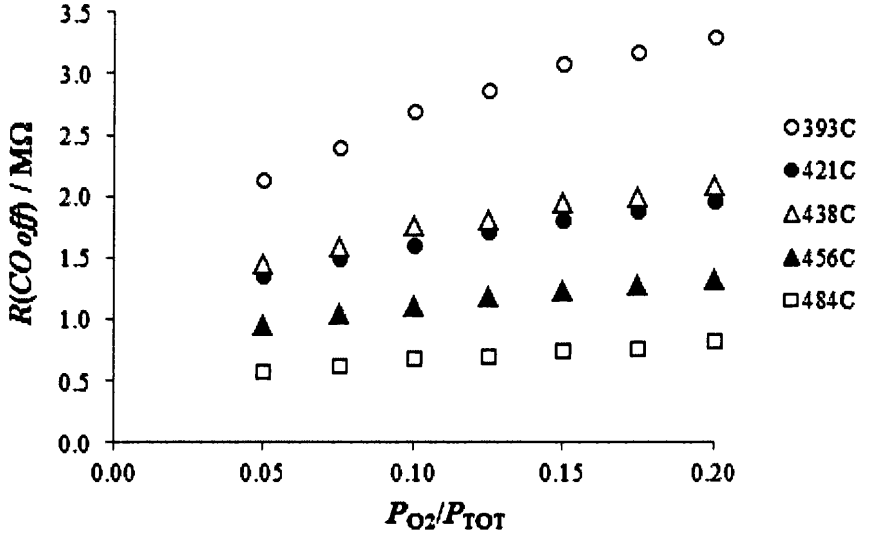

Fig. 5.4. A plot showing the variation of sensor resistance as a function of P_{O2}/P_{TOT} at different temperatures, with no CO present.

5.4.3. Estimation of α, R_0 and K_O

When formulating the model, it was mentioned that it is useful to express $1/\theta_O(CO\ on)$ as a function of P_{CO}/P_{TOT}, as in Eq. (5.32), an assertion which is justified by the observation that the two parameters are expected to exhibit a linear relationship when k_{r2} is sufficiently high. To realise why a direct proportionality between $1/\theta_O(CO\ on)$ and P_{CO}/P_{TOT} might be useful, it is instructive to first consider how both $\theta_O(CO\ on)$ and $\theta_O(CO\ off)$ may be determined from resistance measurements. According to Eq. (5.30), the resistance, R, is related to θ_O via two physical variables, namely R_0 and α. If the values of these parameters are known, it is therefore possible to deduce θ_O at any given time. Taking the natural logarithm of Eq. (5.30), $\ln(R)$ is expected to vary in direct proportion to θ_O^2. Moreover, the equation suggests that a plot of $\ln(R)$ as a function of θ_O^2 has gradient α and y-intercept $\ln(R_0)$, providing estimates for these two variables. Unfortunately, since θ_O cannot be measured directly, construction of the plot is not trivial.

In order to continue, Eq. (5.29) should be considered. This equation relates θ_O to P_{O2}/P_{TOT} in the absence of CO, through a third unknown parameter, K_O. Without additional information, it is clear that $\theta_O(CO\ off)$ cannot be calculated from measurements of P_{O2}/P_{TOT} as K_O is yet to be determined. However, after measuring R at multiple values of P_{O2}/P_{TOT} in the absence of CO, Eq. (5.29) and Eq. (5.30) may be used to construct multiple plots of $\ln(R)$ versus $\theta_O(CO\ off)^2$ for different "guess" values of K_O. For each K_O value, the gradient of the plot yields an estimate for α while the y-intercept is equal to $\ln(R_0)$. The requirement of a linear relationship potentially allows some of the K_O estimates to be discarded, as this behaviour does not necessarily exist for all of the guess values. Yet the value of K_O may not be sufficiently constrained by this consideration alone.

At this stage, it is helpful to investigate the relationship between R and P_{CO}/P_{TOT} at a particular value of P_{O2}/P_{TOT}. After measuring $R(CO\ on)$, Eq. (5.30) allows $\theta_O(CO\ on)$ to be calculated for each guess value of K_O from the corresponding estimates of α and $\ln(R_0)$. It is subsequently possible to plot $1/\theta_O(CO\ on)$ against P_{CO}/P_{TOT} for each K_O estimate. Provided that k_{r2} is much greater than $k_{r1}(P_{CO}/P_{TOT})$, $1/\theta_O(CO\ on)$ is expected to vary in direct

proportion to P_{CO}/P_{TOT} with the y-intercept equal to $1/\theta_O(CO\ off)$. These requirements impose additional constraints on the value of K_O.

As an example, one may consider a value of K_O which results in a direct proportionality between $\ln(R)$ and P_{O2}/P_{TOT}. In addition, the corresponding plot of $1/\theta_O(CO\ on)$ versus P_{CO}/P_{TOT} at a particular P_{O2}/P_{TOT} value is linear over the measured range but the y-intercept does not equal the expected value of $1/\theta_O(CO\ off)$. This estimate of K_O is unsuitable, as it does not satisfy all of the requirements imposed by the theory. Although the relationship between $1/\theta_O(CO\ on)$ and P_{CO}/P_{TOT} plot is linear over the concentration range of the resistance measurements, the fact that the extrapolated y-intercept differs from the expected value of $1/\theta_O(CO\ off)$ indicates that this proportionality would not be observed at lower concentrations.

Fig. 5.5 illustrates an iterative procedure to determine K_O at a particular temperature. Starting with a guess value of K_O, a plot of $\ln(R)$ vs $\theta_O(CO\ off)^2$ is constructed and used to deduce the relationship between $1/\theta_O(CO\ on)$ and P_{CO}/P_{TOT} at constant P_{O2}/P_{TOT}. If the requirements of the two plots are not simultaneously satisfied by the K_O estimate, as described above, the guess value is modified and the procedure repeated. By iterating in this way, it is possible to obtain a well-constrained estimate of K_O, as well as the corresponding values of α and R_0.

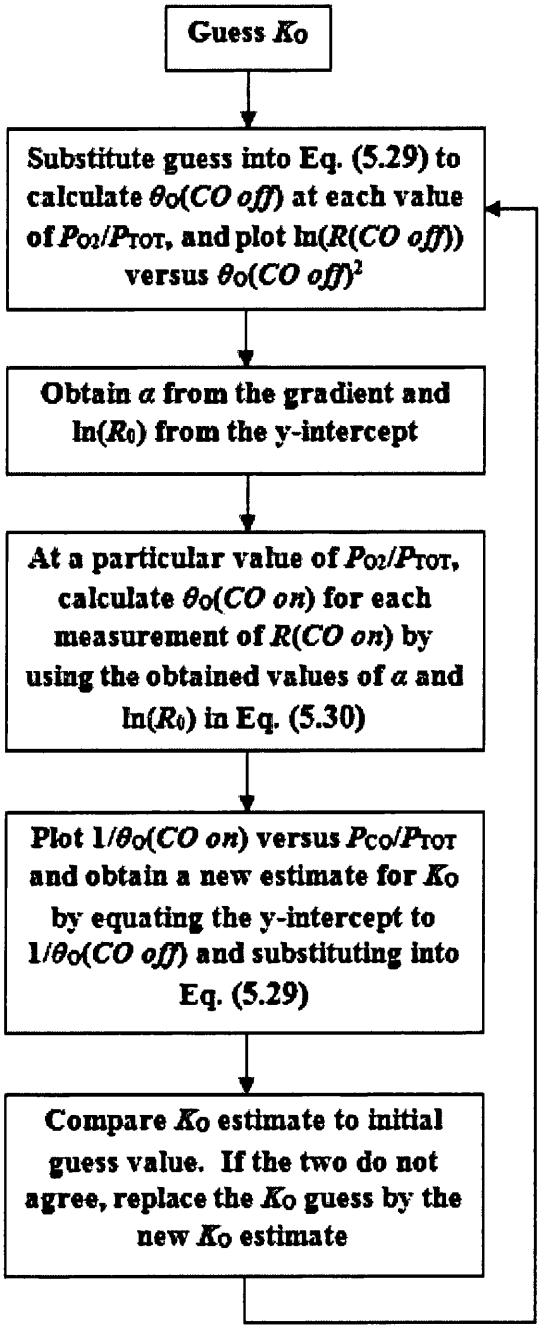

Fig. 5.5. A flowchart illustrating an iterative procedure for precisely estimating α, R_0 and K_O.

5.4.4. Resistance measurements at different concentrations of O_2

In order to obtain accurate estimates for α and R_0 at each working temperature, the resistance of the sensor was measured at different partial pressures of oxygen. The remainder of the gas environment consisted of pure nitrogen, with no CO present. According to Eq. (5.30), R is anticipated to exhibit an exponential relationship with θ_O^2 if the ZnO particles are sufficiently large. As shown by Fig. 5.6, this was observed experimentally at every temperature, with the gradients and y-intercepts from least-squares linear fits providing estimates for α and $\ln(R_0)$, respectively. However, the form of each plot is dependent on K_O, and this is not well constrained by this experiment alone. As discussed, it is necessary to investigate the effects of CO to obtain more precise estimates of K_O. It should be noted that Fig. 5.6 has been constructed using the final K_O estimates obtained from the iterative approach outlined in Fig. 5.5.

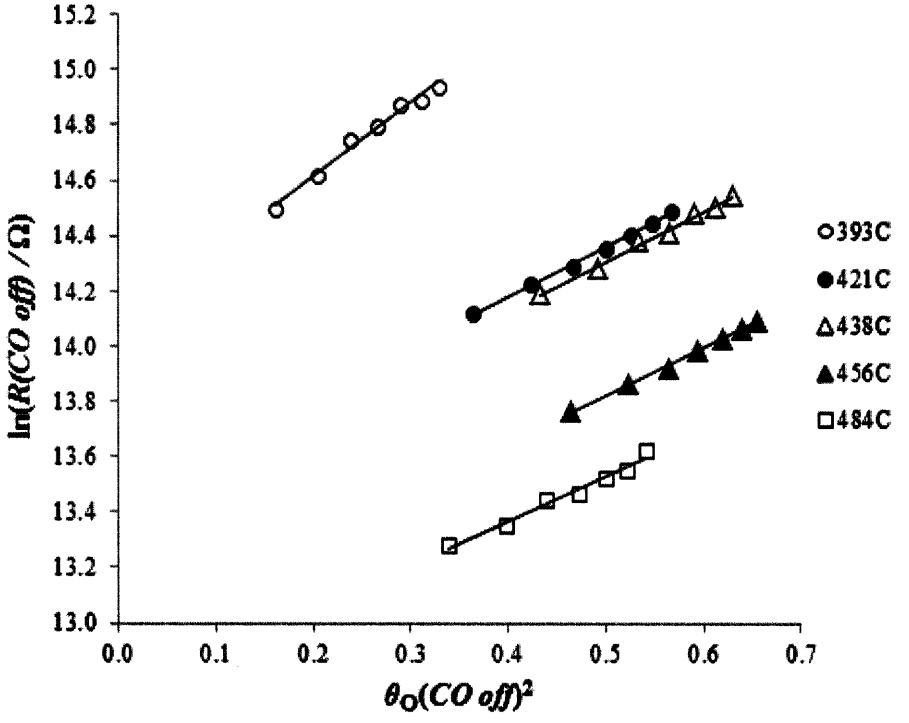

Fig. 5.6. A plot of $\ln(R(CO\ off))$ as a function of $\theta_O(CO\ off)^2$ at different working temperatures. The value of P_{O2}/P_{TOT} is varied between 0.05 and 0.2 in each case, in steps of 0.025. A least-squares linear fit is applied to each data-set, and all fits have an R^2 value of 0.98 or higher.

5.4.5. Response measurements at different concentrations of CO

To observe the relationship between $1/\theta_O(CO\ on)$ and P_{CO}/P_{TOT}, the response of the sensor was measured at different concentrations of CO with P_{O2}/P_{TOT} maintained at a value of 0.2 throughout. Plots of $1/\theta_O(CO\ on)$ versus P_{CO}/P_{TOT} are shown in Fig. 5.7; at each temperature, the K_O value used is the same as for the corresponding plot in Fig. 5.6. There is a clear linearity in the results at every temperature, indicating that k_{r2} is much greater than $k_{r1}(P_{CO}/P_{TOT})$ and the second reaction step in Eq. (5.3) occurs much more rapidly than the first.

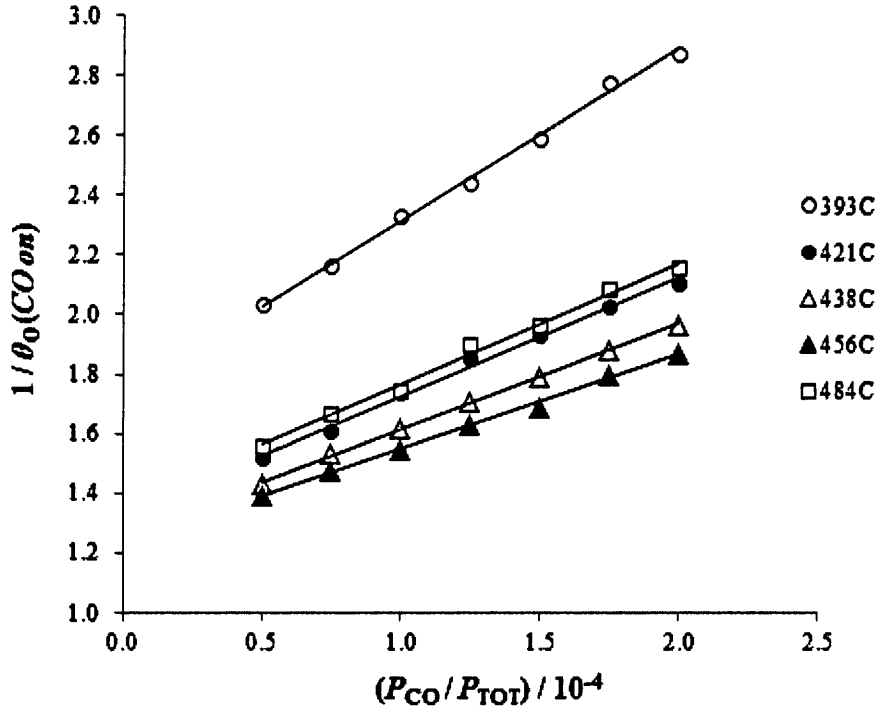

Fig. 5.7. A plot of $1/\theta_O(CO\ on)$ as a function of P_{CO} at different working temperature. The CO concentration is varied in the range 50–200 ppm in steps of 25 ppm. A least-squares linear fit is applied to each data-set, and all fits have an R^2 value of 0.99 or higher.

From Fig. 5.6 and Fig. 5.7 it is possible to infer the values of K_O, α and R_0. Together, these provide the means to fit the model to response and recovery curves and estimate further reaction parameters. However, the precision of the estimates is reliant on the effectiveness of the iteration procedure outlined in Fig. 5.5. After using an initial value of K_O, $K_O(in)$, to plot

$1/\theta_O(CO\ on)$ as a function of P_{CO}/P_{TOT}, the y-intercept provides a new K_O estimate, $K_O(out)$. If the two K_O values differ, $K_O(out)$ is used as the initial estimate in the next step of the iteration. As shown by Fig. 5.8, it is informative to consider the disparity between the two K_O values as a function of $K_O(in)$, as this determines the precision of the final K_O estimate yielded by the iteration process. To aid comparison between temperatures, the magnitude of the difference between $K_O(in)$ and $K_O(out)$ is expressed as a percentage of $K_O(in)$. At each temperature, it is apparent that the magnitude of the difference increases rapidly away from the point of agreement. The final value of K_O output by the iteration procedure is therefore well constrained, as even small deviations in the estimate lead to significant inconsistencies between $K_O(in)$ and $K_O(out)$.

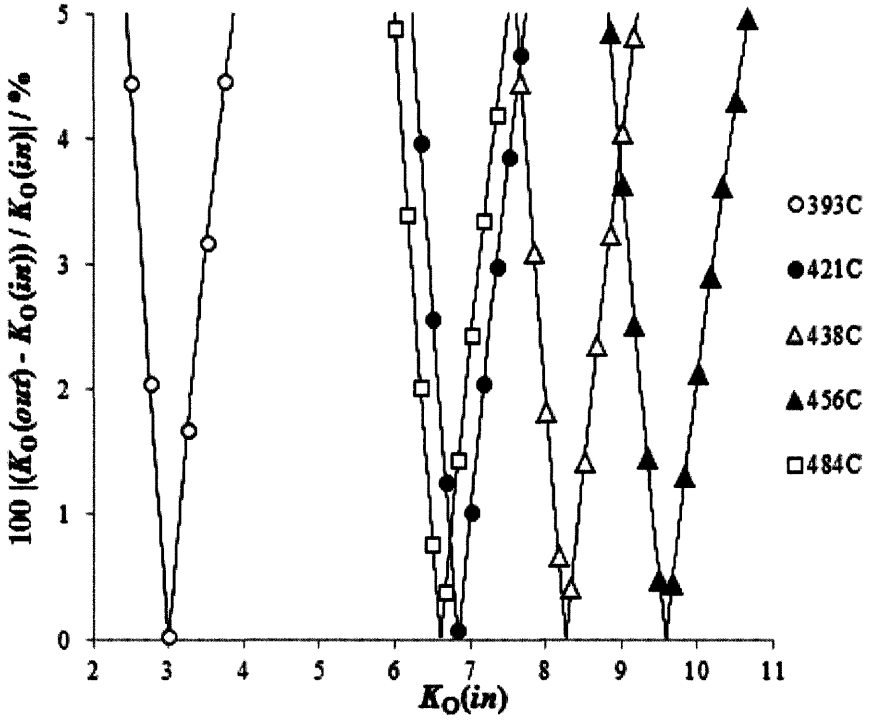

Fig. 5.8. A plot of the magnitude of the percentage difference between the initial value of K_O used in an iteration step, $K_O(in)$, and the K_O estimate obtained from the y-intercept of Fig. 5.7, $K_O(out)$, as a function of $K_O(in)$.

It is apparent from Fig. 5.8 that there exists a temperature at which K_O is maximised, as the x-intercept of the plot is higher for a temperature of 456°C than for temperatures above or below this value. This is shown more explicitly in Fig. 5.9, which depicts K_O as a function of

temperature. Also plotted is the response of the sensor, defined by Eq. (5.31), to 200 ppm CO. The peak response approximately coincides with the maximum K_O value, which suggests that the sensitivity of the sensor to CO is determined predominantly by the oxygen coverage. At the lower temperatures, there is little energy available for the formation of O^- ions and hence K_O is low. Similarly, the reaction between CO molecules and O^- ions is slow, leading to a low sensor response. As the temperature is increased, O^- ions form more rapidly and react with CO at an enhanced rate. However, the rate of O^- formation cannot rise indefinitely, as it is limited by the concentration of unoccupied surface sites. Moreover, the reverse reaction, shown in Eq. (5.2), also increases with temperature, resulting in K_O decreasing at sufficiently high temperature values. Although the probability of a CO molecule reacting with an O^- ion is increased at these temperatures, the lowered concentration of O^- ions leads to a suppressed reaction rate and a corresponding decrease in the sensor response.

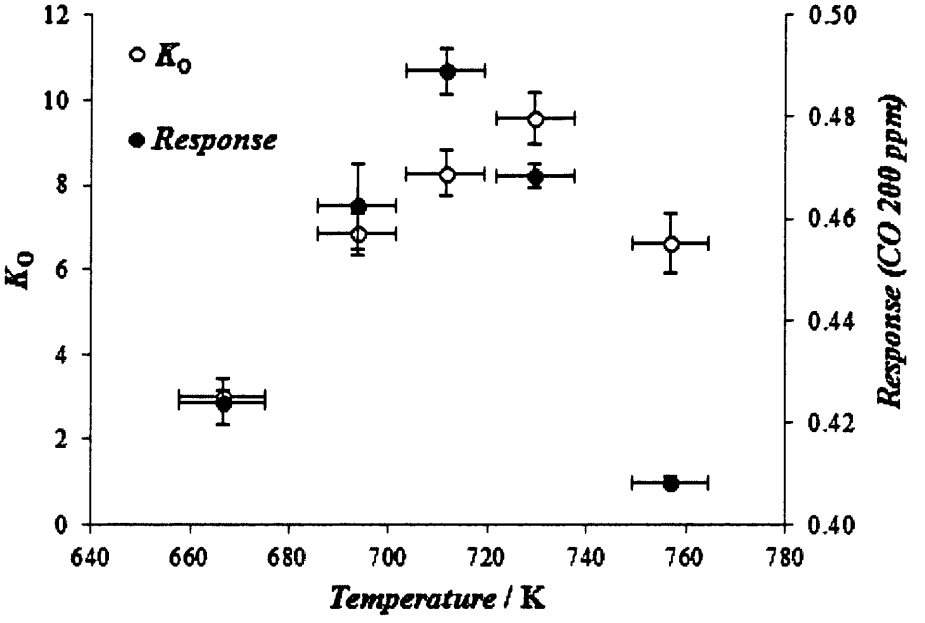

Fig. 5.9. A plot of K_O (left-hand axis) and response to 200 ppm CO (right-hand axis) as a function of temperature.

5.4.6. Fitting the theoretical model to response and recovery curves

Once estimates for α and K_O have been obtained, it is possible to fit the model to response and recovery traces using Eq. (5.24) and Eq. (5.28) respectively. However, it is still necessary to manually input estimates for two of three further parameters, namely k_{-1}, k_{r1} and k_{r2}. The third of these variables can be calculated from the other two using the measured gradient from Fig. 5.7 in conjunction with Eq. (5.32). It is worth remembering that the linear trends observed in Fig. 5.7 are indicative of a k_{r2} value that is far greater in magnitude than $k_{r1}P_{CO}/P_{TOT}$. A further observation is that the best fits to the response and recovery curves are obtained by assuming that k_{r2} is much larger than k_{-1}. These approximations vastly simplify the process of selecting appropriate parameter values as they remove all dependence on k_{r2} from the pre-exponential factors in both Eq. (5.24) and Eq. (5.28). In effect, the k_{r2} dependence is confined to the exponent itself, and therefore only influences the response or recovery at low values of t. Consequently, fits to the response and recovery curves are only weakly affected by even large changes in k_{r2}. It is therefore only necessary to estimate a single parameter accurately, simplifying the fitting procedure and ensuring that it delivers unique solutions. The resulting fits to the response and recovery traces at a CO concentration of 200 ppm are displayed in Fig. 5.10 and Fig. 5.11, respectively; data are normalised with respect to the starting resistance and successive curves are arbitrarily offset to aid comparison.

The plots clearly show that the response and recovery rates increase with temperature. It has been noted that Eq. (5.23), describing the time variation of θ_{CO}, is an approximation which is only justified when θ_O changes sufficiently slowly. It shall be demonstrated later that this is indeed the case for every response and recovery curve described in this investigation.

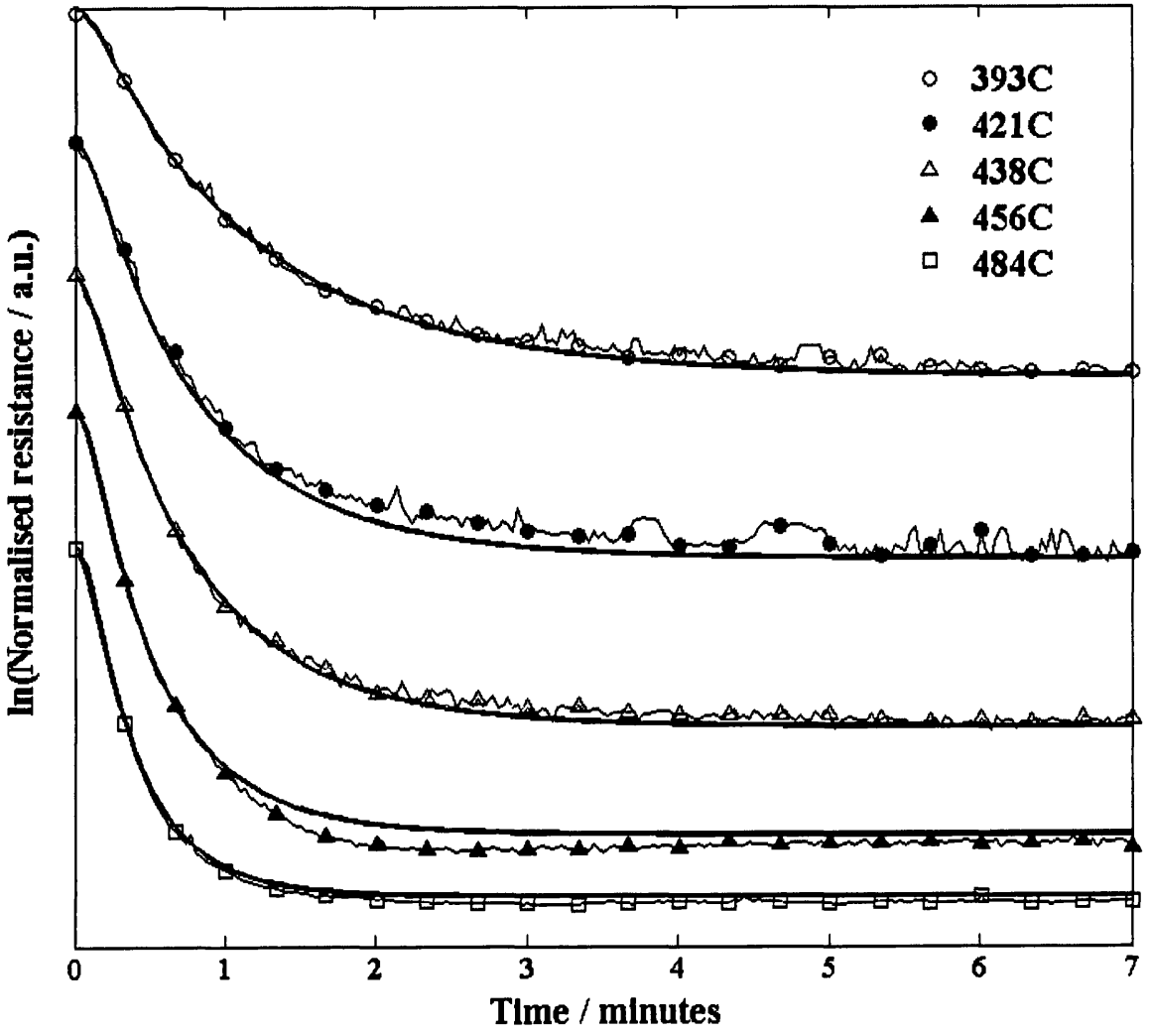

Fig. 5.10. Response curves at different working temperatures and a CO concentration of 200 ppm, fitted using Eq. (5.24) and altering k_{-1} and k_{r2} manually. The curves are normalised with respect to the starting resistance, and the fit to each response curve is depicted by a thick black line. Successive curves are arbitrarily offset to aid comparison.

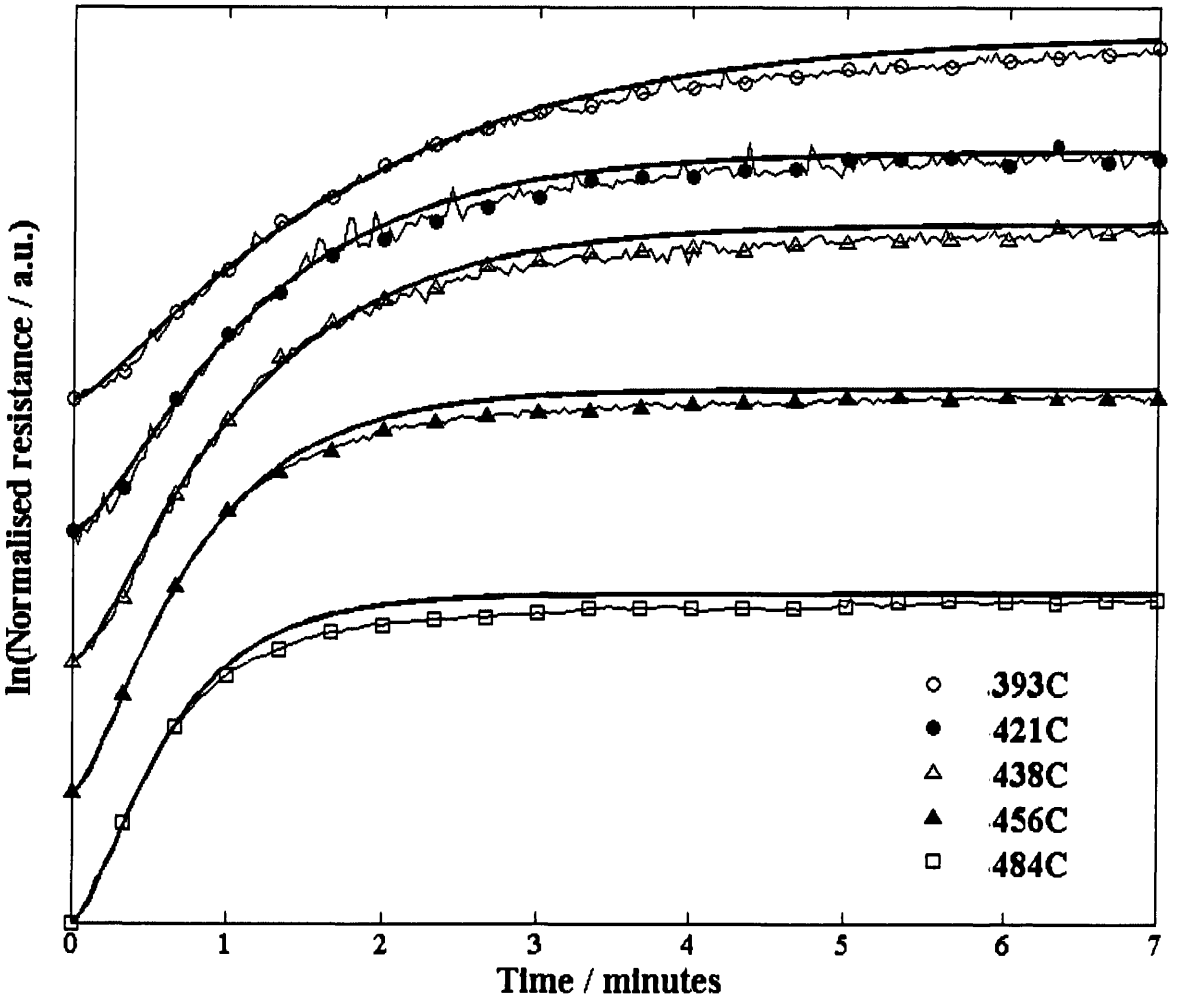

Fig. 5.11. Recovery curves at different working temperatures and a CO concentration of 200 ppm, fitted using Eq. (5.28) and altering k_{-1} and k_{r2} manually. The curves are normalised with respect to the starting resistance, and the fit to each response curve is depicted by a thick black line. Successive curves are arbitrarily offset to aid comparison.

5.4.7. Estimating the activation energies of the surface reactions

Having fitted the theoretical model to the resistance measurements, it is possible to further investigate the physics of the surface reactions by comparing the reaction parameters obtained under different conditions. Fig. 5.12 and Fig. 5.13 show the k_1 and k_{r1} values obtained from the fits in Fig. 5.10 and Fig. 5.11 plotted as a function of temperature; it is clear in both cases that the since the rate constant increases with temperature, so too does the corresponding reaction rate.

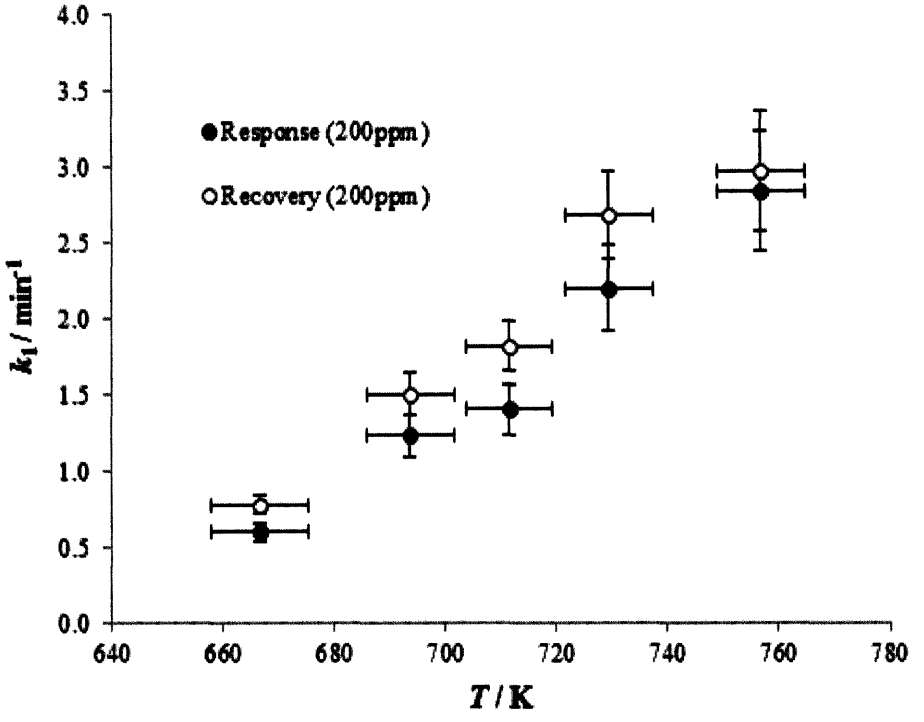

Fig. 5.12. A plot showing the variation of k_1 values, estimated from the fits to the response and recovery curves in Fig. 5.10 and Fig. 5.11, respectively, as a function of temperature.

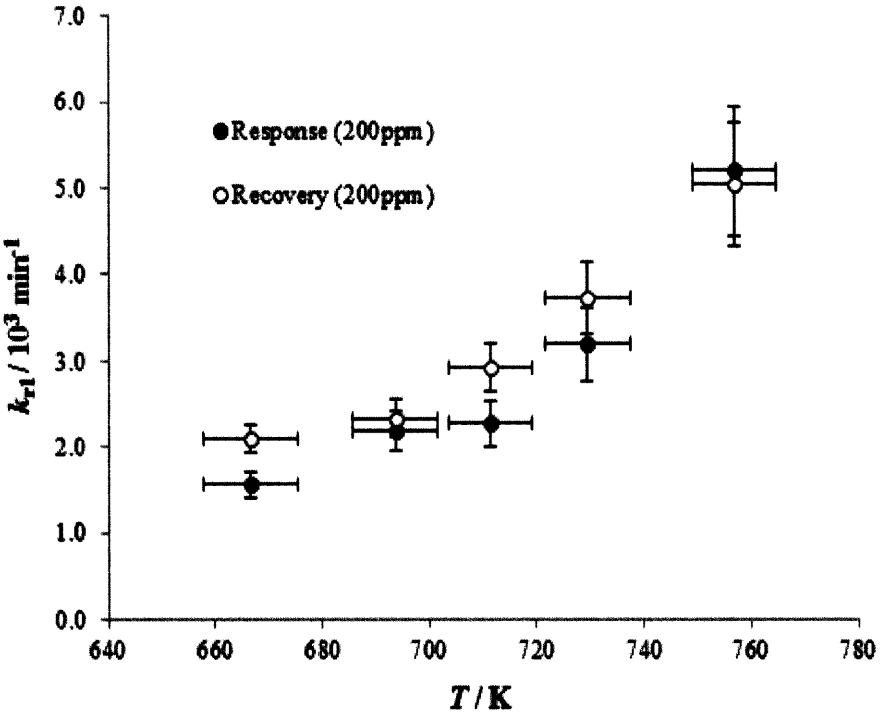

Fig. 5.13. A plot showing the variation of k_{r1} values, estimated from the fits to the response and recovery curves in Fig. 5.10 and Fig. 5.11, respectively, as a function of temperature.

It is often found that the rate of a chemical reaction exhibits an exponential dependence on temperature, so useful kinetic parameters may be obtained from an Arrhenius plot, wherein the natural logarithm of the rate constant is plotted as a function of $1/T$. The rate constant, k_i, is related to the molar activation energy, E_i, of the reaction through the equation

$$\ln(k_i) = \ln(\lim_{T\to\infty} k_i) - \frac{E_i}{R_M T} \tag{5.33}$$

where R_M is the molar gas constant. For instance, the energy barrier for the formation of O^- ions from molecular oxygen may be deduced by constructing an Arrhenius plot for rate constant k_1, as shown in Fig. 5.14. Using values obtained from the measured response at a CO concentration of 200 ppm, a least-squares linear fit of the data yields an activation energy estimate of 72 ± 9 kJ mol^{-1}. If the recovery curves are considered instead, an alternative estimate of 63 ± 10 kJ mol^{-1} is obtained. These values are of similar magnitude to the activation energies of similar processes reported elsewhere; separate investigations into the

ionisation of oxygen at the surface of ZnO report activation energies of 69 kJ mol^{-1} [18] and 83 kJ mol^{-1} [19], while another study calculates the energy barrier for the formation of O^- ions on TiO_2 as 77 kJ mol^{-1} [20].

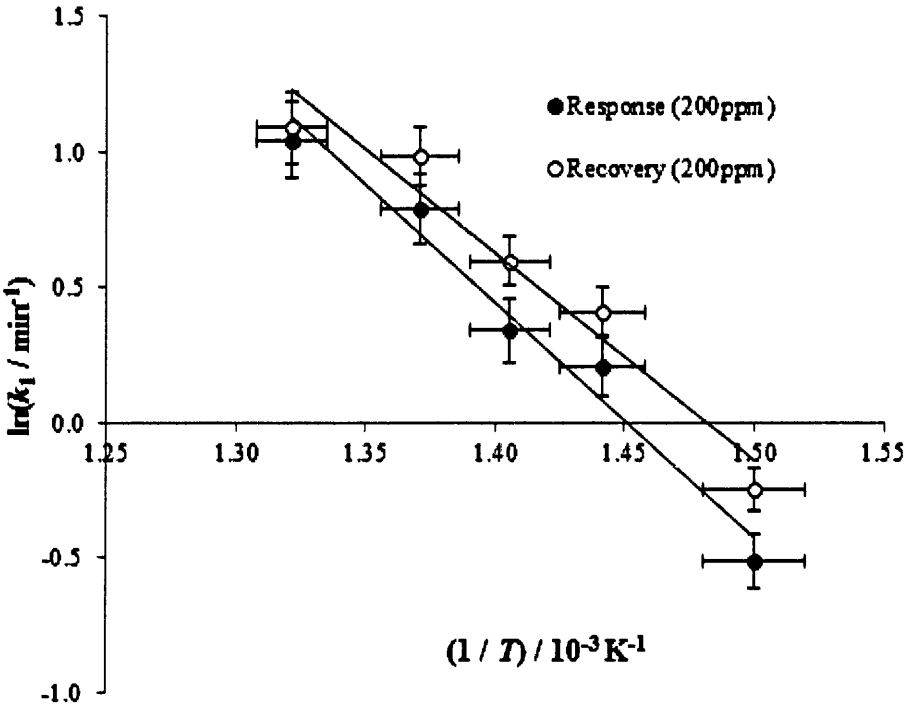

Fig. 5.14. A plot of $\ln(k_1)$ as a function of $1/T$, constructed using response and recovery curves at a CO concentration of 200 ppm. A least-squares linear fit is applied to each data-set as shown, and R^2 values of 0.97 and 0.95 are calculated for the fits to the response and recovery data, respectively.

Fig. 5.15 depicts an Arrhenius plot for the rate constant k_{r1}, corresponding to the reaction of O^- ions with CO. Considering the response and recovery curves separately, as before, it is apparent that the expected linearity exists for both sets of results. Using Eq. (5.33) to interpret Fig. 5.15 and again employing a least-squares linear fit, the response curves yield an activation energy estimate of 54 ± 9 kJ mol^{-1}, whereas the recovery curves lead to a value of 42 ± 7 kJ mol^{-1}. These estimates are consistent with previous research, in which activation energies of 39–42 kJ mol^{-1} have been deduced through measurement of the reaction kinetics and computational modelling [21–24].

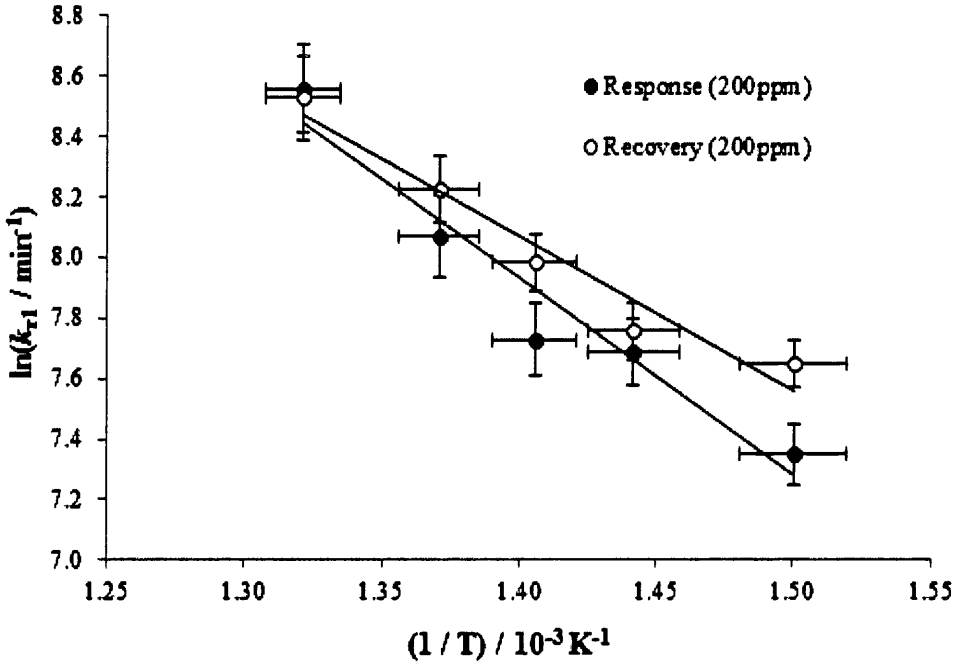

Fig. 5.15. A plot of $\ln(k_{r1})$ as a function of $1/T$, constructed using response and recovery curves at a CO concentration of 200 ppm. A least-squares linear fit is applied to each data-set as shown, and R^2 values of 0.94 and 0.95 are calculated for the fits to the response and recovery data, respectively.

5.4.8. Investigating the temperature-dependence of the surface potential

To explore the nature of the potential barrier at the ZnO surface, one may consider how the resistance in the absence of O^- or CO_2^- ions, R_0, varies as a function of temperature. When the applied electric potential is sufficiently low, thermoelectronic emission theory dictates that for a porous semiconductor containing a concentration $n_{C,S}$ of free surface electrons, the resistance, R, obeys the relation [15]

$$R \propto \frac{\sqrt{T}}{n_{C,S}} \tag{5.34}$$

as shown in Chapter 1. It is known that in a typical semiconductor, $n_{C,S}$ is given by [25]

$$n_{C,S} = N_C \exp\left(-\frac{E_{C,S}-E_F}{k_B T}\right) \tag{5.35}$$

where E_F and E_C are the Fermi Energy and the energy of the conduction band minimum at the surface, respectively, and k_B is Boltzmann's constant. The pre-exponential factor, N_C, scales in direct proportion to $T^{3/2}$. The value of $E_{C,S}$ depends on the concentration of ions adsorbed at the surface, which is a temperature-dependent quantity. However, in the absence of O^- or CO_2^- ions, the magnitude of the surface potential barrier, and therefore $E_{C,S}$, is assumed to remain constant as the temperature is varied. In addition, if the range of measured temperatures is sufficiently small, the variation of E_F may also be neglected. Combining Eq. (5.34) with Eq. (5.35) and imposing the condition that no O^- or CO_2^- ions are present, one obtains the expression

$$\ln(R_0) + \ln(T) = \frac{E_{C,S}-E_F}{k_B T} + A \tag{5.36}$$

where A is a temperature-independent constant. If, as predicted, $E_{C,S}$-E_F remains constant over the measured range of temperatures, a plot of the sum of $\ln(R_0)$ and $\ln(T)$ as a function of $1/T$ ought to be linear with gradient equal to $(E_{C,S}$-$E_F)/k_B$. Fig. 5.16, which utilises the $\ln(R_0)$ estimates obtained from Fig. 5.6, demonstrates that this linearity exists within the experimental error, and the gradient of a least-squares linear fit yields an estimate of 590 ± 90 meV for $E_{C,S}$-E_F. It should be emphasised that this value is only applicable in the absence of O^- or CO_2^- ions, and is increased by an amount equal to $\alpha\theta_O^2 k_B T$ when such ions are present.

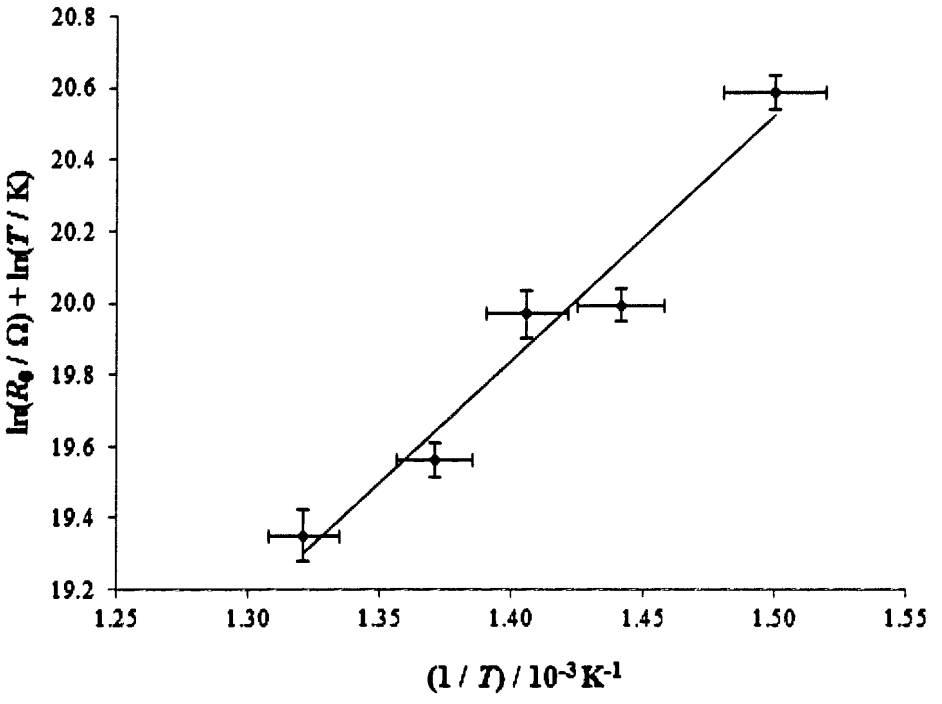

Fig. 5.16. A plot of $\ln(R_0)+\ln(T)$ as a function of $1/T$, constructed using estimates obtained from Fig. 5.6. A least-squares linear fit is applied to the data as shown, and has a calculated R^2 value of 0.96.

It is possible to verify the accuracy of the estimated $E_{C,S}$-E_F value through use of XPS. After annealing a sample of LBZA nanosheets on silicon at 500°C, the valence band was scanned at room temperature using monochromatic X-rays of energy 1486.6 eV. Since the XPS measurements were performed under ultra-high vacuum, one may infer that the surface was free of both O^- and CO_2^- surface species. As shown by Fig. 5.17, which depicts the XPS spectrum of the sample at low binding energies, the valence band maximum was measured at a binding energy of more than 3 eV, which is measured relative to the Fermi level. Applying a protocol reported elsewhere [26], the energy of the valence band maximum relative to the Fermi level, E_F-$E_{V,S}$, may be estimated from the intersection of two least-squares linear fits either side of the cut-off in the XPS valence-band scan, as shown in the plot. In this instance, a value of 3.11 ± 0.05 eV is obtained for E_F-$E_{V,S}$.

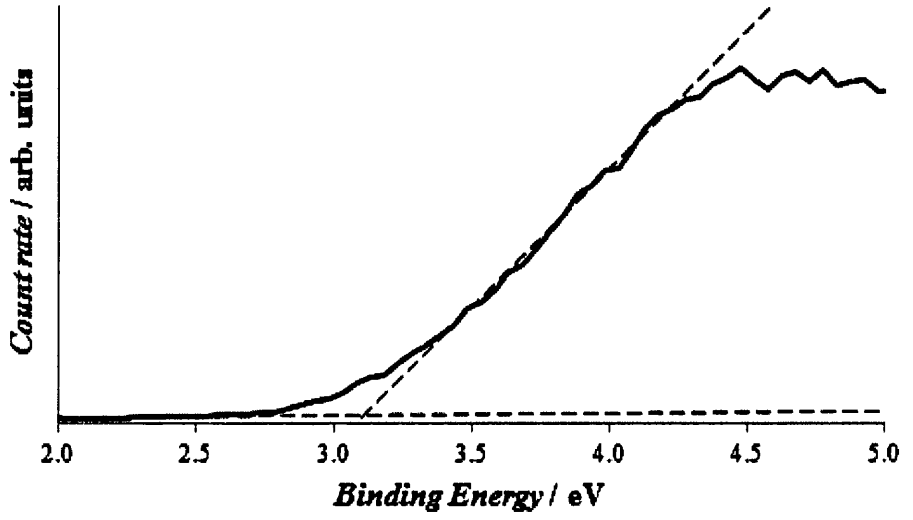

Fig. 5.17. A plot displaying a valence band XPS spectrum of ZnO nanosheets annealed in dry air at 500°C. Also shown are the least-squares linear fits (dashed lines) used to estimate the energy of the valence band maximum relative to the Fermi level, E_F-$E_{V,S}$. The measurements were obtained at room temperature, using monochromatic X-rays of energy 1486.6 eV.

To calculate the energy difference between the Fermi level and the conduction band minimum, it is necessary to first determine the value of the band-gap. To this end, the ZnO nanosheets were further examined using photoluminescence spectroscopy, illuminating the sample using a He-Cd laser source of wavelength 325 nm. The resulting spectrum, displayed in Fig. 5.18, exhibits a near-band-edge peak at a wavelength of 377 nm, from which the value of $E_{C,S}$-$E_{V,S}$ may be estimated as 3.36 eV (assuming an exciton binding energy of 60 meV, as in Chapter 4). In turn, $E_{C,S}$-E_F has a calculated value of 240 ± 50 meV, which is significantly lower than the estimate obtained from Fig. 5.16. It is important to recognise, however, that the two estimates are not directly comparable due to the different experimental conditions present in each case; while the results in Fig. 5.16 were obtained using a 400 mL min^{-1} gas flow at temperatures close to 400°C, the XPS spectrum in Fig. 5.17 was measured in ultra-high vacuum at room temperature (approximately 25°C). Indeed, it is possible that the concentrations of intrinsic surface species such as hydroxyl radicals vary as a function of temperature, resulting in the surface potential changing between 25°C and 400°C even when no O^- or CO_2^- ions are present. It was also demonstrated in Chapter 1 that the value of E_F is

influenced by temperature, and it will be shown that $E_{C,S}$-E_F is therefore expected to change by a significant amount as the temperature is increased from 25°C to 400°C.

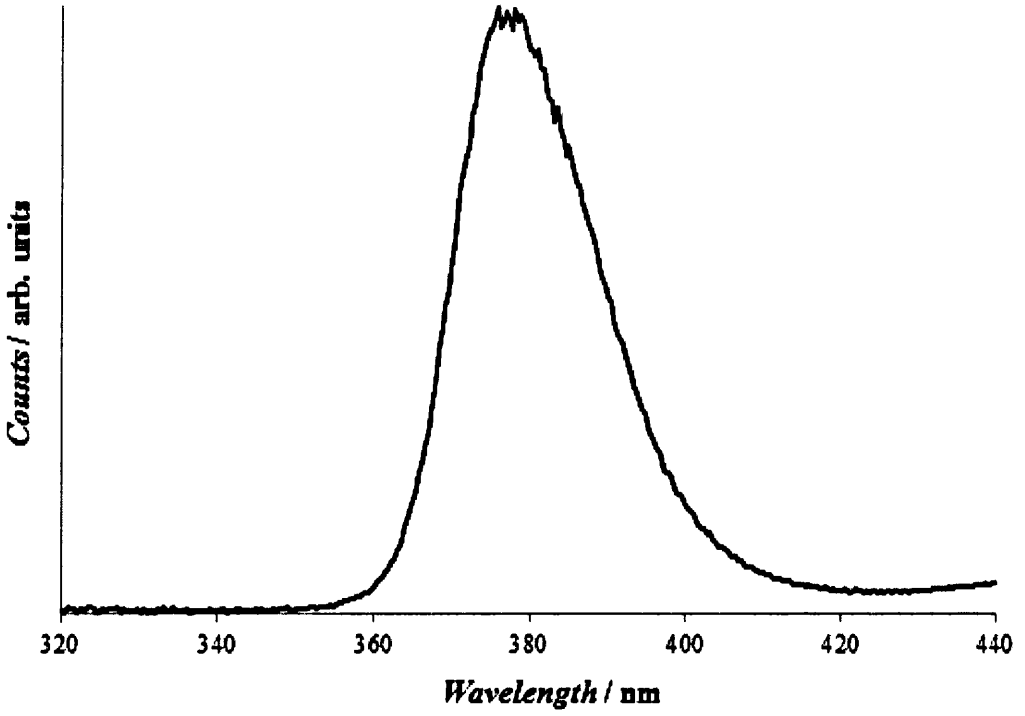

Fig. 5.18. A plot showing the near-band-edge (NBE) peak in the photoluminescence spectrum of ZnO nanosheets annealed at 500°C.

Revisiting the theory outlined in Chapter 1, one may show that in the bulk of a degenerate semiconductor containing uncompensated donor states, E_F is related to the energies of the donor states, $E_{D,b}$, and conduction band minimum, $E_{C,b}$, via the equation [27]

$$E_F = E_{D,b} + k_B T \ln\left(\frac{1}{2g}\left(-1 + \sqrt{1 + 4g\frac{N_D}{N_C}\exp\left(\frac{E_{C,b}-E_{D,b}}{k_B T}\right)}\right)\right) \tag{5.37}$$

where N_D is the concentration of donor states, which have spin degeneracy g, and N_C is the effective density of states in the conduction band, given by

$$N_C = 4\sqrt{2}\left(\frac{\pi m^* k_B T}{h^2}\right)^{\frac{3}{2}} \tag{5.38}$$

Here, m^* is the effective mass of conduction electrons and h is Planck's constant. Studies in the literature report characteristic values of $2.2\text{x}10^{-31}$ kg (0.24 times the mass of a free electron) [28–31] and 700 meV [32,33] for m^* and $E_{C,b}$-$E_{D,b}$, respectively, while estimates of N_D typically vary between 10^{17} cm^{-3} and 10^{19} cm^{-3} [34,35]. Assuming that the donor level consists predominantly of states which may each contain two electrons but cannot doubly-ionise, it is appropriate to employ a g value of two. If one further assumes that N_D adopts a value of 10^{18} cm^{-3}, E_F-$E_{D,b}$ is calculated as 330 meV at 25°C, decreasing to approximately 260 meV at 400°C. By alternatively assuming that the donor states are able to contain just one electron, thereby decreasing g to a value of one, one obtains an E_F-$E_{D,b}$ estimate of 340 meV at 25°C and 280 meV at 400°C. Subtracting the 25°C estimates of E_F-$E_{D,b}$ from the assumed $E_{C,b}$-$E_{D,b}$ value of 700 meV yields corresponding $E_{C,b}$-E_F estimates of 360 meV and 370 meV for g values of one and two, respectively, each of which is greater than the measured value of $E_{C,S}$-E_F from Fig. 5.17. This scenario is clearly not possible unless downward band-bending exists at the surface, which in turn necessitates electron-donation by the surface species. If, as assumed hitherto, the ZnO is instead depleted of electrons close to the surface, alternative values must be sought for some or all of the physical parameters in Eq. (5.37).

Having calculated the value of $E_{C,S}$-E_F, it is possible to go further by estimating the magnitude of the surface potential energy, $q\phi_B$. At temperatures close to 400°C, the value of $E_{C,S}$-E_F was calculated as approximately 590 meV in the absence of O^- or CO_2^- ions while an $E_{C,b}$-E_F estimate of 420–440 meV may be inferred from the values of E_F-$E_{D,b}$ calculated above (again assuming an $E_{C,b}$-$E_{D,b}$ value of 700 meV). Subtracting $E_{C,b}$-E_F from $E_{C,S}$-E_F provides an estimate for the surface potential energy, $q\phi_B$, which is in this case is approximately 150–170 meV. As detailed previously, this value is increased by an amount $k_BT\alpha\theta_O^2$ when O^- or CO_2^- ions are present.

It is important to recall that estimation of $E_{C,S}$-E_F from Fig. 5.16 may only be justified if the thermoelectronic emission model is valid, and it was shown in Chapter 1 that this is only true for systems in which the mean free path of electrons is larger than the width of the potential barrier. In cases where the surface potential is very large, it is more appropriate to make use of the drift-diffusion model of current flow, yielding the relationship

$$R \propto \frac{c(T)}{n_{C,S}\sqrt{\phi_B}} \tag{5.39}$$

where $c(T)$ is a function that depends on a variety of temperature-dependent quantities, as outlined in Chapter 1. Since ϕ_B is directly proportional to θ_O^2, it follows that

$$\ln(R) = \ln(R_0) + \alpha\theta_O^2 - \ln(\theta_O) \tag{5.40}$$

where α and R_0 are temperature-dependent constants, as before, and do not depend on θ_O. In contrast to Eq. (5.30), which is applicable in the case of the thermoelectronic emission model, Eq. (5.40) implies that $\ln(R)$ may not be directly proportional to θ_O^2 due to the presence of a non-linear θ_O-dependent term. As all five plots in Fig. 5.6 demonstrate a clear proportionality between $\ln(R)$ and θ_O^2 over the measured range of P_{O2}/P_{TOT} values, any prediction of a non-linear relationship between these quantities would be patently incompatible with experiment. It transpires, however, that the inclusion of the logarithmic θ_O-dependent term in Eq. (5.40) is indeed consistent with the observations of Fig. 5.6; as predicted by this equation, plotting the sum of $\ln(R)$ and $\ln(\theta_O)$ as a function of θ_O^2 at each temperature reveals a linear relationship over a wide range of K_O values. As a consequence of this behaviour, it is not possible to verify the applicability of either of the proposed conductivity models from Fig. 5.6 alone. Nonetheless, the estimated surface potential energy in the absence of O^- or CO_2^- ions, calculated as 150–170 meV, is only up to three times larger than the thermal energy at 400°C, so is not sufficiently large for the drift-diffusion conduction model to be representative of the system.

As a final consideration, it is interesting to examine the behaviour of α as the temperature is varied. It was demonstrated in Chapter 1 that this parameter is influenced by several physical variables, including the permittivity and the concentration of surface sites, and has an explicit inverse proportionality to temperature. Fig. 5.19 shows a plot of the calculated α values as a function of $1/T$, which indicates that while the relationship is linear within experimental error between the four highest temperatures, α is much higher than expected at a temperature of 393°C. This divergence from the expected trend implies that some of the physical parameters in Eq. (1.11), which defines α, are themselves dependent on temperature; it has been

demonstrated elsewhere, for instance, that the permittivity of ZnO and other semiconductors do not necessarily remain constant with changing temperature [36,37].

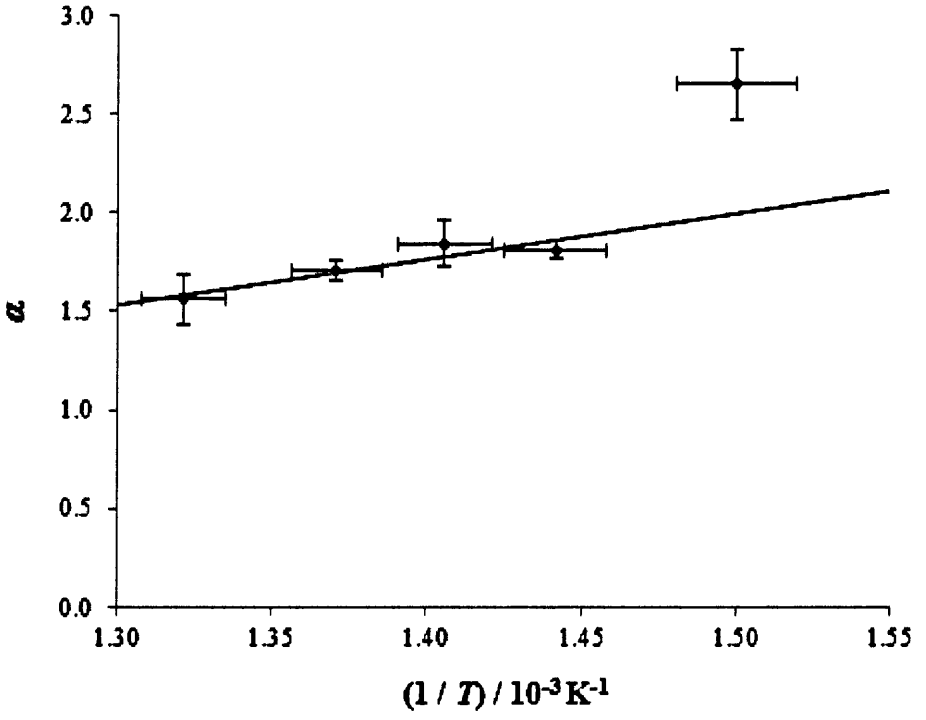

Fig. 5.19. A plot showing the estimated values of α as a function of $1/T$. A least-squares line-of-best-fit has been fitted to the data points corresponding to the highest four temperatures, and has an R^2 value of 0.86.

5.4.9. Experimental justification of Eq. (5.23)

Earlier in the chapter, formulae were constructed to describe the variation of θ_{CO} during the response or recovery of the sensor. In particular, Eq. (5.22) provides an exact solution for θ_{CO}, but its use is limited by the dependence on θ_O in the third term, which couples the equation to Eq. (5.17). As a result, these two equations must be solved simultaneously, but each is too complicated for the solutions to be obtained analytically. In cases where $\ln(\theta_O)$ varies much more slowly than $\ln([CO_2^-])$, it is possible to overcome this difficulty by neglecting the final term of Eq. (5.22), thereby removing the explicit dependence on θ_O. Although this approximation is not applicable to all systems, it is important to recall that the form of $\theta_O(t)$ may be calculated prior to estimating the rate constants of the system. The values of K_O, α and $\ln(R_0)$ may be determined by measuring the equilibrium sensor resistance

as a function of the partial pressures of O_2 and CO, and these parameters alone are required to deduce the value of θ_O for any non-equilibrium resistance measurement. This is an important point, as the calculated relationship between R and θ_O is therefore solely dependent on the conditions at the start and end of the response or recovery curve. As previously mentioned, these regimes are always well described by the approximate form of Eq. (5.22) given by Eq. (5.23), and hence $\theta_O(t)$ is unaffected by the disparities between the two equations.

After calculating $\theta_O(t)$ from the various resistance measurements, the response and recovery curves may be fitted using Eq. (5.17) in order to estimate the rate constants of the system. This procedure requires knowledge of $\theta_{CO}(t)$, which is described exactly by Eq. (5.22). Solving Eq. (5.22) requires use of an integrating factor, $f(t)$, that allows the equation to be written in the form

$$\frac{\mathrm{d}}{\mathrm{d}t}\left(f(t)\theta_{CO}(t)\right) = k_{r1}\left(\frac{P_{CO}}{P_{TOT}}\right)f(t) \tag{5.41}$$

Comparison with Eq. (5.22) shows that an appropriate expression for $f(t)$ is

$$f(t) = \theta_O(t)\exp(\gamma_{CO}t) \tag{5.42}$$

where γ_{CO} is given by

$$\gamma_{CO} = k_{r1}\left(\frac{P_{CO}}{P_{TOT}}\right) + k_{r2} \tag{5.43}$$

For a response curve, integration of Eq. (5.41) yields the solution

$$\theta_{CO}(t) = k_{r1}\left(\frac{P_{CO}}{P_{TOT}}\right)\frac{1}{\theta_O(t)}\int_0^t \theta_O(t')\exp\left(\gamma_{CO}(t'-t)\right)\mathrm{d}t' \tag{5.44}$$

where time, t, is zero at the point of CO turn-on. If k_{r1} and k_{r2} are known, it is therefore possible to determine a function $\theta_{CO}(t)$ that satisfies Eq. (5.41). Unfortunately, if the rate constants are themselves estimated through fitting of the response curves using Eq. (5.17), $\theta_{CO}(t)$ can only be found through iteration. After formulating an initial "guess" for $\theta_{CO}(t)$, it

is possible to determine k_{r1} and k_{r2} by fitting the response curve using Eq. (5.17) as discussed in section 5.45. Substituting the k_{r1} and k_{r2} estimates into Eq. (5.22) allows $\theta_{CO}(t)$ to be recalculated, which may then be used in Eq. (5.17) as before to obtain revised values of k_{r1} and k_{r2}. Continuous iteration of this procedure eventually yields k_{r1} and k_{r2} estimates that are consistent with the calculated forms of both $\theta_{CO}(t)$ and $\theta_O(t)$.

Similar considerations may be applied to the sensor recovery. Here, the partial pressure of CO is zero and so Eq. (5.22) becomes

$$\frac{d\theta_{CO}}{dt} = -\theta_{CO}\left(k_{r2} + \frac{d}{dt}(\ln(\theta_O))\right) \tag{5.45}$$

where t is zero at the point of CO turn-off. Eq. (5.45) integrates to give

$$\theta_{CO}(t) \propto \frac{1}{\theta_O(t)}\exp(-k_{r2}t) \tag{5.46}$$

Imposing the condition that

$$\lim_{t\to 0}\theta_{CO}(t) = \frac{k_{r1}\left(\frac{P_{CO}}{P_{TOT}}\right)}{k_{r1}\left(\frac{P_{CO}}{P_{TOT}}\right)+k_{r2}} \equiv \frac{\varepsilon_{CO}}{\gamma_{CO}} \tag{5.47}$$

$\theta_{CO}(t)$ is given by

$$\theta_{CO}(t) = \frac{\theta_O(CO\ on)}{\theta_O(t)}\frac{\varepsilon_{CO}}{\gamma_{CO}}\exp(-k_{r2}t) \tag{5.48}$$

where $\theta_O(CO\ on)$ denotes the equilibrium value of θ_O in the presence of CO. As with the sensor response, θ_{CO} can only be determined iteratively due to the presence of k_{r2} in Eq. (5.48).

From the discussions above, it has been shown how θ_O may be calculated at any point during the response or recovery of the sensor, provided that α, $\ln(R_0)$ and K_O are known.

Moreover, it is possible to determine θ_{CO} at any given time using an iterative procedure, in turn allowing estimation of the rate constants of the system. However, while this method is generally valid, it requires the response and recovery curves to be repeatedly fitted, altering the values of rate constants between successive fits. This is a time-consuming undertaking, especially if the initial estimates of the rate constants are far from their true values. Where possible, it is therefore convenient to make approximations in the theory in order to decouple the differential equations of θ_O and θ_{CO}, allowing the rate constants to be determined from a single curve fit.

To remove the dependence of θ_{CO} on θ_O, particular conditions must first be satisfied. As discussed previously, the general equation for θ_{CO}, given by Eq. (5.22), is coupled to Eq. (5.17) unless

$$\left|\frac{\mathrm{d}}{\mathrm{d}t}(\ln(\boldsymbol{\theta_O}))\right| \ll \boldsymbol{k_{r1}}\left(\frac{\boldsymbol{P_{CO}}}{\boldsymbol{P_{TOT}}}\right) + \boldsymbol{k_{r2}} \tag{5.49}$$

During the recovery of the sensor, P_{CO}/P_{TOT} is zero and so the condition is more stringent. Simplification of the analysis is therefore only possible for systems which respond and recover sufficiently slowly. To assess whether Eq. (5.49) is satisfied, it is necessary to estimate the rate of change of θ_O as a function of time for each response and recovery curve.

Although the time derivatives of θ_O may simply be estimated from the variation between successive resistance measurements, it is potentially helpful to instead construct an analytic function that accurately represents the data. In this way, random fluctuations in a plot of θ_O versus t may be ignored when calculating the gradient at each point. In the present experiment, the variation of θ_O during sensor response is found to be well-represented by a function of the form

$$\boldsymbol{\theta_O(t) = A\exp(-\gamma_{CO} a t) + B\left(1 - \exp(-\gamma_{CO} b t)\right) + C} \tag{5.50}$$

where

$$\gamma_{CO} = k_{r1}\left(\frac{P_{CO}}{P_{TOT}}\right) + k_{r2} \tag{5.51}$$

A, B, C, a and b are constant fitting parameters, and t is taken to be zero at the point of CO turn-on. The boundary conditions of Eq. (5.50) require that

$$B = A + \theta_O(CO\ on) - \theta_O(CO\ off) \tag{5.52}$$

$$C = \theta_O(CO\ off) - A \tag{5.53}$$

and

$$b = \frac{aA}{B} \tag{5.54}$$

The remaining parameters, A and a, are unconstrained, and must be set as appropriate to produce an accurate fit to the data. From Eq. (5.50), the first time derivative of $\ln(\theta_O)$ may be calculated using the equation

$$\frac{d}{dt}(\ln(\theta_O)) = \gamma_{CO}\frac{bB\exp(-\gamma_{CO}bt) - aA\exp(-\gamma_{CO}at)}{A\exp(-\gamma_{CO}at) + B(1-\exp(-\gamma_{CO}bt)) + C} \tag{5.55}$$

After fitting to each response curve using Eq. (5.50), as depicted in Fig. 5.20, the magnitude of $d(\ln(\theta_O))/dt$ is plotted as a fraction of k_{r2} in Fig. 5.21. It is clear that Eq. (5.49) is indeed satisfied for the duration of each response curve, as the magnitude of $d(\ln(\theta_O))/dt$ is less than 6% of k_{r2} in all cases. There is therefore little difference between the θ_{CO} solutions yielded by Eq. (5.22) and Eq. (5.23).

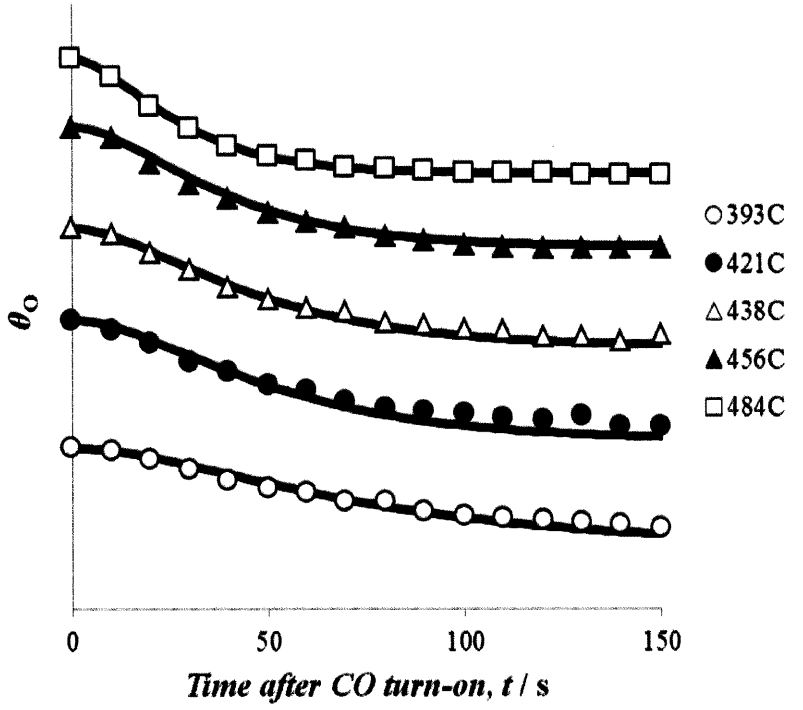

Fig. 5.20. Response curves at different working temperatures and a CO concentration of 200 ppm, fitted using Eq. (5.50). The markers correspond to θ_O values obtained from resistance measurements, while each fit is shown by a black line.

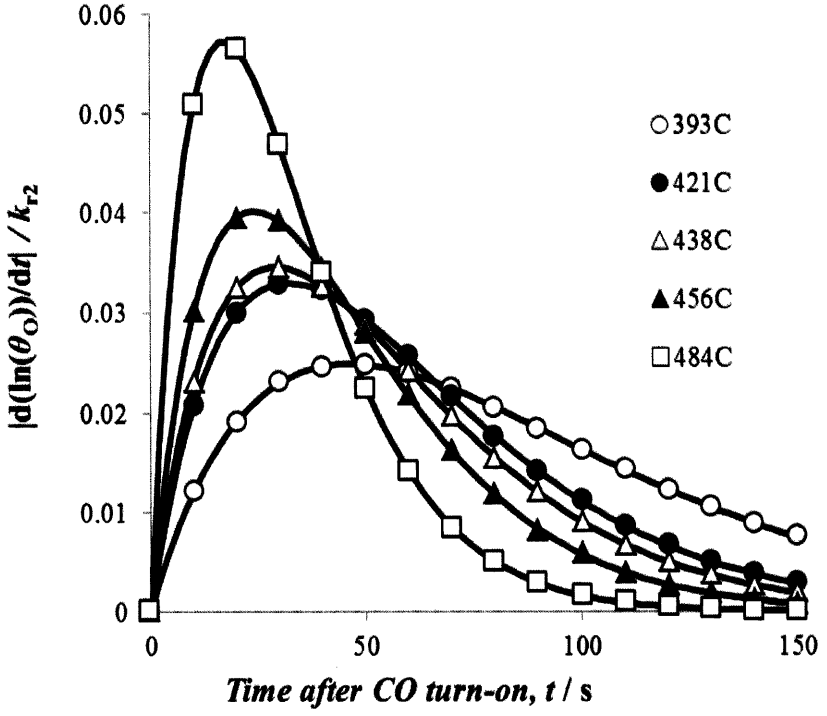

Fig. 5.21. A plot of $|d(\ln(\theta_O))/dt|/k_{r2}$ as a function of time after CO turn-on at different working temperatures, with CO present at a concentration of 200 ppm.

To further justify use of Eq. (5.23), it is instructive to compare the approximated form of θ_{CO} to the more accurate solution obtained from Eq. (5.22). Defining the "percentage error in θ_{CO}" as

$$\textbf{\textit{Percentage error in }}\theta_{CO} = 100\left(\frac{\theta_{CO}(acc.)-\theta_{CO}(approx.)}{\theta_{CO}(acc.)}\right)\% \qquad (5.56)$$

where $\theta_{CO}(acc.)$ and $\theta_{CO}(approx.)$ are the solutions of Eq. (5.22) and Eq. (5.23) respectively, Fig. 5.22 displays $\theta_{CO}(approx.)$ as a function of time after CO turn-on, while Fig. 5.23 shows how the percentage error in θ_{CO} varies over the same period. The general form of $\theta_{CO}(acc.)$ is given by Eq. (5.44), and a physical solution is found by requiring that $\theta_{CO}(acc.)$ is zero at the point of CO turn-on. As expected, the percentage error in θ_{CO} tends to zero at large t and reaches a maximum when the magnitude of $d(\ln(\theta_O))/dt$ is highest. However, the error remains small for the duration of each response curve, with all maxima less than 5% in value. This further vindicates the use of Eq. (5.23). It is interesting to note that since $d(\ln(\theta_O))/dt$ is negative for all t, $\theta_{CO}(acc.)$ is always greater than or equal to $\theta_{CO}(approx.)$.

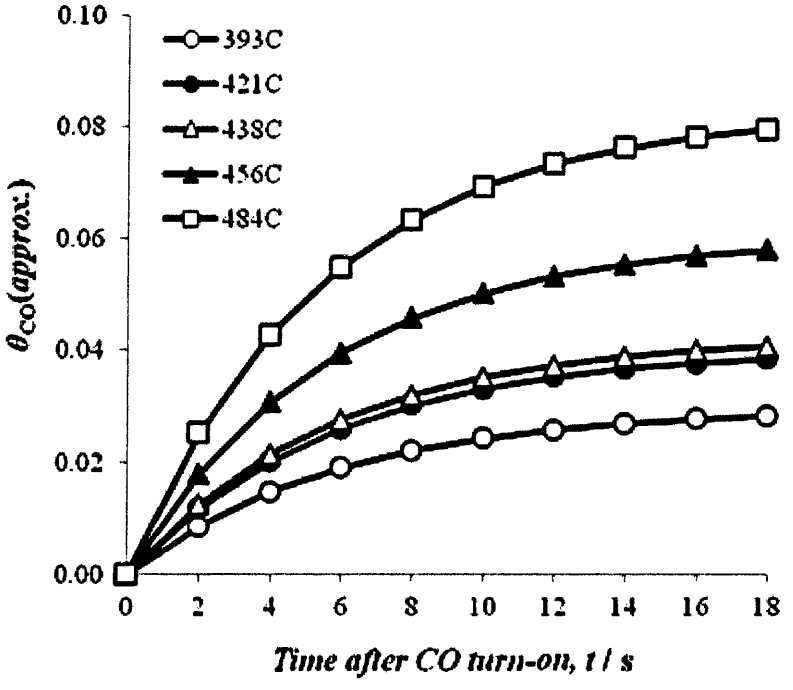

Fig. 5.22. A plot showing the variation of $\theta_{CO}(approx.)$ following CO turn-on at different working temperatures and a CO concentration of 200 ppm, constructed using Eq. (5.23).

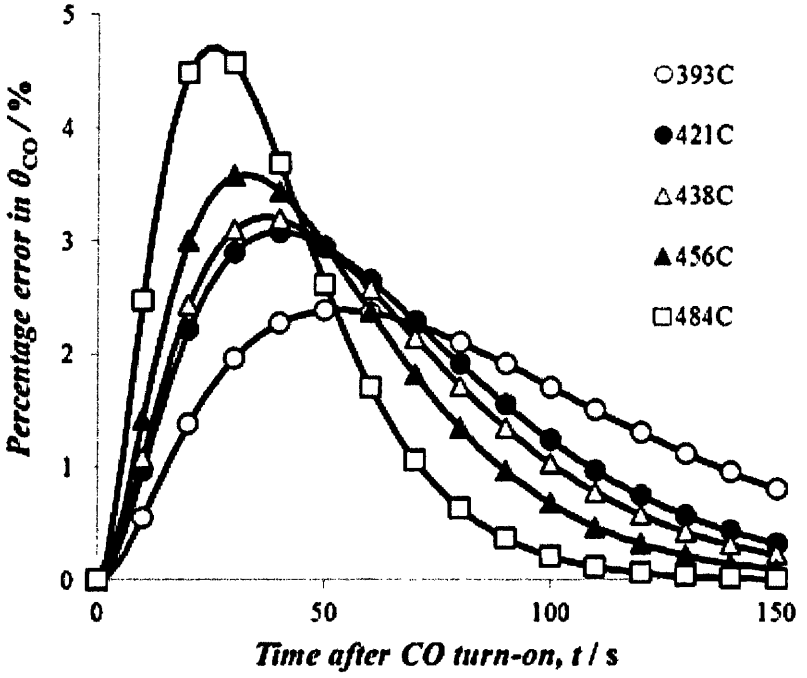

Fig. 5.23. A plot of the percentage error in θ_{CO}, as defined by Eq. (5.56), as a function of time after CO-turn on at different working temperatures, with CO present at a concentration of 200 ppm.

A similar approach may be used to analyse the sensor recovery. Again, θ_O is well-represented by Eq. (5.50), with t now zero at the point of CO turn-off and

$$\gamma_{CO} = k_{r2} \tag{5.57}$$

To satisfy the boundary conditions,

$$B = \theta_O(CO\ off) - \theta_O(CO\ on) + A \tag{5.58}$$

and

$$C = \theta_O(CO\ on) - A \tag{5.59}$$

As before,

$$b = \frac{aA}{B} \tag{5.60}$$

and the remaining parameters, A and a, must be set to appropriate values. Fig. 5.24 shows the variation of θ_O during each recovery curve, as well as the fits provided by Eq. (5.50). The ratio of $|d(\ln(\theta_O))/dt|$ to k_{r2} during sensor recovery, calculated using Eq. (5.55), is plotted in Fig. 5.25. As was the case for the response of the system, the ratio remains small for the duration of the recovery, satisfying Eq. (5.49). This observation indicates that it is reasonable to neglect the θ_O-dependent term in Eq. (5.22), as before.

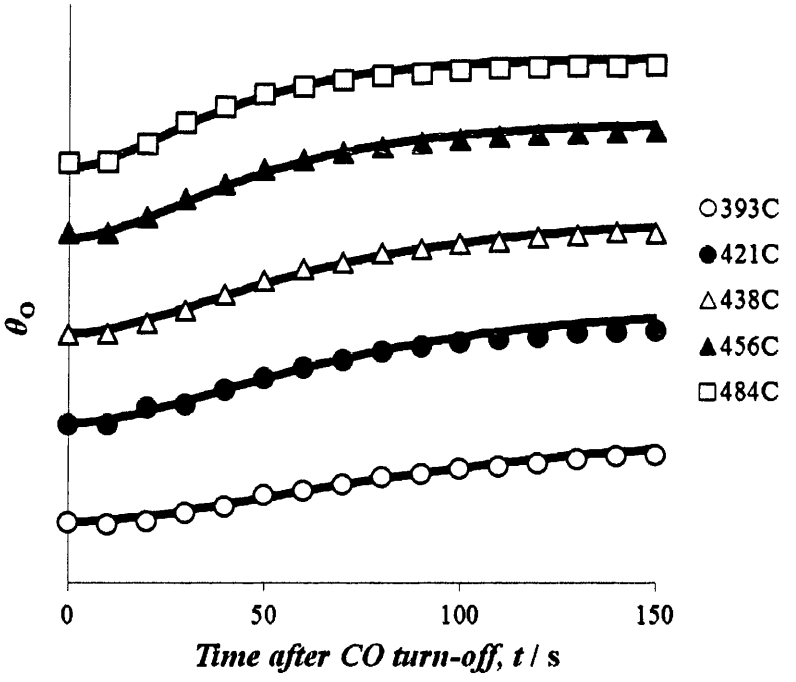

Fig. 5.24. Recovery curves at different working temperatures and a CO concentration of 200 ppm, fitted using Eq. (5.50). The markers correspond to θ_O values obtained from resistance measurements, while each fit is shown by a black line.

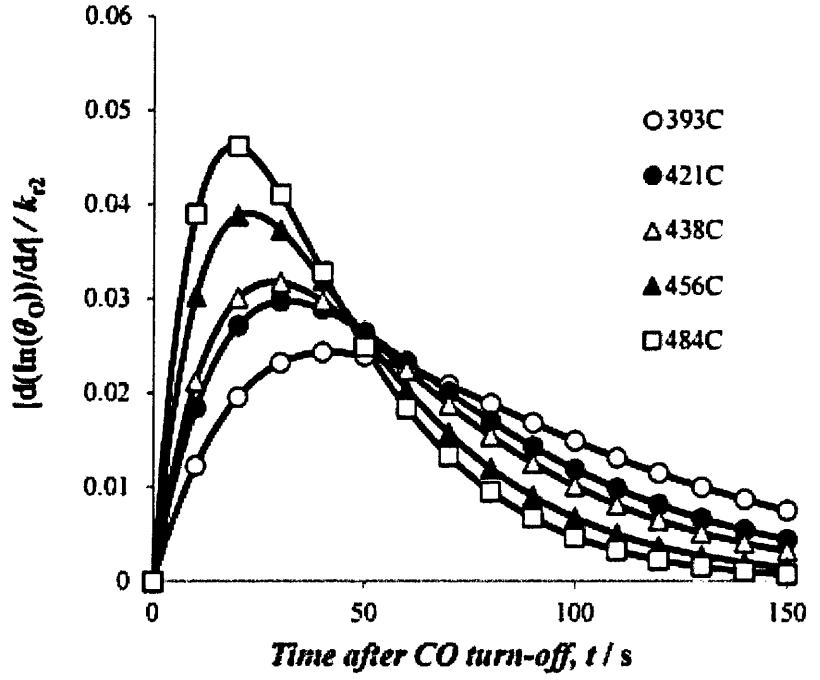

Fig. 5.25. A plot of $|d(\ln(\theta_O))/dt|/k_{r2}$ as a function of time after CO turn-off at different working temperatures. At t < 0, CO was present at a concentration of 200 ppm.

To determine the error in θ_{CO} as a function of time during sensor recovery, it is necessary to first calculate $\theta_{CO}(acc.)$ using Eq. (5.44). The form of $\theta_{CO}(acc.)$ is much simpler than before, and after solving Eq. (5.23) it is evident that

$$\frac{\theta_{CO}(acc.)}{\theta_{CO}(approx.)} = \frac{\theta_O(CO\ on)}{\theta_O(t)} \tag{5.61}$$

Consequently,

$$\textbf{Percentage error in } \theta_{CO} = 100\left(1 - \frac{\theta_O(t)}{\theta_O(CO\ on)}\right)\% \tag{5.62}$$

so the percentage error in θ_{CO} continually increases in magnitude after the point of CO turn-off, and $\theta_{CO}(acc.)$ is always less than $\theta_{CO}(approx.)$. Eq. (5.62) suggests that for a highly responsive system, where $\theta_O(CO\ off)$ is much greater than $\theta_O(CO\ on)$, the percentage error in θ_{CO} becomes large towards the end of the sensor recovery. Indeed, Fig. 5.26, which depicts the percentage error in θ_{CO} as a function of time from the measured data, shows that 150 s

after turn-off of the CO the percentage error in θ_{CO} reaches magnitudes of around 50%. It has already been shown by Fig. 5.25, however, that the magnitude of $d(\ln(\theta_O))/dt$ is small for the duration of every recovery curve, remaining less than 5% of k_{r2} in all cases. As with the sensor response, this indicates that it is reasonable to use Eq. (5.23) in place of Eq. (5.22). Moreover, it is clear from the steady-state solutions of these two equations that the values of $\theta_{CO}(acc.)$ and $\theta_{CO}(approx.)$ must agree both prior to CO introduction and at long times following CO turn-off. To understand this apparent paradox, one must note that although the magnitude of the difference between $\theta_{CO}(acc.)$ and $\theta_{CO}(approx.)$ tends to zero during the sensor recovery, so too does the value of θ_{CO}. This behaviour is illustrated quantitatively by Fig. 5.27, which plots $\theta_{CO}(approx.)$ as a function of time during the sensor recovery at each temperature. The percentage error in θ_{CO} is therefore directly proportional to the ratio of two negligible quantities at large values of t, and becomes undefined in the limit as t goes to infinity.

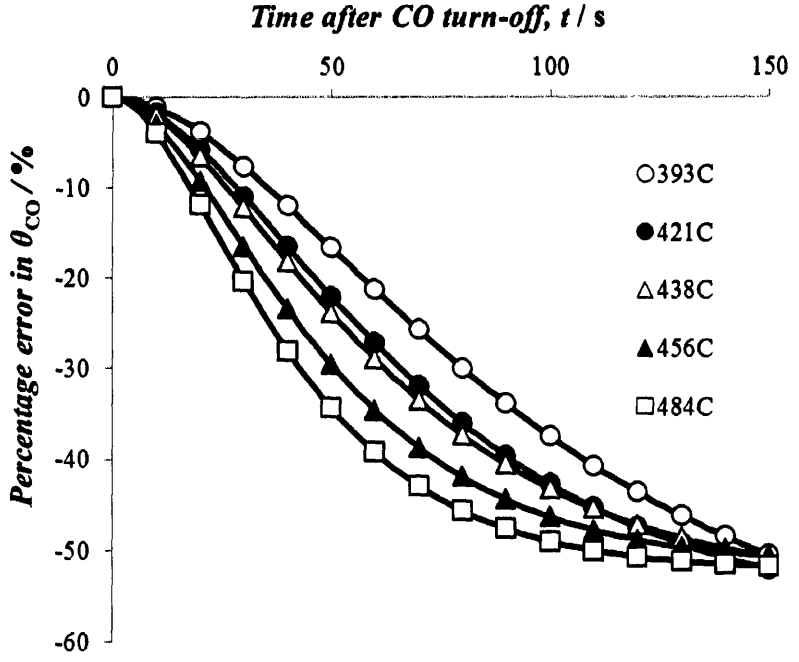

Fig. 5.26. A plot of the percentage error in θ_{CO}, as defined by Eq. (5.56), as a function of time after CO turn-off at different working temperatures. At t < 0, CO was present at a concentration of 200 ppm.

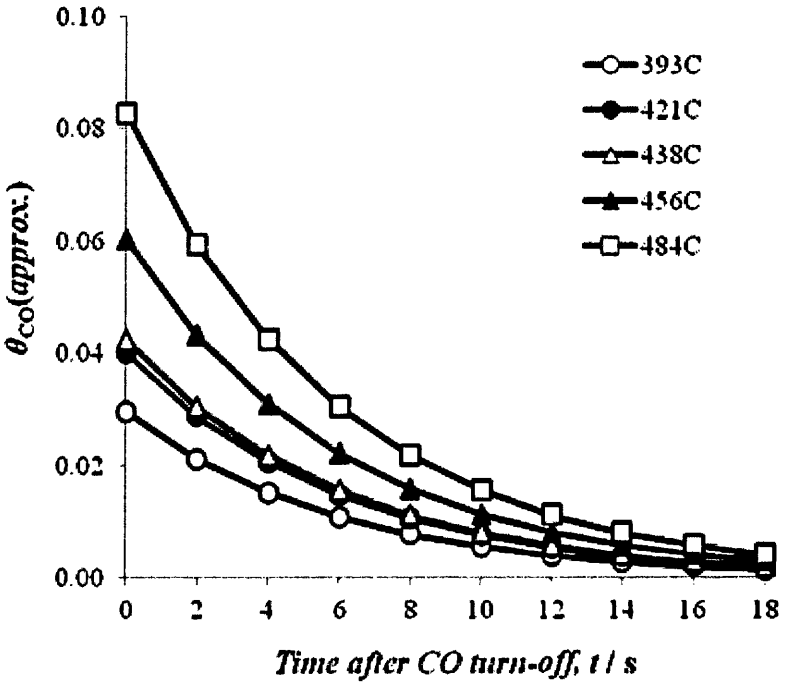

Fig. 5.27. A plot showing the variation of θ_{CO}(*approx.*) following CO turn-off at different working temperatures, constructed using Eq. (5.23). At t < 0, CO was present at a concentration of 200 ppm.

In summary, the resistance measurements suggest that while Eq. (5.23) does not produce an exact solution for θ_{CO}, it does provide a close approximation. During both the response and recovery of the sensor, the rate of change of θ_O is sufficiently small that the θ_O dependence in Eq. (5.22) may be justifiably ignored.

5.5. Conclusions

Through consideration of the kinetics of the surface reactions, a mathematical model has been developed to describe the measured response of a zinc oxide nanosheet-based sensor to carbon monoxide gas. Fitting of the response and recovery curves was facilitated by assuming the carbon monoxide reacts with surface oxygen ions via an Eley-Rideal mechanism, neglecting the reactions of carbon monoxide adsorbed at bare surface sites.

To complement the response measurements, additional tests were conducted to explore the physics of the system in the absence of carbon monoxide. From these experiments, it became possible to calculate the surface concentration of oxygen ions at a particular electrical resistance, providing the means to determine the rate of reactions occurring at the zinc oxide surface. Furthermore, comparison between the estimates acquired at different working temperatures allowed the activation energies for these processes to be evaluated. In particular, the activation energy for the reaction between O^- ions and carbon monoxide was estimated as 54 ± 9 kJ mol^{-1} or 42 ± 7 kJ mol^{-1} from the response and recovery curves respectively. The energy barrier for the formation of O^- ions was found to be 72 ± 9 kJ mol^{-1} from the sensor response and 63 ± 10 kJ mol^{-1} from the recovery. These values are comparable to estimates existing in the literature, corroborating the validity of both the model and the experimental procedure. In the absence of O^- or CO_2^- ions, the energy difference between the Fermi level and the conduction band minimum at the surface is estimated as 590 ± 90 meV. The theory and methodology presented herein provides a useful and novel way to relate the electrical response of a chemiresistive sensor to the underlying physics of the reactions at its surface, and has potential to facilitate the development and optimisation of practical detectors for real-world applications. The following chapter aims to further this approach by considering sensors where rapid oxidation occurs, either due to the high reactivity of the reducing gas or the catalytic effects of surface additives.

References

[1] A. Setkus, Heterogeneous reaction rate based description of the response kinetics in metal oxide gas sensors, 87 (2002) 346–357.

[2] K. Grass, The Kinetics of Carbon Monoxide Oxidation on Tin(IV) Oxide Supported Platinum Catalysts, J. Catal. 172 (1997) 446–452. doi:10.1006/jcat.1997.1886.

[3] V.P. Zhdanov, Impact of surface science on the understanding of kinetics of heterogeneous catalytic reactions, Surf. Sci. 500 (2002) 966–985.

[4] S. Bai, T. Guo, D. Li, R. Luo, A. Chen, C.C. Liu, Intrinsic sensing properties of the flower-like ZnO nanostructures, Sensors Actuators, B Chem. 182 (2013) 747–754. doi:10.1016/j.snb.2013.03.077 Flower-like ZnO nanostructures.

[5] S. Nakata, S. Akakabe, M. Nakasuji, K. Yoshikawa, Gas Sensing Based on a Nonlinear Response: Discrimination between Hydrocarbons and Quantification of

Individual Components in a Gas Mixture., Anal. Chem. 68 (1996) 2067–72. doi:10.1021/ac9510954.

[6] H. Busse, M. Voss, D. Jerdev, B. Koel, M. Paffett, Adsorption and reaction of gaseous H (D) atoms with D (H) adatoms on Pt (111) and Sn/Pt (111) surface alloys, Surf. Sci. 490 (2001) 133–143. doi:10.1016/S0039-6028(01)01323-1.

[7] I. Kocemba, J. Rynkowski, The influence of catalytic activity on the response of Pt/SnO2 gas sensors to carbon monoxide and hydrogen, Sensors Actuators, B Chem. 155 (2011) 659–666. doi:10.1016/j.snb.2011.01.026.

[8] A. Varpula, S. Novikov, A. Haarahiltunen, P. Kuivalainen, Transient characterization techniques for resistive metal-oxide gas sensors, Sensors Actuators B Chem. 159 (2011) 12–26. doi:10.1016/j.snb.2011.05.059.

[9] A. Fort, M. Mugnaini, S. Rocchi, M.B. Serrano-Santos, V. Vignoli, R. Spinicci, Simplified models for SnO2 sensors during chemical and thermal transients in mixtures of inert, oxidizing and reducing gases, Sensors Actuators B Chem. 124 (2007) 245–259. doi:10.1016/j.snb.2006.12.030.

[10] K. Darcovich, F.F. Garcia, C.A. Jeffrey, J.J. Tunney, M.L. Post, Coupled microstructural and transport effects in n-type sensor response modeling for thin layers, Sensors Actuators A Phys. 147 (2008) 378–386. doi:10.1016/j.sna.2008.06.007.

[11] R. Ionescu, E. Llobet, S. Al-Khalifa, J.W. Gardner, X. Vilanova, J. Brezmes, et al., Response model for thermally modulated tin oxide-based microhotplate gas sensors, Sensors Actuators B Chem. 95 (2003) 203–211. doi:10.1016/S0925-4005(03)00420-9.

[12] S. Nakata, K. Takemura, K. Neya, Non-linear dynamic responses of a semiconductor gas sensor: Evaluation of kinetic parameters and competition effect on the sensor response, Sensors Actuators B Chem. 76 (2001) 436–441. doi:10.1016/S0925-4005(01)00652-9.

[13] D.R. Jones, T.G.G. Maffeïs, Analysis of the kinetics of surface reactions on a zinc oxide nanosheet-based carbon monoxide sensor using an Eley-Rideal model, Sensors Actuators B Chem. 218 (2015) 16–24. doi:10.1016/j.snb.2015.04.072.

[14] F Greuter, G Blatter, Electrical properties of grain boundaries in polycrystalline compound semiconductors, Semicond. Sci. Technol. 5 (1990) 111–137.

[15] N. Barsan, U. Weimar, Conduction model of metal oxide gas sensors, J. Electroceramics. 7 (2001) 143–167. doi:10.1023/A:1014405811371.

[16] C. Malagù, V. Guidi, M. Stefancich, M.C. Carotta, G. Martinelli, Model for Schottky barrier and surface states in nanostructured n-type semiconductors, J. Appl. Phys. 91 (2002) 808–814. doi:10.1063/1.1425434.

[17] A. Tarat, R. Majithia, R.A. Brown, M.W. Penny, K.E. Meissner, Synthesis of nanocrystalline ZnO nanobelts via pyrolytic decomposition of zinc acetate nanobelts

and their gas sensing behavior, Surf. Sci. 606 (2012) 715–721. doi:10.1016/j.susc.2011.12.010.

[18] J. Lagowski, E.S. Sproles, H.C. Gatos, Quantitative study of the charge transfer in chemisorption; oxygen chemisorption on ZnO, J. Appl. Phys. 48 (1977) 3566–3575. doi:10.1063/1.324156.

[19] P. V Bakharev, V. V Dobrokhotov, D.N. Mcilroy, A Method for Integrating ZnO Coated Nanosprings into a Low Cost Redox-Based Chemical Sensor and Catalytic Tool for Determining Gas Phase Reaction Kinetics, (2014) 56–68. doi:10.3390/chemosensors2010056.

[20] S. Wendt, P.T. Sprunger, E. Lira, G.K.H. Madsen, Z. Li, J.Ø. Hansen, et al., The role of interstitial sites in the Ti3d defect state in the band gap of titania., Science. 320 (2008) 1755–1759. doi:10.1126/science.1159846.

[21] S. Li, Z. Lu, Z. Yang, X. Chu, The sensing mechanism of Pt-doped SnO2 surface toward CO: A first-principle study, Sensors Actuators, B Chem. 202 (2014) 83–92. doi:10.1016/j.snb.2014.05.071.

[22] B.S. Kang, S. Kim, F. Ren, K. Ip, Y.W. Heo, B.P. Gila, et al., Detection of CO using bulk ZnO Schottky rectifiers, Appl. Phys. A Mater. Sci. Process. 80 (2005) 259–261. doi:10.1007/s00339-004-2666-2.

[23] N. Li, Q.-Y. Chen, L.-F. Luo, W.-X. Huang, M.-F. Luo, G.-S. Hu, et al., Kinetic study and the effect of particle size on low temperature CO oxidation over Pt/TiO2 catalysts, Appl. Catal. B Environ. 142-143 (2013) 523–532. doi:10.1016/j.apcatb.2013.05.068.

[24] J.-M. Ducéré, A. Hemeryck, A. Estève, M.D. Rouhani, G. Landa, P. Ménini, et al., A computational chemist approach to gas sensors: modeling the response of SnO2 to CO, O2, and H2O gases., J. Comput. Chem. 33 (2012) 247–58. doi:10.1002/jcc.21959.

[25] R. Stratton, Surface Barriers at Semiconductor Contacts, Proc. Phys. Soc. Sect. B. 69 (1956) 513–527. doi:10.1088/0370-1301/69/5/303.

[26] M.W. Allen, C.H. Swartz, T.H. Myers, T.D. Veal, C.F. McConville, S.M. Durbin, Bulk transport measurements in ZnO: The effect of surface electron layers, Phys. Rev. B - Condens. Matter Mater. Phys. 81 (2010) 1–6. doi:10.1103/PhysRevB.81.075211.

[27] G.G. Roberts, N. Apsley, R.W. Munn, Temperature Dependent Electronic Conduction in Semiconductors, Phys. Rep. 60 (1980) 59–150.

[28] W.S. Baer, Faraday Rotation in ZnO: Determination of the Electron Effective Mass, Phys. Rev. 154 (1967) 785–789.

[29] L.E. Brus, Electron–electron and electron-hole interactions in small semiconductor crystallites: The size dependence of the lowest excited electronic state, J. Chem. Phys. 80 (1984) 4403. doi:10.1063/1.447218.

[30] M. Oshikiri, Y. Imanaka, F. Aryasetiawan, G. Kido, Comparison of the electron effective mass of the n-type ZnO in the wurtzite structure measured by cyclotron resonance and calculated from first principle theory, Phys. B Condens. Matter. 298 (2001) 472–476. doi:10.1016/S0921-4526(01)00365-9.

[31] B.K. Meyer, H. Alves, D.M. Hofmann, W. Kriegseis, D. Forster, F. Bertram, et al., Bound exciton and donor–acceptor pair recombinations in ZnO, Phys. Status Solidi. 241 (2004) 231–260. doi:10.1002/pssb.200301962.

[32] F.A. Selim, M.H. Weber, D. Solodovnikov, K.G. Lynn, Nature of native defects in ZnO, Phys. Rev. Lett. 99 (2007) 85502. doi:10.1103/PhysRevLett.99.085502.

[33] M.W. Allen, S.M. Durbin, Influence of oxygen vacancies on Schottky contacts to ZnO, Appl. Phys. Lett. 92 (2008) 90–93. doi:10.1063/1.2894568.

[34] D.C. Look, D.C. Reynolds, J.R. Sizelove, R.L. Jones, C.W. Litton, G. Cantwell, et al., Electrical properties of bulk ZnO, Solid State Commun. 105 (1998) 399–401. doi:10.1016/S0038-1098(97)10145-4.

[35] R. Tena-Zaera, J. Elias, C. Levy-Clement, I. Mora-Sero, Y. Luo, J. Bisquert, Electrodeposition and impedance spectroscopy characterization of ZnO nanowire arrays, Phys. Status Solidi a-Applications Mater. Sci. 205 (2008) 2345–2350. doi:10.1002/pssa.200779426.

[36] M. Soosen Samuel, J. Koshy, A. Chandran, K.C. George, Dielectric behavior and transport properties of ZnO nanorods, Phys. B Condens. Matter. 406 (2011) 3023–3029. doi:10.1016/j.physb.2011.04.070.

[37] J. Krupka, J. Breeze, A. Centeno, N. Alford, T. Claussen, L. Jensen, Measurements of permittivity, dielectric loss tangent, and resistivity of float-zone silicon at microwave frequencies, IEEE Trans. Microw. Theory Tech. 54 (2006) 3995–4000. doi:10.1109/TMTT.2006.883655.

Chapter 6 – Exploring the properties of rapid gas reactions

6.1. Introduction

In the previous chapter, the CO response characteristics of a ZnO nanosheet-based sensor were studied in order to estimate various activation energies and rate constants of the system. The device demonstrated a high sensitivity to CO at temperatures around 400°C, and it was shown that this could be attributed to a high surface coverage of oxygen ions. However, the theoretical treatment used to describe the oxidation of CO is not necessarily appropriate in all cases; indeed, it is clear from the outset that the model is only suited to those gases which react in a one-to-one molar ratio with surface oxygen ions and do not significantly chemisorb to the ZnO surface. Moreover, it was shown that the theory may only be used when the response and recovery of the sensor are sufficiently slow, so is unlikely to be representative of gases which oxidise much more rapidly than CO. To analyse such systems, the model must therefore be adapted to provide a more apposite description of the surface reactions.

When developing a gas sensor, it is crucial to consider the requirements of the relevant application. The high temperatures employed in the previous chapter, for instance, may not be practical in certain real-world situations, so it is important to explore ways to reduce the temperatures required whilst maintaining a high sensor response. This is often achieved through use of surface catalysts, typically nanoparticles of noble metals such as platinum, palladium or gold, which lower the activation energy of oxidation [1–22]. At the surface of a typical surface catalyst, the reaction is likely to proceed via a Langmuir-Hinshelwood process involving adsorbed gas molecules [23–29] rather than the Eley-Rideal mechanism assumed in Chapter 5; in general, therefore, a catalysed system must be described using an alternative formalism to that employed previously.

To investigate systems containing surface catalysts or rapidly oxidising gases, this chapter explores the reactions of various reducing gases on ZnO nanosheets which either have no surface additives or are decorated by gold nanoparticles. By measuring the electrical responses of the different sensors to varying concentrations of H_2, CO and CH_4 over a range of temperatures, it shall be demonstrated that important qualitative conclusions may be drawn in each case regarding the nature of the associated reaction mechanisms.

6.2. Experimental methods

Following the procedure described in Chapter 3, LBZA nanosheets were prepared in aqueous suspension and centrifuged into de-ionised water over five five-minute cycles. An aqueous suspension of gold nanoparticles was produced using the Turkevich technique [30], adding 1 mL of aqueous chloroauric acid (25 mmol L^{-1}) to a 24 mL volume of aqueous sodium citrate tribasic dihydrate (2.5 mmol L^{-1}) whilst boiling under reflux with rapid stirring. The concentration of chloroauric acid in the combined solution was four times higher than in the archetypal experiment described in Chapter 3, and was deliberately selected in order to obtain a concentrated suspension of poly-dispersed gold aggregates. In this way, a high coverage of gold could be realised on the final gold-catalysed ZnO nanosheet-based sensor. The gold nanoparticle suspension was added to LBZA nanosheet residue following the final five-minute centrifuge stage, while deionised water was added to a second batch of LBZA nanosheet residue. The two suspensions were subsequently centrifuged for a further 90 minutes at 4°C, discarding the final supernatant in each case and replacing it with deionised water. A 100 μL volume of each suspension was drop-cast onto an alumina gas-sensing substrate and dried at 60°C, and the two substrates were annealed together in a tube furnace at 500°C for 30 minutes under a 900 mL min^{-1} flow of dry air.

Gas sensing tests were performed using a custom-built gas sensing chamber, as outlined in Chapter 3. A continuous 400 mL min^{-1} total flow was used throughout, maintaining a 4:1 ratio of N_2 to O_2 and adjusting the flow rate of each reducing gas to control its concentration in the system. Each sensor was exposed to concentrations of H_2, CO and CH_4 between 50 ppm and 200 ppm, at temperatures ranging from 100°C to 450°C. During each sensing test,

the reducing gas was admitted to the system after one minute and turned off after a further fifteen minutes. In order to characterise the form of the ZnO nanosheets and gold nanoparticles, the sensors were inspected using a Hitachi S4800 field emission scanning electron microscope with the accelerating voltage set at 5 kV.

6.3. Results and discussions

6.3.1. Sensor characterisation

To observe the form of the sensing material on each sensor, they were examined using SEM following the sensing experiments. The images for the non-catalysed ZnO nanosheets, as depicted in Fig. 6.1 (a) and Fig. 6.1 (b), show that the constituent nanoparticles were of comparable size to those measured in Chapter 5. Conversely, the nanosheets of the gold-coated sensor, shown in Fig. 6.1 (c) and Fig. 6.1 (d), were observed to consist of sub-10 nm nanoparticles; indeed, measurement of the nanoparticles was limited by the resolution of the SEM. Although the reason for this difference is unclear, it is worth noting that residual citrate ions were likely to exist on the surface of the gold-decorated LBZA nanosheets following centrifugation. During the synthesis of gold nanoparticles via the Turkevich reaction, these ions act as reducing agents for the gold precursor but also inhibit the formation of large gold aggregates [30–34]. It is possible that the ions perform a similar role during the thermal decomposition of LBZA to ZnO, suppressing Ostwald ripening of the ZnO nanoparticles [35–38] and thereby limiting the mean nanoparticle size. This simple argument is contradicted, however, by observations displayed in Chapter 3; although the gold nanoparticles depicted in Fig. 3.3 were synthesised using the same concentration of sodium citrate as in the present chapter, the underlying ZnO nanosheets consist of much larger grains than those shown in Fig. 6.1 (d) despite the same annealing procedure being used in each case. As fabrication of the gold nanoparticles in Fig. 3.3 was achieved using a much lower concentration of chloroauric acid than those in Fig. 6.1 (d), it is plausible that Ostwald ripening of the ZnO is most strongly affected by the concentration of this precursor. A high coverage of gold nanoparticles is apparent in Fig. 6.1(c), and Fig. 6.1(d) indicates that significant aggregation of the gold has occurred. Indeed, the gold aggregates are much larger

than those shown in Fig. 3.3, which may again be attributed to the comparatively low concentration of chloroauric acid used in the latter case.

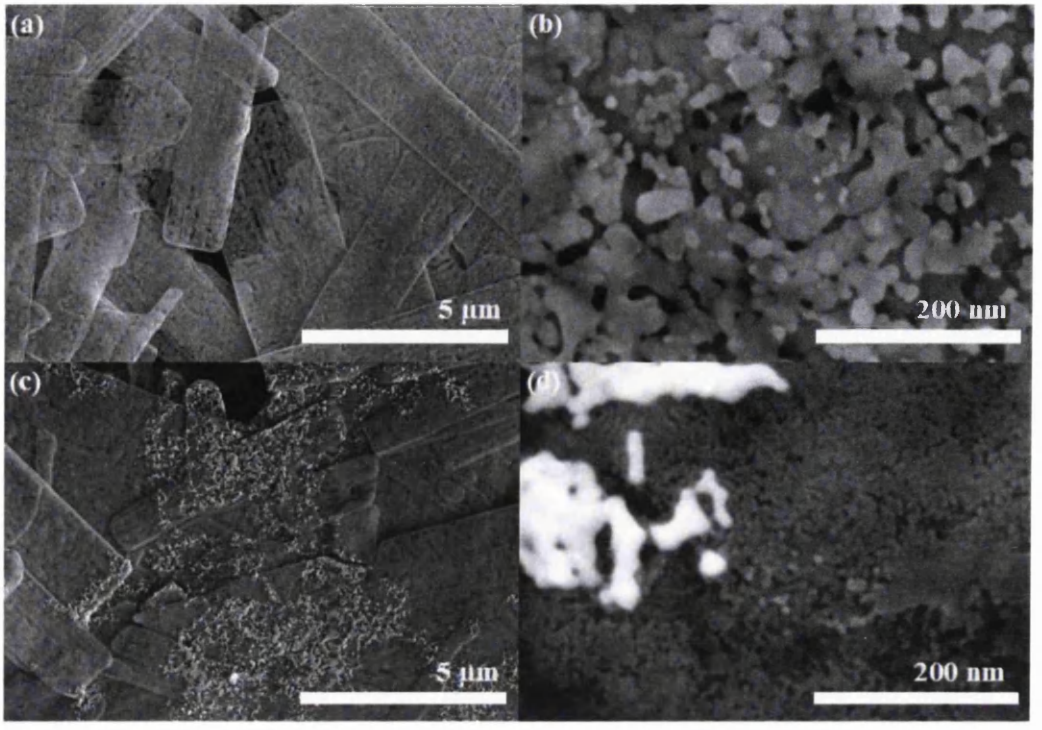

Fig. 6.1. SEM images showing ZnO nanosheets without surface catalysts ((a) and (b)) and coated in gold nanoparticles ((c) and (d)).

6.3.2. The response to CO, H_2 and CH_4 as a function of temperature

The response characteristics of the two sensors are depicted in Fig. 6.2, which shows the variation of the response to 200 ppm of different gases as a function of temperature. It is immediately apparent that the gold nanoparticles had a catalytic effect on the oxidation of CO and H_2, as the response at a given temperature was increased by their presence. Most notable is the response to 200 ppm of H_2, which was not only enhanced by the catalyst but also remained almost independent of temperature above 200°C. This trend was not repeated for CO or CH_4, with both sensors exhibiting a negligible response to these gases below 300°C. Indeed, comparison of Fig. 6.2 (a) and Fig. 6.2 (b) shows that the sensitivity to 200 ppm of CH_4 was not improved significantly by the gold nanoparticles, and the gas was not detected by either sensor below 400°C. It is possible that the low CH_4 responses may be partially attributed to the fact that, unlike H_2 and CO, it is stoichiometrically not possible for CH_4 to

oxidise in a single reaction step, and it has been shown elsewhere that the reaction instead proceeds through several organic intermediates [39–42].

The plots displayed in Fig. 6.2 illustrate the catalytic effects of the gold nanoparticles, but it is important to note that the results are not consistent with those obtained in Chapter 5. In the absence of a catalyst, the response of the ZnO nanosheets to 200 ppm of CO was only around 0.11 at 420°C, contrasting the sensor used in Chapter 5 which yielded a response of 0.46 at a similar temperature. Moreover, a peak in the response was previously observed at around 440°C, whereas the response of the current control sensor was found to increase as the temperature was raised above 450°C. Although the two sensors were fabricated in a similar manner, it is important to recall that an extended centrifuge time was used when preparing the LBZA nanosheets for the present experiment. It is possible that the decreased sensitivity of the control sensor may be attributed to this difference in the LBZA preparation procedure. For conciseness, the sensor from Chapter 5 shall henceforth be referred to as Sensor S (where the letter "S" alludes to the short centrifuge time used during preparation of the LBZA), whereas the non-catalysed and gold-catalysed sensors introduced in this chapter shall be named Sensor L (here, the letter "L" refers to the longer centrifuge time employed) and Sensor Au, respectively.

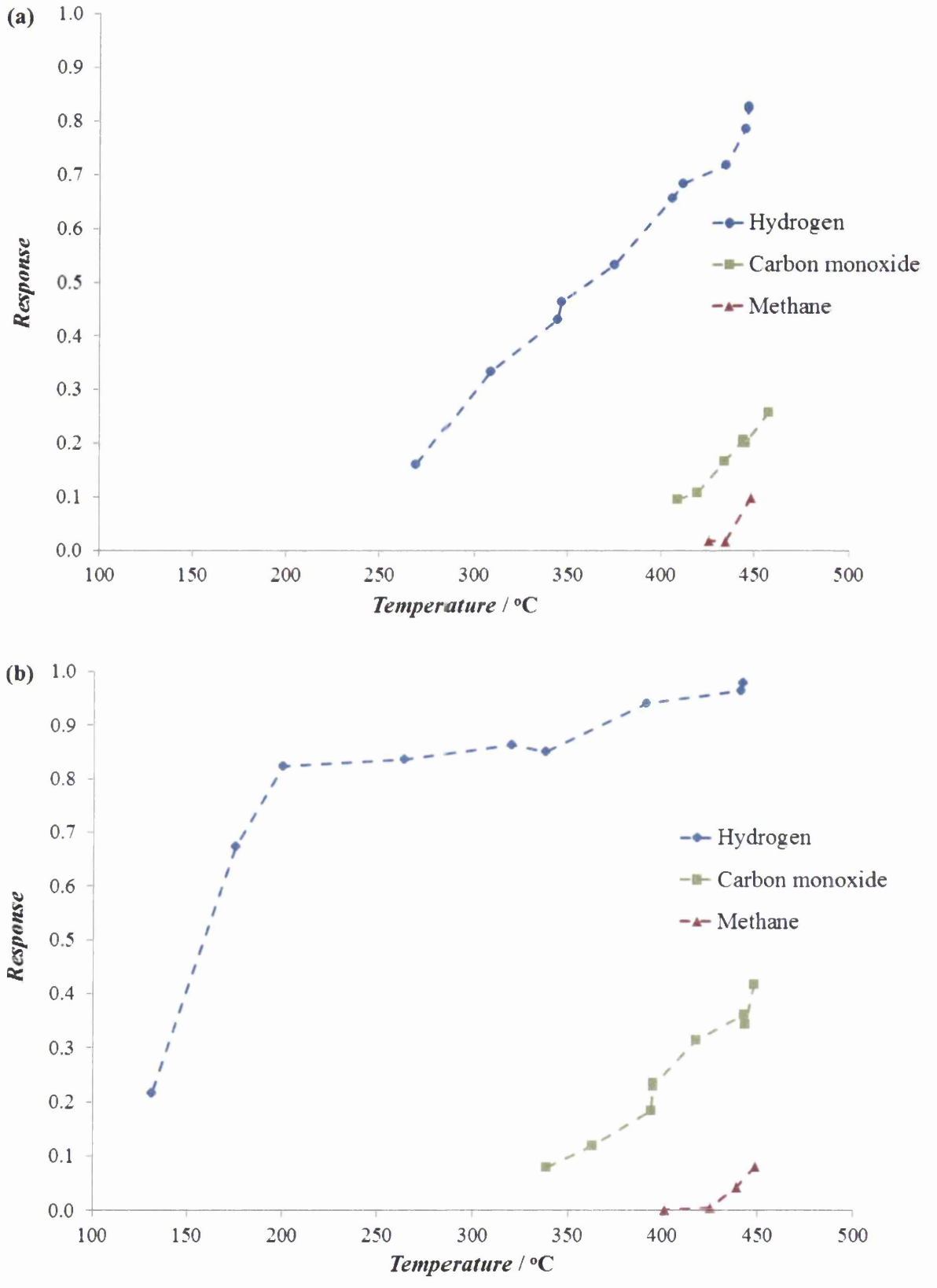

Fig. 6.2. Plots depicting the responses of Sensor L (a) and Sensor Au (b) as a function of temperature. Each response test was conducted at a P_{O2}/P_{TOT} value of 0.2.

6.3.3. The variation of resistance as a function of temperature

As the resistance of a chemiresistive sensor depends strongly on the concentration of ions present at its surface, significant insights into the surface dynamics may be gleaned by considering how the sensor resistance varies as a function of temperature. For a constant concentration of surface ions, the resistance is expected to decrease exponentially with increasing temperature due to a higher proportion of electrons having sufficient energy to migrate between semiconductor grains. Moreover, a higher temperature increases the probability of electron promotion from inter-band donor states to the conduction band, thereby increasing the concentration of conduction electrons. If, however, the concentration of surface ions is itself temperature-dependent, one may observe an alternative relationship between resistance and temperature. By exploring this behaviour in the absence of any reducing gas, it is therefore possible to determine how the concentration of O^- ions varies as a function of temperature at the surface of a particular device. In the case of Sensor S, which was characterised in Chapter 5, the equilibrium constant for oxygen ionosorption, K_O, was shown to reach a peak value of approximately 9.6 at around 460°C, decreasing to a value of 3.0 at ~390°C. This variation suggests that the concentration of O^- ions correlated positively with temperature between the two temperatures, acting to oppose any decrease in the resistance with increasing temperature.

To consider the relationship between resistance and temperature in a more quantitative manner, it is instructive to recall theory outlined in Chapter 1 and employed in the previous chapter. From Eq. (5.30) it follows that

$$\frac{\mathrm{d}}{\mathrm{d}T}\ln(R) = \frac{\mathrm{d}}{\mathrm{d}T}\ln(R_0) + \frac{\mathrm{d}}{\mathrm{d}T}\left(\alpha\theta_O^2\right) \tag{6.1}$$

where T is temperature, R is the resistance, θ_O is the proportion of surface sites that are occupied by surface ions, R_0 is the resistance in the absence of surface ions and α is a temperature-dependent constant, as defined previously. Using thermoelectronic emission theory, it was also established in Chapter 5 that

$$R_0 \propto \frac{1}{T}\exp\left(\frac{E_{C,S}-E_F}{k_B T}\right) \tag{6.2}$$

where $E_{C,S}$ is the energy of the conduction band minimum at the surface in the absence of surface ions, E_F is the Fermi energy and k_B is Boltzmann's constant. Substituting this relation into Eq. (6.1), one obtains the expression

$$\frac{d}{dT}\ln(R) = \frac{d}{dT}(\alpha\theta_O^2) - \frac{1}{k_B T^2}(E_{C,S} - E_F + k_B T) \tag{6.3}$$

which shows explicitly the positive and negative contributions to the derivative of ln(R) with respect to T.

In Fig. 6.3, which plots the natural logarithm of the sensor resistance as a function of temperature for Sensors S and L, the inverse proportionality between ln(R) and T in each case suggests that the relationship was dominated by the second term on the right-hand side of Eq. (6.3). In the case of Sensor S, ln(R) decreased at a rate of approximately 1.4 x 10^{-2} K^{-1} over the measured range of temperatures, while the estimated gradient for Sensor L has a lower value of -4.7 x 10^{-3} K^{-1}. To verify the work of the previous chapter, it is possible to utilise the measured d ln(R)/dT value of Sensor S to calculate a new estimate of $E_{C,S}$-E_F for this device. To achieve this goal, it is helpful to first recognise that

$$\frac{d}{dT}(\alpha\theta_O^2) = \theta_O\left(\theta_O\frac{d\alpha}{dT} + 2\alpha\frac{d\theta_O}{dT}\right) \tag{6.4}$$

which may be evaluated at a particular temperature by using estimates of α, θ_O, dα/dT and dθ_O/dT obtained in Chapter 5. At 440°C, for example, θ_O was estimated as 0.78 and α had a calculated value of 1.84, while Fig. 5.9 and Fig. 5.19 yield dθ_O/dT and dα/dT estimates of 1.5 x 10^{-3} K^{-1} and -4.4 x 10^{-3} K^{-1}, respectively. Substituting these quantities into Eq. (6.4), one obtains a predicted d($\alpha\theta_O^2$)/dT value of 1.6 x 10^{-3} K^{-1} which, in conjunction with Eq. (6.3) and the measured value of d ln(R)/dT, leads to an $E_{C,S}$-E_F estimate of approximately 640 meV. This value is consistent with the previous estimate of 590 meV within the experimental error of 90 meV, and therefore further substantiates the model and methodology employed in Chapter 5.

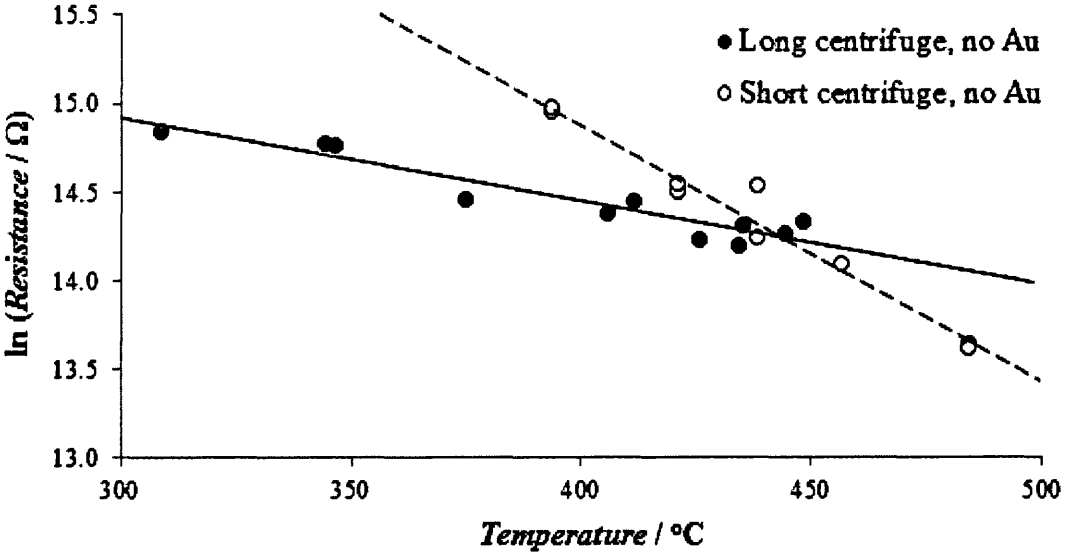

Fig. 6.3. A plot showing the natural logarithm of the resistance as a function of temperature for Sensors S and L, where P_{O2}/P_{TOT} is 0.2 and no reducing gas is present. Lines-of-best-fit have been fitted to each set of data using the least-squares method, shown solid for Sensor L and dashed for Sensor S, and have R^2 values of 0.89 and 0.97 for Sensor L and Sensor S, respectively.

In the case of Sensor Au, a significantly different relationship between resistance and temperature was observed. As shown by Fig. 6.4, the resistance remained approximately constant below 300°C but increased sharply at higher temperatures. The natural logarithm of the resistance is plotted as a function of temperature above 300°C in Fig. 6.5, which shows direct proportionality between the two quantities with a gradient of approximately 1.6×10^{-2} K^{-1}. Using Eq. (6.1), this behaviour indicates that $d(\alpha\theta_O^2)/dT$ was larger than $d\ln(R_0)/dT$ above 300°C, and the sensor must therefore have exhibited a high value of $d\theta_O/dT$ if $d\alpha/dT$ was negative as before. Critically, however, it was shown in Chapter 1 that the assumed relationship between R and T expressed in Eq. (5.30), from which Eq. (6.1) derives, is only valid when the width of the depletion region between semiconductor grains is much smaller than the grain size. It is clear from Fig. 6.1 (d) that this criterion may not have been satisfied in the case of Sensor Au due to the sub-10 nm diameter of each ZnO nanoparticle; indeed, it is even possible that the entirety of sensing material was influenced by the surface potential, thereby invalidating the boundary conditions of Poisson's equation which were employed in Chapter 1 [43]. The positive correlation between R and T depicted in Fig. 6.5 may be

attributed in part, therefore, to the diminutive nature of the constituent ZnO nanoparticles altering the form of the surface potential in Eq. (5.30).

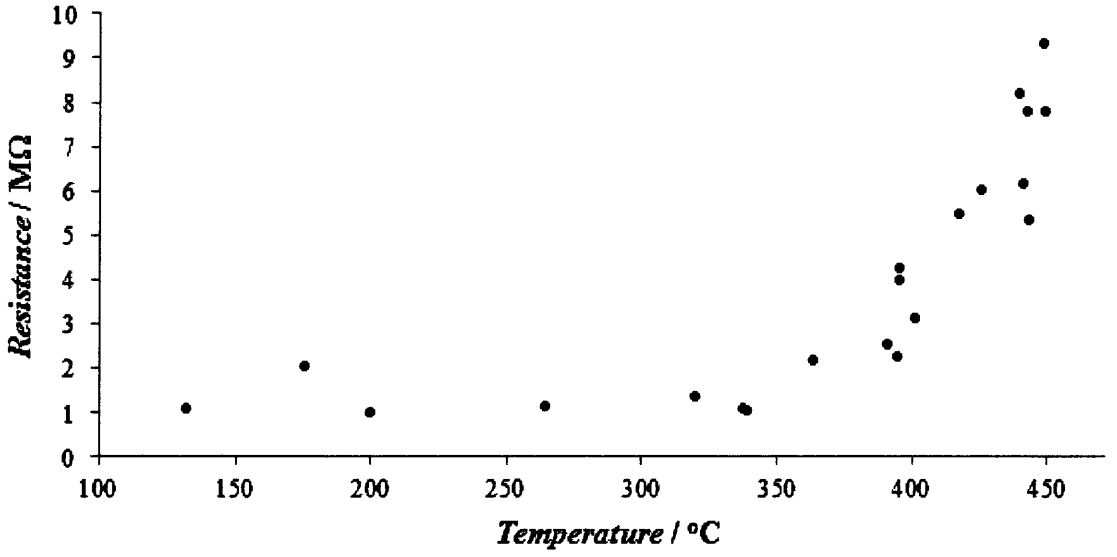

Fig. 6.4. A plot showing the resistance of Sensor Au as a function of temperature, where P_{O2}/P_{TOT} is 0.2 and no reducing gas is present.

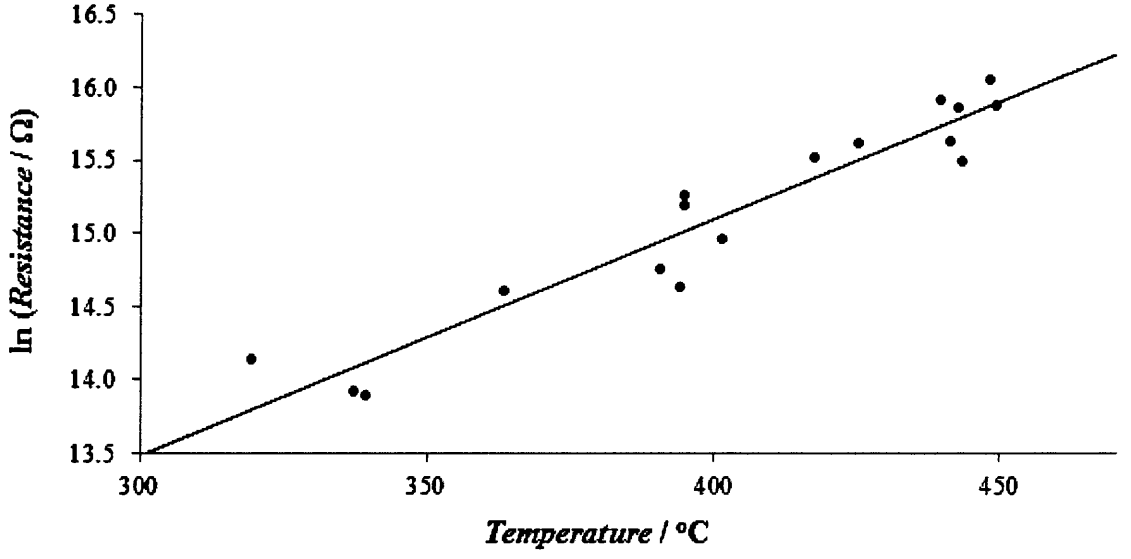

Fig. 6.5. A plot showing the natural logarithm of resistance as a function of temperature for Sensor Au, where P_{O2}/P_{TOT} is 0.2 and no reducing gas is present. Also plotted is a least-squares line-of-best-fit to the data, which has a R^2 value of 0.91.

6.3.4. The kinetics of H_2 oxidation

It was demonstrated in the previous section that the decoration of ZnO nanosheets by gold nanoparticles leads to a positive correlation between the sensor resistance and temperature. From this behaviour, it was proposed that the gold may have a considerable catalytic effect on the ionosorption of oxygen (although this is tentative suggestion due to the low size of the ZnO nanoparticles in Sensor Au, as discussed in the previous section). The catalytic properties of gold are also evident in the sensitivity of Sensor Au to CO, which exhibited a much larger response at a given temperature than the non-functionalised control device, Sensor L. The most significant difference between these two sensors, however, was in their responses to H_2; it was shown in Fig. 6.2 that while Sensor L produced a response of around 0.3 to 200 ppm of this gas at 300°C, the same concentration led to a Sensor Au response of over 0.8 at 200°C. In this section, the oxidation of H_2 in the presence of gold nanoparticles is considered in greater detail, and the theory developed in Chapter 5 is adapted to explore the dynamics of this reaction.

In order to compare the responses of the three sensors under particular conditions, one may simplistically plot the resistance of each device measured during exposure to a reducing gas. Fig. 6.6 depicts such a plot for hydrogen gas at a concentration of 200 ppm, with the sensors maintained at a temperature of 440°C. The problem with this approach, however, is that the absolute resistance of a sensor does not solely depend on the intrinsic electrical properties of the sensing material, but also its coverage and thickness. It is therefore possible for two devices with identical sensing properties to exhibit different resistances under a particular set of experimental conditions. For this reason it is difficult to reach any significant conclusions through comparison of the absolute resistance values of different sensors. Moreover, when analysing Fig. 6.6 it is difficult to compare the responses of different sensors due to their differing starting resistances, thereby limiting the usefulness of the plot.

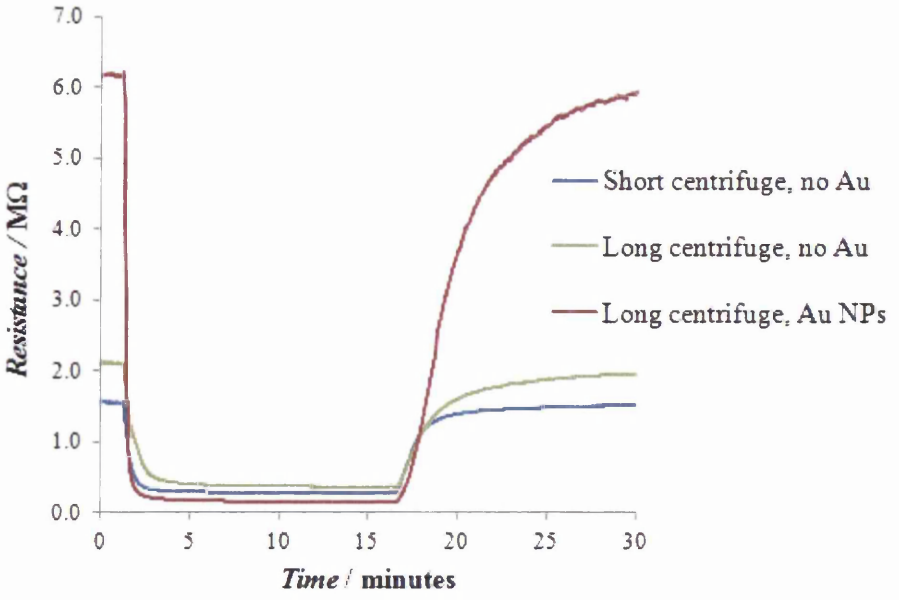

Fig. 6.6. A plot showing the resistances of the three sensors during exposure to 200 ppm of H_2 at 440°C. Each response test was conducted at a P_{O2}/P_{TOT} value of 0.2.

To better understand the differences between the Sensors S, L and Au, Fig. 6.7 compares the normalised response and recovery curves of the devices when exposed to 200 ppm of H_2 at approximately 440°C. More specifically, for each device the resistance has been normalised with respect to the mean resistance prior to the introduction of H_2. The plot shows that the sensitivity of Sensor L was almost identical to that of Sensor S at this temperature, with both producing a response of 0.82–0.83. Sensor Au, by contrast, exhibited a corresponding response of approximately 0.98. To facilitate comparison between the response and recovery rates of the different sensors, Fig. 6.7 (b) plots the variation of the "response-normalised resistance", R_{resp}, defined by the formula

$$R_{resp} = 1 - \frac{R(H_2\ off) - R}{R(H_2\ off) - R(H_2\ on)} \tag{6.5}$$

where R is the measured resistance and $R(H_2\ on)$ and $R(H_2\ off)$ are the equilibrium resistances in the presence and absence of H_2, respectively. From Eq. (6.5), the first time-derivative of R_{resp} is given by

$$\frac{dR_{resp}}{dt} = \frac{1}{Response}\frac{d}{dt}\left(\frac{R}{R(H_2\ off)}\right) \tag{6.6}$$

The gradient of R_{resp} is therefore equal to the gradient of the normalised resistance, as plotted in Fig. 6.7 (a), divided by the sensor response. Fig. 6.7 (b) shows that the kinetics of the response were different for the two non-functionalised devices, as Sensor S responded and recovered at a significantly higher rate than Sensor L. Sensor Au responded more rapidly than both of these devices, but also recovered at the lowest rate of the three sensors.

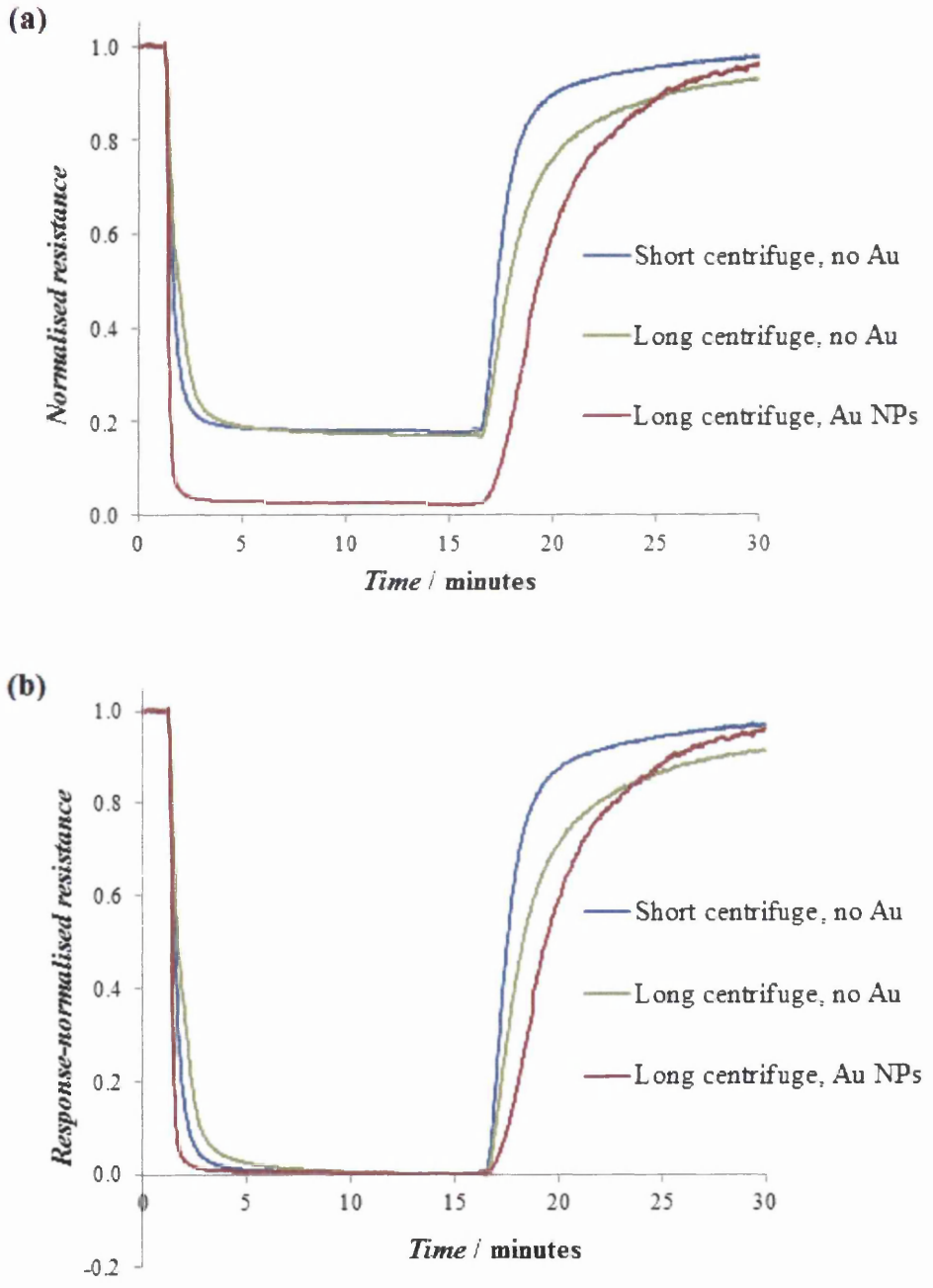

Fig. 6.7. Plots showing the responses of the three sensors to 200 ppm of H_2 at 440°C, normalised with respect to the starting resistance (a) or the response (b). Each response test was conducted at a P_{O2}/P_{TOT} value of 0.2.

Despite the similarity of their H_2 responses at 440°C, Sensors S and L displayed markedly different sensitivities to H_2 at 390°C; as shown by Fig. 6.8, the response of Sensor S to 200 ppm of H_2 did not vary significantly between the two temperatures, whereas Sensor L had a response of just 0.66 at 390°C. As before, Sensor Au exhibited both the highest sensitivity and the highest rate of response, but also recovered more slowly than the other two sensors.

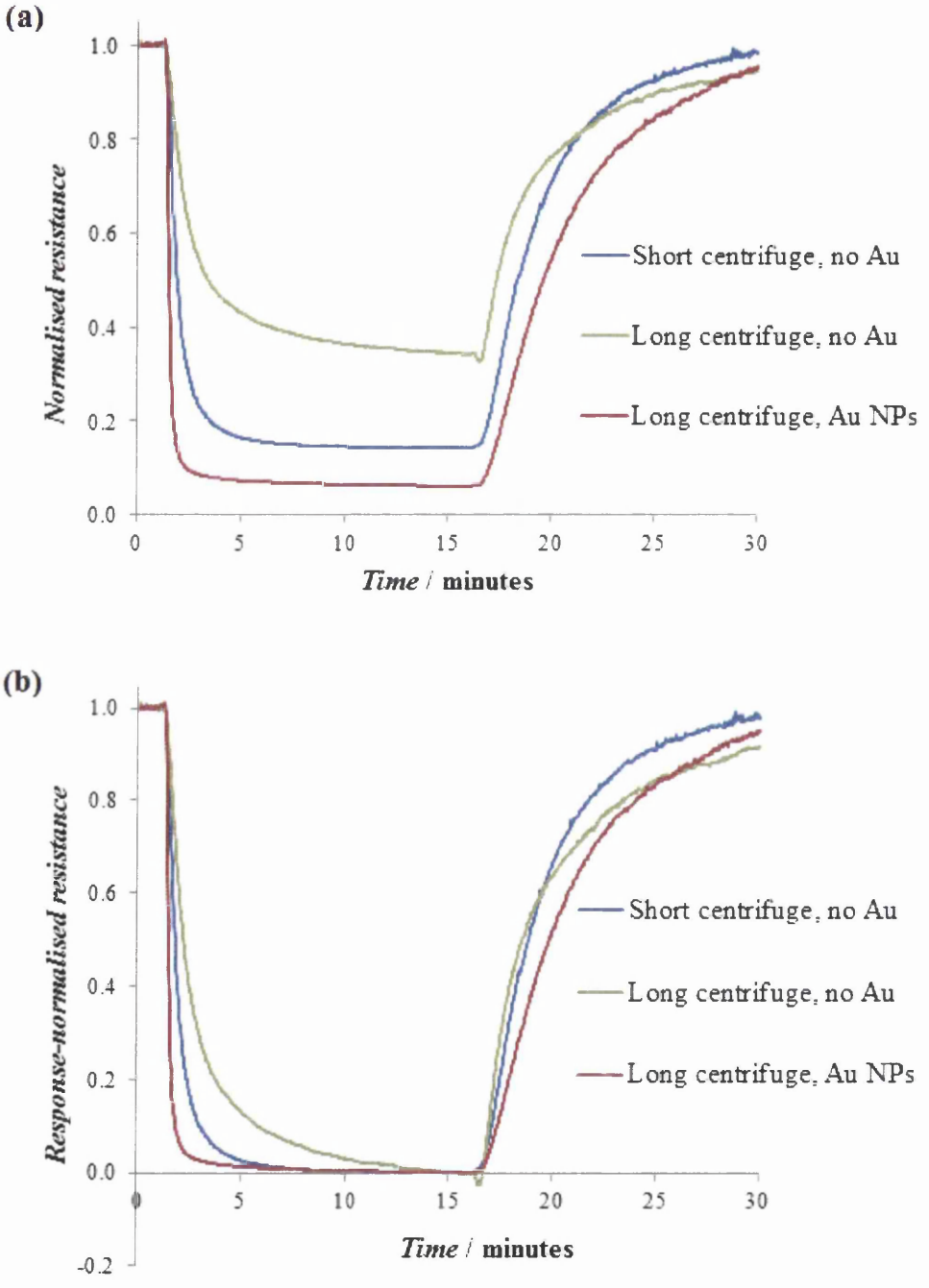

Fig. 6.8. Plots showing the responses of the three sensors to 200 ppm of H_2 at 390°C, normalised with respect to the starting resistance (a) or the response (b). Each response test was conducted at a P_{O2}/P_{TOT} value of 0.2.

It was previously observed that while Sensor Au exhibited a response of over 0.8 to 200 ppm of H_2 at temperatures as low as 200°C, the corresponding response of Sensor L was negligible at this temperature. However, Fig. 6.9 shows that despite the rapid response of Sensor Au at low temperatures, the rate of recovery was substantially diminished. Indeed, at temperatures of 175°C and below there was no discernible recovery of the sensor resistance over the time-scale of the measurement, and it was necessary to temporarily elevate the temperature to recover the initial resistance value.

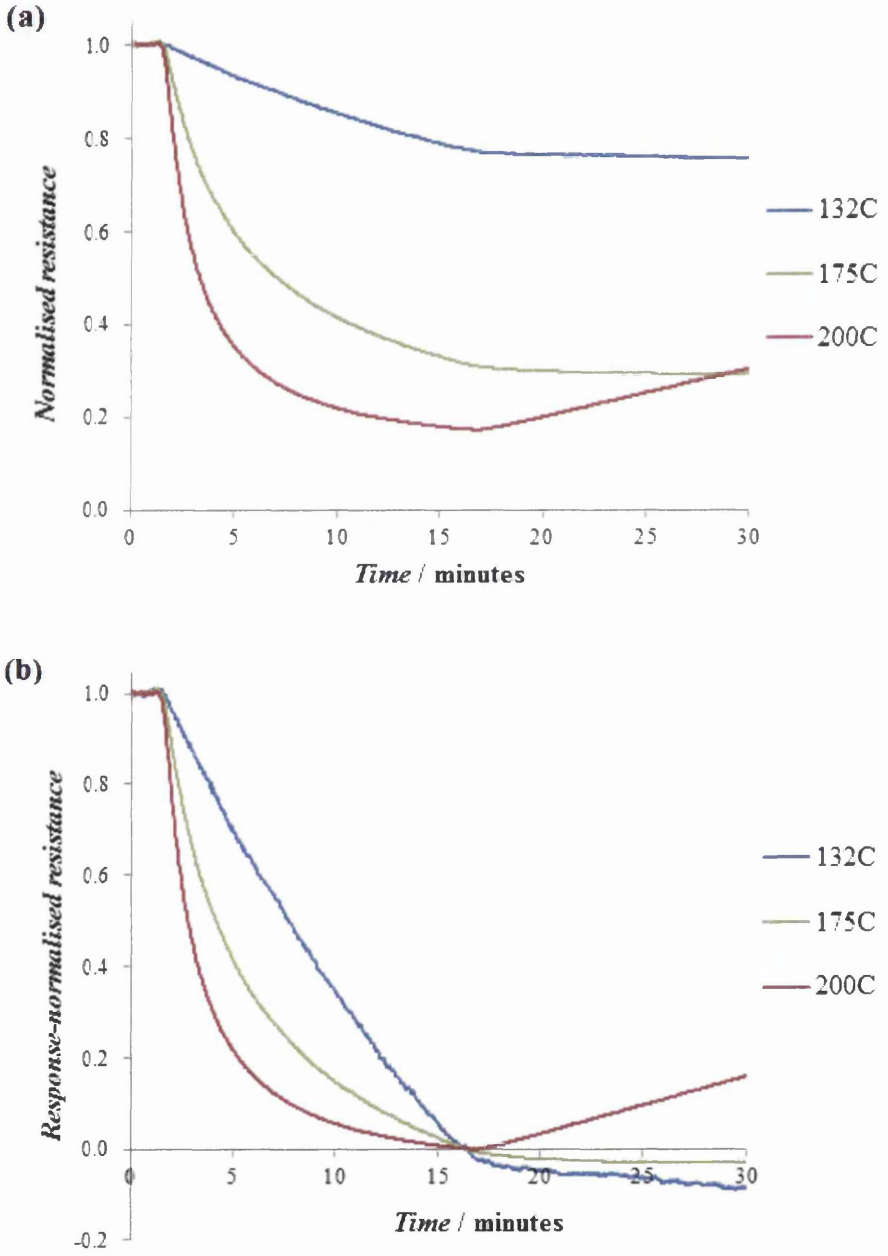

Fig. 6.9. Plots showing the responses of the Sensor Au to 200 ppm of H_2 at low temperatures normalised with respect to the starting resistance (a) or the response (b). Each response test was conducted at a P_{O2}/P_{TOT} value of 0.2.

It is important to verify whether the results of Sensors S and L depicted in Fig. (6.7), Fig. (6.8) and Fig (6.9) are consistent with the model formulated in Chapter 5. Above all, the theory should be compatible with the observed similarity of the H_2 responses at 440°C, whilst predicting disparate sensitivities at 390°C. It is worth noting that the different response and recovery rates of the two sensors, combined with their contrasting relationships between resistance and temperature, indicate that they possessed dissimilar reaction dynamics. It is therefore surprising that the H_2 responses of these devices converged at 440°C, particularly since the CO responses at this temperature were significantly different. Fig. 6.10 illustrates this point more clearly, showing that while Sensor S exhibited a response of 0.49 to 200 ppm of CO, Sensor L had a corresponding response of just 0.21. Indeed, the response of Sensor S was the highest of the three sensors, exceeding the measured Sensor Au response of 0.37.

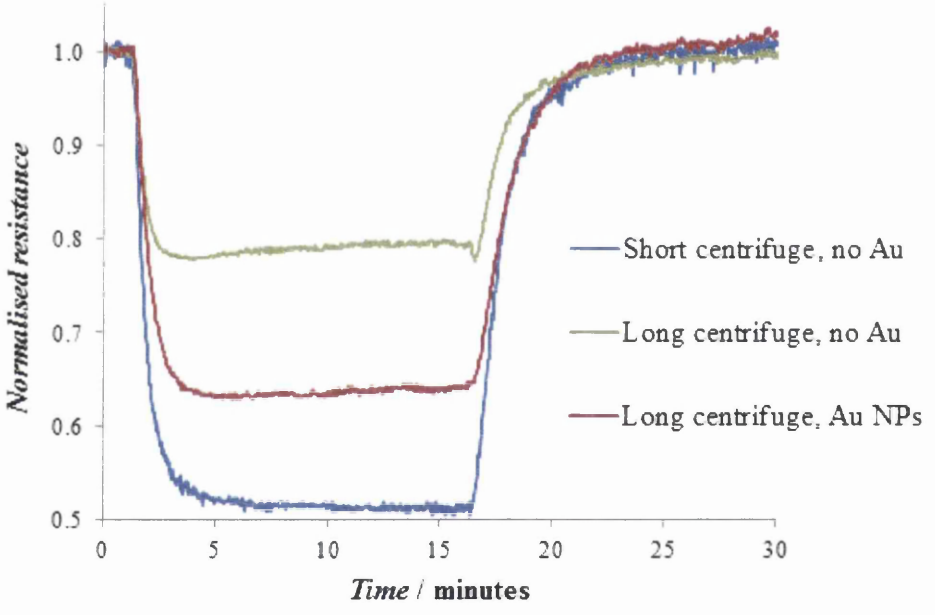

Fig. 6.10. A plot showing the responses of the three sensors to 200 ppm of CO at 440°C, normalised with respect to the starting resistance. Each response test was conducted at a P_{O2}/P_{TOT} value of 0.2.

In the previous model, the rate of O^- formation in the presence of a reducing gas, X, was described by the expression

$$\frac{d[O^-]}{dt} = k_1 \left(\frac{P_{O2}}{P_{TOT}}\right)^{\frac{1}{2}} (n_{sites} - [O^-] - [OX^-]) - k_{-1}[O^-] - k_{r1}\left(\frac{P_X}{P_{TOT}}\right)[O^-] \qquad (6.7)$$

where P_{O2} and P_X are the partial pressures of O_2 and X, respectively, P_{TOT} is the total system pressure, k_1, k_{-1}, and k_{r1} are temperature-dependent rate constants and $[O^-]$ and $[OX^-]$ are the surface concentrations of O- ions and OX^- intermediates, respectively. If P_X is zero, the equilibrium concentration of O^- ions is given by

$$[O^-](X\,off) = \frac{k_1\left(\frac{P_{O2}}{P_{TOT}}\right)^{\frac{1}{2}} n_{sites}}{k_1\left(\frac{P_{O2}}{P_{TOT}}\right)^{\frac{1}{2}} + k_{-1}} \tag{6.8}$$

so the value of $[O^-](X\,off)$ is expected to increase in direct proportion to n_{sites}, the total concentration of surface sites. When exposed to molecules of X, the O^- ions react to form OX^- intermediates which subsequently desorb as stable, electrically neutral molecules of OX. The rate of formation of the OX^- intermediates is dictated by the formula

$$\frac{d[OX^-]}{dt} = k_{r1}\left(\frac{P_X}{P_{TOT}}\right)[O^-] - k_{r2}[OX^-] \tag{6.9}$$

where k_{r2} is another temperature-dependent rate constant. Summing Eq. (6.7) and Eq. (6.9) leads to

$$\frac{d}{dt}([O^-] + [OX^-]) = k_1\left(\frac{P_{O2}}{P_{TOT}}\right)^{\frac{1}{2}}(n_{sites} - [O^-] - [OX^-]) - k_{-1}[O^-] - k_{r2}[OX^-] \tag{6.10}$$

Hence, the equilibrium concentration of surface ions may be written as

$$\left([O^-](X\,on) + [OX^-](X\,on)\right) = \frac{k_1\left(\frac{P_{O2}}{P_{TOT}}\right)^{\frac{1}{2}} n_{sites}}{k_1\left(\frac{P_{O2}}{P_{TOT}}\right)^{\frac{1}{2}} + k_{-1} + (k_{r2} - k_{-1})\frac{k_{r1}\left(\frac{P_X}{P_{TOT}}\right)}{k_{r1}\left(\frac{P_X}{P_{TOT}}\right) + k_{r2}}} \tag{6.11}$$

It may be shown from Eq. (6.8), Eq. (6.11) and Eq. (5.31) that the total sensor response to reducing gas X is given by

$$Response = 1 - \exp\left(-\alpha\frac{\eta^2 - 1}{\eta^2}\theta_O(X\,off)^2\right) \tag{6.12}$$

where $\theta_O(X\ off)$ is equal to $[O^-](X\ off)/n_{sites}$ and

$$\eta = 1 + \frac{k_{r1}\left(\frac{P_X}{P_{TOT}}\right)(k_{r2} - k_{-1})}{\left(k_{r1}\left(\frac{P_X}{P_{TOT}}\right) + k_{r2}\right)\left(k_1\left(\frac{P_{O2}}{P_{TOT}}\right)^{\frac{1}{2}} + k_{-1}\right)} \tag{6.13}$$

Due to the plethora of reaction parameters in Eq. (6.12), it is difficult to reconcile this equation with the observations in Fig. 6.7; if, as reasoned above, the values of variables such as α, k_1, k_{-1}, k_{r1} and k_{r2} were different for Sensors S and L, one would not expect their H_2 responses to be equal. It is possible that this disparity between experiment and theory results from the assumption that P_{H2} remains constant during the gas response; the high sensor response to H_2 implies that this gas oxidises much more rapidly than CO, and the reaction may therefore significantly diminish the concentration of gaseous H_2 in the vicinity of the ZnO surface.

To account for the time-dependence of P_{H2}, one must construct a differential equation to describe the variation of the H_2 concentration at the sensor surface, $[H_2]$. It is to be assumed that H_2 is continuously introduced to the surface region at a rate equal to $k_{flow}[H_2]_0$, where k_{flow} is the gas flow rate and $[H_2]_0$ denotes the concentration of H_2 passed into the system. Similarly, H_2 departs from the region at a rate $k_{flow}[H_2]$. According to the existing model, the rate of H_2 oxidation is governed by a temperature-dependence rate constant, k_{r1}, and is directly proportional to the concentration of O^- ions at the surface, $[O^-]$, and the ratio of P_{H2} to P_{TOT}. Combining these considerations,

$$\frac{d[H_2]}{dt} = k_{flow}([H_2]_0 - [H_2]) - k_{r1}\left(\frac{P_{H2}}{P_{TOT}}\right)[O^-] \tag{6.14}$$

If the total pressure exerted on the surface per unit mole of gas is p_{mol}, and the total area of the surface is A, the partial pressure of H_2 may be expressed as

$$P_{H2} = Ap_{mol}[H_2] \tag{6.15}$$

Similarly, the total pressure at the surface is given by

$$P_{TOT} = Ap_{mol}([N_2] + [O_2] + [H_2]) \tag{6.16}$$

where $[N_2]$ and $[O_2]$ are the concentrations of nitrogen and oxygen, respectively. As $[O_2]$ is large and $[H_2]$ represents a very low proportion of the total concentration of gases in the system, P_{TOT} may be regarded as a constant. It follows from Eq. (6.14) that the equilibrium value of $[H_2]$ is given by

$$[H_2](H_2\ on) = \frac{[H_2]_0}{1+\frac{k_{r1}}{k_{flow}}\left(\frac{Ap_{mol}}{P_{TOT}}\right)[O^-](H_2\ on)} \tag{6.17}$$

To continue, it is helpful to assume that the H_2 oxidation occurs in a single-step, so that the formation of H_2O^- intermediates need not be considered. This assumption is equivalent to taking the rate constant of the second oxidation step, k_{r2}, to infinity. Implementing this simplification and substituting Eq. (6.17) into Eq. (6.11), one obtains

$$[O^-](H_2\ on)\left(k_1\left(\frac{P_{O2}}{P_{TOT}}\right)^{\frac{1}{2}} + k_{-1} + \frac{k_{r1}\left(\frac{Ap_{mol}}{P_{TOT}}\right)[H_2]_0}{1+\frac{k_{r1}}{k_{flow}}\left(\frac{Ap_{mol}}{P_{TOT}}\right)[O^-](H_2\ on)}\right) = k_1\left(\frac{P_{O2}}{P_{TOT}}\right)^{\frac{1}{2}} n_{sites} \tag{6.18}$$

The general solution of Eq. (6.18) is complicated, so it is prudent to consider the limiting scenarios. For instance, in the case where k_{r1} is very small, Eq. (6.18) simplifies to

$$\lim_{k_{r1}\to 0}[O^-](H_2\ on) = \frac{k_1\left(\frac{P_{O2}}{P_{TOT}}\right)^{\frac{1}{2}} n_{sites}}{k_1\left(\frac{P_{O2}}{P_{TOT}}\right)^{\frac{1}{2}} + k_{-1} + k_{r1}\left(\frac{P_{H2}}{P_{TOT}}\right)} \tag{6.19}$$

Due to the low rate of oxidation, P_{H2} remains approximately constant during the course of the response. As expected, one recovers Eq. (6.11) with k_{r2} taken to infinity and $[H_2O^-]$ set equal to zero.

Although the algebra is more involved, it is possible to explore alternative regimes of Eq. (6.18). By rearranging the formula, one may show that

$$[O^-](H_2\ on) = \frac{1+b\left(\frac{P_{H2}}{P_{TOT}}\right)_0 - acn_{sites}}{2a}\left(-1 \pm \sqrt{1+\frac{4acn_{sites}}{\left(1+b\left(\frac{P_{H2}}{P_{TOT}}\right)_0 - acn_{sites}\right)^2}}\right) \tag{6.20}$$

for a generalised system, where

$$a \equiv \frac{k_{r1}}{k_{flow}}\left(\frac{Ap_{mol}}{P_{TOT}}\right) \tag{6.21}$$

$$b \equiv \frac{k_{r1}}{k_1\left(\frac{P_{O2}}{P_{TOT}}\right)^{\frac{1}{2}} + k_{-1}} \tag{6.22}$$

$$c \equiv \frac{k_1\left(\frac{P_{O2}}{P_{TOT}}\right)^{\frac{1}{2}}}{k_1\left(\frac{P_{O2}}{P_{TOT}}\right)^{\frac{1}{2}} + k_{-1}} \tag{6.23}$$

and $(P_{H2}/P_{TOT})_0$ denotes the ratio of P_{H2} to P_{TOT} in the absence of H_2 oxidation. At 440°C, all three sensors exhibited a large response to H_2 at a concentration of 200 ppm. It is therefore likely that the corresponding k_{r1} value of each sensor was high, so the product acn_{sites} cannot be considered a small quantity as in the first example. If $b(P_{H2}/P_{TOT})_0$ is much less than one, the square root in Eq. (6.20) may be replaced by the binomial approximation

$$\sqrt{1+\frac{4acn_{sites}}{\left(1+b\left(\frac{P_{H2}}{P_{TOT}}\right)_0 - acn_{sites}\right)^2}} \approx \frac{(1+acn_{sites})}{\left(1+b\left(\frac{P_{H2}}{P_{TOT}}\right)_0 - acn_{sites}\right)}\left(1+\frac{b\left(\frac{P_{H2}}{P_{TOT}}\right)_0(1-acn_{sites})}{(1+acn_{sites})^2}\right) \tag{6.24}$$

Although Eq. (6.20) has two formal solutions, use of Eq. (6.24) leads to just one physical solution given by

$$\lim_{P_{H2}\to 0}[O^-](H_2\ on) = cn_{sites}\left(1-\frac{b\left(\frac{P_{H2}}{P_{TOT}}\right)_0}{1+acn_{sites}}\right) \tag{6.25}$$

or

$$\lim_{P_{H2}\to 0}[O^-](H_2\ on) = [O^-](H_2\ off)\left(1 - \frac{b\left(\frac{P_{H2}}{P_{TOT}}\right)_0}{1+a[O^-](H_2\ off)}\right) \tag{6.26}$$

When the relationship between $[O^-](H_2\ on)$ and P_{H2}/P_{TOT} is described by Eq. (6.26), the behaviour of the response differs to that predicted previously. When k_{r1} is large but the H_2 concentration is low, as in the example above, it may be shown using Eq. (6.8), Eq. (6.26) and Eq. (5.31) that the response is given approximately by

$$\lim_{P_{H2}\to 0} Response = 1 - \exp\left(-\alpha \frac{2bc^2\left(\frac{P_{H2}}{P_{TOT}}\right)_0}{1+acn_{sites}}\right) \tag{6.27}$$

which may also be written as

$$\lim_{P_{H2}\to 0} Response = 1 - \exp\left(-\frac{2\alpha}{n_{sites}^2} \frac{b\left(\frac{P_{H2}}{P_{TOT}}\right)_0 [O^-](H_2\ off)^2}{1+a[O^-](H_2\ off)}\right) \tag{6.28}$$

For systems in which k_{r1} is very large, it may be reasonable to additionally assume that the product $a[O^-](H_2\ off)$ is much greater than one as a is directly proportional to k_{r1}. In these cases one may use the definitions of a and b to show that

$$\lim_{P_{H2}\to 0} Response = 1 - \exp\left(-\frac{2\alpha}{n_{sites}} \frac{k_{flow}\left(\frac{P_{H2}}{P_{TOT}}\right)_0 \theta_O(H_2\ off)}{\left(\frac{Ap_{mol}}{P_{TOT}}\right)\left(k_1\left(\frac{P_{O2}}{P_{TOT}}\right)^{\frac{1}{2}} + k_{-1}\right)}\right) \tag{6.29}$$

which, unlike Eq. (6.12), has no dependence on k_{r1}. It is therefore apparent that if H_2 is admitted to the system at a sufficiently low concentration and oxidises at a high enough rate, the measured response is not influenced by the precise kinetics of the reaction. The physical reasoning for this result is that while increasing k_{r1} enhances the probability of reaction between surface O^- ions and an incident molecule of H_2, the concentration of H_2 close to the ZnO surface is lowered as the molecules oxidise faster than they can be replenished. The reaction is therefore self-limiting, allowing two sensors with different values of k_{r1} to exhibit similar responses to a particular concentration of H_2. It is also worth noting that since α is

directly proportional to n_{sites}^2, the exponent of Eq. (6.29) has a much weaker dependence on n_{sites} than that of Eq. (6.12). It follows that a response characterised by Eq. (6.29) is less strongly influenced by the morphology and composition of the ZnO surface, again resulting in a smaller difference between the responses of two disparate sensors.

Returning to Fig. 6.7, Sensor Au exhibited a higher response to H_2 than the other two sensors at 440°C and, as shown by Fig. 6.8, reducing the temperature to 390°C did not have a significant effect on the sensitivity or the rates of response or recovery. Furthermore, when H_2 was present at a concentration of 200 ppm, Fig. 6.2 shows that Sensor Au produced a response of more than 0.8 at temperatures greater than 200°C; by contrast, the corresponding response of Sensor L was only 0.16 at 270°C, and became negligible when the temperature was decreased below 250°C. Despite Sensor Au responding more rapidly to H_2 than the non-functionalised sensors, the corresponding recovery rate was lower at every temperature within the measured range. This trend was not repeated between the non-functionalised devices, particularly at 440°C; at this temperature, Sensor S responded and recovered at a significantly higher rate than Sensor L. To explain the observations it is necessary to digress from the models formulated in this chapter and the last, instead considering possible catalytic mechanisms.

The catalysis of H_2 oxidation by noble metal nanoparticles, which was reviewed in Chapter 2, is often attributed to a "hydrogen spillover" phenomenon [44–50]. In this process, H_2 dissociates at the metal surface to form atomic H radicals which subsequently migrate to the ZnO surface. As the radicals encounter O^- ions they react to form OH^- intermediates, which may in turn interact to produce a stable molecule of H_2O according to the equation

$$\boldsymbol{2OH^- \rightarrow O^- + H_2O + e_s^-} \tag{6.30}$$

where e_s^- denotes a surface electron. Assuming that Sensor Au responded to H_2 via the spillover mechanism, the low recovery rate of the sensor suggests that the formation of O^- ions was inhibited following turn-off of the H_2. As noted in Chapter 2, previous studies have demonstrated that the OH^- species formed during H_2 dissociation are long-lived [51–54], and may therefore impede the recovery of the sensor resistance. The negligible recovery

observed at temperatures of 175°C and below indicates that while the catalyst facilitated the oxidation of H_2 at these temperatures, the subsequent removal of OH^- radicals did not occur at a significant rate.

6.4. Conclusions

Through application and adaptation of the theory developed in Chapter 5, the reactions of different gases at the surface of gold-coated ZnO have been explored. In accordance with previous reports [55–62], the response of ZnO nanosheets to CO was shown to be significantly increased by the presence of gold nanoparticles. The sensitivity to H_2 demonstrated an even larger enhancement, with a gold-decorated sensor producing a response of over 0.8 to 200 ppm of H_2 at temperatures above 200°C despite a non-functionalised control sensor exhibiting no discernible response below 250°C. It is thought that the improved sensitivity may be attributed to a "hydrogen spillover" mechanism, wherein H_2 molecules dissociate at the gold surface to produce rapidly oxidising OH^- radicals.

To investigate how the preparation of the LBZA precursor affects the response characteristics of the finished ZnO nanosheet-based sensor, two non-functionalised sensors were produced using different fabrication protocols. In the preparation of the first sensor, LBZA nanosheets were centrifuged into deionised water over five five-minute cycles. The second device, by contrast, consisted of LBZA nanosheets which were centrifuged using four five-minute phases followed by a final centrifugation step of 90 minutes. Despite SEM images of the two sensors showing that they contained nanoparticles of similar mean size, the responses of these devices differed significantly. In the case of CO, for instance, a longer centrifugation procedure substantially diminished both the response and the response rate of the sensor. Furthermore, in the absence of a reducing gas the resistance was found to decrease more gradually with increasing temperature following the more prolongued centrifugation. From these observations, it is evident that the composition of the ZnO depends strongly on the preparation of the LBZA precursor.

Coating the nanosheets with gold nanoparticles also had an appreciable effect on their morphology. Most notably, SEM showed that the gold-decorated nanosheets were comprised of much smaller nanoparticles than those of the non-functionalised sensors, possibly due to residual citrate ions from the gold nanoparticle suspension suppressing Ostwald ripening of the ZnO during thermal decomposition of the LBZA. In addition to enhancing the rates of both CO and H_2 oxidation, decoration by gold nanoparticles was shown to produce a positive correlation between sensor resistance and temperature above 300°C, with no reducing gas present. It was recognised that this trend may be partially attributed to the sub-10 nm mean diameter of the constituent ZnO nanoparticles, which is likely to be too small for the surface potential to adopt the form described in Chapter 1. For this reason, it is difficult to use the measured relationship between the resistance and temperature to assess whether the gold aggregates have a catalytic effect on the ionosorption of oxygen.

In the previous chapter, a phenomenological model was used to analyse the kinetics of CO oxidation. When applied to the case of H_2, however, it was not possible to reconcile the theory to the measured responses of the non-functionalised sensors. In particular, the model could not explain why the responses of the two devices contrasted below 400°C but were almost identical at 440°C. According to the theory from Chapter 5, if the surface site concentration and reaction rate constants are different for two sensors, the responses should also be different. To explain the convergence of the responses at high temperature, it was necessary to account for the decrease in the H_2 partial pressure close to the ZnO surface; due to the high oxidation rate of H_2, the concentration close to the surface is lower than in the bulk surroundings. By considering the time-dependence of gas concentrations in this way, it is possible to extend the methodology from Chapter 5 to gases that are oxidised more readily than CO.

References

[1] P. Rai, Y.S. Kim, H.M. Song, M.K. Song, Y.T. Yu, The role of gold catalyst on the sensing behavior of ZnO nanorods for CO and NO 2 gases, Sensors Actuators, B Chem. 165 (2012) 133–142. doi:10.1016/j.snb.2012.02.030.

[2] Q. Xiang, G. Meng, Y. Zhang, J. Xu, P. Xu, Q. Pan, et al., Ag nanoparticle embedded-ZnO nanorods synthesized via a photochemical method and its gas-sensing properties, Sensors Actuators, B Chem. 143 (2010) 635–640. doi:10.1016/j.snb.2009.10.007.

[3] R.K. Joshi, Q. Hu, F. Alvi, N. Joshi, A. Kumar, Au Decorated Zinc Oxide Nanowires for CO Sensing, J. Phys. Chem. C. 113 (2009) 16199–16202. doi:10.1021/jp906458b.

[4] S. Ren, G. Fan, S. Qu, Q. Wang, Enhanced H2 sensitivity at room temperature of ZnO nanowires functionalized by Pd nanoparticles, J. Appl. Phys. 110 (2011). doi:10.1063/1.3647310.

[5] C.M. Chang, M.H. Hon, I.C. Leu, Outstanding H2 sensing performance of Pd nanoparticle-decorated ZnO nanorod arrays and the temperature-dependent sensing mechanisms, ACS Appl. Mater. Interfaces. 5 (2013) 135–143. doi:10.1021/am302294v.

[6] X. Deng, S. Sang, P. Li, G. Li, F. Gao, Y. Sun, et al., Preparation, characterization, and mechanistic understanding of Pd-decorated ZnO nanowires for ethanol sensing, J. Nanomater. 2013 (2013). doi:10.1155/2013/297676.

[7] C. Jiajun, W. Kai, W. Zhou, Vertically Aligned ZnO Nanorod Arrays Coated with SnO2/Noble Metal Nanoparticles for Highly Sensitive and Selective Gas Detection, Nanotechnology, IEEE Trans. 10 (2011) 968–974. doi:10.1109/TNANO.2010.2091423.

[8] H.T. Wang, B.S. Kang, F. Ren, L.C. Tien, P.W. Sadik, D.P. Norton, et al., Hydrogen-selective sensing at room temperature with ZnO nanorods, Appl. Phys. Lett. 86 (2005) 1–3. doi:10.1063/1.1949707.

[9] L.C. Tien, P.W. Sadik, D.P. Norton, L.F. Voss, S.J. Pearton, H.T. Wang, et al., Hydrogen sensing at room temperature with Pt-coated ZnO thin films and nanorods, Appl. Phys. Lett. 87 (2005) 1–3. doi:10.1063/1.2136070.

[10] C. Li, L. Li, Z. Du, H. Yu, Y. Xiang, Y. Li, et al., Rapid and ultrahigh ethanol sensing based on Au-coated ZnO nanorods., Nanotechnology. 19 (2008) 035501. doi:10.1088/0957-4484/19/03/035501.

[11] C.S. Rout, S. Hari Krishna, S.R.C. Vivekchand, A. Govindaraj, C.N.R. Rao, Hydrogen and ethanol sensors based on ZnO nanorods, nanowires and nanotubes, Chem. Phys. Lett. 418 (2006) 586–590. doi:10.1016/j.cplett.2005.11.040.

[12] X. Liu, M.H. Liu, Y.C. Luo, C.Y. Mou, S.D. Lin, H. Cheng, et al., Strong metal-support interactions between gold nanoparticles and ZnO nanorods in CO oxidation, J. Am. Chem. Soc. 134 (2012) 10251–10258. doi:10.1021/ja3033235.

[13] X. Xue, Z. Chen, L. Xing, C. Ma, Y. Chen, T. Wang, Enhanced Optical and Sensing Properties of One-Step Synthesized Pt - ZnO Nanoflowers, (2010) 18607–18611.

[14] V.R. Shinde, T.P. Gujar, C.D. Lokhande, Enhanced response of porous ZnO nanobeads towards LPG: Effect of Pd sensitization, Sensors Actuators, B Chem. 123 (2007) 701–706. doi:10.1016/j.snb.2006.10.003.

[15] X. Liu, J. Zhang, X. Guo, S. Wu, S. Wang, Amino acid-assisted one-pot assembly of Au, Pt nanoparticles onto one-dimensional ZnO microrods, Nanoscale. 2 (2010) 1178–1184. doi:10.1039/c005273f.

[16] M. Haruta, T. Kobayashi, H. Sano, N. Yamada, Novel gold catalysts for the oxidation of carbon monoxide at a temperature far below 0.DEG.C., Chem. Lett. (1987) 405–408. doi:10.1246/cl.1987.405.

[17] B. Bahrami, A. Khodadadi, M. Kazemeini, Y. Mortazavi, Enhanced CO sensitivity and selectivity of gold nanoparticles-doped SnO2 sensor in presence of propane and methane, Sensors Actuators, B Chem. 133 (2008) 352–356. doi:10.1016/j.snb.2008.02.034.

[18] S.-J. Chang, T.-J. Hsueh, I.-C. Chen, B.-R. Huang, Highly sensitive ZnO nanowire CO sensors with the adsorption of Au nanoparticles., Nanotechnology. 19 (2008) 175502. doi:10.1088/0957-4484/19/17/175502.

[19] N.S. Ramgir, Y.K. Hwang, S.H. Jhung, I.S. Mulla, J.S. Chang, Effect of Pt concentration on the physicochemical properties and CO sensing activity of mesostructured SnO 2, Sensors Actuators, B Chem. 114 (2006) 275–282. doi:10.1016/j.snb.2005.05.016.

[20] L. Mädler, T. Sahm, A. Gurlo, J.D. Grunwaldt, N. Barsan, U. Weimar, et al., Sensing low concentrations of CO using flame-spray-made Pt/SnO2 nanoparticles, J. Nanoparticle Res. 8 (2006) 783–796. doi:10.1007/s11051-005-9029-6.

[21] Y. Zhang, J. Xu, P. Xu, Y. Zhu, X. Chen, W. Yu, Decoration of ZnO nanowires with Pt nanoparticles and their improved gas sensing and photocatalytic performance., Nanotechnology. 21 (2010) 285501. doi:10.1088/0957-4484/21/28/285501.

[22] C.-M. Chang, M.-H. Hon, I.-C. Leu, Improvement in CO sensing characteristics by decorating ZnO nanorod arrays with Pd nanoparticles and the related mechanisms, RSC Adv. 2 (2012) 2469. doi:10.1039/c2ra01016j.

[23] A. Setkus, Heterogeneous reaction rate based description of the response kinetics in metal oxide gas sensors, 87 (2002) 346–357.

[24] K. Grass, The Kinetics of Carbon Monoxide Oxidation on Tin(IV) Oxide Supported Platinum Catalysts, J. Catal. 172 (1997) 446–452. doi:10.1006/jcat.1997.1886.

[25] V.P. Zhdanov, Impact of surface science on the understanding of kinetics of heterogeneous catalytic reactions, 500 (2002) 966–985.

[26] S. Bai, T. Guo, D. Li, R. Luo, A. Chen, C.C. Liu, Intrinsic sensing properties of the flower-like ZnO nanostructures, Sensors Actuators, B Chem. 182 (2013) 747–754. doi:10.1016/j.snb.2013.03.077 Flower-like ZnO nanostructures.

[27] S. Nakata, S. Akakabe, M. Nakasuji, K. Yoshikawa, Gas Sensing Based on a Nonlinear Response: Discrimination between Hydrocarbons and Quantification of Individual Components in a Gas Mixture., Anal. Chem. 68 (1996) 2067–72. doi:10.1021/ac9510954.

[28] H. Busse, M. Voss, D. Jerdev, B. Koel, M. Paffett, Adsorption and reaction of gaseous H (D) atoms with D (H) adatoms on Pt (111) and Sn/Pt (111) surface alloys, Surf. Sci. 490 (2001) 133–143. doi:10.1016/S0039-6028(01)01323-1.

[29] I. Kocemba, J. Rynkowski, The influence of catalytic activity on the response of Pt/SnO2 gas sensors to carbon monoxide and hydrogen, Sensors Actuators, B Chem. 155 (2011) 659–666. doi:10.1016/j.snb.2011.01.026.

[30] S.K. Sivaraman, S. Kumar, V. Santhanam, Monodisperse sub-10 nm gold nanoparticles by reversing the order of addition in Turkevich method--the role of chloroauric acid., J. Colloid Interface Sci. 361 (2011) 543–7. doi:10.1016/j.jcis.2011.06.015.

[31] J. Kimling, M. Maier, V. Okenve, V. Kotaidis, H. Ballot, a Plech, et al., Turkevitch method for gold nanoparticle synthesis revisited, J. Phys. Chem. B. 110 (2006) 15700–15707.

[32] S. Kumar, K.S. Gandhi, R. Kumar, Modeling of Formation of Gold Nanoparticles by Citrate Method †, Ind. Eng. Chem. Res. 46 (2007) 3128–3136. doi:10.1021/ie060672j.

[33] N.G. Bastús, J. Comenge, V. Puntes, Kinetically controlled seeded growth synthesis of citrate-stabilized gold nanoparticles of up to 200 nm: Size focusing versus ostwald ripening, Langmuir. 27 (2011) 11098–11105. doi:10.1021/la201938u.

[34] J. Polte, T.T. Ahner, F. Delissen, S. Sokolov, F. Emmerling, A.F. Thünemann, et al., Mechanism of gold nanoparticle formation in the classical citrate synthesis method derived from coupled in situ XANES and SAXS evaluation, J. Am. Chem. Soc. 132 (2010) 1296–1301. doi:10.1021/ja906506j.

[35] M.A. Gondal, Q.A. Drmosh, Z.H. Yamani, T.A. Saleh, Synthesis of ZnO2 nanoparticles by laser ablation in liquid and their annealing transformation into ZnO nanoparticles, Appl. Surf. Sci. 256 (2009) 298–304. doi:10.1016/j.apsusc.2009.08.019.

[36] V. Noack, A. Eychmüller, Annealing of nanometer-sized zinc oxide particles, Chem. Mater. 14 (2002) 1411–1417. doi:10.1021/cm011262i.

[37] D. Raoufi, Synthesis and photoluminescence characterization of ZnO nanoparticles, J. Lumin. 134 (2013) 213–219. doi:10.1016/j.jlumin.2012.08.045.

[38] R. Finsy, On the critical radius in Ostwald ripening, Langmuir. 20 (2004) 2975–2976. doi:10.1021/la035966d.

[39] F. Quaranta, R. Rella, P. Siciliano, S. Capone, M. Epifani, L. Vasanelli, A novel gas sensor based on SnO 2 rOs thin film for the detection of methane at low temperature, Sensors And Actuators. (1999) 350–355.

[40] T. Kawabe, S. Shimomura, T. Karasuda, K. Tabata, E. Suzuki, Y. Yamaguchi, Photoemission study of dissociatively adsorbed methane on a pre-oxidized SnO2 thin film, Surf. Sci. 448 (2000) 101–107. doi:10.1016/S0039-6028(99)00997-8.

[41] Y. Yamaguchi, Y. Nagasawa, S. Shimomura, K. Tabata, Reaction model for methane oxidation on reduced {SnO2} (110) surface, Int. J. Quantum Chem. 74 (1999) 423–433.

[42] Z. Su, S. Qin, D. Tang, H. Yang, C. Hu, Theoretical study on the reaction of methane and zinc oxide in gas phase, J. Mol. Struct. THEOCHEM. 778 (2006) 41–48. doi:10.1016/j.theochem.2006.08.041.

[43] C. Malagù, V. Guidi, M. Stefancich, M.C. Carotta, G. Martinelli, Model for Schottky barrier and surface states in nanostructured n-type semiconductors, J. Appl. Phys. 91 (2002) 808–814. doi:10.1063/1.1425434.

[44] U. Roland, T. Braunschweig, F. Roessner, On the nature of spilt-over hydrogen, J. Mol. Catal. A Chem. 127 (1997) 61–84. doi:10.1086/447782.

[45] G.M. Pajonk, Contribution of spillover effects to heterogeneous catalysis, Appl. Catal. A Gen. 202 (2000) 157–169. doi:10.1016/S0926-860X(00)00522-6.

[46] D.A. Panayotov, J.T. Yates, Spectroscopic Detection of Hydrogen Atom Spillover from Au Nanoparticles Supported on TiO2 : Use of Conduction Band Electrons, J. Phys. Chem. C. 111 (2007) 2959–2964.

[47] S. Shukla, S. Seal, L. Ludwig, C. Parish, Nanocrystalline indium oxide-doped tin oxide thin film as low temperature hydrogen sensor, Sensors Actuators, B Chem. 97 (2004) 256–265. doi:10.1016/j.snb.2003.08.025.

[48] N.A. Joy, C.M. Settens, R.J. Matyi, M.A. Carpenter, Plasmonic based kinetic analysis of hydrogen reactions within Au-YSZ nanocomposites, J. Phys. Chem. C. 115 (2011) 6283–6289. doi:10.1021/jp112228h.

[49] E. V. Benvenutti, L. Franken, C.C. Moro, FTIR Study of Hydrogen and Carbon Monoxide Adsorption on Pt/TiO2, Pt/ZrO2, and Pt/Al2O3, Langmuir. 15 (1999) 8140–8146. doi:10.1021/la990195s.

[50] J.M. Lee, J.E. Park, S. Kim, S. Kim, E. Lee, S.J. Kim, et al., Ultra-sensitive hydrogen gas sensors based on Pd-decorated tin dioxide nanostructures: Room temperature operating sensors, Int. J. Hydrogen Energy. 35 (2010) 12568–12573. doi:10.1016/j.ijhydene.2010.08.026.

[51] D.A. Panayotov, J.T. Yates, Spectroscopic detection of hydrogen atom spillover from Au nanoparticles supported on TiO2: Use of conduction band electrons, J. Phys. Chem. C. 111 (2007) 2959–2964. doi:10.1021/jp066686k.

[52] H. Pan, J. Luo, H. Sun, Y. Feng, C. Poh, J. Lin, Hydrogen storage of ZnO and Mg doped ZnO nanowires, Nanotechnology. 17 (2006) 2963–2967. doi:10.1088/0957-4484/17/12/023.

[53] S.H. Lim, J. Luo, Z. Zhong, W. Ji, J. Lin, Room-Temperature Hydrogen Uptake by TiO 2 Nanotubes, 44 (2005) 4124–4126.

[54] W.H. Doh, P.C. Roy, C.M. Kim, Interaction of hydrogen with ZnO: Surface adsorption versus bulk diffusion, Langmuir. 26 (2010) 16278–16281. doi:10.1021/la101369r.

[55] D. Widmann, R.J. Behm, Activation of molecular oxygen and the nature of the active oxygen species for co oxidation on oxide supported au catalysts, Acc. Chem. Res. 47 (2014) 740–749. doi:10.1021/ar400203e.

[56] M. Olea, M. Kunitake, T. Shido, Y. Iwasawa, TAP study on CO oxidation on a highly active Au/Ti(OH)4* catalyst, Phys. Chem. Chem. Phys. 3 (2001) 627–631.

[57] L.C. Wang, H.J. Jin, D. Widmann, J. Weissmüller, R.J. Behm, Dynamic studies of CO oxidation on nanoporous Au using a TAP reactor, J. Catal. 278 (2011) 219–227. doi:10.1016/j.jcat.2010.12.007.

[58] S.T. Daniells, A.R. Overweg, M. Makkee, J.A. Moulijn, The mechanism of low-temperature CO oxidation with Au/Fe2O3 catalysts: A combined Mossbauer, FT-IR, and TAP reactor study, J. Catal. 230 (2005) 52–65. doi:10.1016/j.jcat.2004.11.020.

[59] M. Kotobuki, R. Leppelt, D.A. Hansgen, D. Widmann, R.J. Behm, Reactive oxygen on a Au/TiO2 supported catalyst, J. Catal. 264 (2009) 67–76. doi:10.1016/j.jcat.2009.03.013.

[60] D. Widmann, Y. Liu, F. Schüth, R.J. Behm, Support effects in the Au-catalyzed CO oxidation - Correlation between activity, oxygen storage capacity, and support reducibility, J. Catal. 276 (2010) 292–305. doi:10.1016/j.jcat.2010.09.023.

[61] T. Fujitani, I. Nakamura, Mechanism and active sites of the oxidation of CO over Au/TiO2, Angew. Chemie - Int. Ed. 50 (2011) 10144–10147. doi:10.1002/anie.201104694.

[62] M. Haruta, When gold is not noble: Catalysis by nanoparticles, Chem. Rec. 3 (2003) 75–87. doi:10.1002/tcr.10053.

Concluding remarks

To better understand the physical properties of chemiresistive gas sensors, the formulation of representative phenomenological models is crucial. In recent years there has been a considerable effort by researchers to develop such theories, and many have managed to relate the measured electrical response of sensors to the dynamics of the underlying surface reactions. It is notable, however, that these studies have hitherto stopped short of quantitatively estimating the rate constants and activation energies of these reactions, primarily due to the multitude of fitting parameters required to provide a precise description of the system.

The aim of this work was to analyse the reaction mechanisms of zinc oxide nanosheet-based chemiresistive gas sensors in a more comprehensive manner, and to extend the analysis to devices which are catalysed by surface additives. After using a range of experimental procedures to explore the morphology and surface chemistry of the nanosheets in Chapter 4, the high-temperature oxidation of carbon monoxide at the zinc oxide surface was considered from physical first-principles in Chapter 5. The activation energies of particular surface reactions were evaluated by measuring the electrical resistance of the sensor in a range of gas environments at several different temperatures, and these results were corroborated by similar values reported elsewhere. The success of the study was due in large part to the novel experimental approach which has not, to the author's knowledge, been employed previously. The same methodology may be used in conjunction with different phenomenological models, allowing a similar analysis to be applied to other chemiresistive systems.

While Chapter 5 demonstrated a useful technique for investigating the oxidation of carbon monoxide at a zinc oxide surface, it was recognised in Chapter 6 that the procedure is not directly applicable to all reducing gases. Moreover, many practical sensing systems are complicated due to the presence of surface catalysts which provide alternative reaction pathways for a particular gas, thereby invalidating the Eley-Rideal approach used in the model. With no surface additives present, the hydrogen responses of two zinc oxide

nanosheet-based sensors were found to converge at 440°C despite differing significantly at lower temperatures, an observation which is incompatible with the theory developed in Chapter 5. It was surmised that the high oxidation rate of hydrogen resulted in a significant decrease in the hydrogen concentration close to the zinc oxide surface, thereby suppressing the sensor response. To account for this phenomenon, the previous model was modified by constructing a differential equation to describe the concentration of gaseous hydrogen at the surface, and it was subsequently shown that the sensor response at low concentrations becomes independent of the oxidation kinetics when the corresponding rate constant is sufficiently large.

An even larger response to hydrogen was observed in the presence of gold nanoparticles; in this case, the response to a 200 ppm concentration of hydrogen remained above 80% at temperatures as low as 200°C, despite non-functionalised sensors exhibiting no discernible response to the same proportion of hydrogen below 250°C. This behaviour indicates that the gold allowed the hydrogen to react via an alternative reaction pathway with lower associated activation energy. Although it was postulated that the gold expedites dissociation of the hydrogen molecule to produce reactive radicals, this hypothesis was based on previous research rather than the work presented herein. It is clear that the reasoning offered in Chapter 6 ought to be verified experimentally, specifically by developing an appropriate phenomenological model of the system as in Chapter 5. Assuming that the catalysed oxidation of hydrogen proceeds following dissociation of the diatomic molecule, the model should follow a Langmuir-Hinshelwood formalism of similar form to the examples cited in Chapter 2.

Despite the reactions of carbon monoxide and hydrogen being comprehensively scrutinised through Chapters 5 and 6, the response to methane was only fleetingly considered. Analysis of methane oxidation was inhibited by the poor sensitivity of the devices to this gas, with both non-functionalised and gold-catalysed sensors producing a negligible response to 200 ppm of methane at temperatures below 420°C. It is possible, however, that a more sizeable response could be achieved by simply modifying the procedure used to prepare the zinc oxide nanosheets; it was discovered, for instance, that the sensitivity to carbon monoxide was substantially enhanced by centrifuging the LBZA precursor for a shorter amount of time prior

to deposition. Indeed, even more significant changes might be expected from varying the temperature at which the zinc oxide nanosheets are annealed, particularly as Chapter 4 showed that the annealing temperature influenced both the morphology and the surface chemistry of the material. Moreover, decoration of the LBZA precursor by gold nanoparticles resulted in sub-10 nm zinc oxide nanoparticles following a 500°C anneal, possibly due to residual reactants from the gold nanoparticle suspension suppressing Ostwald ripening of the zinc oxide. It is therefore conceivable that the morphology of the nanosheets could be reproducibly controlled by adding an appropriate surfactant to the LBZA suspension following centrifugation. A proper analysis of the relationship between the zinc oxide preparation procedure and the subsequent gas sensing properties would be highly instructive, helping to relate the properties of the zinc oxide surface to the electrical responses of the sensor and thereby aiding the development of practical chemiresistive devices.

Future work

Within this thesis it has been demonstrated that particular physical and chemical characteristics of metal oxide nanostructures may be investigated through measurement of their gas responses at high temperature. However, despite the success of the theory and methodology detailed herein, the studies identified several experimental results which are worthy of further investigation.

In Chapter 4, zinc oxide nanosheets were prepared using a variety of annealing conditions in order to identify their effect on the morphology and surface chemistry of the material. Unfortunately, due to time limitations it was not possible to explore the influence of every annealing parameter; only the annealing temperature was varied between samples. To improve upon existing knowledge of the zinc oxide formation process, it would be beneficial to explore other variables such as the gas flow rate through the tube furnace during annealing or the oxygen concentration within the gas.

As another potential area of further study, it would also be interesting to build upon the X-ray photoelectron spectroscopy (XPS) work carried out in Chapter 4. By analysing the relative intensities of the O 1s and Zn 2p signals of differently-annealed zinc oxide samples, it was inferred that the concentration of oxygen-containing surface groups increases as a function of annealing temperature. From such tests, however, it is not straightforward to elucidate the nature of the surface species, nor their origin. If one were to examine the samples using a technique such as Fourier transform infra-red (FTIR) spectroscopy, it would be possible to better understand the chemistry of the surface groups; each chemical bond resonates at a well-defined frequency, and therefore produces a peak at a characteristic frequency in the infra-red absorption spectrum of the material. To supplement these experiments, one may also use a temperature-programmed desorption (TPD) technique, similar to those discussed in Chapter 2, to investigate the variety of species present at the surface of each sample. By heating the samples *in situ* within the analysis chamber of the XPS instrument, for instance, the XPS spectra could be measured at a variety of temperatures

in order to determine the characteristic desorption temperatures of the oxygen-containing surface species.

The use of XPS was not limited to the chemical characterisation of the zinc oxide nanosheets; in Chapter 5, the technique was employed alongside photoluminescence (PL) spectroscopy to determine the Fermi level position relative to the conduction band edge at the surface of the nanostructures. As was noted in the chapter, however, this estimate could not be directly compared to the corresponding value obtained from prior response measurements due to the differing experimental conditions of the two studies. More specifically, while the XPS valence band scans were recorded under ultra-high vacuum (UHV) conditions at room temperature, the gas sensing experiments were conducted at temperatures close to 400°C and using a 400 mL min^{-1} gas flow rate. Since the Fermi energy is a temperature-dependent quantity, as discussed in detail in Chapter 1, it was therefore not possible to relate the two experiments in a meaningful manner. Yet although the criterion of a UHV environment is indispensible in XPS, it is possible to perform the measurements at higher temperatures, potentially matching those of the gas sensing investigations. Repeating the XPS valence band scans at elevated temperatures would be invaluable in further verifying the suitability of the theory and methodology developed within Chapter 5.

The ability to heat a sample during XPS analysis is a feature which could facilitate even more ambitious experiments than those already considered. For instance, one could record XPS spectra of zinc oxide nanosheets over a range of temperature values, thereby allowing the Fermi energy (relative to the edge of the conduction or valence band) to be plotted as a function of temperature. It is apparent from the theory outlined in Chapter 1 and reiterated in Chapter 5, specifically Eq. (1.80) (repeated as Eq. (5.37)), that such an experiment could potentially reveal important information regarding the nature and concentrations of defects within the material. As an additional consideration it has been noted that, despite the absence of gas-induced surface species such as O^- and CO_2^- ions, long-lived species such as OH-groups may persist at the zinc oxide surface in a UHV environment. These species extract electron density from the surface, leading to the formation of a region of depleted electrons and an associated surface potential. However, in many modern XPS instruments, such as the Kratos AXIS Supra system employed in the present experiments, it is possible to remove a

plethora of surface contaminants via argon bombardment of the sample surface, thereby diminishing the surface potential. By using XPS valence band scans to measure the surface Fermi energy both before and after argon bombardment, it would therefore be possible to approximate the intrinsic surface potential as the difference of the two Fermi energy values.

As well as supplementing the results of the gas sensing investigations using other techniques, these studies could themselves be expanded. It may be recalled, for example, that one of the differential equations utilised in Chapter 5, Eq. (5.23), was only valid in certain special cases. In particular, it was shown that approximation of the more precise differential equation, Eq. (5.22), was justified in cases where the fractional surface coverage by O^- and CO_2^- ions varied sufficiently slowly. Whilst use of Eq. (5.23) in place of Eq. (5.22) simplified the analysis of subsequent resistance and response measurements, it was suggested in Section 5.4.9 that an iterative protocol would allow the results to be interpreted more precisely using Eq. (5.22), without invoking the aforementioned approximation. It would be informative to carry out this more accurate analysis to obtain more precise estimates of each reaction parameter, and in doing so further verify the validity of the corresponding values acquired in Chapter 5.

Due to the time-consuming nature of each gas sensing test, the investigations conducted in Chapters 5 and 6 were limited to just three sensors. Had time permitted, it would have been interesting to explore how the reaction dynamics vary between differently-annealed zinc oxide nanosheets, or between nanosheets decorated by surface catalysts of differing proportions. The influence of other stages in the sensor fabrication could also be examined; in Chapter 6, for instance, it was discovered that the gas sensing properties depend strongly on factors such as the centrifugation time used during LBZA preparation. Moreover, the Ostwald ripening of nanoparticles within the nanosheets was seemingly suppressed by the presence of a gold nanoparticle suspension during centrifugation, although the effect was more pronounced for a higher concentration of chloroauric acid. It would therefore be beneficial to conduct a systematic investigation into the effects of different chemical species during the centrifugation step, both in relation to the morphology and internal structure of the resulting zinc oxide nanosheets and their electrical properties.

Contents